Institute of Engineering Surveying and Space Geodesy

School of Civil Engineering

THE DEVELOPMENT OF A 3-PASS PERSISTENT SCATTERER ALGORITHM USING THE INTEGER AMBIGUITY SEARCH METHOD

Mark Andrew Warren, MSc

Thesis submitted to the University of Nottingham

for the degree of Doctor of Philosophy

July 2007

Abstract

Differential interferometric synthetic aperture radar (InSAR) is a well used technique for measuring deformations, but often suffers greatly from effects due to atmospheric differences occurring between different SAR images. Recently a new set of techniques have been developed called Persistent Scatterer techniques, which take advantage of the high number of SAR images available to try and model out the atmospheric effects. To aid this process, all present techniques make use of a Digital Elevation Model (DEM) to remove the interferometric phase due to topography, but as a consequence this contaminates the phase values with an unknown error due to the DEM, which has to be modelled out in the processing chain. In this thesis a new Persistent Scatterer (PS) method is proposed that does not use a DEM to remove the topographic phase component, but rather one of the interferograms used in the study, and hence does not need to calculate topographic height corrections. This is achieved by using the Integer Ambiguity Search (IAS) 3-Pass differential technique. The developed algorithms are then tested and assessed over two test sites in central London, UK.

The overall conclusions of the research are summarised below. The IAS 3-pass differential interferometry method gives a differential result that is more consistent with 2-pass results than with traditional 3-pass results. By using the IAS 3-pass method, it is possible to do a PS InSAR analysis without recourse to a DEM or needing to derive any topographic information. The developed IAS PSInSAR algorithms have been tested using simulated data, which has shown that the methods developed can identify small scale target motion over a period of a few years. The IAS PSInSAR algorithms were also tested using real SAR data, the results of which are consistent with GPS results of the test site and previous independent investigations.

Acknowledgements

Contents

7

List of Figures

8

List of Tables

1. Subsidence Monitoring

1.1 Subsidence

Subsidence is a type of land deformation that can be described as a sinking of the surface. It is a problem that occurs over the whole world though there are many different causes of it. It is estimated that in the U.K. over the last 10 years it has cost insurance companies over £300 million per year (*Haynes et al 2001*). Although usually only small, surface movements can cause great pressure on structures both above and below ground. In urban areas of the U.K. subsidence is often caused by either seasonal changes in, for example, clay (*Bingley et al 1999*), or mining subsidence (*Stow 1996*). Other major causes of subsidence could be soil compaction, soil shrinkage, water extraction, seismic and volcanic activity (*Whittaker and Reddish 1989*). An example of (extreme) subsidence can be seen below in Figure 1.1.

Figure 1.1 An example of (extreme) subsidence. Road collapsed beneath a bus, due to failure of weathered chalk above an abandoned mine, in Norwich, U.K. (*Waltham 1989*)

1.2 Measurement Techniques

Subsidence can involve very small movements of the surface over long periods of time, for example a slow landslide, or conversely large movements over short times, for example resulting from earthquakes. The method employed to measure subsidence depends on the scale of deformation involved, the time periods of the subsidence phenomenon and how hazardous the environment is, not to mention the "human" factors such as cost and surveying time. Classical methods for subsidence measurement usually require levelling surveys. Over the past 10 to 15 years, the methods employed have changed from these traditional levelling surveys to more modern satellite based techniques such as the Global Positioning System (GPS) and Synthetic Aperture Radar Interferometry (InSAR). This is partly due to the fact that these methods can be available at any time of day, in any weather and require less man power (therefore being cheaper).

1.2.1 GPS

The Global Positioning System (GPS) consists of a constellation of satellites (approx 24), with each one emitting a uniquely coded signal. A receiver can then pick up these signals and calculate the (pseudo-)range from the satellite to the receiver using code or carrier phase. At least 4 satellites must be in view for the receiver to calculate its 3-dimensional position. A more detailed overview on GPS for deformation monitoring is given in chapter 6.3.

1.2.2 InSAR

Synthetic Aperture Radar (SAR) is a kind of radar that is often used for Earth imaging purposes. What makes this kind of radar particularly useful is that it synthesises a long antenna (which is needed for high azimuth resolution) by combining echoes that it has received (*Ulaby et al 1982*). This means that the antenna size on the satellite can be relatively small with no loss of resolution. Satellite Radar Interferometry is a method of using satellite borne radar for

measuring distance/motion. SAR Interferometry (InSAR) is basically the combination of the phase measurements from two SAR images to create an interference pattern. This is called the interferogram, and appears as a series of "fringes", which can be related to changes in distance between the Earth surface and the radar. These changes in distance can then be related to topographic height, and with further processing techniques give an indication of surface motion. More information on these techniques is given in later chapters of this thesis.

1.3 Integrable Monitoring

The two techniques of GPS and InSAR are proving to be very useful in the monitoring of subsidence. The two techniques are complimentary to each other as can be seen from the comparisons in Table 1.1 below. But integrating the two techniques together has often proved difficult in the past.

	GPS	InSAR (ERS/Envisat)
Specialist Equipment Required by User	GPS receiver & antenna	None
Data	Free	Cost per SAR image
Spatial Coverage	Global capability - but only at receiver site. Resolution discrete points	Global - image approx. 100km * 100km. Resolution approx. 25m
Temporal Coverage	Continuous operation	Once every 35 days
Field Operatives	Requires receiver to be set up in field	No man power required
Parameter	3-Dimensional position vector	1-Dimensional line-of-sight
Archive Data	Depends on receiver locations and if data is publicly available	Available back catalogue of data from 1992 (ERS)

Table 1.1 Comparison of the two techniques: GPS and SAR Interferometry

Different methods of using the two techniques together have been proposed. The "Double Interpolation Double Prediction" method proposed and demonstrated by *Ge et al (2000)*, uses the GPS to derive atmospheric and orbital corrections for the InSAR data, and then uses the corrected InSAR data to 'densify' the GPS observations. *Williams et al (1998)*, and *Zebker et al (1997)*, present similar techniques of using the GPS to remove, or at least reduce, the

atmospheric effects on the SAR data. An obvious limitation with these techniques is that they require the GPS and interferometry data to be gathered at the same time. *Fernandez et al (2003),* used GPS to 'fill in the holes' in the InSAR data where the coherence is too low to get good measurements from the SAR data. Another method of integrating the two techniques is by using the GPS to 'validate' the InSAR data. Here the GPS time series is simply compared to, or overlaid with, the InSAR deformation to compare the measurements, as in *Colesanti et al (2003b).*

Leijen et al (2005), proposed a method for integrating the measurements of InSAR with GPS where the two sets of data are processed together in a least squares framework. This is the only approach where a 'real' integration of the two techniques as deformation measurement tools takes place. This approach may be used with a special method of InSAR called Persistent Scatterer (PS) InSAR (see chapter 5). PS InSAR uses certain pixels within a stack of SAR data to generate time series of deformation and to get a good integration result in the least squares solution, the 3D position of the PS point data is required to be known accurately.

1.4 Research Motivation

Subsidence is a global problem; it widely occurs on every continent, and is particularly of interest in built up and highly populated regions. As previously mentioned it can be a very costly thing, especially if buildings or roads are located on the subsiding ground. The detection and monitoring of subsidence can also be a very expensive process as well. A relatively new technique of radar interferometry, called Persistent Scatterer Synthetic Aperture Radar Interferometry (PSInSAR), may allow much cheaper and easier subsidence monitoring. Current methods of PSInSAR make use of a Digital Elevation Model (DEM) as a model of the local topography. These DEMs are inaccurate and introduce an error which must be solved for in the PSInSAR process.

The Integer Ambiguity Search (IAS), developed at the University of Nottingham's Institute of Engineering Surveying and Space Geodesy, gives a

method for reconstructing the absolute phase of the radar signal. Using this technique it is possible to calculate the 3-dimensional position (in an Earth centred Earth fixed Cartesian coordinate system) of the InSAR data. It also has the potential to enable improvements to be made to the 3-pass differential InSAR method.

In this thesis, it is proposed that a PSInSAR framework can be developed to take advantage of the IAS method's 3-pass technique, to allow a PSInSAR analysis without needing to model the topographic height. This is an important potential advance, since it removes the source of error relating to the reference surface from the processing chain, which could allow a greater certainty in the final results. It will also allow an easier 'error budgeting' since there is one less source of error.

Another advantage with using the IAS within the PSInSAR framework could come with analysing the results. Because the IAS gives 3-d positions within a geodetic frame it should allow for easier integration with other monitoring techniques such as GPS. For example, the integration of GPS and InSAR data through a least squares solution will need the data to be in the same coordinate system.

At the present time there is much research being done in the field of PSInSAR. Many different algorithms have been proposed that follow different processing chains or use a different selection of Persistent Scatterers. No one method is considered "the best" and a current European Space Agency research project titled "Persistent Scatterer Interferometry Codes Cross-Comparison and Certification", or PSIC4 for short, aims to test the adequacy of the different algorithms over the same test site and report the findings to the scientific community (*Raucoules et al 2005*). The PSIC4 project was commissioned after discussions about the uncertainty, accuracy and trustworthiness of PSInSAR measurements.

The aims and objectives of this PhD project are as follows:

- Validate that the Integer Ambiguity Search method works with real SAR data.

- Test the theory that the Integer Ambiguity Search method can improve upon current 3-pass Differential Interferometry by using experimental results.

- Develop a Persistent Scatterer algorithm and processing chain that does not output a topographic height model, i.e. it does not need to calculate reference surface corrections.

- Test and validate the developed Persistent Scatterer algorithm and processing chain using a suitable test site.

1.5 Outline of the Thesis

The thesis is broadly organised into two sections; conventional SAR Interferometry and Persistent Scatterer Interferometry. The first section consists of chapters 2, 3 and 4 and are organised as follows. Chapter 2 gives an introduction to Synthetic Aperture Radar, outlining the basics of radar remote sensing and the image geometry. Chapter 3 then goes a stage further and introduces the interferometric techniques of SAR processing. The steps for producing an interferogram are discussed and illustrated along with the limitations of SAR Interferometry. The differential InSAR techniques are also introduced and discussed along with their respective limitations. Chapter 4 then introduces the concept of the phase ambiguity, i.e. the fact that the absolute phase of the radar signal is unknown, and the process of phase unwrapping. The Integer Ambiguity Search method is discussed and demonstrated using some data of London, UK. The IAS differential interferometry method is also discussed, demonstrated and compared to other differential interferometry techniques. A discussion then follows on how, and under which circumstances, it is possible to improve a differential InSAR result by using a coarse DEM.

The second section of the thesis is dedicated to the methods of Persistent Scatterer Interferometry, and consists of chapters 5 to 9. Chapter 5 gives an introduction to Persistent Scatterer Interferometry and outlines the algorithm that pioneered the persistent scatterer methods; the Permanent Scatterer Technique (*Ferretti et al 1999*). It then goes on to describe the IAS Linear PSInSAR algorithm and highlight the differences between this and the Ferretti algorithm. Chapter 6 provides an introduction to the test sites that are used to test and assess the algorithm. Two test sites within the City of London have been chosen; Greenwich and Westminster. Chapter 7 describes the software that has been developed to implement the PSInSAR algorithms, and then demonstrates the algorithms using simulated data. Chapter 8 shows and discusses the results attained from the algorithm when tested on the real SAR data at the two test sites. Chapter 9 then goes on to describe a further PSInSAR algorithm for preserving non-linear deformation (*Ferretti et al 2000a*) and also describes the IAS non-linear algorithm. The IAS non-linear algorithm is then tested with simulated data and the results shown before the algorithm is tested using the two previous test sites. The results from the real data are then discussed.

Finally, chapter 10 summarises the results of the author's research and concludes the thesis. A discussion then follows on possible future research with the IAS PSInSAR algorithms.

2. Synthetic Aperture Radar

2.1 Brief History of Radar

Radar is an acronym for RAdio Detection And Ranging. The basic use of a radar is as a measuring device, whether it be for distance or time. It operates in the microwave portion of the Electromagnetic Wave Scale, usually with wavelengths between 1mm and 1m. It was originally developed in the early part of the 20th Century as a method for detecting ships and aircraft for military defence purposes *(Ulaby et al 1981),* but is now also widely used as a method of imaging. A lot of the early advances of radar came during the period leading up to (and including) World War II, with Germany, Great Britain and the US all developing radar systems *(Curlander and McDonough 1991).* The evolution from using radar as a location device to an imaging tool came with the application of the Side Looking Airborne Radar (SLAR) in the 1950s. SLARs (also known as Real Aperture Radars (RAR)) allowed a much finer resolution because they could have a larger antenna due to it being fixed parallel to the aircraft. These were used throughout the 60s and 70s for land mapping campaigns. One such campaign involved mapping 500 000 km^2 of the United States (*Ulaby et al 1981*). From this work in SLAR, the design of Synthetic Aperture Radar (SAR) systems was born. SAR is basically a SLAR which includes some further signal processing of the transmitted and received signal.

Using the understanding of airborne radars and with the extent of knowledge on space technology, it wasn't long before research turned to space-borne SAR. The first (non-military) experiments of SAR took place in the 1960's and 70's using rockets and the Apollo 17 lunar orbiter *(Curlander and McDonough 1991)*; however it wasn't until the end of the 70's before a satellite with SAR capability was launched; the Seasat mission in 1978 *(Elachi 1991)*. This was followed by the Shuttle Imaging Radar missions and Soviet missions of the 1980's. In the early 1990's, three more satellites bearing SAR were launched: the European Space Agency's (ESA) ERS-1, Japan's JERS-1 and the Soviet's Almaz-1. These were quickly followed by Canada's Radarsat and ESA's ERS-2

in the mid 1990's, and more recently by ESA's Envisat and NASA's Shuttle Radar Topography Mission (SRTM). For more detail on the history of radar see, for example, *(Curlander and McDonough 1991)*.

2.2 Radar Basics and Operation

So far, radar has been put into the context of its history. This section gives an introduction to what an Imaging Radar is and identifies some of its properties. Throughout this thesis, radar discussions will be restricted to satellite-borne radar systems.

Before an in-depth discussion of radar, it is prudent to define the terminology of an electromagnetic wave. The diagram below in Figure 2.1 shows an electromagnetic wave, describing the terminology of *wavelength, amplitude* and *phase.* Some examples of electromagnetic waves are: light, X-rays, radiowaves, microwaves and gamma rays.
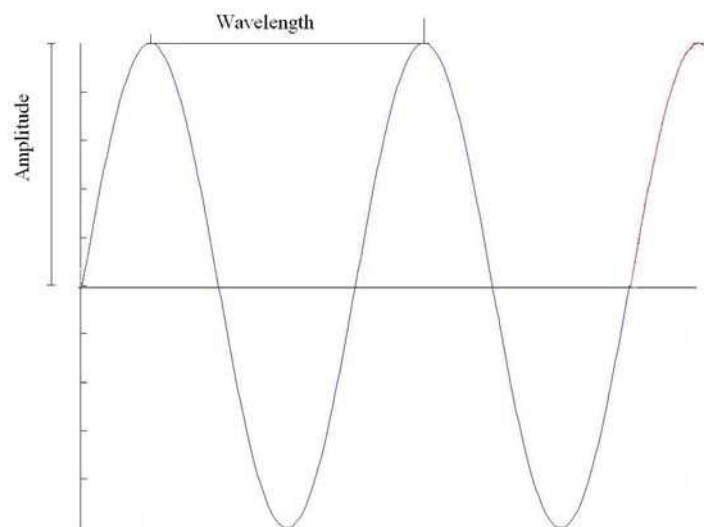
Figure 2.1 An electromagnetic wave. The wavelength is defined as the distance between consecutive peaks, the amplitude as the maximum height of the peak and the phase as the fractional part of a wavelength, shown in red.

The basic operation of radar is as follows (see Figure 2.2). Radar is an active sensor; it emits a pulse of electromagnetic radiation from the transmitting antenna and then listens for the returning echo at the receiving antenna. Most

radar systems use the same antenna for transmitting and receiving. When the return pulse is received various signal parameters are stored. These can include the phase, amplitude and receive time of the return signal as well as the polarisation *(Skolnik 2001)*. The Doppler frequency and the time delay between transmit and receive can also be derived from the data. The time delay, τ, can be used to calculate the range distance using the simple $r = c \cdot \tau / 2$ equation, where *r* is the range and *c* the speed of light.
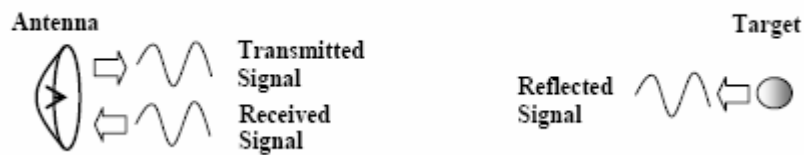
Figure 2.2 Basic operation of a radar. Signal is transmitted from antenna, bounces off target and antenna receives the reflected signal. From *(Sowter 2003a)*

The return pulses can then be collected together to generate an image if this is desired. The above example in Figure 2.2 is greatly simplified, since with each transmitted signal, more than one target is likely to reflect the signal. For each pulse these targets can be arranged in the order in which they were received, which in turn can give the range of the targets. A form of image display that has been in use since the 1940's is the plan-position indicator (PPI). The radar antenna is rotated about an axis and the return echoes form a circular image, with range given from the centre of the circle *(Ulaby et al 1981)*. These displays are often still used in aeroplanes and ships for navigation purposes.

2.3 Radar for Remote Sensing

2.3.1 What is Remote Sensing?

Remote Sensing is a term used to describe a group of techniques that can give information about something without actually physically touching the object. *Lillesand and Kiefer (2004)* define it as: "*Remote Sensing is the science and art of obtaining information about an object, area, or phenomenon through the analysis of data acquired by a device that is not in contact with the object, area,*

or phenomenon under investigation." A simple example would be photography. The result (photograph) can give you information of the subject without the user (photographer) actually being in contact with the subject. More obvious examples of instruments for remote sensing and Earth monitoring applications are: photogrammetry, LiDAR, radar and other satellite imagery techniques.

2.3.2 Why use Radar for Remote Sensing?

The first question that should be answered is why should we use radar as a remote sensing tool? As mentioned previously, radar is an active sensor. This means that it emits its own illumination. This allows radar to be used at any time of day, no matter if there is sunlight or not, giving it an advantage over optical techniques. Another advantage of radar is that the microwave wavelengths used allow it to "see" through clouds *(Ulaby et al 1981)*. This allows the interpretation of the radar images no matter if the sky was overcast or not. These two reasons show the benefits of using radar where optical imaging might fail, but there is also the reason to use radar because it gives a different *kind* of result, or a complimentary result. For example a radar image gives different information than an optical image *(Lillesand and Kiefer 2004)*. Also, microwaves are able to penetrate vegetation and soil depending on the wavelengths used and the water content of the soil. This thesis concentrates on using the SAR Interferometry (InSAR) technique. As the name suggests, SAR Interferometry uses Synthetic Aperture Radar, which is a Side Looking Radar.

2.4 Side Looking Airborne Radar

Side Looking Airborne Radars (SLARs) are the basic radar of remote sensing imaging applications. As their name suggests, they are pointed perpendicular to the direction of travel at an angle above the nadir. A discussion follows on SLAR basics including the geometry and resolution of radars. This then leads onto describing the basic operability of SAR.

2.4.1 Geometry

The geometry of the Side Looking Radar is best described using a picture, see Figure 2.3 below. The radar antenna is moving in the direction of its velocity vector, and viewing/imaging in the direction perpendicular to this. The radar moves in the *azimuth* direction and views to the *range* direction. The *satellite track* or *nadir track* is the path the satellite follows projected onto the surface in the *nadir* direction. The *look angle* is the angle between the satellite nadir and the radar beam. It is common notation to describe the look angle as being between the nadir and the centre line of the radar beam. The *azimuth beamwidth* of the radar is equal to the wavelength divided by the antenna length, and determines the size of the area illuminated, in the azimuth direction, of each pulse. The *swath width*, or size of the illuminated area in the range direction, is determined by the *elevation beamwidth* which is equal to the wavelength divided by the antenna width. This together with the look angle determines the area imaged. The edge of the radar image nearest to the radar is called *near-range*, and the furthest is called *far-range*.
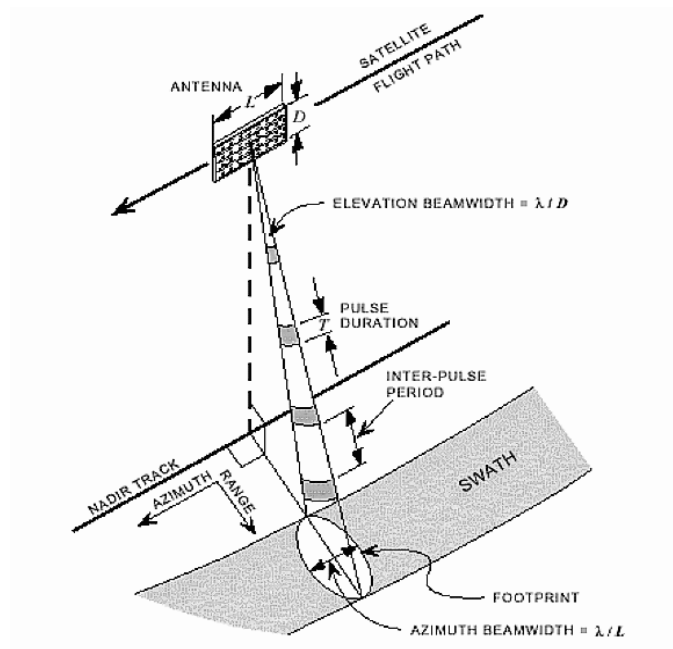
Figure 2.3 Geometry of a Side Looking Radar *(Olmsted 1993)*

As the radar moves along it flies in a straight line emitting short pulses at a rate called the *Pulse Repetition Frequency* (PRF). The returns of each one of these pulses makes up a range line in the radar image. The pulse returns are arranged

25

parallel so as to form an image. Each pixel of this image has two associated coordinates: an a*zimuth time* coordinate which gives the time the range line was imaged, and a r*ange time* coordinate which gives the elapsed time between transmitting and receiving the pulse echo. The range time coordinate may be given as a range value (metres) instead. The term range can be confusing when discussing radar images; the terms *slant-range* and *ground-range* are used to distinguish between distances relating to radar geometry and ground respectively. This is illustrated in Figure 2.4, where S is the satellite, and the range between two targets T1 and T2 is shown in both slant range and ground range.
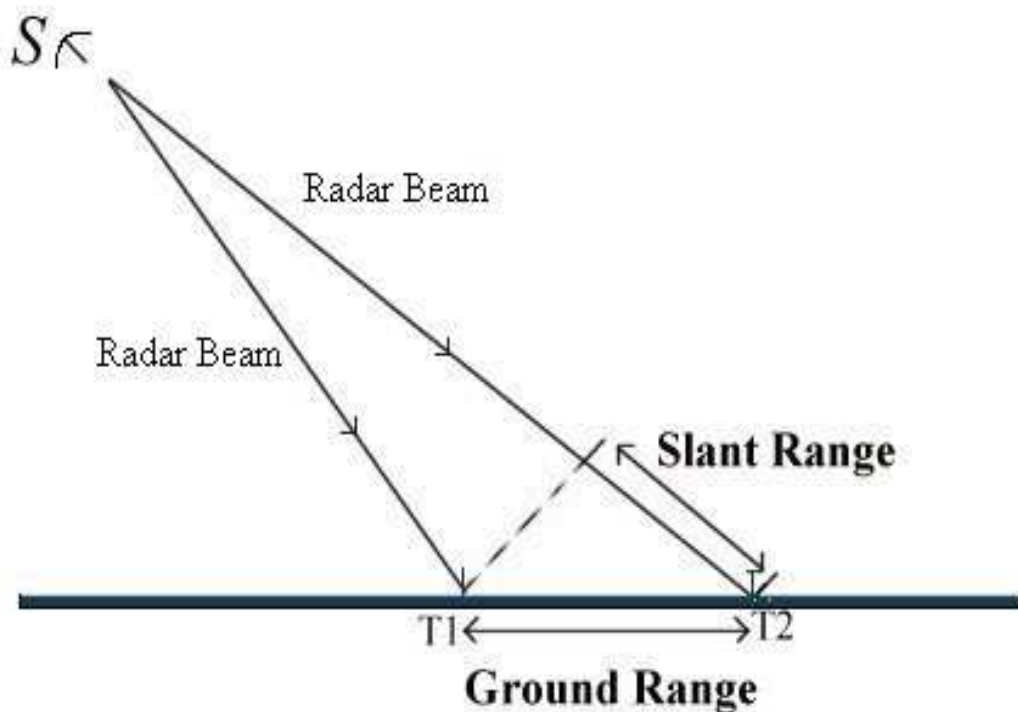
Figure 2.4 The geometric difference between slant and ground ranges.

2.4.2 Spatial Resolution

Spatial resolution is defined as the shortest distance between two points such that they can be distinguished as separate points in the radar image *(Curlander and McDonough 1991)*. This is obviously a very important aspect of Imaging Radars, which would ideally have a resolution high enough to resolve any two points. In practice this is not possible. The spatial resolution can be described in two separate parts; *range resolution* and *azimuth resolution*.

2.4.2.1 Range Resolution

The range resolution describes the spatial resolution in the range direction, i.e. for each pulse, what is the minimum separation (in ground-range) of two targets such that they can be resolved in the radar image. This is equivalent to having two separate echoes received at the radar. For this to occur, the separation of the two targets (A and B say) must be such that the pulse cannot travel from point A to B and back to A again before the whole pulse has been reflected from A *(Curlander and McDonough 1991)*. That is, the two targets A and B must be separated by a distance (in slant range) greater than half the pulse length. Figure 2.5a shows this from a geometrical point of view. Two objects A and B will not give two resolvable echoes at the radar S, whereas the two targets C and D will be discernable. Figure 2.5b shows the same thing in terms of the pulse responses. This implies that a shorter pulse width will give a higher spatial resolution in the range direction, as Eqn 2.1 shows,

$$R_G = \frac{R_S}{Sin\theta} = \frac{c\tau}{2Sin\theta} \qquad \qquad 2.1$$

where R_G is the resolution (in ground range), R_S the resolution in slant range, τ is the pulse length and θ the incident angle. But due to the relationship between pulse width and pulse energy, this is only true up to certain limits for a reliable Signal to Noise Ratio (SNR) *(Curlander and McDonough 1991)*.

Because of the SNR limits, a pulse compression technique is applied such that a long, low power pulse can simulate a very short, high powered pulse. This is achieved using frequency modulation, with the returns being processed accordingly to remove this effect (*Ulaby et al 1982*), and gives the updated range resolution equation:

$$R_G = \frac{c}{2B\sin\theta} \qquad \qquad 2.2$$

where B is the bandwidth of the pulse.
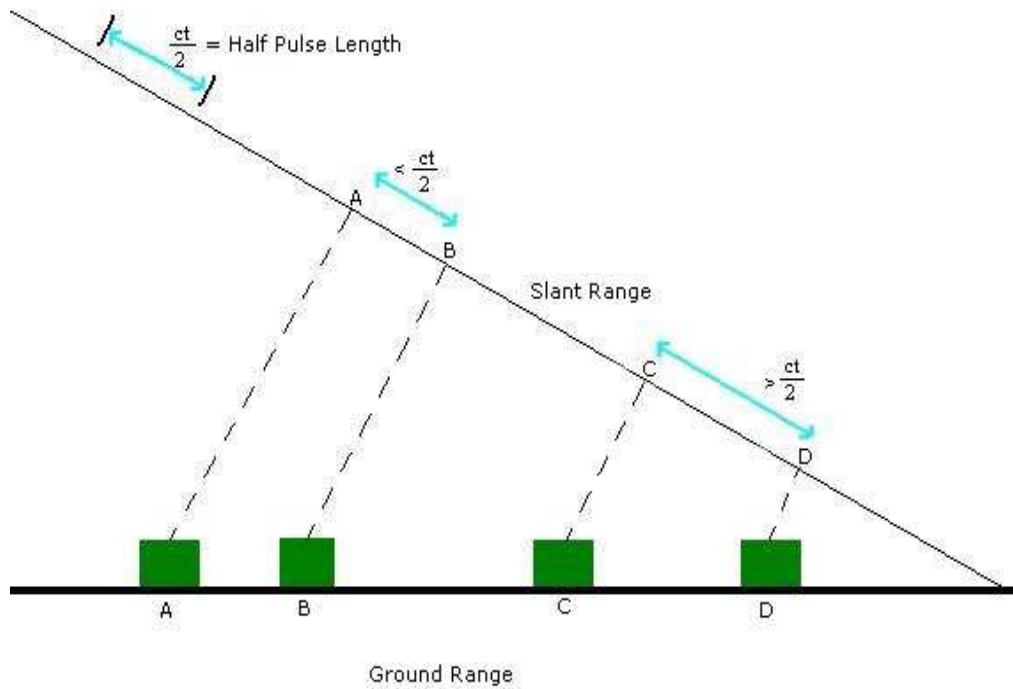
Figure 2.5a. Range resolution: geometry. A geometrical view of two targets, A and B, that will be inseparable in the radar image since they are separated by less than half a pulse length; targets C and D will give separate responses in the image because they are separated by greater than half a pulse length.
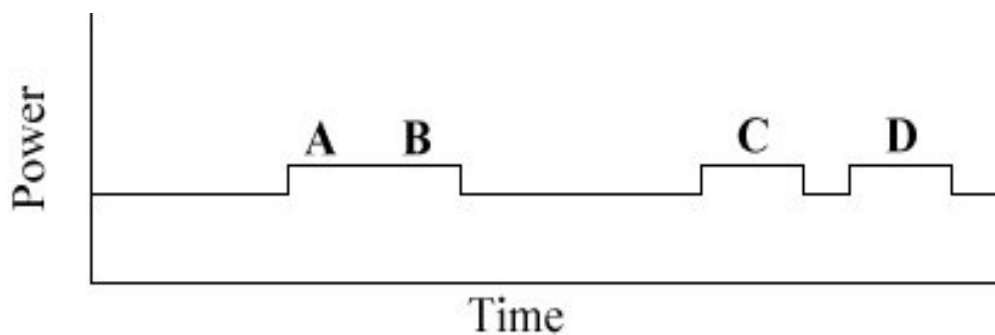
Figure 2.5b. Range resolution: pulses. The equivalent of Figure 2.5a in terms of pulses received by the radar. The returns from A and B overlap and so will be detected as one response, whereas C and D do not overlap and so will give separate responses.

2.4.2.2 Azimuth Resolution

The azimuth resolution describes the spatial resolution in the azimuth direction. For two objects (at the same range value) to be resolved in the azimuth direction they need to be in different pulse returns (never in the same one), i.e. they need to be separated by at least the size of the illumination on the surface. This is given by the azimuth beamwidth, β, and the slant range, R_S, to the surface:

$$R_A = \beta R_S = \frac{\lambda R_S}{L} \qquad\qquad 2.3$$

where λ is the radar wavelength and L the size of the radar antenna. It can be seen that a large antenna length and small wavelength will give a better resolution, but that the resolution deteriorates with range from the satellite. Figure 2.6 shows the azimuth resolution deteriorating as slant range increases.
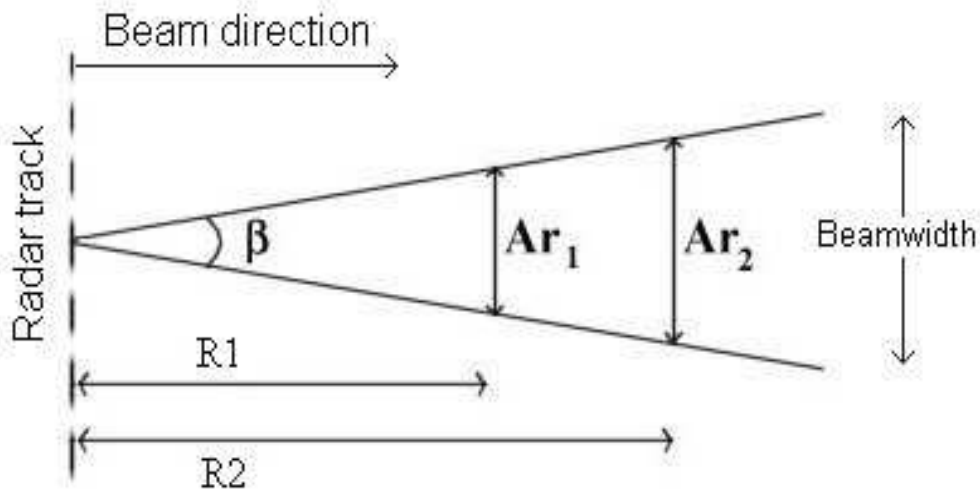
Figure 2.6 Azimuth resolution. Different resolutions, Ar_i, given by slant range Ri and azimuth beamwidth β.

The size of antenna is a limiting factor for SLAR, and it is impractical to have a large antenna on a satellite. This is a difficulty for using satellite SLAR as a remote sensing tool. To quote an example from *(Curlander and McDonough 1991)*, "*The Seasat antenna at an altitude of 800km would attain a SLAR resolution of 18km*". That is with an antenna size of approx. 10m. This apparent limitation is overcome by SAR systems (see section 2.5).

2.4.3 Geometrical Distortions

SLAR images have three main geometrical distortions associated with the side looking aperture: *foreshortening*, *layover* and *shadow*. They are described in turn below and illustrated in Figures 2.7, 2.8 and 2.9.

Foreshortening is the name given to the phenomenon shown in Figure 2.7. The front slopes of raised features appear shorter than the back slopes in radar

images, giving the appearance that they "lean" towards the radar. This occurs when the terrain slope is less than the incident angle *(Curlander and McDonough 1991).*
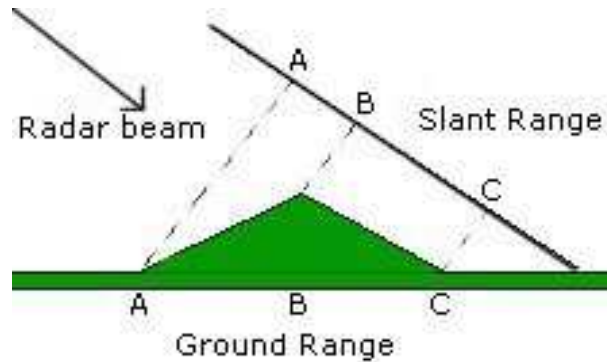
Figure 2.7 Foreshortening: length AB appears much shorter in slant range than in ground range.

Figure 2.8 describes Layover, which occurs when the terrain slope is much greater than the incidence angle *(Curlander and McDonough 1991).* In the image it would appear that the top of the slope is "laying over" the bottom.
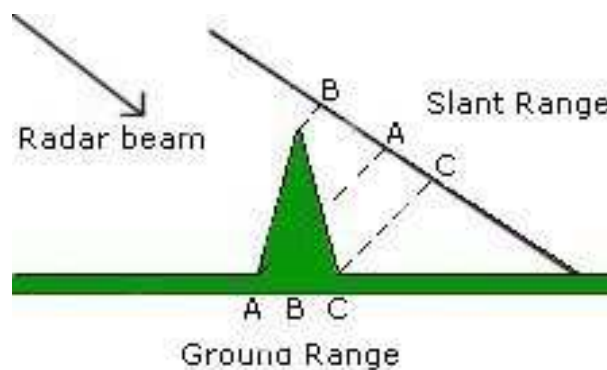
Figure 2.8 Layover: point B appears before point A in slant range.

Finally, shadow is shown in Figure 2.9. This occurs when the terrain blocks the signal from hitting anything behind it, and so occurs on steep back slopes and results in a dark area on the radar image.
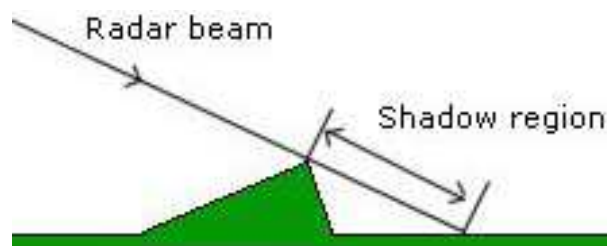
Figure 2.9 Shadow: terrain blocks radar signal

2.5 Synthetic Aperture Radar

Synthetic Aperture Radar (SAR) systems are a special case of SLAR that overcome the problems of poor azimuth resolution by utilising some further signal processing algorithms. By observing the Doppler shift of a target response as the radar moves along track it is possible to synthesise a much larger antenna. The SAR principle is shown in Figure 2.10. The target T is in each of the pulse returns from the radar as it moves along, in the direction of V, the distance S metres shown. From the processing of these returns an antenna length of S metres is synthesised, from the real aperture size R. The azimuth resolution limit for this process is *(Ulaby et al 1982)*

$$R_A = \frac{L}{2}$$ 2.4

where L is the antenna length, which seems counter-intuitive that a smaller antenna should lead to a better resolution. This can be partly explained by the fact that a smaller antenna size will lead to a larger beamwidth, meaning a target will be in more returns and hence a larger aperture can be synthesised.
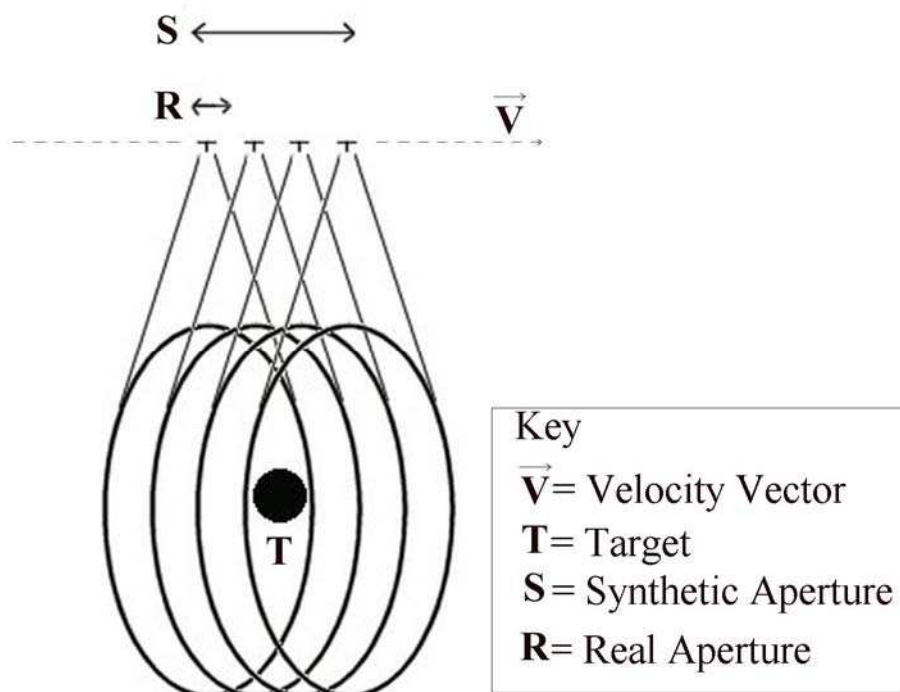
Figure 2.10 Synthetic Aperture principle. The target T is in many radar returns, from an antenna with length R, moving along the direction V. Processing can synthesise an antenna length S.

This assumes 1-look statistics, that is, that the full size synthetic aperture is used. What is more usual is that a greater number of looks is used, say N. With N-looks it means that the synthetic aperture is split up into N non-overlapping segments, to generate N independent images *(Ulaby et al 1982)*. These are then averaged together resulting in an image with lower *speckle* noise (see section 2.7) but resulting in a degradation of spatial resolution. The azimuth resolution of an N-look SAR image is given by

$$R_A = \frac{NL}{2}$$
2.5

For a more detailed analysis see *Ulaby et al (1982), Curlander and McDonough (1991)*.

2.6 Radar Equation and Backscatter

The part of the reflected radar signal that is received back at the radar is called *backscatter,* and is of obvious importance. In a radar image, if the backscatter of a particular resolution cell is high then the image pixel will be bright; alternatively for low backscattering values the pixels will be dark. There are various parameters that can have an effect on the amount of backscatter received by the radar: wavelength of the transmitted pulse, polarisation, incidence angle, surface roughness and moisture content (*Ulaby et al 1986*). The parameter of prime importance to radar imaging interpretation is the surface roughness. Figure 2.11 shows the backscattering characteristics of various surface types.

The moisture content of the surface target affects the backscatter due to the change of the *dielectric constant*. The dielectric constant tends to increase as the water content increases, which affects the depth of penetration by the radar signal (*Sabins 1997*). This usually leads to an increase in backscattering.

The surface roughness (which is related to the surface type: forest, water, rock etc) is the main (uncontrollable) effect that affects the backscattering. This is best explained in Figure 2.11.
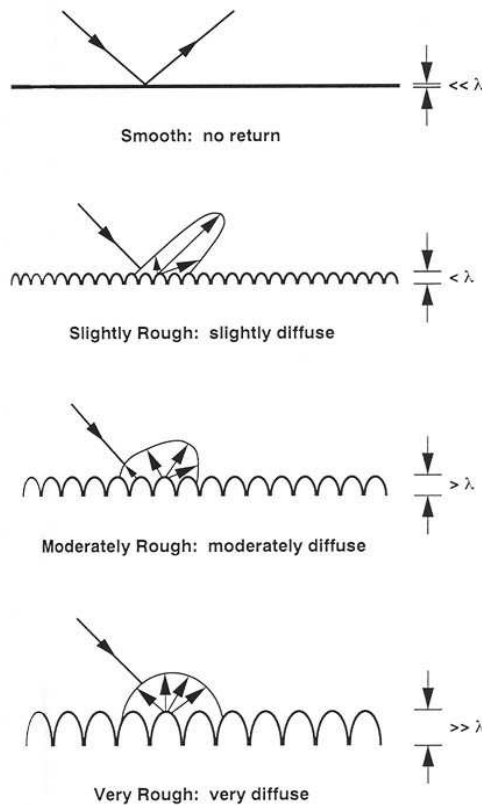
Figure 2.11 Surface scattering effects from differing surface roughness *(Farr 1993)*

Smooth surfaces (such as calm water) act as *specular* reflectors *(Lillesand and Kiefer 2004),* do not reflect much signal back to the radar and so will appear black in the image. A rough surface acts as a *diffuse* reflector and will reflect more of the signal back to the radar. These appear as shades of grey in the radar image depending on how much backscatter is received. Typically, bright returns will be received from *corner* reflections, double bounces or surfaces orientated such that most of the signal rebounds towards the receiver.

The radar parameters (wavelength, polarisation and look angle) all affect the backscatter. As previously stated, the wavelength of the microwave radiation can alter the penetration depth of and cause different responses over vegetated and forest areas. The polarisation (the orientation of the magnetic and electric fields) of the radiation can also affect the backscatter due to a different response from different surface types *(Sabins 1997)*.

To relate the characteristics of the radar parameters and the target, the radar equation is used. The radar equation for a point target is defined as *(Curlander and McDonough 1991)*

$$SNR = \frac{PG\sigma A}{(4\pi R^2)^2 kFTB}$$ 2.6

where SNR is the signal-to-noise ratio, P is the transmitted power, G is the antenna gain, σ is the cross sectional area of the scatterer, A is the antenna area, R is the target range and k, F, T and B describe the noise in the receiver. σ is usually normalised to σ^0 (sigma-nought) and measured in dB and is the parameter of most interest (after the radar design process) giving information about the target. σ^0, the average radar cross section per unit area, gives the area of a scatterer that would return the received power at the antenna (*Campbell 1996*).

2.7 Speckle

Speckle is a thermal noise term inherent in all radar images. On a radar image it appears as a grainy texture *(Goodman 1976)*. It occurs due to the coherent nature of radar. With multiple scatterers in the resolution cell the signal suffers constructive and destructive interference and, because of this, if the same resolution cell was imaged twice from slightly different geometries, two different results could be received *(Li and Goldstein 1990)*. Speckle has a multiplicative effect on the image intensity, that is, the mean and standard deviation are linked. So for a brighter target response, we get more noise. For the phase of a resolution cell however, a zero-mean complex Gaussian number represents it (*Zebker and Villasenor 1992*). As previously stated speckle can be reduced by taking multiple looks or by using some specialised filters *(Lopes et al 1993)*.

2.8 Phase of a Resolution Cell

The phase of a resolution cell is constructed from different components. In the most general terms, the phase is made up of two components: geometry and scattering *(Bamler and Hartl 1998)*. The geometrical component is the phase

value due to the range from the radar, i.e. the number of cycles from the antenna to target and back again. For the resolution cell this is often equivalent to the distance from radar to centre of cell. The scattering phase component is due to the interaction of the radar signal with the targets in the resolution cell. For single point scatterer targets (i.e. one reflector in the resolution cell) the phase will relate to this target. For Gaussian scatterers (i.e. a high number of random scatterers in the resolution cell) the phase of a single cell contains no useful information (*Zebker and Villasenor 1992*).

In reality the phase will be made up of extra components, for example there could be terms due to atmospheric refraction, thermal and random noise. Speckle will also occur since the resolution cell will usually include multiple scatterers.

2.9 Summary

An introduction to radar for remote sensing has been given with an emphasis on space-borne radar. The geometry and the terminology of remote sensing radar have been described for side-looking systems. Synthetic Aperture Radar (SAR) has been introduced and its advantages over Real Aperture Radars (RAR) have been described. The Radar Equation and the scattering effects of microwaves have been shown, together with a description of speckle and the phase of the radar resolution cells.

3. SAR Interferometry

3.1 Interference

Interferometry is a technique that studies the interference patterns created from two waves. This is not a new technique. For example, two classical science experiments that demonstrate the interference of (light) waves are Newton's rings and Young's slits, which were carried out hundreds of years ago. Figure 3.1 below helps to show how two waves interfere. Where the interfering waves are in-phase, *constructive* interference occurs and the amplitude of the resulting wave is increased. Where the waves are out of phase, *destructive* interference occurs and the amplitude of the resulting wave is decreased.
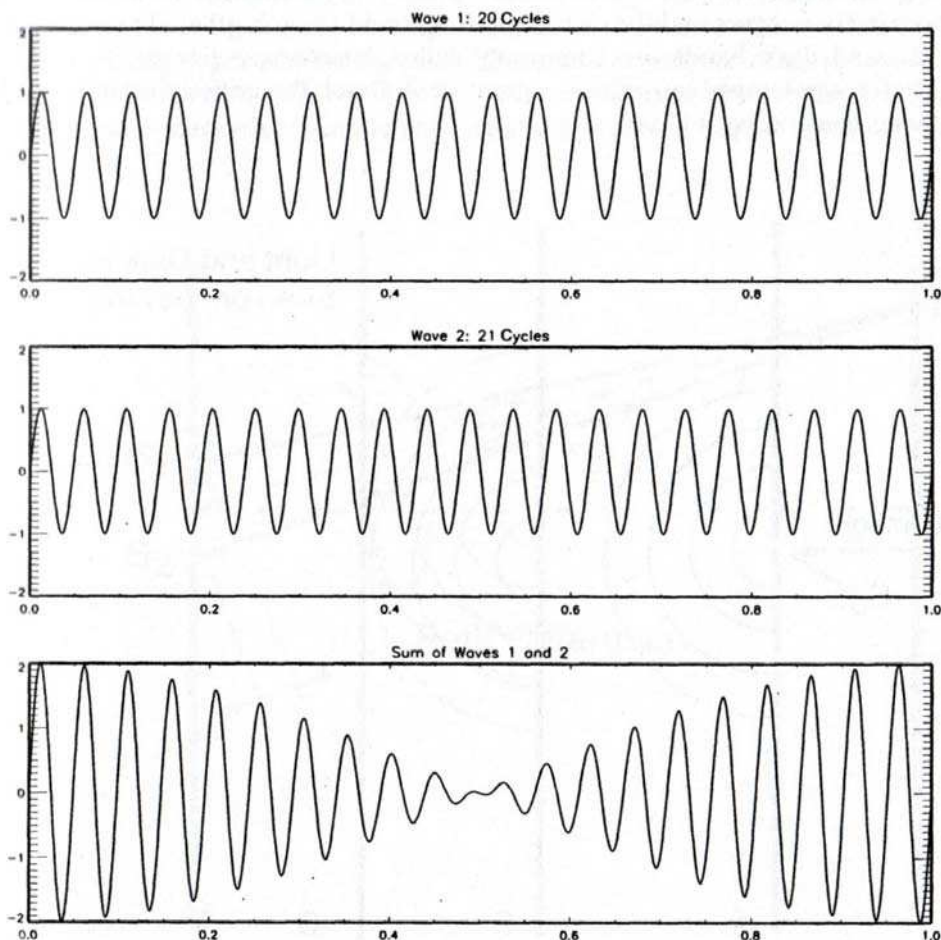
Figure 3.1: Constructive and destructive interference. Plots 1 and 2 show two waves which cycle in and out of phase. Plot 3 shows the interference of the two waves, the amplitude increases when they are in phase and decreases where they are out of phase. (*Ghiglia and Pritt 1998*)

3.2 Interferometry

SAR Interferometry (InSAR) is a scientific technique that exploits the phase difference between two SAR images. In other words, the interference pattern between the phase of the two SAR images is formed. This is known as the *interferogram*. The interferogram (or interferometric phase) contains the data of the relative geometries of the two SAR images *(Massonnet and Feigl 1998)*. When viewed, the interferogram appears as a series of *fringes* denoting where the interferometric phase completes a full cycle (0-2π radians).

The first InSAR results for Earth Observation were created using airborne radar data *(Graham 1974)*. Here they were concerned with using the phase differences to model the topography of the surface. The interferometric phase is a measure of the difference in the phase between the two SAR images, which in turn can be related to difference in radar signal path length (see Figure 3.2). Using the aircraft positions it is then possible to relate this path difference to surface topography. This is the main application of SAR interferometry: topographic mapping/DEM generation *(Small 1998)* but it is also often used for land classification *(Askne and Smith 1996*).

Early space based InSAR results were achieved using data from the Seasat satellite *(Goldstein et al 1988)* and the Shuttle Imaging Radar (SIR) missions *(Gabriel and Goldstein 1988)*. The SIR missions were the precursors to the Shuttle Radar Topography Mission (SRTM) of 2000 *(Jordan et al 1996)*, where a SAR on board the space shuttle imaged the Earth to generate a near-global DEM from the interferometric analysis of the resulting data. An important part of InSAR history was when the European Space Agency's ERS-1 satellite was launched in 1991, which had an onboard SAR. This satellite allowed SAR images to be acquired and made freely available with near global coverage. Having only one antenna on board, interferometric analyses are done using the *repeat-pass* style. This is where the satellite images the area twice on separate orbital passes. This is different to the SRTM space shuttle mission where the SAR had a dual antenna system with a fixed separation. Here, one antenna

transmits whilst both receive the echoes. The echoes will be received at different times at each antenna, related to their baseline separation.

Due to the high grade components of the ERS-1 satellite, the SAR products it developed were of high quality. For interferometry to give the best results the satellite positions need to be known accurately. This led to precise orbits being generated for the ERS satellites which had much better accuracy than the nominal orbit information *(Closa 1998; Reigber et al 1996)*. During different phases of its lifetime, ERS-1 had different orbital repeat periods. The nominal repeat period was 35 days. The ice phases saw ERS-1 have a repeat period of 3 days. This would allow an improvement to the temporal decorrelation effect (see section 3.5)

In 1995 ESA launched a second SAR capable satellite, ERS-2, with the same instrument characteristics as ERS-1. Put into a similar orbit as ERS-1 it allowed interferometry to be performed using both sensors; one image from ERS-1, one from ERS-2. ERS-2 was put into an orbit 24 hours behind ERS-1, allowing interferometry to be performed with a short *temporal baseline*, or separation, between image observations. Interferograms made up of two images separated by this 1 day baseline are called Tandem pairs.

As previously stated, the main uses for interferometry have been for topographic mapping and for land classification. With further processing, however, it is possible to allow the identification of surface changes. This uses a technique known as *Differential Interferometry* (see section 3.7).

3.3 The Interferometric Configuration

It is necessary for further discussions to now identify the important factors for interferometry and discuss the geometric configuration. Figure 3.2 shows a typical spaceborne InSAR configuration. S1 and S2 denote the satellite positions when the first and second SAR images were taken. The 3 dimensional distance between them is called the (*geometric*) *baseline* and is denoted as B in Figure 3.2. The *perpendicular baseline,* $B\perp$, is the component of B in the

direction perpendicular to the S1 look direction. R1 and R2 denote the *ranges* to the target T from satellite positions S1 and S2 respectively.
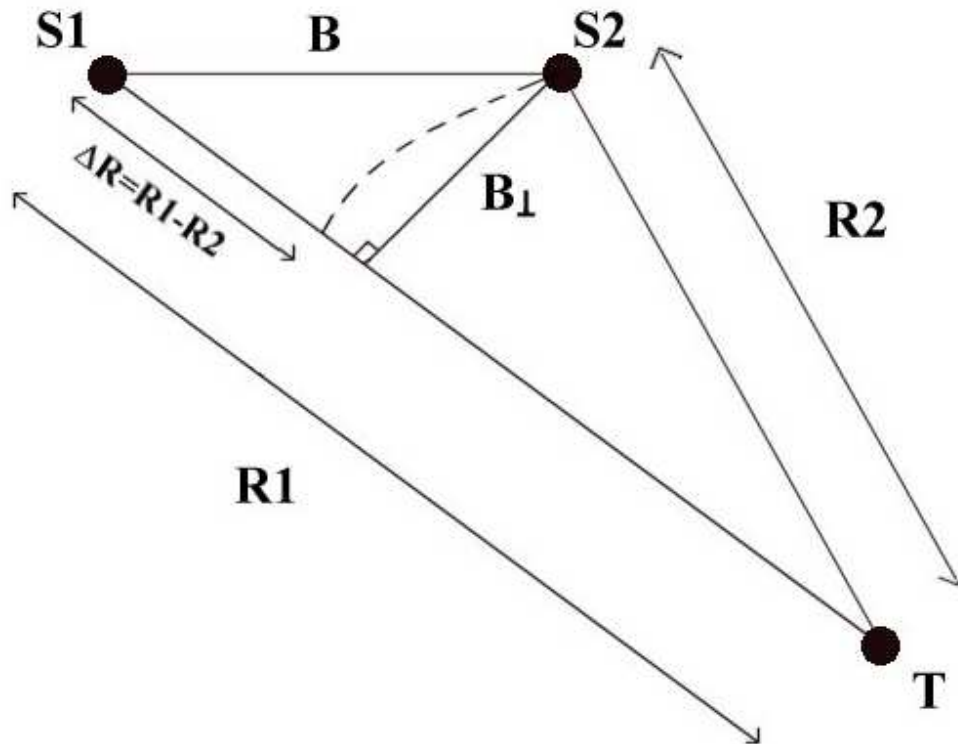
Figure 3.2 Interferometric Configuration. Satellites S1 and S2 have ranges to target T R1 and R2 respectively. The separation between the satellites is called the baseline and is denoted by B.

The difference between the two ranges is denoted ΔR and is related to the interferometric phase. The two way signal travelling this extra distance ΔR will have travelled:

$$\frac{2}{\lambda}\Delta R \hspace{6cm} 3.1$$

wavelengths, where λ is the signal wavelength, then the phase ϕ related to ΔR (the interferometric phase) is given by:

$$\phi = \frac{4\pi}{\lambda}\Delta R \hspace{5.5cm} 3.2$$

There is a maximum value for the baseline after which interferometric analyses with baselines greater than this value will give meaningless results, due to the fringe rate being too high (>2π per resolution cell). This is known as the *critical baseline*. For ERS 1/2 in areas of flat terrain this has a value of approximately 1.1km *(Bamler and Hartl 1998)*.

3.4 Forming the Interferogram

Recall from section 3.2 that the interferogram is the interference pattern between two SAR images. The interferometric processing chain can be split up into several different stages. The processing chain, starting from SLC (Single Look Complex) data is outlined below. SLC data is SAR data which has already been focused, i.e. the raw SAR data is passed through some complicated algorithms that utilise the range and Doppler information of the data to focus it (*Ulaby et al 1982*; *Curlander and McDonough 1991*). The data is complex data, i.e. it contains information about the phase and the amplitude of the radar signal. All SAR data used in this study were ESA SLC data. The main steps in generating the interferogram are highlighted below in bullet points.

- Coregister the two SAR images
    - Generate coregistration equations
    - Resample the *slave* image
- Create the complex interferogram
- Extract and filter the phase interferogram
- Flatten the interferogram
- Generate a coherence image

There is plenty of literature available on forming the interferogram, for example *(Hanssen 2001)* and *(Small 1998)*. In this study all interferograms have been formed using the Doris software available from Delft University *(Kampes and Usai 1999)*. A description of the above steps follows.

3.4.1 Image Coregistration

The first stage of the processing chain is the coregistration of the two SAR images. Because with repeat pass satellite interferometry the two images are taken at different times, on slightly different orbits and with different start-stop times, they will not be of exactly the same area. Due to the satellite geometry they will almost certainly have some small rotation between them. This must be

40

addressed since for interferometry it is vital that the two images are registered to sub-pixel accuracy (*Hanssen 2001*) as described below. The coregistration is usually split up into two stages; the first being a coarse coregistration to find the approximate line and pixel offset, and the second stage is a fine coregistration to get the sub-pixel accurate offsets.

Coarse coregistration is usually performed either using the orbit information together with the Range and Doppler equations (see Equations 4.8 and 4.9), or by calculating the correlation between the power of the two images at various points. Using either of these techniques can usually give the image row and column offsets to within 2 or 3 pixels.

Fine coregistration is usually performed by a cross-correlation technique either using the full complex data (coherent registration) or either of the amplitude or phase of the signal (incoherent registration). For a set of windows over the images the correlation is calculated, which yields an offset vector for that window. Then these offset vectors can be used to determine a polynomial equation to calculate the offsets for every pixel in the slave image. *Just and Bamler (1994)* suggest that an accuracy of $1/8^{th}$ of a pixel in coregistration is sufficient for interferometry, since it yields a negligible 4% decrease in the coherence (assuming relatively small squint angles). The coherence can be described as the correlation between the two SAR images and is discussed in section 3.5.

3.4.2 Resampling

This stage uses the coregistration equation derived from the previous step and an interpolation kernel to resample the slave image. This is required so that the two SAR images are on the same grid, so they can be easily compared and the interferogram formed. The choice of kernel function depends on how accurate the answer needs to be and how much computational time is available. *Hanssen and Bamler (1999)* suggest that using a 6-point cubic convolution is a good method. It should be pointed out that the resampled slave size is at most the size of the overlap between the master and slave images.

3.4.3 Interferogram Formation

The interferogram can now be formed using the master and resampled slave images. Because the SAR images are complex (have amplitude and phase information) the *complex interferogram* can be formed by multiplying one SAR image with the conjugate of the other. This results in multiplying the amplitudes but differencing the phase information. Interferometry applications are generally only interested in the phase information and the term *interferogram* is used to describe the *phase interferogram*. An example of which is shown in Figure 3.3.
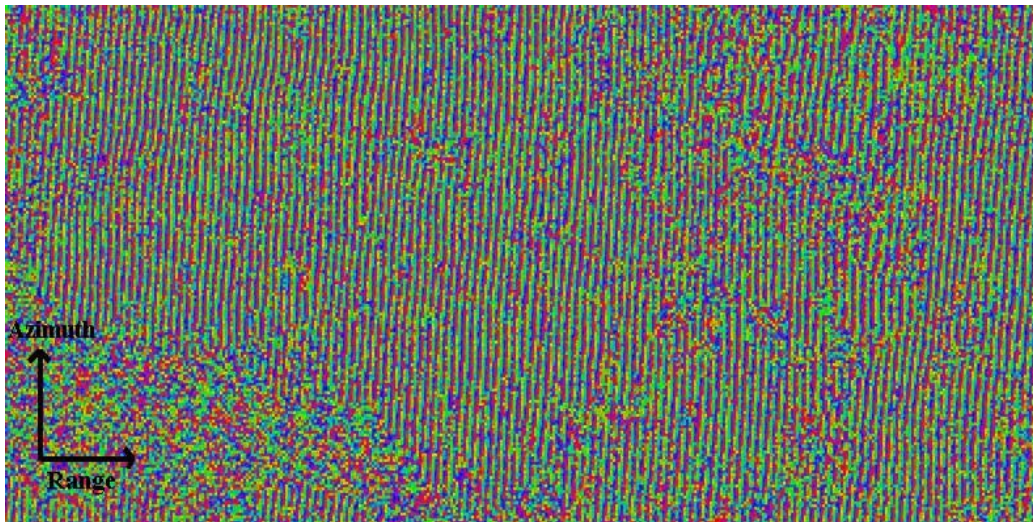
Figure 3.3. An example of a (phase) interferogram: constructed from an ERS Tandem pair, dates 9th and 10th November 1995.

This is a 2-dimensional array or image that holds the phase information of the two SAR images. The phase increases rapidly in the range direction and appears as coloured fringes, where each fringe represents the phase value modulo 2π. The rapid increase is due to the natural increase in distance from the sensor across the image, which can be modelled by using an ellipsoidal Earth model such as the WGS84 ellipsoid.

3.4.4 Filtering and Noise Reduction

Noise reduction and filtering techniques are commonly applied to the interferogram to "clean up" the product for easier interpretation and future processing (such as phase unwrapping). It is common to apply some filtering techniques after the interferogram is formed (*a posteriori* filtering), but also during the coregistration\resampling stages before interferogram construction (*a priori* filtering).

3.4.4.1 A priori filtering

This usually consists of filtering the SAR data in both the azimuth and range directions separately with the overall aim of increasing the signal-to-noise ratio. As an example this can be achieved using bandpass filtering in the frequency domain of the signal to remove non-overlapping parts of the two SAR signals (*Hanssen 2001*).

3.4.4.2 A posteriori filtering

The most commonly used technique here is multilooking (*Goldstein et al 1988*). This reduces the noise in the interferogram by simply averaging the complex data. It is often applied with multiples of a ratio of 1:5 (range : azimuth) as this creates almost square pixels (ESA SLC pixel size is approximately 20m in (ground) range and 4m in azimuth).

There are other filters that can be applied to the phase information of the interferogram. Two such filters are a spatial convolution and the Goldstein filter (*Goldstein and Werner 1998*). A spatial convolution filter is equivalent to a square boxcar filter, which tend to work well in flat areas (*Hanssen 2001*) but can fail in areas of high fringe rate. The Goldstein filter, on the other hand, is an adaptive filter that filters depending on the fringe rate.

3.4.5 Phase Flattening

Usually before filtering or multilooking the phase, it is *flattened*. This is where a reference phase is subtracted from the phase interferogram. The reference phase is either produced from a digital elevation model of the scene area, or if no ground truth is available, a satellite-ellipsoid model. This is undertaken to reduce the fringe rate of the interferogram and is essential for phase unwrapping methods because of the need for small phase gradients (see chapter 4). The flattened example from Figure 3.3 is shown below in Figure 3.4, where the WGS84 ellipsoid has been used as the Earth model. Because the reference phase used was a flat (i.e. no topography) ellipsoidal model, the resulting flattened interferogram shows fringes which, ideally, relate to the changes in topography.
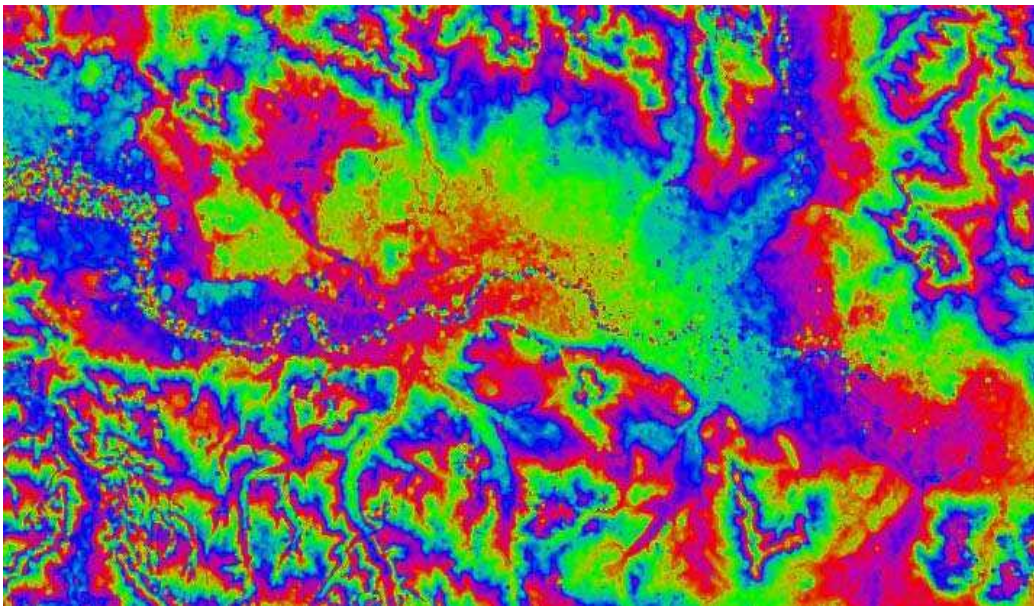
Figure 3.4 An example of a flattened interferogram: covering same area as Fig. 3.3; also some phase noise filtering has been performed.

3.5 Coherence Image and Decorrelation

The coherence image (or complex correlation) is an important by-product of the interferogram formation. It is basically the result of a correlation test between the two SAR images and gives an evaluation of the reliability of the phase values (*Zebker and Villesenor 1992*). It is calculated thus:

$$\gamma = \left| \frac{\langle M.S^* \rangle}{\sqrt{\langle |M|^2 \rangle \langle |S|^2 \rangle}} \right| \qquad 3.3$$

where γ is the coherence, M and S the complex pixel values for the master and slave respectively, and $\langle\ \rangle$ represents the averaging over a neighbourhood. Values for γ range between 0 and 1 where a value of 0 means there is no correlation and 1 means perfect correlation between the two signals. If the pixel (and surrounding neighbourhood) has a high correlation value then the scattering properties of the pixel have not changed much between the two SAR images, giving more confidence in the phase value. Often these areas tend to be in urban environments. Areas of low coherence have low phase reliability. Such areas could be due to expanses of water, agricultural activity, or other regions that could change between SAR acquisitions. The coherence image that relates to the interferogram from Figures 3.3 and 3.4 is shown below.

Figure 3.5. An example of a coherence image: corresponding to interferograms from Figs. 3.3 and 3.4; the river Thames can be easily identified from this image.

The two main types of decorrelation in interferograms are temporal decorrelation and geometric decorrelation, and can be minimised by selecting suitable SAR images to construct the interferogram from. In general, temporal decorrelation can be minimised by selecting SAR images with a short temporal baseline. For instance, data from the ERS Tandem mission (1 day temporal

baseline) will generally have a higher coherence than data from a 35 day repeat. This is because during the course of 1 day very little will change to the observation area *(Zebker et al 1994a)*. For larger time periods this is not true, for example vegetation can grow changing the scattering characteristics of the resolution cell. Urban areas generally remain coherent over long time frames.

Geometric decorrelation can be minimised in a similar way, by selecting SAR images that have small geometric baselines. As the distance between the SAR images grows (i.e. as the baseline increases), the look angles of the SAR differ by more and therefore the scattering in the resolution cell differs more *(Li and Goldstein 1990)*.

3.6 Limitations of Interferometry

As previously stated, the interferometric phase is related to the topography of the scene. In an ideal world this would be exact and there would be no phase corruption. Unfortunately this is not true and the phase will be erroneous, probably due to a number of sources including (but not limited to): speckle noise, atmospheric pertubations, temporal decorrelation, geometric decorrelation and orbital inaccuracies.

Speckle has been discussed previously and for interferometric purposes is usually dealt with by averaging pixels, known as complex multilooking (*Goldstein et al 1988*). Temporal and geometric decorrelation effects have also been discussed in the previous section.

Inaccuracies in the orbit will obviously cause errors to occur in the phase and reveal themselves as a phase slope across the image *(Zebker et al 1994a)*. This can be corrected by using ground control to estimate what the correct phase should be and modelling the slope. Also by using precise orbits the phase quality will improve due to the higher orbit accuracy.

The size of the geometric baseline has an effect on how sensitive the interferogram is to height change. Larger baselines give an interferogram that is

more sensitive to height change, i.e. for larger baseline interferograms, a cycle of phase relates to less change in height than for a smaller baseline interferogram *(Bamler and Hartl 1998)*. Due to the baseline decorrelation, a trade off between height sensitivity and phase noise must be attained.

Changes in the atmosphere between the two SAR images have a detrimental effect on the interferometric phase since these differences will propagate through into the interferogram. For short baseline interferograms used for DEM generation this is not too important due to the low height sensitivity *(Hanssen and Feijt 1996)*. But it does become more important for differential interferometry techniques (see chapter 3.7), where the magnitude of the error is not dependent on baseline (*Zebker et al 1997*). Due to the nature of the atmosphere, the phase errors it causes are spatially correlated but with a high variation both temporally and spatially *(Hanssen and Feijt 1996)*. This makes it virtually impossible to remove the atmospheric anomalies using only a single interferogram. Further discussions on atmosphere effects on interferometry can be found in *(Hanssen 2001), (Williams et al 1998)* and *(Zebker et al 1997)* amongst others.

So far, the limitations discussed have mainly been linked to errors in the phase values. But there are more basic and obvious limitations such as getting the data. The present SAR capable satellites are not dedicated SAR satellites; they also have other instruments on board, some of which might not be able to operate at the same time as the SAR. The power consumption of the SAR is also a factor as to how long it can operate for. Moreover, the repeat cycle of the satellite is a limiting factor for data collection. For example the ESA ERS and Envisat satellites have a 35 day repeat period, which might not be as often as required for a particular study.

3.7 Differential Interferometry

Differential interferometry is a technique that looks at differences that have occurred in the phase between SAR images. As previously stated, the interferogram contains information about the topography of the scene. By comparing two interferograms, or an interferogram with a digital elevation model, information about changes in the surface topography can be derived. First demonstrated for spaceborne SAR in 1989 *(Gabriel et al 1989)* it showed that measurements of surface change could be made at the centimetre level. Since then, it has been used to successfully study land deformation *(Zebker et al 1994a)*, earthquakes *(Zebker et al 1994b)*, volcanoes (*Massonnet et al 1995*), glacier motion *(Goldstein et al 1993)*, landslides *(Fruneau et al 1996)* and subsidence *(Massonnet et al 1997)*. There are two broad techniques of differential interferometry: Two-pass and Multi-pass techniques. These are summarised below.

3.7.1 Two-Pass Differential Interferometry

Two-pass differential interferometry, as the name suggests, involves two SAR images but also requires a digital elevation model (DEM). An interferogram is formed from the two SAR images which span an event of interest, for example an earthquake. The DEM is then used to remove the phase relating to topography from the interferogram to leave the differential phase *(Massonnet et al 1993),* which is a combination of the other phase sources including those due to deformation, atmosphere and noise. Any errors present in the phase of the interferogram or in the DEM will be passed through into the differential phase.

3.7.2 Multiple-Pass Differential Interferometry

The most common form of this involves three SAR images (and is hence called 3-pass). From these, two interferograms are formed such that they share a common master image *(Gabriel et al 1989).* The images are selected such that one interferogram spans the event of interest, known as the deformation

interferogram, whilst the other interferogram is formed from the two images either after or before the event, known as the topographic interferogram. The topographic interferogram is assumed to be a good model for the topography. Both interferograms are flattened with respect to an ellipsoid model and the topographic interferogram is then unwrapped (see chapter 4). The topographic phase is then scaled by the ratio of the perpendicular baselines and subtracted from the deformation interferogram *(Zebker et al 1994b)*

$$\phi_{diff} = \phi_{defo} - \frac{B\perp_{defo}}{B\perp_{topo}}\phi_{topo} \qquad\qquad 3.4$$

where ϕ_{diff} is the differential phase, ϕ_{defo} the deformation interferogram phase, ϕ_{topo} the unwrapped topographic interferogram phase, $B\perp_{defo}$ the perpendicular baseline of the deformation interferogram and $B\perp_{topo}$ the perpendicular baseline of the topographic interferogram. Again, any errors present in the respective phases of the two interferograms will be passed into the differential phase. Since the interferograms have been flattened with respect to an ellipsoid model, there is likely to be an erroneous phase slope in the differential phase. This is due to the altitude difference between the ellipsoid and the topography, but it can be removed a posteriori with the use of distributed ground control.

The other multi-pass technique in use is 4-pass, which requires four SAR images to construct the two interferograms. As there is no common image in the two interferograms further processing must be undertaken to coregister the two interferograms. This method is only usually used if there is no suitable dataset for 3-pass interferometry.

3.7.3 Suitable Configurations

Differential interferometric results can be "improved" or optimised by using the best configuration available. When using a 2-pass method you will get a better result by using a more accurate DEM. Also, better results will be obtained if the interferogram phase is clean of temporal and geometric decorrelation noise.

When using a 3-pass method, the relative size of the baselines can have a great effect. Examining equation 3.4 shows that if the baseline of the topographic pair is greater than that of the deformation pair, then any phase errors in the topographic phase will be scaled down in the differential phase. But this baseline should not be so large as to cause much geometric decorrelation in the topographic phase.

In most cases, the 2-pass method is usually considered to be the best choice, based on the fact that, if an accurate DEM is available then the errors from that are likely to be smaller than the atmospheric errors introduced from an additional interferogram in the 3-pass method.

3.7.4 Limitations of DInSAR

The limitations of differential InSAR (DInSAR) are mainly due to the quality of the input data. The phase quality is the main limiting factor. Any noise in the interferometric phase will be propagated through into the differential phase. In general the source of largest error will be the atmosphere, which can often swamp the phase that is being investigated (*Hanssen 1998*; *Massonnet and Rabaute 1993*). For 3-pass DInSAR this is worse because there are two interferograms, and therefore 2 atmospheric effects. For 2-pass DInSAR there is only one atmospheric phase error but there is the additional error due to the DEM. This can be minimised by using the most accurate topographic model available.

Data availability is also a major limitation to the technique. For areas where no DEM exists, 2-pass DInSAR is not an option. But it can also be difficult getting suitable SAR images to form the interferograms. For example, an earthquake could occur in an area that hasn't been imaged for a number of months or years, meaning that large temporal decorrelation is likely to be present in an interferogram spanning the event, although this is not such a concern for urban areas, or regions of stable reflectivity, which can stay coherent over large time scales.

3.8 Summary

The principle of SAR interferometry (InSAR) has been introduced, together with various applications that it can be used for and the processing algorithms used to generate the interferogram. Various limitations to interferometry and noise components of the phase have been discussed. Differential InSAR has been introduced and the two main techniques: 2-pass and 3-pass, have been described. Applications of DInSAR have been identified and the limitations of the method have been highlighted.

4. Phase Ambiguity

4.1 Introduction

The interferometric phase is ambiguous; it is only known modulo 2π. In other words, the only part of the phase recorded is the fractional part of the wavelength. There is no information on the number of whole wavelengths (cycles) that have preceded it. Figure 4.1 helps explain this; the recorded phase is shown in red – but there is no information on the number of whole wavelengths that preceded this. This integer number of cycles, or wavelengths, is known as the *phase ambiguity* and labelled as N in Figure 4.1. To use the interferometric phase for topographic mapping or positioning, it is important to be able to relate the phase of one interferogram pixel to another. This requires one of two things: either the integer ambiguity for each pixel must be calculated, or if not, the phase should be reconstructed such that it is all relative to a particular interferogram pixel. This process of relative phase reconstruction is known as *phase unwrapping*.
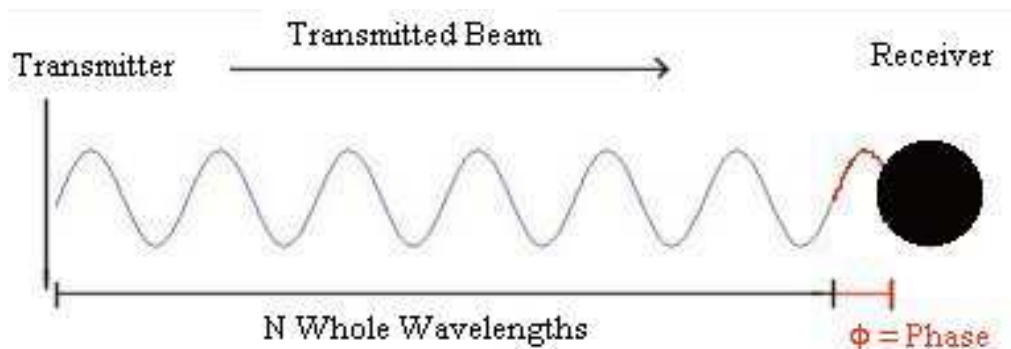
Figure 4.1 The phase ambiguity: the recorded phase is ϕ but there is no information on N, the phase ambiguity.

4.2 Phase Unwrapping

The phase unwrapping problem is simple to describe but, in general, very difficult to solve. In basic terms it is the process of adding the correct integer multiple of 2π to every point on the interferogram *(Goldstein et al 1988)*. For

noiseless phase which is sampled sufficiently, i.e. such that adjacent phase differences, or *gradients,* are less than $|\pi|$, the phase unwrapping process is straightforward (*Werner et al 2002*).

Figure 4.2 shows a 1-dimensional example of phase unwrapping. The black line represents the phase modulo 2π, the *wrapped phase,* whilst the red line shows the *unwrapped phase.* A brief overview of phase unwrapping follows; for a detailed view including phase unwrapping algorithms see *Ghiglia and Pritt (1998).*
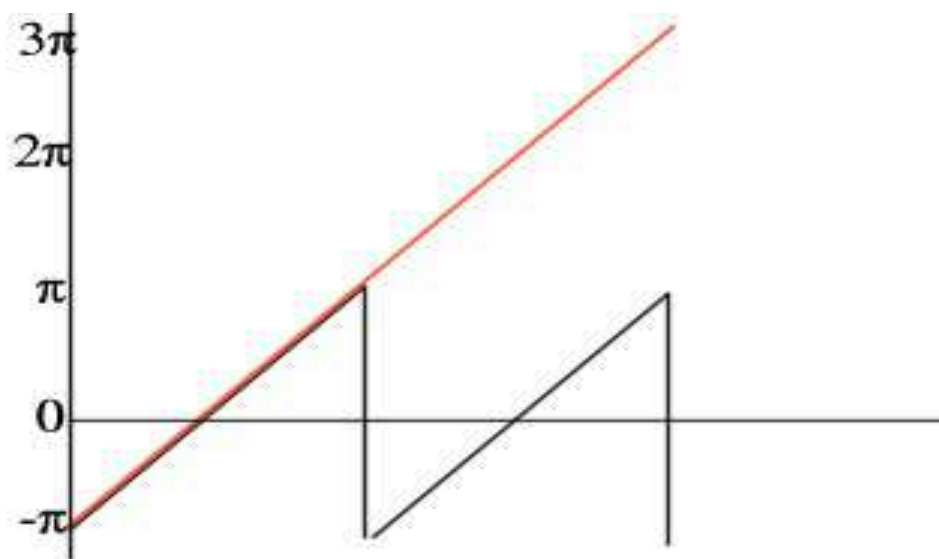
Figure 4.2 Example of 1-dimensional phase unwrapping. The wrapped phase is shown as the black line, the unwrapped phase as the red line.

4.2.1 Two-Dimensional Phase Unwrapping

In 2-dimensions the process is much the same, except that there are phase gradients in two orthogonal directions. The gradients between adjacent pixels are calculated, and then they are integrated (or summed) over a path of interest *(Ghiglia and Pritt 1998).* This results in an unwrapped interferogram where the phase values are relative to the pixel at the start of the integration path. Unfortunately, in general, this is impossible because of the wrapped nature of the phase and sources of phase noise. For example, the phase gradients could be described by an increase in phase, or equally by a decrease in phase. To

overcome this problem an assumption that the phase gradients are less than π radians in magnitude is made. To help meet this assumption the interferometric phase is flattened as much as possible. If a DEM of the area is available then this is used, else a model of the ellipsoid can be used. In regions of high noise, such as areas of layover and shadow, the phase unwrapping becomes extremely difficult because the noise can "push" the phase gradients over π magnitude, giving the appearance of a gradient in the opposite direction.

4.2.2 Residues

The process described above appears trivial but is complicated further by *residues*. Residues can be caused by zero-magnitudes, phase discontinuities, noise, inconsistent phase gradients and aliasing in the complex signal *(Ghiglia and Pritt 1998)*. They can be identified in the phase data by examining closed loops of phase (Figure 4.3). By integrating the gradients of each 2 x 2 group of pixels, the sum helps identify if there is a residue located there. If the sum equals zero then there is no residue, but if it equals $+2\pi$ or -2π then there is a positive or negative residue respectively.
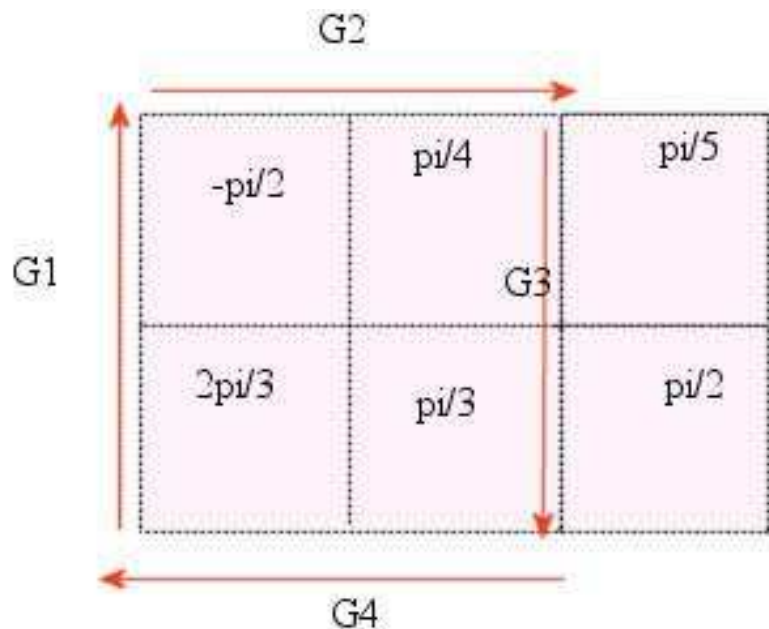
Figure 4.3 Identification of phase residues: by summing gradients in closed loops.

Using Figure 4.3 as an example, the sum of the gradients of the left hand group of 4 pixels is:

54

$$G1 + G2 + G3 + G4 = \frac{5\pi}{6} + \frac{3\pi}{4} + \frac{\pi}{12} + \frac{\pi}{3} = 2\pi \qquad\qquad 4.1$$

Hence there is a residue located between the 4 pixels. Because the sum equals $+2\pi$ the residue is said to have a positive *charge*. Now examining the right hand group of 4 pixels the sum is:

$$-\frac{\pi}{12} - \frac{\pi}{20} + \frac{3\pi}{10} - \frac{\pi}{6} = 0 \qquad\qquad 4.2$$

hence there is no residue here.

If not treated correctly, residues can corrupt the unwrapped phase. To counteract this possibility the path-following methods such as the *branch-cut* phase unwrapping algorithm *(Goldstein et al 1988)* connect up the residues, using branch-cuts, such that the total charge of connected residues is 0. In other words one of two situations must occur: either there are an equal number of positive and negative residues connected, or the connected residues are *earthed* (connected to the edge of the interferogram). This recreates the path independent problem provided that no path crosses a branch-cut. There exist other techniques such as least squares phase unwrapping algorithms *(Ghiglia and Pritt 1998)* which do not explicitly deal with the residues.

4.2.3 Phase Unwrapping Conclusions

Phase unwrapping is a complicated task. Although a multitude of algorithms exist for solving the problem *(Goldstein et al 1988)*, *(Constantini 1998)*, *(Chen and Zebker 2000)*, *(Ghiglia and Pritt 1998)*, none of them are perfect. Due to the phase noise and terrain effects (e.g. layover), unwrapping of InSAR phase is made very difficult. It remains one of the most important limiting factors for InSAR applications.

4.3 Integer Ambiguity Search

In 2003, *Sowter (2003a)* proposed the Integer Ambiguity Search (IAS) process. By assuming low phase noise in the interferogram and using an accurate enough ground control point (GCP) it is possible to retrieve the *absolute* phase

ambiguity for an image pixel. When combined with an unwrapped phase interferogram, this can allow the absolute phase of every pixel whose phase is relative to the pixel of interest to be reconstructed. Through this technique it is also possible to position the InSAR data in an absolute geodetic reference frame, such as an Earth Centred Earth Fixed Cartesian frame of reference. The process is described below.

4.3.1 Integer Ambiguity Search Process

The IAS method for deriving the ambiguity is heavily dependent on the InSAR satellite geometry. By implementing a set of equations that relate the geometry and the phase value, together with a ground control point, allows an estimate of the ambiguity to be derived. Consider the InSAR geometry of Figure 4.4, with a coordinate system centred at the master satellite position A1.
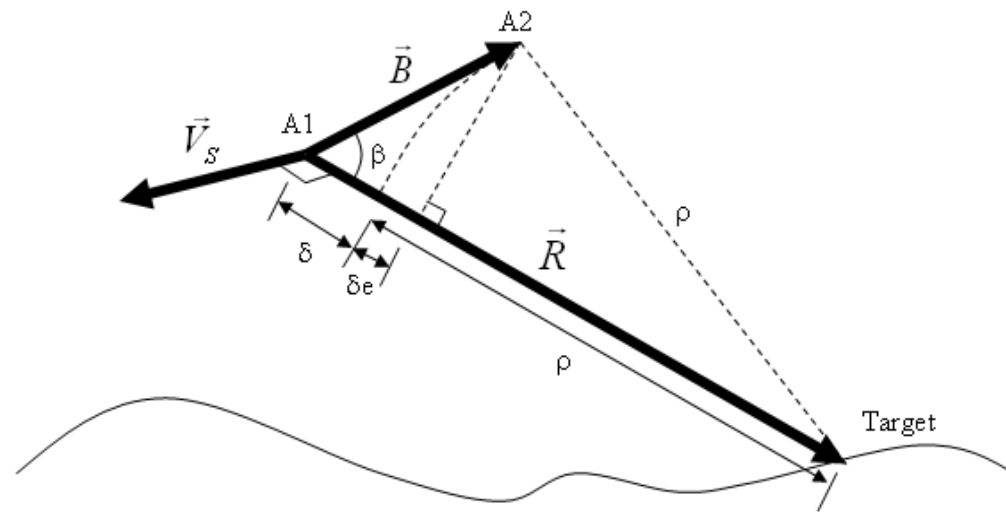
Figure 4.4. InSAR Geometry centred at master satellite position: A1 (from *Sowter et al 2004*).

The two satellites, master and slave, and target are at positions A_1, A_2 and T respectively. The velocity vector of the master satellite is described by $\vec{V}_S$, the baseline vector by $\vec{B}$, the master range vector by $\vec{R}$ and the angle between the baseline and range vector as β. The satellite positions and velocity can be calculated from the orbit data, as can the baseline vector. Estimates for the ranges ρ and ρ+δ can be obtained from the master and slave row and column information. δe can be calculated from the geometry using *(Sowter 2003a)*:

$$\delta e = \frac{B^2 - \delta^2}{2(\rho + \delta)} \qquad\qquad 4.3$$

where $B = |\vec{B}|$. The angle β can then be calculated, by using the cosine rule, as:

$$B\cos\beta = \frac{(\rho + \delta)^2 + B^2 - \rho^2}{2(\rho + \delta)} \qquad\qquad 4.4$$

But it can also be shown that β can be calculated as (see Figure 4.4):

$$B\cos\beta = (\rho + \delta) - \rho + \delta e = \delta + \delta e \qquad\qquad 4.5$$

Recall from chapter 3 the equation for the interferometric phase:

$$\phi_{abs} = \frac{4\pi}{\lambda}(\rho_1 - \rho_2) \qquad\qquad 4.6$$

where ϕ_{abs} is the full absolute phase, ρ_1 and ρ_2 are the master and slave ranges respectively and λ is the radar wavelength. Substituting equation 4.6 into 4.5 gives:

$$B\cos\beta = \frac{\lambda\phi_{abs}}{4\pi} + \delta e \qquad\qquad 4.7$$

Equation 4.7 then describes the connection between the satellite geometry and the (absolute) interferometric phase.

Now, still considering the geometry model of Figure 4.4, if the master satellite A_1 has position vector (0, 0, 0) and the target has position (x, y, z), then the range from A_1 to the target can be described, by the Range Equation, as:

$$|R|^2 = (\rho + \delta)^2 = x^2 + y^2 + z^2 \qquad\qquad 4.8$$

Also, if we consider the Doppler Equation for zero-doppler data we have:

$$\vec{R} \cdot \vec{V} = V_x x + V_y y + V_z z = 0 \qquad\qquad 4.9$$

where the velocity vector $\vec{V} = (V_x, V_y, V_z)$.

Finally, we have the equation defined by:

$$B_x x + B_y y + B_z z = \vec{B} \cdot \vec{R} = |B||R|\cos\beta = B(\rho + \delta)\cos\beta \qquad 4.10$$

where $\vec{B} = (B_x, B_y, B_z)$, which shall be called the InSAR Equation. After substitution of 4.7 into 4.10 we have a set of three equations that can be used to position the InSAR data: equations 4.8, 4.9 and 4.11.

$$B_x x + B_y y + B_z z = (\rho + \delta)(\frac{\lambda \phi_{abs}}{4\pi} + \delta e) \qquad\qquad 4.11$$

The only unknowns in this set of equations are the target position (x, y, z) and the absolute phase ϕ_{abs}. Recall, from Figure 4.1, that the absolute phase is

$$\phi_{abs} = \phi + 2\pi\Delta n \qquad\qquad 4.12$$

where ϕ is the wrapped interferometric phase and Δn is the integer ambiguity.

Global Navigation Satellite Systems (GNSS) such as the Global Positioning System (GPS) have well known algorithms that can aid getting integer ambiguities *(Dixon 1991)*. One such method that uses the carrier phase signal of the GPS satellites constitutes a search for the carrier phase integer ambiguity around an estimated value. The IAS is a similar process *(Sowter 2003a)*. If a GCP is known in the vicinity of the target then it can be used to "guide" the search to the correct ambiguity value. Using an estimate for Δn the set of three equations defined above can be solved to get the target position (x, y, z). By comparing the GCP with the solved for target location for different values of Δn, the correct value of Δn can be found (Figure 4.5), by selecting the value which gives the location closest to the GCP.
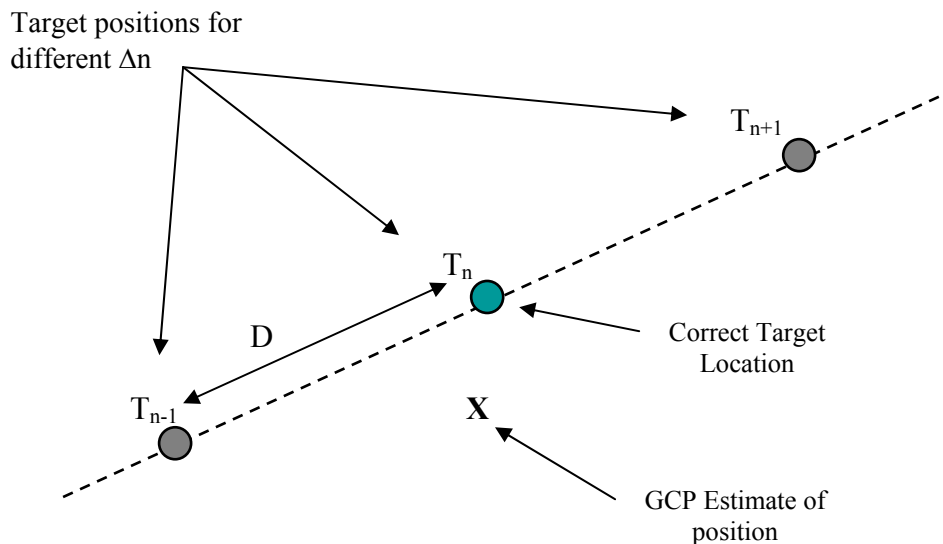
Figure 4.5 Ambiguity search process principle (*Sowter 2003a*)

For this to work some assumptions, or restrictions, have to be made about the data. The most important of these is that the GCP is known accurately enough, i.e. to within half the distance that separates the estimated target positions *(Sowter 2003a)*, i.e. half of D in Figure 4.5. If this restriction is not met then an incorrect Δn will be selected. The uncertainty in positioning the GCP onto the correct point in the SAR image must also be taken into account. The length D can be calculated, to first order, by *(Sowter 2003a)*:

$$D = \frac{\lambda R}{2B \sin \beta} \qquad \qquad 4.13$$

which is related to the height ambiguity *(Massonnet and Feigl 1998)*.

4.3.2 Benefits of the IAS

The Integer Ambiguity Search (IAS) allows the integer ambiguity to be identified. Through this, the absolute phase at the pixel of interest can be reconstructed which allows for absolute positioning of the pixel in a geodetic frame. This has very important implications for InSAR. Most methods for positioning InSAR data into a geodetic frame are two step algorithms. First the phase is converted to height, usually through the use of an approximate equation, and then the height values are georeferenced (*Small 1998*). By being able to position the data absolutely through one set of equations allows a cleaner, less error-prone result. The set of equations used are very simple and similar to radargrammetric approaches *(Leberl 1990)*, which are well known and have well known error budgets. The error budgeting is far simpler using a 1 step group of simple equations than for a more complicated 2 step algorithm.

Though a ground control point (GCP) is needed for the IAS, errors in the GCP are not propagated into the positioning accuracy. This is because it is an integer search; so as long as the GCP is within the bounds described from equation 4.13 the correct integer value will be selected. Obviously if the GCP is not known to this accuracy then integer errors (multiplied by 2π) in the absolute phase will occur.

Also, because the method allows absolute positioning, this should allow integration with other techniques such as GPS to be easier. Both GPS and the IAS methods use similar trilateration based techniques to derive positions, and both give results in a geodetic reference frame.

The IAS can also be used for DEM generation techniques and has important implications for differential interferometry. These are described in the next two sections.

4.4 DEM Generation Application

Digital Elevation Models can be generated from InSAR data using various algorithms *(Rodriguez and Martin 1992, Schwabisch 1998a, Small 1998)*. One method common in the literature uses the height ambiguity formula to convert the unwrapped phase values into height, which if required, are then corrected using GCPs before being geocoded. The height ambiguity can be shown to be *(Hanssen 2001)*:

$$\frac{dh}{d\phi} = \frac{\lambda}{4\pi} \frac{R \sin \theta}{B \perp}$$

4.14

where the left hand side is rate of change of height with respect to phase and θ is the look angle. Multiplying this by the unwrapped phase value gives an approximate height. Because the unwrapped phase values are not likely to be absolute, correction of the height with GCPs is required (*Zebker et al 1994b*). The corrected height values are then geocoded using one of many methods e.g. *(Schwabisch 1998b)* and *(Hellwich 1999)*.

The IAS DEM generation technique is an extension to the process described in 4.3.1. If the phase is unwrapped prior to doing the ambiguity search, then all the phase values in the interferogram are relative to each other (assuming phase unwrapping performed correctly). This suggests that if the ambiguity search is performed at a (row, column) of the interferogram, then that ambiguity applies to the whole interferogram. Therefore, using one GCP it is possible to recreate the absolute phase for the entire interferogram. In practice, if a distribution of GCP is available it is wise to do an IAS analysis for each point, and accept the

modal ambiguity value. This is because atmospheric, baseline and unwrapping errors are likely to appear in the interferogram causing possible erroneous results. The set of equations 4.8, 4.9 and 4.11 can then be solved on a pixel by pixel basis for the entire interferogram, resulting in a Earth Centred Earth Fixed Cartesian x, y, z value for each pixel. This can then easily be resampled to the required reference frame, e.g. UTM Eastings, Northings and Height.

This process has been tested using ESA ERS SAR data of the London region, UK and is the subject of *(Sowter et al 2006)*. The main results are repeated here.

4.4.1 Demonstration over London

London was chosen as the test region because data from a network of GPS stations was available for evaluation purposes. The GPS network was originally set up primarily to tie in data from tide gauges to absolute ground levels *(Bingley et al. 1999)*. The GPS station locations relative to the Thames Region are shown in Figure 4.6. The topography of the region varies slowly from sea level to heights of around 300m.
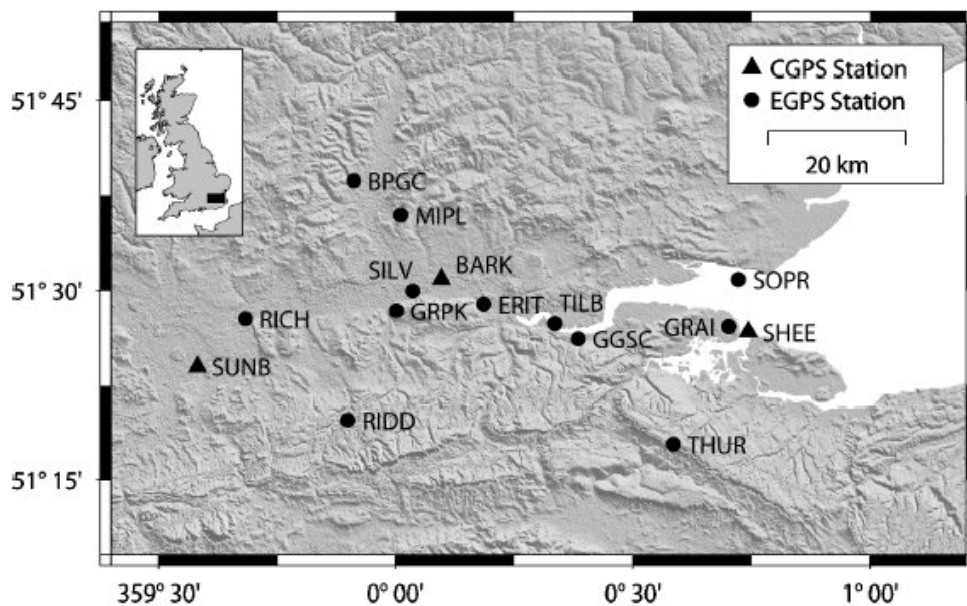
Figure 4.6 London GPS station location map. The GPS network is primarily used for the absolute fixing of tide gauges and land levels *(Sowter et al 2006)*.

An interferogram was generated using two SAR images from the Tandem Mission, with dates 9th and 10th November 1995. These were supplied by Infoterra Ltd. The Doris software was used to process the data together with precise orbits from Delft Technical University. The interferogram was then unwrapped using the SNAPHU software from Stanford University (*Chen and Zebker 2001*).

Each of the GPS stations was projected onto the interferogram using a range-Doppler algorithm together with the satellite orbit data. One of the GPS points was selected as a seed point and the interferometric phase was then interpolated using a bilinear interpolation method to get an estimate of the phase at the GPS point. The phase of the interferogram was then "normalised" to this point by adding multiples of 2π such that the phase at the GPS seed point equalled its wrapped value. The integer ambiguity was then calculated for this point and applied to the phase at each pixel to create the absolute phase interferogram. As a check, the ambiguity was also calculated at each of the other GPS stations (without normalising the phase data to them). In theory, the ambiguity should be the same at each point, but in practice this was not the case. Table 4.1 shows the GPS stations and their respective ambiguity value. It can be seen that, with the exception of BARK, the ambiguity values increase as column number increases. This is most likely due to an error in the baseline values, which as stated in chapter 3 can cause a phase slope across the interferogram. The phase slope, estimated to be 1.5 fringes, was removed from the interferogram. The position of the InSAR data at each GPS point was then calculated using the system of equations described in section 4.3.1, and transformed to map coordinates in the OSGB36 datum.

Table 4.2 shows the differences between the GPS derived locations and the equivalent located InSAR positions. It was decided to remove BARK and ERIT from further processing due to very low coherence levels. The BARK GPS station is located on a 40m high concrete tower and is foreshortened on the SAR image, and so the phase here may not be representative of the geometry. The ERIT GPS station is located on a pier that extends into the River Thames, leading to very poor coherence and hence a low confidence in the phase value.

GPS Station	Interferogram Column	Ambiguity
SHEE	150	-1979
GRAI	215	-1979
THUR	290	-1979
GGSC	692	-1979
TILB	784	-1979
ERIT	1042	-1979
BARK	1210	-1980
SILV	1305	-1979
GRPK	1346	-1979
MIPL	1409	-1979
RIDD	1426	-1979
TOPR	1510	-1979
BPGC	1613	-1978
RICH	1907	-1978
SUNB	2049	-1978

Table 4.1 London GPS station ambiguity information: interferogram column position and their ambiguity value.

GPS station	Coherence	Easting error (m)	Northing error(m)	Height error(m)	Absolute error(m)
SHEE	0.688457	10.759	-2.108	-3.995	11.66875186
GRAI	0.648959	13.476	-2.64	-5.062	14.63543713
THUR	0.398139	30.487	-5.988	-11.639	33.17799925
GGSC	0.459621	-1.21	0.237	0.493	1.327899846
TILB	0.549784	-10.773	2.111	4.447	11.84439357
SILV	0.329762	-4.213	0.826	1.872	4.683591464
GRPK	0.351199	-3.817	0.749	1.706	4.247461124
MIPL	0.440293	5.555	-1.086	-2.503	6.188895701
RIDD	0.535939	8.805	-1.73	-3.981	9.81678593
TOPR	0.349209	9.206	-1.802	-4.2	10.27801732
BPGC	0.388851	31.134	-6.085	-14.391	34.83466753
RICH	0.586853	34.522	-6.769	-16.534	38.87108181
SUNB	0.728588	-11.073	2.174	5.391	12.50601799
Mean	0.496588769	8.681384615	-1.700846154	-3.722769231	14.92930773
St Dev	0.136291758	15.47507368	3.033289299	6.907767466	12.43916958

Table 4.2 Errors between GPS and InSAR positioning: results in OSGB36 Eastings, Northings and Heights.

The absolute errors between the two positioning results (GPS and InSAR) can be seen to vary in magnitude from approx. 1m up to 40m. This could be explained, for a point such as THUR, to be due to the low coherence value, but this is not true of every point. The Easting errors show a bias of approx. 9m in magnitude, which could be due to errors in the satellite-target range since this runs in a near east-west direction at this latitude. This would suggest a slant range error of approx. 3.6m in magnitude, which is well within the error budget for ERS satellites (*Sowter et al 1990*).

The Northing and height errors are smaller in magnitude than the Easting errors. Northing errors will mainly be due to inaccuracies in the orbits and azimuth time, whereas height errors will again be affected by slant range errors. The height standard deviation of 6.9m is within broad agreement with other authors e.g. *(Li and Goldstein 1990)*.

There are two main problems with using these GPS points to test the accuracy of the InSAR positioning. The first problem being that the majority of the GPS points are located along side the River Thames. This creates coherence problems and results in a lower confidence in the phase accuracy. The second problem is that the GPS points are not likely to be representative of the main scatterer in the radar resolution cell. GPS stations are generally located in open spaces, away from large structures that could cause problems in the data processing. Obviously, in an urban environment, this is not always easy and so some stations will have structures nearby which are more likely to be the dominant scatterer of the radar signal.

As well as the GPS data a 3rd party DEM was available, provided by Infoterra Ltd., with 50m postings and a claimed RMS of 2.5m. This was used as a reference DEM to see how the IAS generated DEM compared to it. A map of the differences is shown in Figure 4.7. The majority of the magnitude of errors are within 10m, but in some areas this can reach nearly 20m. There are regions where the magnitude of the error is large (20m), i.e. the dark patch on the top right and the white patch to the left of the image. These could be due to localised phase unwrapping errors in the interferogram, or maybe phase errors due to atmospheric anomalies. There are also some topographic effects present which suggest a slight misregistration between the two DEMs.

In conclusion, therefore, the method of using the IAS to generate a DEM and for positioning InSAR data has been demonstrated. The positioning results compared to GPS locations gave errors which are in broad agreement with other authors. The DEM generation method described still contains some of the errors

present in other techniques; primarily due to errors in the phase and the orbit data.
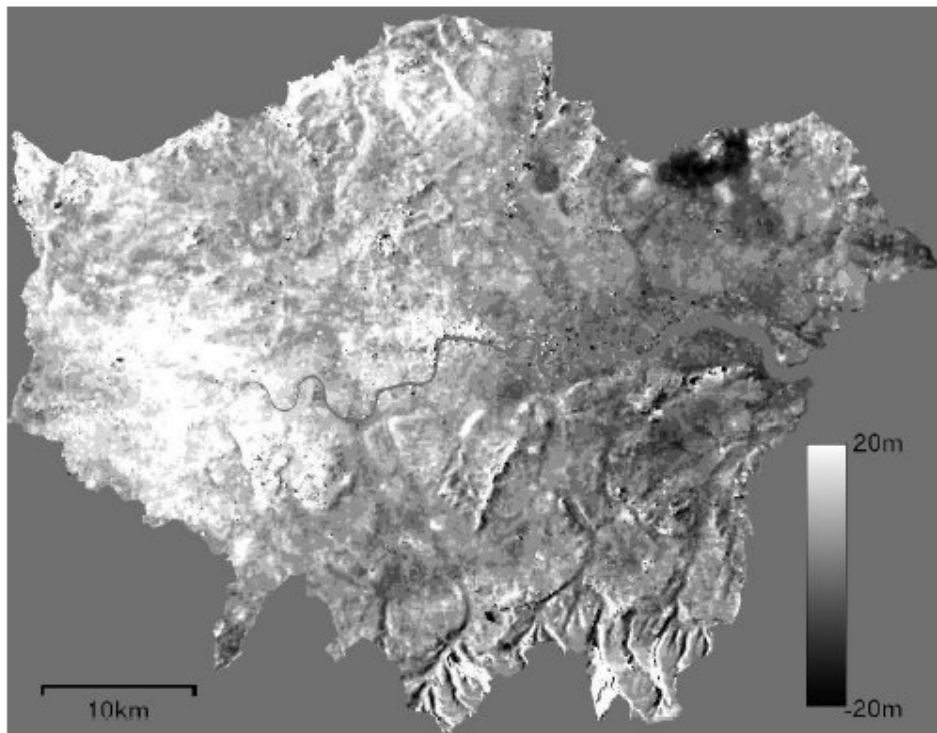
Figure 4.7 Map of differences between IAS generated DEM and 3rd party DEM. Errors range from +20m to -20m.

4.5 Differential Interferometry Application

4.5.1 Method

The implications of the Integer Ambiguity Search process for differential interferometry were first suggested in 2003 *(Sowter 2003b)*. Suppose the 3-pass geometry of Figure 4.8, where P_1, P_2 and P_3 are the master, topographic slave and deformation slave satellites respectively; B_{12} and B_{13} are the respective topographic and deformation baselines; β_{12} and $\beta_{12} + \gamma$ are the angles between the respective baselines and master range vector.

65
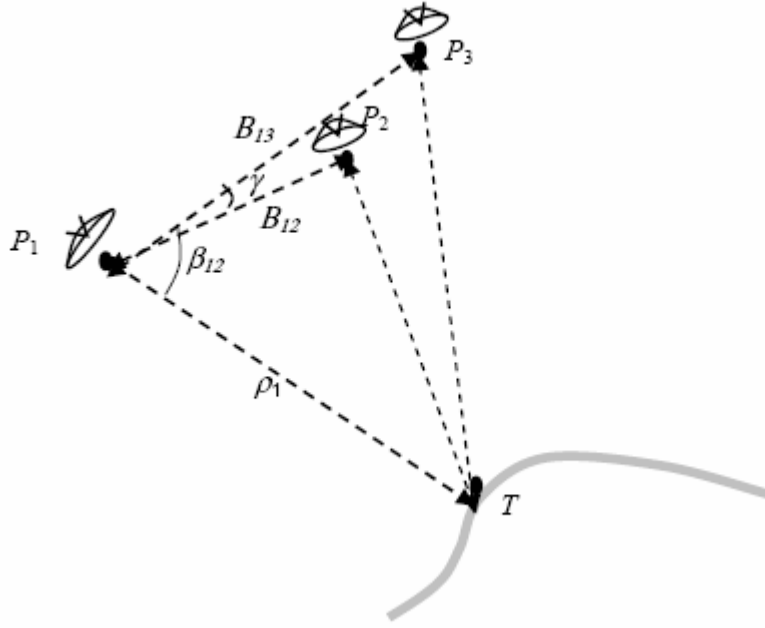
Figure 4.8 3-pass differential InSAR geometry (from *Sowter 2003b*)

Then for each interferogram setup, i.e. the topographic and deformation pairs, there is equation 4.7, which when rearranged gives:

$$\frac{4\pi}{\lambda} B_{12} \cos\beta_{12} = \phi_{12} + 2\pi\Delta n_{12} + \frac{4\pi}{\lambda}\delta e_{12} \qquad 4.15$$

$$\frac{4\pi}{\lambda} B_{13} \cos(\beta_{12} + \gamma) = \phi_{13} + 2\pi\Delta n_{13} + \frac{4\pi}{\lambda}\delta e_{13} \qquad 4.16$$

Constructing β_{13} as $\beta_{12} + \gamma$ assumes that the three satellites and the target T are all in the same plane. Generally this is not the case and so some processing must be done to take this into account. Using simple vector mathematics it is possible to rotate the topographic slave satellite, say, so that it lies in the plane P_1P_3T and calculate γ from the geometry of this new arrangement.

The difference of the two above equations, equation 4.17, should be equal to zero if there is no surface change between the three SAR images (assuming no noise or atmospheric errors).

$$\Phi = \frac{1}{B_{13}}(\phi_{13} + 2\pi\Delta n_{13} + \frac{4\pi}{\lambda}\delta e_{13}) - \frac{1}{B_{12}}(\phi_{12} + 2\pi\Delta n_{12} + \frac{4\pi}{\lambda}\delta e_{12})$$

$$-(\frac{4\pi}{\lambda}\cos(\beta_{12} + \gamma) - \frac{4\pi}{\lambda}\cos\beta_{12}) \qquad 4.17$$

When this is non-zero there has been a differential change *(Sowter 2003b)*. The change is assumed to occur in the deformation interferogram, and can therefore be given as a change in the range of P_3. This is equivalent to:

$$\partial\rho = \frac{\lambda}{4\pi} B_{13} \Phi \qquad\qquad 4.18$$

or keeping in terms of the phase:

$$\partial\phi = (\phi_{13} + 2\pi\Delta n_{13} + \frac{4\pi}{\lambda}\delta e_{13}) - \frac{B_{13}}{B_{12}}(\phi_{12} + 2\pi\Delta n_{12} + \frac{4\pi}{\lambda}\delta e_{12})$$
$$- B_{13}(\frac{4\pi}{\lambda}\cos(\beta_{12}+\gamma) - \frac{4\pi}{\lambda}\cos\beta_{12}) \qquad 4.19$$

where $\partial\phi$ is the differential phase.

As with the DEM generation case, the interferograms should be unwrapped so that the IAS will result in the absolute phase for each pixel of the interferograms. Obviously a separate IAS analysis must take place for both the topographic and the deformation pairs, since they will have different integer ambiguity values.

4.5.2 Error Analysis

It now seems appropriate for a brief discussion on possible sources of error and their effects. The main sources of error present in the IAS DInSAR method that differ from the traditional 3-pass method are: the integer ambiguity values Δn_{12}, Δn_{13} and the angle γ.

It is conceivable that errors in the integer ambiguity values will occur, due to phase noise, baseline errors and GCP inaccuracies. This is more likely to occur in large baseline interferograms due to the closer spacing of the ambiguities (see equation 4.13). If a number of GCPs are available it is recommended to calculate the ambiguity value at each one, using the unwrapped phase data, and use the modal value in the processing. If an incorrect value is chosen, the effect on the final result is different depending on whether it is the topographic or deformation ambiguity. If the error occurs in the deformation ambiguity Δn_{13}, of magnitude *n* say, then the effect is just a linear offset of *2nπ* radians to the

differential result (equation 4.19). This can easily be removed by simply wrapping the differential result (then unwrapping if required). If the error occurs in the topographic ambiguity then it is more difficult to mitigate. This time an ambiguity error of magnitude n would result in an error of $2n\pi B_{13} / B_{12}$. Because the baseline ratio is unlikely to be an integer value, wrapping the result will not remove the effect. To minimise this effect choosing B_{12} such that it is greater than B_{13} would help, but as stated above a larger B_{12} increases the uncertainty in the ambiguity.

The other parameter that differs from the traditional 3-pass technique is the angle γ; although it is implicit in the traditional 3-pass equations in the perpendicular baseline. An error in γ, of magnitude $\delta\gamma$, appears as a slope error in the final differential phase. This can be thought of as the topographic height being offset from its true value, or in other words, as an error of magnitude $\delta\rho$ in the range vector of P_3. This is described in Figure 4.9 below.
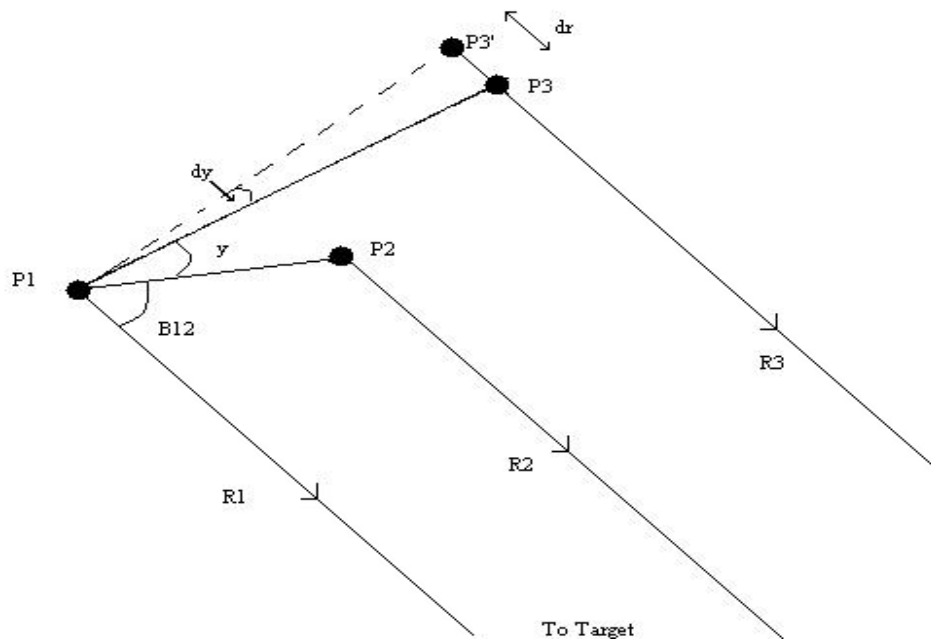
Figure 4.9 Image showing the effect of an error in γ. An error of magnitude $\delta\gamma$ is equivalent to a range change of $\delta\rho$.

The three satellite positions are shown as P1, P2 and P3 with range to target vectors R1, R2 and R3 respectively. An error in γ of $\delta\gamma$ could give an appearance of P3 being at P3` causing a range error of $\delta\rho$.

4.5.3 Results

The method described above has been tested using ESA ERS data of the Landers Earthquake, USA of 1992 *(Warren et al 2004)*. The general deformation of the earthquake was identified, but some erroneous phase fringes were present. These have since been identified as being due to γ not being calculated when all three satellites and target were in the same plane. Another test of the method but with calculating γ correctly is shown below, comparing the differential interferogram generated from the IAS method with one generated from the Doris implementation of the traditional 3-pass method. The data used is of the Bam Earthquake, Iran *(Funning et al 2005)* collected from the ESA Envisat satellite.

The three SAR images that were used to generate the two interferograms are dated 11th November 2003 and 3rd December 2003 for the topographic interferogram, 11th November 2003 and 7th January 2004 for the deformation interferogram. The earthquake occurred on the 26th December 2003. The Doris software together with precise orbits was used to generate the interferograms; and where phase unwrapping has been applied the Stanford SNAPHU software has been used. The topographic interferogram has had some processing applied so as to limit the effect of atmospheric errors in the differential result (see section 4.6).

Figures 4.10 a) and b) show the traditional 3-pass and the IAS 3-pass results respectively. A qualitative analysis of the two images shows them to be very similar (as expected), except that the traditional 3-pass result appears to have an extra fringe across the image. The deformation can clearly be seen as the rapid fringes near the centre of the image. It should be pointed out that no GCPs have been used, in post-processing, to correct either result.
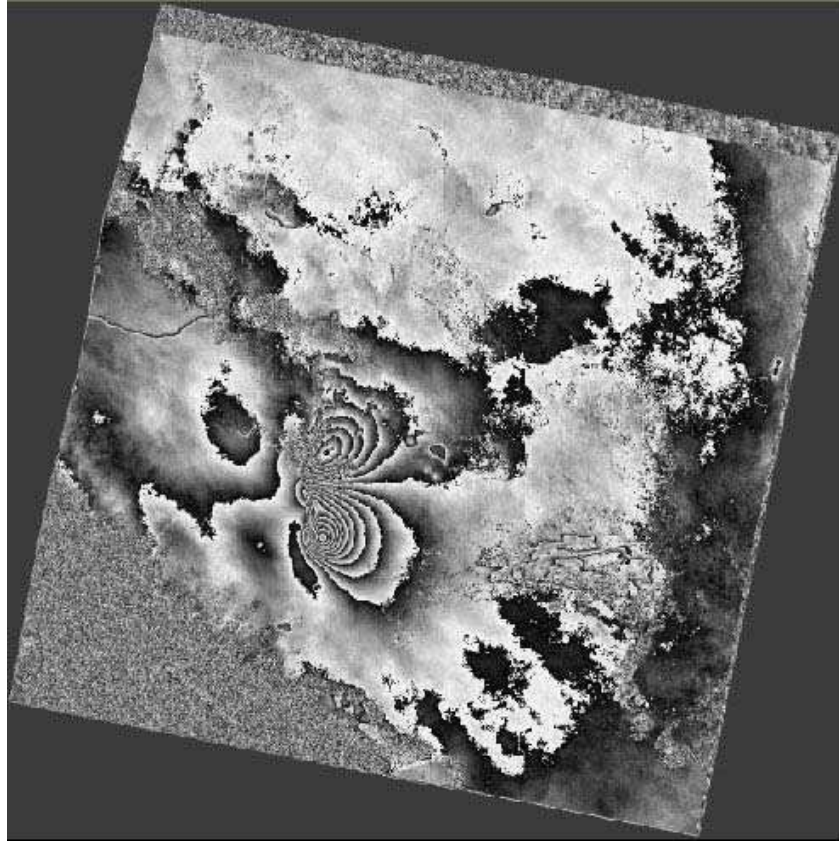
Figure 4.10a) Traditional 3-pass result: generated using the Doris Software.
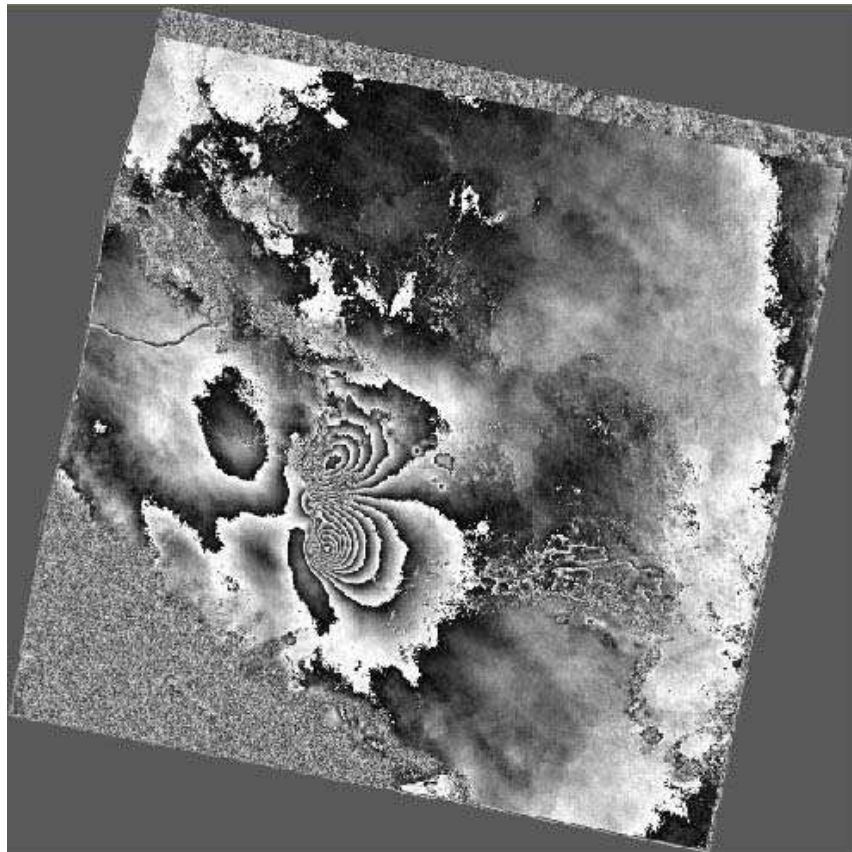
Figure 4.10 b) Integer Ambiguity Search 3-pass result.

For further analysis a 2-pass result was generated using the deformation interferogram together with an SRTM DEM of the area. Because the SRTM data gives heights relative to the geoid and the InSAR data is relative to an ellipsoid, a correction (*NGA WGS84 Geoid Calculator*) was applied to the SRTM heights before generating the 2-pass results. This 2-pass result was then used as a reference for the two 3-pass results. By subtracting the 2-pass result from each 3-pass result it is possible to see the error between the 3-pass and 2-pass differential results. Prior to subtraction, each differential result has been unwrapped using the SNAPHU software. The traditional 3-pass error along a profile across the image is shown below in Figure 4.11a. It can be seen that there is a "random" error in the results, but also a systematic error propagating as a slope. The so-called random error is due, primarily, to errors in the DEM and topographic phase noise. This creates a pixel by pixel error which is, in general, random in nature. The slope is caused by errors between the topography and the ellipsoid model used to flatten the phase data. If there was no topography, i.e. a perfectly flat area, then the ellipsoid and topography would be comparable and the slope would not be present. The SRTM profile of topography is shown in Figure 4.11b.
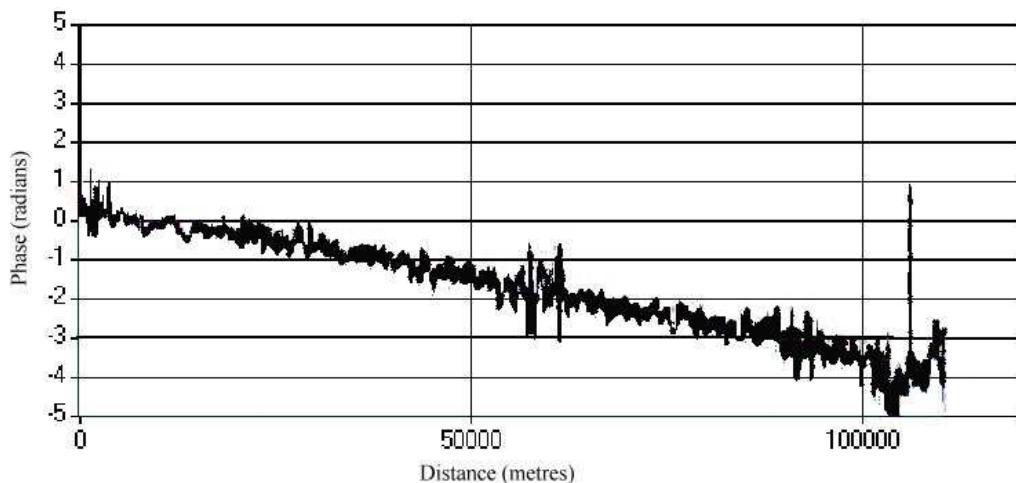
Figure 4.11a Error between the 2-pass and traditional 3-pass differential results. Y-axis measures phase difference in radians, X-axis distance along the profile used.

71
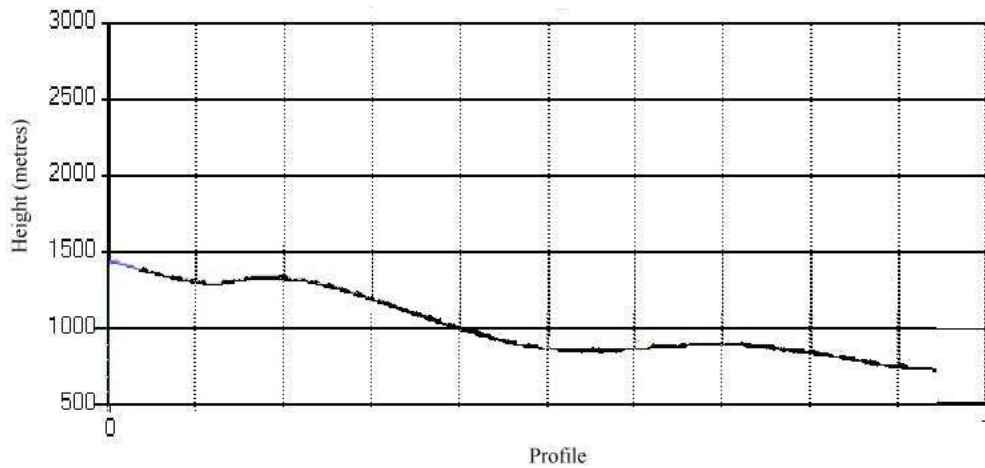
Figure 4.11b SRTM height profile: along the same profile as used for the above analysis in 4.10a.

Figure 4.11c below shows the error between the IAS 3-pass and the 2-pass results along the same profile as the previous analysis. Again the random errors are present but the systematic slope error is no longer perceptible. This is due to the IAS method using the absolute phase and not flattening to an ellipsoid model. Therefore the IAS 3-pass method gives a result closer to the 2-pass method than the traditional 3-pass method. This suggests that 2-pass accuracy could be attained from 3-pass methods in future, without requiring a DEM but rather a set of GCPs.
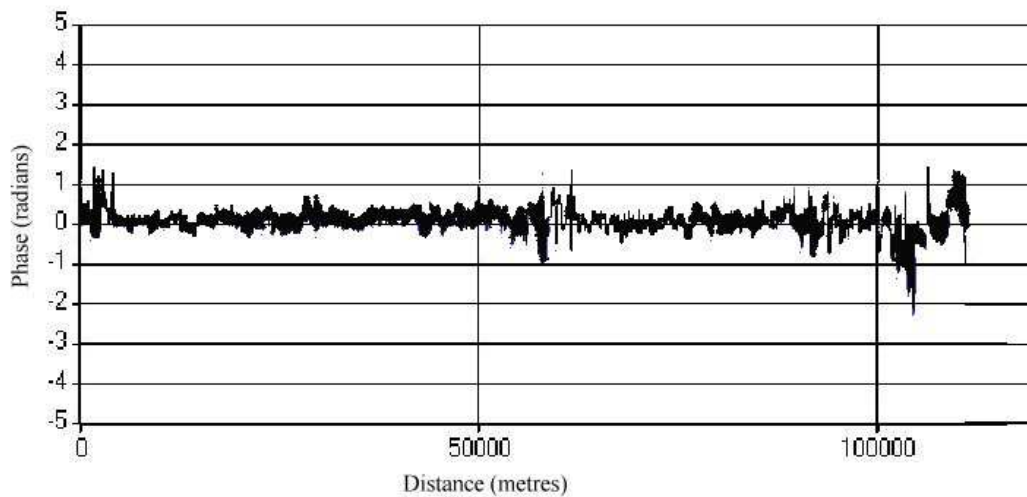
Figure 4.11c Profile of errors between the IAS 3-pass and 2-pass results. The Y-axis shows the phase error in radians, X-axis the distance along the profile.

4.6 DEM "Smoothing" application

This section describes a smoothing application that can be applied to improve differential InSAR results with the aid of a rough DEM. It has previously been described in *(Sowter and Warren 2005)*. It is similar to work done *by (Crosetto 2002)* and *(van der Kooij 1999)* who use related techniques to improve DEM generation.

4.6.1 Smoothing method

In the previous chapter, 2-pass and 3-pass methods of differential interferometry were described. But there is another possibility that was ignored; using a DEM within a 3-pass framework. The DEM can be used together with the topographic interferogram to help isolate the atmospheric and baseline errors within the interferogram. This allows an "improved" topographic interferogram to be used in the 3-pass method.

Consider a 2-pass differential process which gives the following result:

$$\delta\phi_2 = \phi_d + \varepsilon^{DEFO} - \phi_{\mathrm{T}}^{DEFO} \qquad\qquad 4.20$$

where $\delta\phi_2$ is the differential phase from 2-pass, ϕ_d the phase due to deformation only, ε^{DEFO} the phase noise from the deformation interferogram and ϕ_τ^{DEFO} the phase due to a DEM height error of magnitude T (which can be derived from equation 4.14). Similarly a 3-pass process would give:

$$\delta\phi_3 = \phi_d + \varepsilon^{DEFO} - \frac{B_\perp^{DEFO}}{B_\perp^{TOPO}}\varepsilon^{TOPO} \qquad\qquad 4.21$$

where $B_\perp^{TOPO}$ and $B_\perp^{DEFO}$ are the perpendicular baselines of the topographic and deformation interferograms respectively and $\delta\phi_3$ is the differential phase from the 3-pass method.

So for a 2-pass process to be performed on the topographic interferogram would result in:

$$\delta\phi_2^{TOPO} = \varepsilon^{TOPO} - \phi_{\mathrm{T}}^{TOPO} \qquad\qquad 4.22$$

since it is assumed there is no deformation in the topographic interferogram.

Now a spatial averaging filter of suitable size, say 500m – 1km, applied to equation 4.22 should have little affect on the atmospheric phase due to its spatial scale (*Hanssen 2001*). Filtering should reduce the standard deviation of the random height errors and in turn, this could reduce the contribution of the DEM errors in the differential phase. If this filtered phase is removed from the original topographic phase, it results in the *screened* phase:

$$\overline{\phi^{TOPO}} = \Phi + \varepsilon^{TOPO} - \overline{\varepsilon^{TOPO}} + \overline{\phi_{\Upsilon}^{TOPO}} \qquad 4.23$$

where the bar denotes spatial averaged and Φ represents the phase due to topography only. Using this as input into the 3-pass method gives:

$$\overline{\delta\phi_3} = \phi_d + \varepsilon^{DEFO} - \frac{B_{\perp}^{DEFO}}{B_{\perp}^{TOPO}}\left(\overline{\phi_{\Upsilon}^{TOPO}} + \varepsilon^{TOPO} - \overline{\varepsilon^{TOPO}}\right) \qquad 4.24$$

For this to give better results than a 2-pass method it has to be shown that the last term in equation 4.24 is smaller than the last term of equation 4.20. To this end, consider ε can be separated into $\varepsilon = \varepsilon_L + \varepsilon_S$ where ε_L denotes large scale phase errors and ε_S small scale phase errors. Small scale errors are random effects that affect each resolution cell and are related to coherence *(Zebker and Villasenor 1992)*. Large scale errors are due to atmosphere and baseline effects and occur over large areas. As previously stated baseline effects generally result in a gentle phase ramp and have a large spatial scale. The atmospheric effects consist of topography correlated and random components; the random components being at spatial scales usually no finer than 500m (*Hanssen 2001*). Since the spatial averaging filter was applied with a kernel of approx. 500m, it implies:

$$\overline{\varepsilon} = \varepsilon_L + \overline{\varepsilon}_S \qquad 4.25$$

hence

$$\varepsilon^{TOPO} - \overline{\varepsilon^{TOPO}} = \varepsilon_S^{TOPO} - \overline{\varepsilon_S^{TOPO}} \qquad 4.26$$

Using equations 4.14, 4.20, 4.24 and 4.26 it can be shown that the screened 3-pass method is better than the 2-pass method when:

$$T > T_0 \qquad 4.27$$

where the boundary value T_0 is approximately given by:

$$T_0 = \frac{N}{N-1} \frac{\lambda \rho^{DEFO} \sin \theta^{DEFO}}{4\pi B_{\perp}^{TOPO}} \left(\varepsilon_S^{TOPO} - \overline{\varepsilon_S^{TOPO}} \right) \qquad \qquad 4.28$$

where N is given by the NxN DEM postings kernel used to spatially average the data, e.g. for a DEM at 100m postings use a 5x5 kernel to filter at scale of 500m. ρ and θ are assumed to be similar for both TOPO and DEFO interferograms, which is the case for spaceborne InSAR data.

Using 16-look statistics from *(Zebker and Villasenor 1992)* and typical ERS values, Figure 4.12 shows how T_0 varies when using different baseline and coherence values. It assumes a 3x3 averaging kernel has been used, slant range of 1000km and incidence angle of 23°. It can be seen, for example, that using a DEM of 10m accuracy with baseline of 800m and coherence greater than 0.2, it is beneficial to use the screened 3-pass. But for a configuration with DEM accuracy 10m, a baseline of 500m and coherence 0.2, it would be better to use 2-pass.
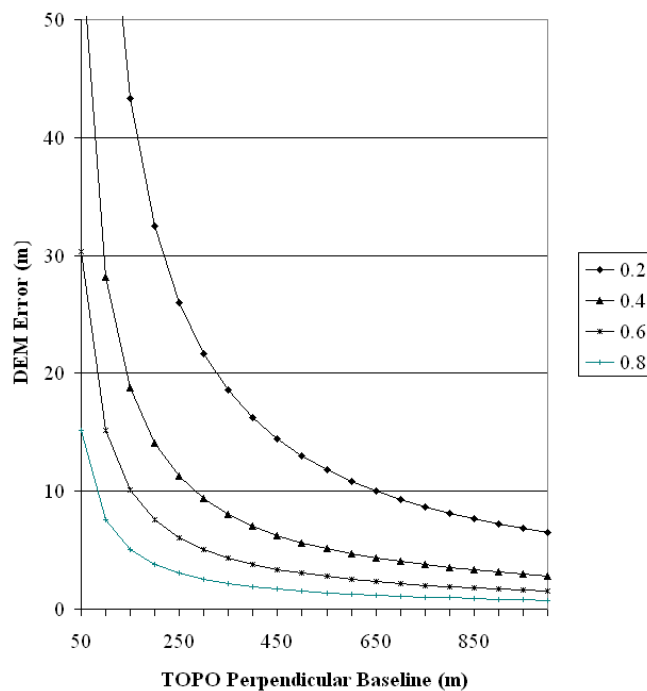
Figure 4.12 Configurations where IAS 3-pass may be better than 2-pass. Curves represent T_0 boundary values for different coherence values. Configurations that give T_0 above the curve will find screened 3-pass to improve upon 2-pass; those below will not. (*Sowter and Warren 2005*)

4.6.2 Smoothing example

The DEM smoothing method to improve upon 2-pass DInSAR has been tested using the data set of Iran described above in section 4.5. An SRTM 90m resolution DEM has also been used. Interferograms were generated using the Doris InSAR processor and precise orbits from Delft Technical University.

The 90m resolution SRTM DEM has an accuracy of approximately 9m RMS in vegetated, rolling topography *(Kocak et al 2005)*. So using Figure 4.12 and a topographic baseline of greater than 350m would suggest that, for coherence values greater than 0.2, screening would benefit the DInSAR product. The topographic baseline for the data used was approx. 500m.

A 2-pass result was generated from the InSAR data. This was repeated twice; once with the original 90m SRTM DEM, to use as a reference result, and once with a degraded 90m SRTM DEM. The degraded DEM was generated using the SRTM DEM with a random noise component added to it with mean 0m and standard deviation 10m. A 3-pass result was generated in the same way as described in section 4.5, with the topographic interferogram being screened using the degraded DEM to remove the estimate of the large scale phase errors. Finally, a 3-pass result was generated without phase screening.

A short profile across the area of deformation was used to compare the different interferogram results obtained. These profiles can be seen below in Figure 4.13. It can be seen that the profiles from the 2-pass with the good DEM and the basic 3-pass both follow a similar curve. The 2-pass result using the degraded DEM deviates from this curve greatly, whereas the smoothed 3-pass result more closely follows the result of 2-pass with a good DEM. This suggests that, for this case, a smoothed 3-pass result improves upon a 2-pass result that uses the same DEM as input. But it also appears that the basic 3-pass result (with no DEM) gives a much smoother curve. This could be due to the fact that the region used was of very high coherence and probably had very little atmospheric phase effects, and so the phase screening approach might not be so useful here.
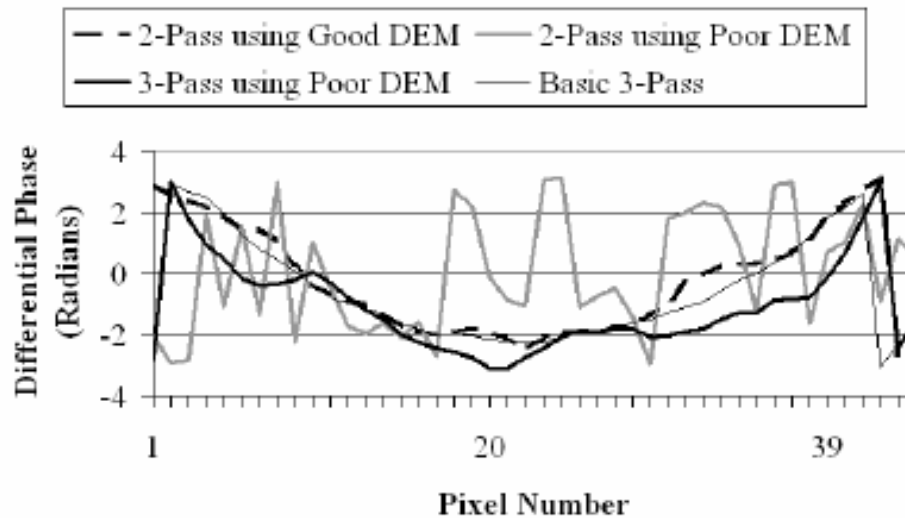
Figure 4.13 Spatial profiles of four DInSAR results. 3-pass using a poor DEM shows a much more consistent result than for 2-pass using the same DEM. (*Sowter and Warren 2005*)

4.7 Summary

This chapter introduced the concept of the phase ambiguity relating to SAR interferometry. Algorithms exist to identify the ambiguity relative to a reference pixel, but are sensitive to noise in the data and will not always give usable results. The Integer Ambiguity Search (IAS) method has been discussed as a way to recreate the absolute phase for pixels close to a nearby GCP, or if prior to this the phase has been unwrapped, then the absolute phase for each pixel can be recreated. Absolute positioning using this method has been described and demonstrated over the city of London, UK. The IAS method allowed possible improvements to be made upon the 3-pass algorithm and this has been demonstrated using data from Iran. Finally, a smoothing procedure for 3-pass interferometry was described, based upon similar procedures used in DEM generation. It was shown that using a 3-pass framework together with the smoothing operation enables a better result than 2-pass differential interferometry alone, if certain criteria are met.

5. Persistent Scatterer Interferometry

5.1 Persistent Scatterers

In 1999, *Ferretti et al (1999)* demonstrated a new technique of interferometry that utilised the whole back catalogue of ERS SAR images for a specific region. This technique was named the *Permanent Scatterers Technique (Ferretti et al, 2001)*. Rather than using every image pixel, the technique only selects certain pixels based upon their phase stability throughout the time evolution of the images. These pixels being called Permanent Scatterers. In the real world these pixels relate to stable, reflective objects such as bare rock, buildings, bridges, lamp posts etc, which makes this technique ideal for monitoring in urban areas. The terms persistent scatterer and permanent scatterer can be interchanged as they generally mean the same, but permanent scatterer tends to be used when related to Ferretti's technique. For the remainder of this thesis the term persistent scatterer (or PS) will be used to describe phase stable pixels.

5.2 Persistent Scatterer Interferometry Review

There are a few different Persistent Scatterer Interferometry (PSInSAR) and similar methods being developed at this time. The most prominent of these are: the Permanent Scatterer Technique (*Ferretti et al 2000a; Ferretti et al 2001*), the Coherent Pixel Technique (*Mallorqui et al 2003; Dominguez et al 2005*), the Spatio-Temporal Unwrapping Network (STUN) algorithm (*Kampes and Nico 2005*), the Interferometric Point Target Analysis (IPTA) algorithms (*Werner et al 2003*), the Small Baseline Subset (SBAS) (*Berardino et al 2002*) and the Stable Point Network (SPN) (*Duro et al 2004*). Even though there are six distinct methods listed, the aims of each method are essentially the same and are as follows.

A large number of SAR images are needed and should be coregistered to a common grid; this is referred to as the *stack* of data. Interferograms are formed from this stack of SAR images, which are then flattened using a DEM to give

the differential phase. Candidate Persistent Scatterer (PS) points are identified by some means (e.g. see *Ferretti et al 2001*, *Mallorqui et al 2003*, *Hooper et al 2004*) and then used in a joint spatial and temporal analysis to identify an estimate of the atmospheric phase screen for each interferogram. After removing this phase screen from the interferograms, an estimate of the deformation and error in the DEM can be made by examining both the temporal evolution and the geometric baseline variation of each pixel.

Persistent scatterer methods have been successfully used to identify seasonal deformation (*Colesanti et al 2003a*), landslide monitoring (*Colesanti et al 2003b*), mining subsidence (*Kircher et al 2003*), volcanic deformation (*Hooper et al 2004*) and urban subsidence (*Ferretti et al 2000b*).

5.3 Ferretti Algorithm Overview

An overview of Ferretti's linear PS algorithm (*Ferretti et al 2001*) will be given here. It was the first algorithm that followed this persistent scatterer approach and is relatively simple. The method is only suitable for small areas, up to a maximum of 5km x 5km, due mainly to assumptions made about the atmosphere; namely that it can be modelled effectively as a linear plane. It involves the following steps:

- Generate interferograms
- Remove topography using a DEM
- Identify candidate PS points from the SAR amplitude statistics
- Use these points to model linear deformation and atmospheric effects
- Generate Atmospheric Phase Screens for each interferogram
- Remove atmosphere from each interferogram
- Recreate differential phase interferograms
- Identify PS points using phase statistics

5.3.1 Candidate PS Point Identification

Ferretti's PS algorithm is a "single master" algorithm. This means that all the interferograms are formed with the same master image, and are therefore all coregistered to the same regular grid. After the SAR images have all been coregistered, an analysis on the stack of SAR data can be undertaken. A large number of SAR images are required for PS techniques, usually at least 30. Before the SAR amplitude data can be analysed, the data should be radiometrically corrected using the ESA calibration factors (*Laur et al 2002*), so that the amplitudes are comparable. Because, by definition, persistent scatterers are phase stable pixels, the phase could be used to identify the PS. But because of the errors present in the phase, e.g. atmospheric and orbit errors, this is generally not possible. The amplitude of the SAR data however is largely unaffected by these contributions, and for high SNR the *amplitude dispersion* can be used as a measure of phase stability (*Ferretti et al 2001*). The amplitude dispersion is calculated on a pixel-by-pixel basis, where the standard deviation in the time direction of each pixel's amplitude is divided by the mean of the same set of amplitude values. This is then tested against a threshold and points with a value less than this threshold are selected as candidate PS points. As a by-product of this, the mean amplitude image created from all the SAR images is available, which has much better speckle statistics than a single image. Often the mean is calculated from the intensity values (amplitude squared) rather than the amplitude itself (*Meadows and Laur 1998*). A comparison is shown in Figure 5.1 of a mean amplitude image of 31 SAR images and the same region in a single SAR image. It can be seen that the mean image appears much cleaner than the single image.
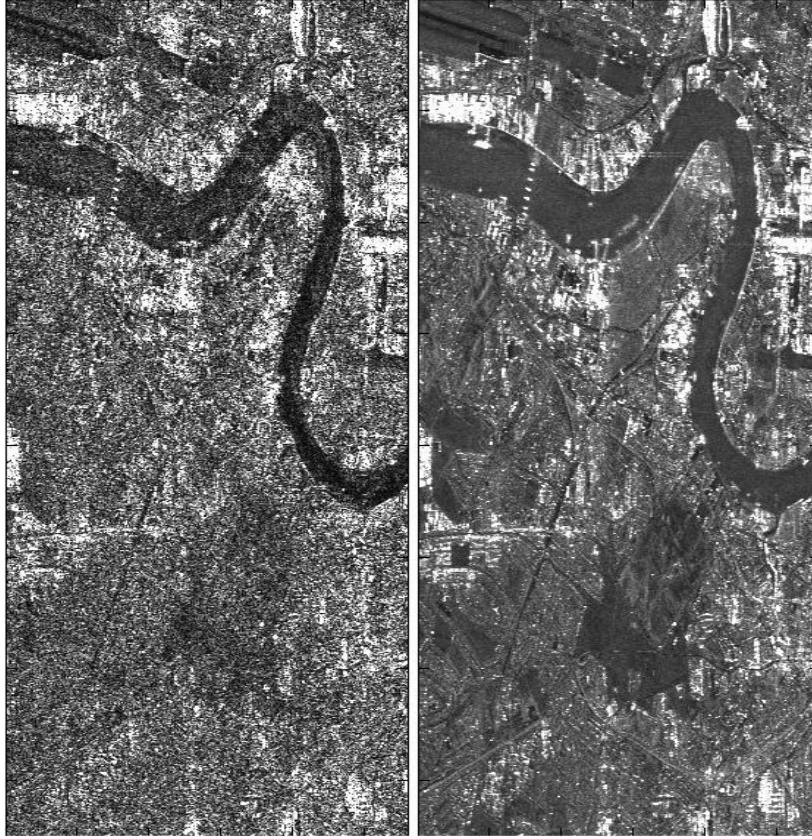
Figure 5.1 SAR amplitude vs averaged SAR amplitude. Left is a single SAR amplitude image of a region in London. Right is the mean amplitude of 31 SAR images of the same region. Note the reduction in speckle.

5.3.2 Phase Analysis

After generation of the interferograms the differential phase is created. A 2-pass method is used employing the best available DEM of the area. To reduce the amount of data, the differential phase not relating to the PS candidates is discarded. The differential phase is given by:

$$\partial\phi = \phi_{atm} + \phi_{orb} + \phi_{defo} + \phi_{DEM} + \phi_n \qquad\qquad 5.1$$

where $\partial\phi$ is the differential phase and $\phi_{atm}, \phi_{orb}, \phi_{defo}, \phi_{DEM}, \phi_n$ are phase terms due to atmosphere, orbit errors, deformation, DEM errors and noise respectively. The phase of interest is ϕ_{defo} whereas the other components can be considered as unwanted noise, which need to be removed. Consider each component separately.

- ϕ_{atm}, ϕ_{orb} - Spatially correlated and essentially random in time. These two cannot be separated and so the atmospheric phase screen solved for is in fact $\phi_{atm} + \phi_{orb}$. It is assumed that this atmospheric phase screen can be modelled as a simple linear plane, with components in the range and azimuth directions, using: $\phi_{aps} = a_0 + a_1 r + a_2 z$ where r and z are range and azimuth of pixel and a_0, a_1, a_2 are the constant and linear parameters.

- ϕ_{defo} - Correlated in time and depending on type of deformation it could be correlated spatially over small regions. In this method, it is assumed that there is only linear deformation occurring and that it can be modelled as: $\phi_{defo} = \frac{4\pi}{\lambda} T_j v$ *(Ferretti et al 2001)* where v is a linear velocity in m/year and T_j is the temporal baseline in years of the jth interferogram.

- ϕ_{DEM} - Correlated up the stack in terms of the geometric baseline and in general is not spatially correlated. It can be modelled approximately as: $\phi_{DEM} = \frac{4\pi B_j}{\lambda R \sin\alpha} \Delta h$ *(Ferretti et al 2001)* where B_j is the baseline of interferogram j, Δh the height error of the DEM in metres and R, α the range and incidence angle of the pixel.

- ϕ_n - Spatially and temporally random noise component, due mainly to geometric and temporal decorrelation. Should be small by definition for a persistent scatterer.

Using this information in an iterative algorithm it is possible to fit these models to the data to estimate the phase components.

5.3.3 Algorithm Overview

The algorithm employed is a relatively simple iterative one. It is shown below in Figure 5.2 in terms of a flow diagram for ease of description.
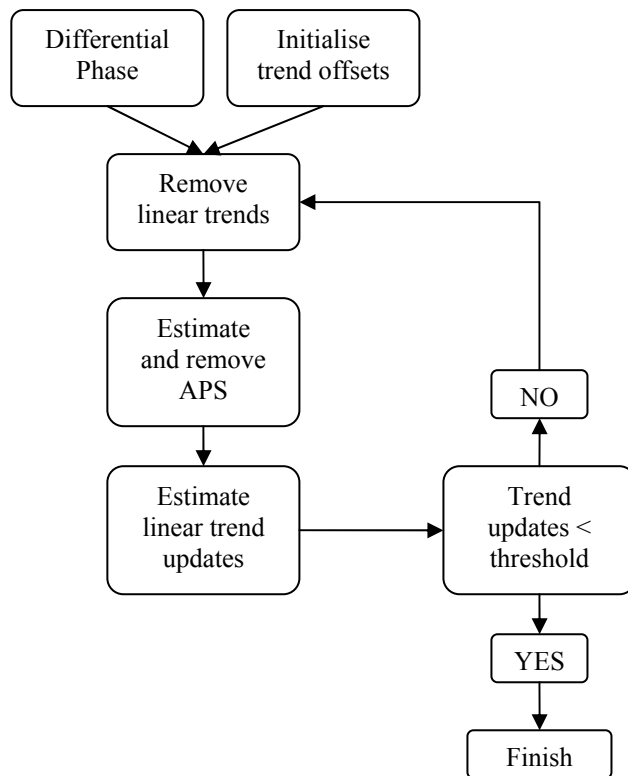
Figure 5.2 Flow diagram of Ferretti linear algorithm: describing the main iterative algorithm of the Ferretti 2-pass linear PS technique.

The final residuals output by the iterative algorithm described are presumed to be atmospheric anomalies that do not fit the planar model and random noise. These residuals are then spatially interpolated and filtered to remove the random noise and estimate the atmosphere at each pixel of the interferogram. These are then removed from each respective interferogram, along with the atmosphere phase plane model of each interferogram. The differential phase is then recalculated for each pixel of each 'atmospheric free' interferogram and a new search for persistent scatterers takes place. This time instead of the amplitudes the phase values are examined. If they fit a linear temporal model to a certain correlation value then they are selected as persistent scatterers. The linear temporal model includes a term related to the deformation velocity and also a term modelling the error from the DEM.

5.4 Limitations and Advantages of PSInSAR

PSInSAR is a powerful new technique. With it, it is possible to identify slow, long term deformations using certain pixels. As with all techniques it has certain advantages, but it also has its disadvantages. These are identified and described in this section.

Advantages

- Can identify slow deformation rates (but only up to 1.4cm per 35 days, using ERS, due to sampling restrictions)
- Spatial array/network of points
- No requirements to go "into the field"
- Can "go back in time" i.e. there exists a substantial back catalogue of data, from 1991 for ERS.
- Costs less than long-term GPS or levelling surveying
- Overcomes the problem that atmospheric anomalies cause in differential interferometry.

Disadvantages

- Reliant on a terrain model – Not such a restraint since SRTM data was made available, but still requires the error component to be modelled out in the processing chain.
- Requires large quantities of data – Has implications for the cost of the many SAR scenes required. Also can mean large computational burden and processing time. If the area to be studied has no SAR back catalogue (i.e. there is no SAR data for the study area) then the PSInSAR method cannot be used until sufficient data has been collected (using ESA Envisat satellite takes approximately 3 years to collect 30 images).
- What *actually* is a PS? – The physical nature of the scatterer is largely unknown, e.g. is it a lamppost, a building or natural bedrock? Other information is required to answer this, such as detailed aerial photographs or digital maps. Even then, due to the spatial resolution of the radar images, positioning the scatterer inside the resolution cell is

ambiguous. For certain applications it is important to know what the PS is, so that its deformation can be judged to be relevant or not; e.g. people measuring tectonic motion may not be interested in scatterers that are not indicative of the natural bedrock, such as lampposts or bridge gantries.

- Persistent Scatterer Positioning – To integrate the PS data with other techniques such as GPS or levelling, the 3D position of the PS point is needed. An accurate position estimate from the terrain model is difficult due to the errors present, although it has recently been shown, using experimental data, that a precision of 1m in the 3D positioning of PS points can be attained (*Perissin and Rocca 2005*).

- Using a model of deformation to identify PS points – The method of identifying PS points by how closely they follow a model is not ideal. If the deformation structure of the pixel is different to that of the model, then the pixel might not be identified as a PS point even if it is one. For example, if a pixel shows strong seasonal deformation then it might not fit a linear model very well but rather a sinusoidal model (*Colesanti et al 2003a*)

5.5 Development of the Linear IAS 3-pass PSInSAR Method

The remainder of this chapter is devoted to the linear IAS 3-pass PSInSAR method developed and covers the rational behind it and the development of the algorithm.

5.5.1 Motivation

Recall from chapter 4 that the Integer Ambiguity Search (IAS) method allowed for the absolute phase to be reconstructed. This had certain benefits for the 3-pass differential interferometry method as described in chapter 4. It was shown that the IAS 3-pass method gave a result which was comparable to the 2-pass method. As discussed above, all previous PSInSAR methods make use of a Digital Elevation Model to follow a 2-pass methodology and then set about modelling the DEM error from the differential phase results. So by using a

DEM a new error source is introduced to the data. Since the IAS 3-pass method allows a differential result similar to the quality of a 2-pass result, it should be possible to create a PSInSAR algorithm using 3-pass.

This may give benefits over the traditional 2-pass PSInSAR techniques, namely:

- No terrain model – By using a 3-pass method to create the differential phase, the use of a DEM is by-passed and so the differential phase will not contain this error source, and there will be no requirement to calculate height corrections.

- Better positioning – The IAS allows the calculation of the 3D position of InSAR data without introducing the errors from using ground control. Also, by using the phase value of the data for the positioning, an improved estimate of its location is hoped to be achieved.

As the first benefit listed above states, no DEM is needed to calculate the differential phase. But unfortunately, the interferogram that is used as the topographic model in the 3-pass method will have errors in the phase due to atmosphere anomalies, orbit uncertainties, deformation and decorrelation noise. These will propagate through into the differential phase. But recall that for PS points the decorrelation noise is small. This implies the main error sources in the phase of the topographic interferogram are spatially correlated, which in general is not true for errors in a DEM. Therefore by using a 3-pass method instead of a 2-pass method in the PSInSAR framework, the DEM error is replaced by a spatially correlated error, which could allow benefits in the solution of the PS algorithm. Also, as stated above, this error is not related to topography but the atmospheric and deformation phase of the topographic interferogram, and can therefore be used as a phase observation within the analysis such that there is no loss of degrees of freedom between the 2-pass and 3-pass PSInSAR methods.

5.5.2 The IAS PSInSAR Algorithm

In this research, it was decided to implement the IAS PSInSAR approach within a simple method – the Ferretti method. This would act as an effective demonstration that 3-pass DInSAR could be used within a persistent scatterer framework. The Ferretti algorithm was used as the basis because it is a single master method. This is important for a 3-pass framework because the 2 interferograms used must share the same master image. Also, in the 2-pass method the DEM is the same for each differential result, so too the topographic interferogram should be the same for each 3-pass differential interferogram. By following these two "constraints", the stack of interferograms will have to be constructed with the same master image. Hence Ferretti's algorithm is a good choice to use as the model. The IAS 3-pass PSInSAR algorithm is summarised in the flow diagram below, with the following sections giving a more detailed description.
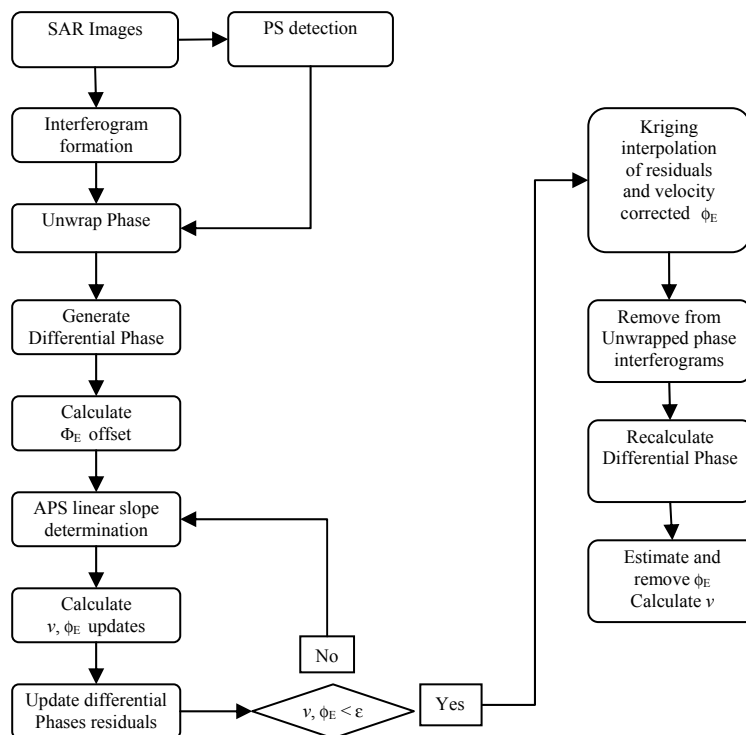
Figure 5.3 Flow diagram of the linear 3-pass IAS PSInSAR method. ϕ_E is the topographic phase error.

5.5.2.1 Interferogram Generation and Candidate PS Point Selection

The foremost stage of the PSInSAR processing is the construction of the interferograms. To do this, a suitable image must first be selected as the master image. The criteria used for the selection are the geometric and temporal baselines of the stack of data when a certain image is used as the master. The image used as master should ideally lie in the middle of the temporal stack, such that the temporal baselines of the interferograms are minimised. Also, the geometric baselines should be distributed either side of 0m (i.e. both positive and negative baselines) with a variety of sizes but with a relatively low mean value of the magnitudes. Interferograms with a geometric baseline greater than the critical baseline can be used in a PSInSAR process.

After selection of the master image the interferograms are formed. They are processed much the same as for a traditional InSAR process except no filtering of the data occurs. This is so the phase at the candidate PS points will not be affected adversely. The final interferogram is not multilooked but left at its original resolution (20m x 4m ground range for ESA ERS SLC data) again for reasons that the phase would not be indicative of the PS point. The interferograms are not flattened with respect to a reference surface at this point. An example of an interferogram created in this way is shown below in Figure 5.4.

After the interferograms have been formed the amplitude images can be resampled onto the same master grid to form a stack, and the process for identifying candidate PS points can begin. The method highlighted in (*Ferretti et al 2001*) is used for this and was described above in section 5.3.1.
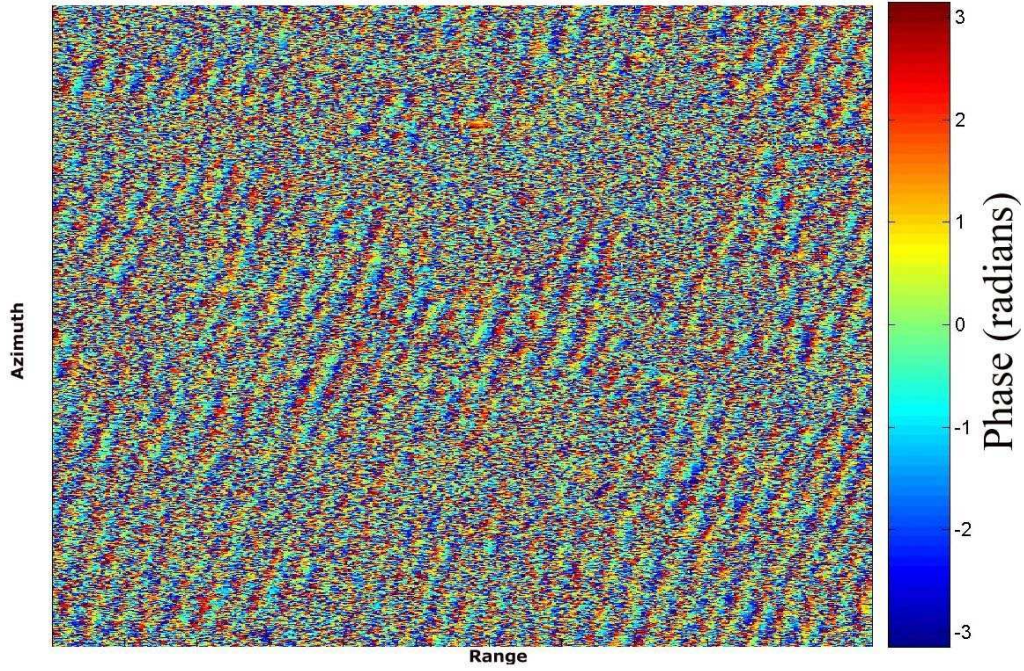
Figure 5.4 Example Interferogram for PSInSAR. Produced as described above – no
multilooking or filtering. Data has been oversampled by a factor of 2 in the range direction.

5.5.2.2 Generation of Differential Interferograms

The formation of the differential phase is the next step in the processing chain.
The IAS method described in chapter 4 is used to do this, with the same
interferogram used as the topographic pair for each differential phase result.
This requires the phase of the interferograms to be unwrapped and the absolute
phase to be formed.

Due to the fact that the phase interferogram has been formed without any
filtering of the noise or any multilooking, traditional 2-dimensional phase
unwrapping algorithms will not work here. It is, however, possible to use a
DEM such as the SRTM data to aid in the unwrapping without a floating point
error being passed on. Consider the phase of the wrapped absolute
interferogram and the DEM respectively:

$$\phi^{Wrapped} = \left(\phi_{Topo} + \phi_{Defo} + \phi_{Atm} + \phi_{Orb} + \phi_{n}\right)^{Wrapped} \qquad 5.2$$

$$\phi_{Simulated} = \phi_{Topo} + \phi_{E} \qquad 5.3$$

where $\phi^{Wrapped}$ is the wrapped interferogram phase, $\phi_{Topo}, \phi_{Defo}, \phi_{Atm}, \phi_{Orb}, \phi_n$ are the phase components due to topography, deformation, atmosphere, baseline orbital errors and decorrelation noise respectively, $\phi_{Simulated}$ is the simulated phase from a DEM and ϕ_E is the error in the topography from the DEM. If, first of all, ϕ_E is considered to be less than π in magnitude, then subtracting equation 5.3 from 5.2 and re-wrapping the result gives:

$$\phi = \left(-\phi_E + \phi_{Defo} + \phi_{Atm} + \phi_{Orb} + \phi_n \right)^{Wrapped} \qquad 5.4$$

If equation 5.3 is now added back onto equation 5.4, the result is:

$$\phi^{SUW} = \phi_{Topo} + \left(\phi_{Defo} + \phi_{Atm} + \phi_{Orb} + \phi_n \right)^{Wrapped} \qquad 5.5$$

where ϕ^{SUW} is the semi-unwrapped interferogram phase, so called because only the topographic phase has been unwrapped. The IAS can then be performed on this using a GCP derived from the DEM if necessary, to construct the absolute phase estimate. An example of an interferogram unwrapped in this way is shown in Figure 5.5a, with a cross section along a row of the image (Figure 5.5b).

If ϕ_E is not less than π in magnitude then equation 5.4 will be the same as before, but when the simulated phase is added back onto it equation 5.5 will become:

$$\phi^{SUW} = \phi_{Topo} + 2\pi\Delta n + \left(\phi_{Defo} + \phi_{Atm} + \phi_{Orb} + \phi_n \right)^{Wrapped} \qquad 5.6$$

where Δn is an integer number. This term comes from the fact that ϕ_E was wrapped in equation 5.4 and then had the absolute (i.e. unwrapped) value ϕ_E added back onto it in equation 5.5.

Therefore it can be concluded that this technique of unwrapping the phase will not introduce a floating point error due to the DEM inaccuracy, but may introduce an integer error. This is likely to be more of a problem for the large baseline interferograms where a complete phase cycle relates to a smaller surface height change, meaning errors in the DEM will relate to a larger phase value.
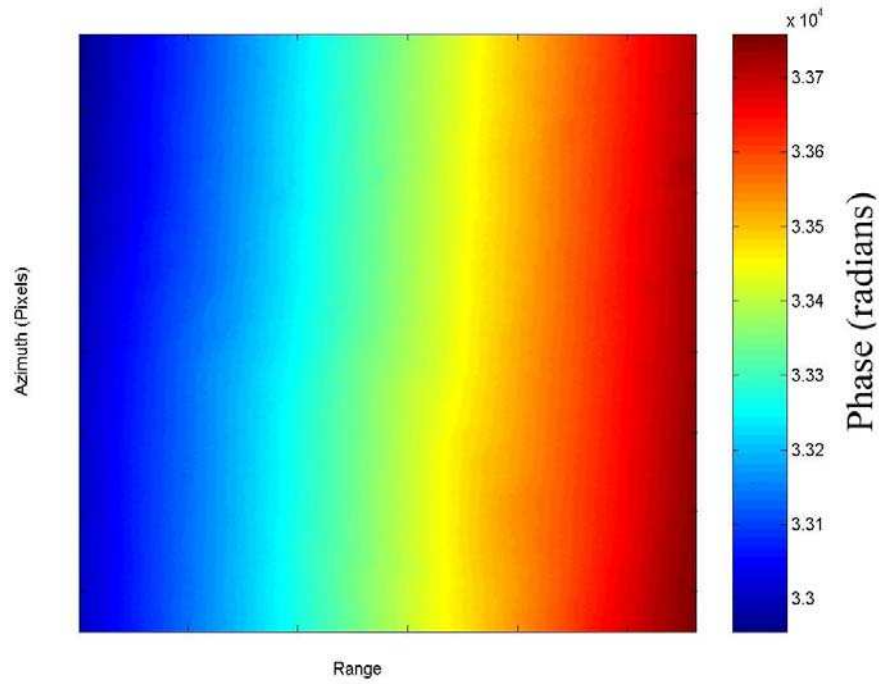
Figure 5.5a. Semi-unwrapped Interferogram. As figure 5.4 but (semi-) unwrapped using the method described in the text.
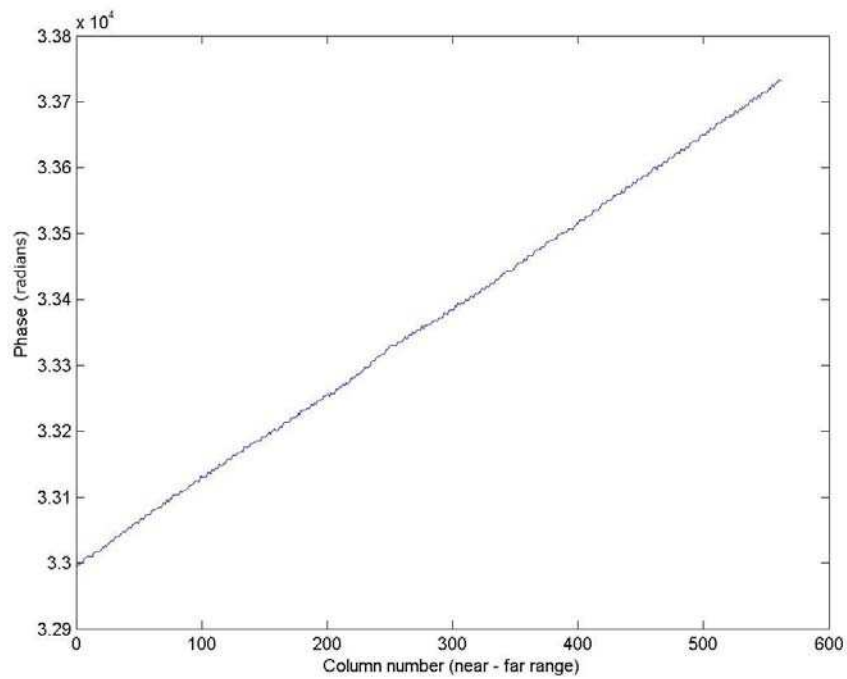
Figure 5.5b Cross section of semi-unwrapped interferogram: along a line of constant azimuth of interferogram shown in Figure 5.5a

After unwrapping the interferograms a suitable pair should be selected as the topographic pair for the differential phase production.

Recall the differential phase equation from chapter 4:

$$\partial \phi = (\phi_{13} + 2\pi \Delta n_{13} + \frac{4\pi}{\lambda} \delta e_{13}) - \frac{B_{13}}{B_{12}} (\phi_{12} + 2\pi \Delta n_{12} + \frac{4\pi}{\lambda} \delta e_{12})$$
$$- B_{13}(\frac{4\pi}{\lambda} \cos(\beta_{12} + \gamma) - \frac{4\pi}{\lambda} \cos \beta_{12})$$

5.7

where the subscripts $_{12}$ related to the topographic pair and $_{13}$ to the deformation pair. The second term on the right hand side of the equation says that the topographic phase is scaled by the ratio of the baselines. If the topographic baseline is larger than the deformation baseline, then the topographic phase will be scaled down, and therefore any errors in the phase will be scaled down too. Conversely, if the topographic baseline is less than the deformation baseline then the topographic phase is scaled up. If the interferogram with the largest baseline is selected as the topographic pair, then in every differential phase interferogram the topographic phase errors are scaled down and will therefore have an effect of less than π in the result. This minimises the effect of the errors but makes it harder to identify the magnitude of this error for removal. If the interferogram with the smallest baseline is selected as the topographic pair, then the error term in the differential phase will be scaled up for each interferogram. Since this will cause a greater effect in the differential phase, it makes it easier to identify for removal. This is demonstrated in Figure 5.6 below. Figure 5.6a shows the effect of an error of 0.5 radians when the baseline ratio is always less than 1, i.e. when the topographic baseline is the largest in the set. Figure 5.6b shows the effect of the same error but when the interferogram with the smallest baseline is chosen as the topographic pair.

There are other effects that might influence the choice of topographic interferogram, such as the temporal baseline of the interferogram. Interferograms with a large temporal baseline will most likely have a larger deformation signal component, and therefore a larger topographic error component since this interferogram should only contain phase due to topography. This factor is not as important as the geometric baseline though, since if a large temporal baseline interferogram with a small geometric baseline is chosen, the error due to deformation is easier to remove from the differential

phase. After selection of a suitable topographic interferogram the differential phase can be generated.
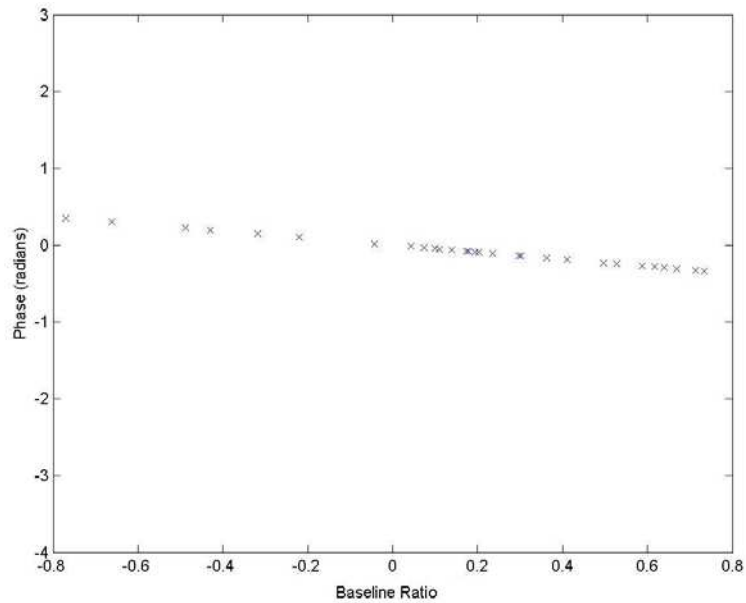
Figure 5.6a Effect of an error in large baseline topographic interferogram. The effect of an error of 0.5 radians in the topographic interferogram when it is the interferogram with the largest baseline
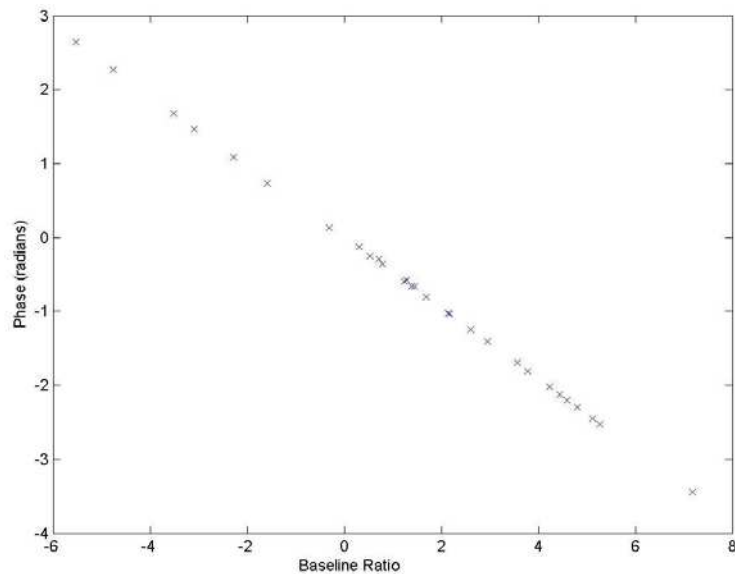
Figure 5.6b Effect of an error in small baseline topographic interferogram. The effect of an error of 0.5 radians in the topographic interferogram when it is the interferogram with the smallest baseline.

5.5.2.3 Removal of the Topographic Phase Error

Suppose the topographic interferogram was made purely of topographic phase, that is, there was no phase due to atmosphere, orbital errors or deformation.

Then the differential phase would be:

$$\partial\phi = \phi_{defo}^{13} + \phi_{atm}^{13} + \phi_{orb}^{13} + \phi_{n}^{13} \qquad 5.8$$

where again ^{13} relates to the deformation pair. If this was the case the algorithm could proceed by looking for strong temporal (deformation) and spatial (APS) trends in the stack of data.

Now consider that the topographic phase is not perfect:

$$\phi^{12} = \phi_{topo}^{12} + \phi_{E}^{12} \qquad 5.9$$

where ϕ_{E}^{12} is the phase error term made up of the sum of the atmospheric, orbital, deformation and decorrelation phase components. Then, using this as the topographic phase, will give the differential phase as:

$$\partial\phi = \phi_{defo}^{13} + \phi_{atm}^{13} + \phi_{orb}^{13} + \phi_{n}^{13} + \frac{B_{13}}{B_{12}}\phi_{E}^{12} \qquad 5.10$$

ignoring the final term of equation 5.7 which implicitly depends on the topographic phase for the construction of angle β_{12}. Recall the unwrapping regime described previously. It only unwrapped the topographic component of the phase so the first four terms in equation 5.10 from the deformation interferogram are still wrapped. That is, equation 5.10 can be written as:

$$\partial\phi = \left(\phi_{defo}^{13} + \phi_{atm}^{13} + \phi_{orb}^{13} + \phi_{n}^{13}\right)^{wrapped} + \frac{B_{13}}{B_{12}}\phi_{E}^{12} \qquad 5.11$$

The differential phase from the IAS method is not automatically wrapped modulo 2π, so if $|\partial\phi| > \pi$ it is due to the last term of equation 5.11.

For each interferogram in the stack of data there is an equation 5.11, which in general terms can be written as:

$$\partial\phi^{i} = \left(\phi_{defo}^{i} + \phi_{atm}^{i} + \phi_{orb}^{i} + \phi_{n}^{i}\right)^{wrapped} + \frac{B_{i}}{B_{j}}\phi_{E}^{j} \qquad 1 \le i \le N, i \ne j \qquad 5.12$$

where j is the topographic pair and i the N-1 deformation pairs. For the same PS pixel on each interferogram the ϕ_{E}^{j} term will be the same, the only difference being the value of B_{i} that scales it. Therefore to estimate ϕ_{E}^{j} we may do a linear regression to the data up the stack in terms of the baselines, where the gradient of the resulting fit is the estimate for ϕ_{E}^{j}. This can then be removed from the

topographic phase and the differential phases recalculated. It is necessary to recalculate the differential phase with the new topographic phase estimate rather than subtract the baseline scaled ϕ_E^j from each differential interferogram because the topographic phase is used to construct the angle β_{12} in equation 5.7. Figure 5.7 below demonstrates the above procedure. Figures 5.7a and 5.7b show the same data, the differential phase, plotted against time and baseline ratio respectively. Figures 5.7c and 5.7d show the differential phase data after correction for the estimated topographic error ϕ_E^j, plotted against time and baseline ratio respectively. The actual value of the topographic error here is 1.603 radians whereas the value estimated and removed is 1.535 radians.
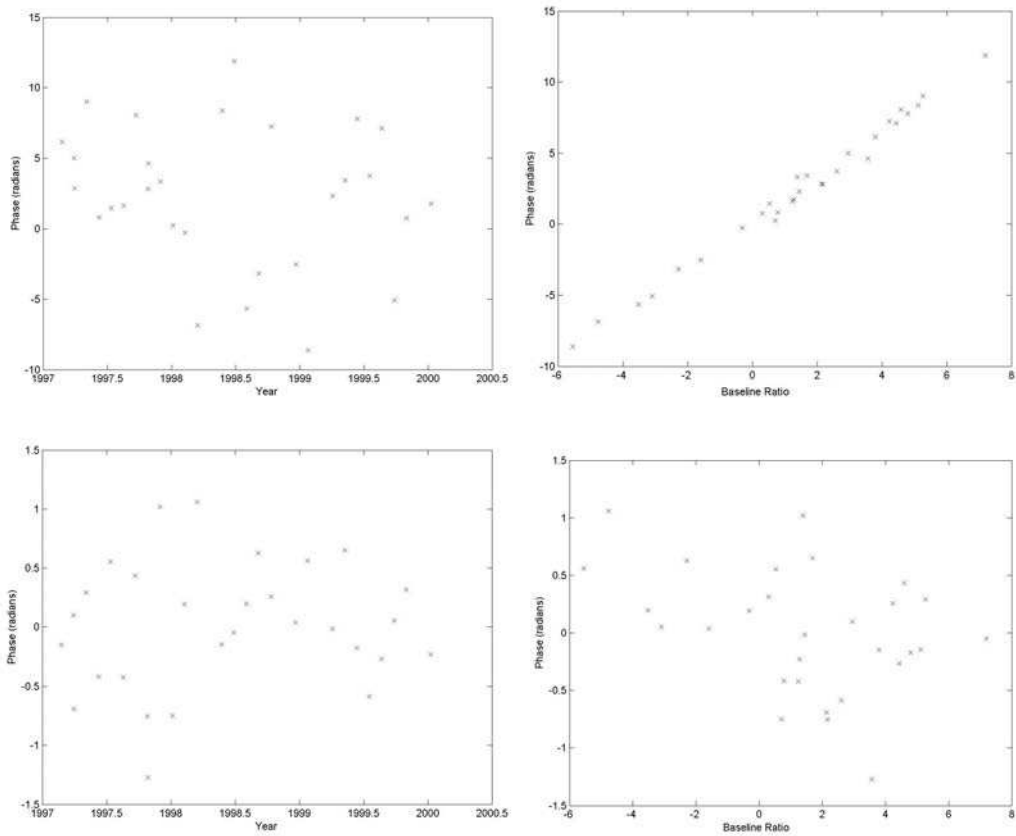
Figure 5.7 Estimation and removal of topographic phase error. a) and b) show the original phase data plotted against time and the baseline ratio respectively, c) and d) show the corrected phase data plotted against time and baseline ratio respectively. Note the change in scale of the phase.

5.5.2.4 The Iterative Procedure: Atmospheric Estimation

With the differential phases corrected for the ϕ_E^j term, the main iterative procedure can begin. This is essentially the same as the algorithm presented in (*Ferretti et al, 2001*). As outlined before, it is required to separate estimates of the atmospheric phase screen from phase due to a linear velocity. It is best explained using the bullet points below.

- For each interferogram, estimate the three parameters required for a linear phase ramp fit: $a_0 + a_1 r + a_2 c$ where r and c are pixel row and column values. This is done by finding the values of a_1 and a_2 that maximise the complex phase equation

$$\Gamma_j = \frac{1}{M} \sum_{m=1}^{M} e^{i\Delta\phi} \cdot e^{-i(a_1 r + a_2 c)} \qquad 5.13$$

where M is the number of candidate PS and $\Delta\phi$ the iterative differential phase, for each interferogram. The parameter a_0 is attained from the argument of Γ_j.

- Remove this phase plane estimate from the differential phases, but also keep the unchanged differential phases ($\Delta\phi_0$ say).

$$\Delta\phi_1 = \Delta\phi_0 - (a_0 + a_1 r + a_2 c) \qquad 5.14$$

- For each candidate PS point, estimate a linear velocity component using the data up the stack. This is done similarly to 5.13 by maximising a complex phase equation, weighted by the value of Γ_j from 5.13:

$$\gamma = \frac{1}{N} \sum_{j=1}^{N} \left| \Gamma_j \right| \cdot e^{i\Delta\phi_1} \cdot e^{-i(\frac{4\pi}{\lambda} T_j v)} \qquad 5.15$$

where N is the number of differential interferograms, T_j is the temporal baseline and v the velocity estimate.

- Sum up the total velocity estimates from previous iterations and remove the linear velocity phase component from the *original* differential phase values $\Delta\phi_0^{old}$:

$$\Delta\phi_0{}^{new} = \Delta\phi_0{}^{old} - \phi_v \qquad\qquad 5.16$$

where ϕ_v is the phase due to the sum of all previous velocity estimates v.

This loop is repeated until the magnitude of the velocity estimates of the *current* iteration are 0 (or less than a certain threshold). This results in an estimate for the planar APS from equation 5.13 and also, if the velocity and ϕ_E^j have been identified correctly, the residual differential phase components $\Delta\phi_0$ with the velocity removed should be phase due to atmosphere that doesn't fit the plane model and decorrelation noise (see equation 5.10).

5.5.2.5 Generation of the APS

At present, the atmospheric phase estimations are only available for the candidate PS points. They need to be spatially interpolated such that there is an estimate for each pixel of the interferogram. Also the decorrelation noise has to be separated from the APS to get the best estimate. This is done here by implementing a Kriging interpolation (*Cressie 1993*). Kriging is an interpolation routine that uses the spatial statistics of the sample data as well as the distance between points to generate weights. This can be achieved using a *semi-variogram*, which is a parameter of the data set and describes the relative variance between points separated by a certain distance (*Cressie 1993*). Kriging can act as either an *exact* interpolator or a *smoothing* interpolator. Since the data at the points being interpolated are expected to contain a random decorrelation noise component, using Kriging as a smoothing interpolator should reduce the magnitude of this random noise. *Meyer et al* (2005) suggest that Kriging is the optimal method for estimating the atmosphere from the residuals of a Persistent Scatterer stack.

5.5.2.6 Generate the Topographic Pair APS

The above method only gives the atmospheric phase screens for the N-1 deformation interferograms. But the ϕ_E^j error term from the topographic pair

also contains an atmospheric component, which may be separated and interpolated to generate the APS for the topographic interferogram. Consider the components of the topographic phase error term:

$$\phi_E^j = \phi_{atm}^j + \phi_{defo}^j + \phi_n^j \qquad \qquad 5.17$$

where the baseline orbital error component has been grouped with the atmospheric term for easier analysis. A linear velocity to model the deformation phase term has already been estimated from the stack of differential interferograms, so this can be used to remove the ϕ_{defo}^j term leaving the atmospheric phase and decorrelation noise terms. As with the deformation interferograms, these remaining terms can be interpolated and smoothed to form an APS for the topographic interferogram.

5.5.2.7 Final Persistent Scatterer Analysis

The atmospheric phase screens for each interferogram can be removed from the original interferograms and the final persistent scatterer search can begin. The differential phases are reconstructed from the updated interferograms and a topographic error term is estimated and removed as before but from every interferogram pixel. For each pixel in the interferogram a linear velocity is fitted to the stacked data, with the *ensemble phase coherence* – a goodness of fit parameter related to the *phase dispersion* (*Ferretti et al 2001*) – used to identify the point as a persistent scatterer or not. The ensemble phase coherence, γ_j, is calculated using equation 5.18

$$\gamma_j = \frac{1}{N}\sum_{n=1}^{N}\exp(i * \partial\phi_j^n) \qquad \qquad 5.18$$

where N is the number of interferograms and $\partial\phi_j^n$ is the differential phase of interferogram *n* at pixel *j*. If the ensemble phase coherence is above a certain threshold then the point is flagged as a PS point. Since the topographic error term contains the deformation phase, this can be used within the stack of data as an extra observation for the linear fit, giving N observations. Hence there is no loss of degrees of freedom between the 3-pass and the 2-pass PSInSAR methods.

5.6 Differences Between Ferretti's 2-Pass and IAS 3-Pass

The following bullet points highlight the differences between the two algorithms described above: Ferretti's 2-pass and the IAS 3-pass algorithms.

- Input data – The obvious difference here is that the 2-pass algorithm uses a DEM which introduces a new error source that must be removed, whereas the 3-pass algorithm uses an interferogram in place of the DEM. This too introduces an error term but due to the nature of it (i.e. it containing spatially correlated atmosphere and a deformation term) it can be estimated and removed before the latter part of the processing chain.

- If there are N+1 SAR images available for the analysis, then the 2-pass method will have N differential interferograms whereas the 3-pass method will only have N-1. This reduces the number of observations available for the initial candidate PS point analysis (see Table 5.1).

- Another difference, albeit small, is how the velocity and topographic error terms are identified in the iterative loop. The 2-pass algorithm uses a 2-dimensional periodogram to identify both velocity and topographic error terms together. The 3-pass method identifies an initial topographic error estimate from a linear fit to the differential data which contains the unwrapped baseline scaled topographic error. Then the velocity is estimated in the iterative loop before a final update to the topographic error estimate is made.

- The topographic error term is treated differently between the two methods. The 2-pass topographic error comes from the DEM, and when identified can be used to correct the DEM to make it more accurate at the PS points locations. With the 3-pass method the error term is from interferogram errors and not topography (see equation 5.17), which can be separated after the initial candidate PS point analysis by utilising the estimate of the deformation velocity and Kriging the residuals. In the same way with the deformation interferograms, the atmospheric phase screen can be removed from the topographic pair. In the final PS

analysis this error will therefore be mainly deformation and decorrelation noise, and can be fed into the linear velocity fit as another observation.

	2-Pass	3-Pass
Number of Interferograms	N	N
Number of Differential Interferograms	N	N-1
Number of APS solved	N	N
Number of Velocity Observations Available (post APS removal)	N	N
Height corrections required	Yes	No

Table 5.1 Comparison of terms solved for in 2-pass and 3-pass PSInSAR methods

5.7 Summary

The relatively new technique of persistent scatterer interferometry has been introduced, and described with respect to the Permanent Scatterer method of *Ferretti et al (2001)*. The advantages for using this methodology for surveying purposes have been outlined, along with some disadvantages. Two major disadvantages of the method are: the calculation of topographic height corrections and the positioning accuracy of the PS points for integration with other data. A 3-pass PSInSAR method has been introduced, with the aim of overcoming these two disadvantages. The methodology of the technique has been described and differences from Ferretti's method have been highlighted.

6. Data and Test Site

6.1 Introduction

The previous chapter introduced a new algorithm for Persistent Scatterer Interferometry based on the IAS 3-pass technique. This chapter discusses the data and the test site used to test the algorithm. The selection of the test site has been based on various criteria. The first criterion was that the region should contain a large urban area. This is important for selecting the PS points. Secondly, there should be a suitable amount of SAR imagery available, usually greater than 30 images are needed for a PS analysis (*Ferretti et al 2001*). The images should also be regularly acquired, e.g. there should not be large gaps in the data stack. This is to aid the processing since missing samples in the time series analysis will hinder the data fitting. The third criterion for selecting the test region was whether additional data was available or an analysis of the region had been previously performed. Additional data could mean either data from other surveying techniques such as the Global Positioning System (GPS), levelling surveys to compare the deformation found with the PSInSAR method or data from aerial/satellite imagery of the region to aid in the identification of PS points.

Taking into account the criteria listed it was suggested that London be used as the test site. London is a large urban area and has been regularly imaged by the ERS 1/2 satellites. There is also a GPS network that monitors the Thames Region which incorporates London. Large areas of the City of London have had extensive surveying performed, including previous InSAR and PSInSAR analyses (*NPA Group Ltd; Vexcel Corp.*). There is also an extensive amount of high-resolution aerial imagery available for London.

The remainder of this chapter discusses the London region in more depth, gives an overview of GPS for land deformation surveying and also describes the GPS network in the Thames Region. The chapter finishes with a description of the SAR data used within the project.

6.2 London

The city of London is located in the South Eastern corner of the United Kingdom, approximately at latitude of 51.5 degrees North and longitude 0 degrees. It is a large urban metropolis that covers approximately 1,500 square kilometres of land. The land cover of London includes residential, business, commercial, park and agricultural land in the periphery. The geography of London is fairly flat. There are few hills in the city and most of these are below 30 metres in height.

Previous recent studies of London using SAR interferometry have identified some areas that show subsidence. One such area is a piece of land in the Westminster region of London, where an extension to the Underground Rail Network was constructed in the late 1990s. At least three different research teams have identified this area of subsidence; groups at *NPA Ltd*, *Vexcel* and *Lawerence Livermore National Laboratory,* showing subsidence magnitudes of a few cm in total over 3 or 4 years.

There may be other areas of London showing subsidence or heave that occur due to the underlying geology. The geology of the London and Thames region is predominantly clay, chalk, sand and peat (*Environment Agency Report 2006*) (See Figure 6.1). Clay has a seasonal shrink/swell effect where in the wet months the clay swells, and in the dry months it shrinks. Vegetation also affects the shrink/swell since trees extract large quantities of water causing shrinkage (*Bingley et al 1999*). This shrink/swell can also cause an overall subsidence effect. Previous studies of the London Clay have reported 12mm of heave over a 3 year period (*Driscoll 1983*; *Driscoll 1984*), and magnitudes up to 50mm have been reported elsewhere.
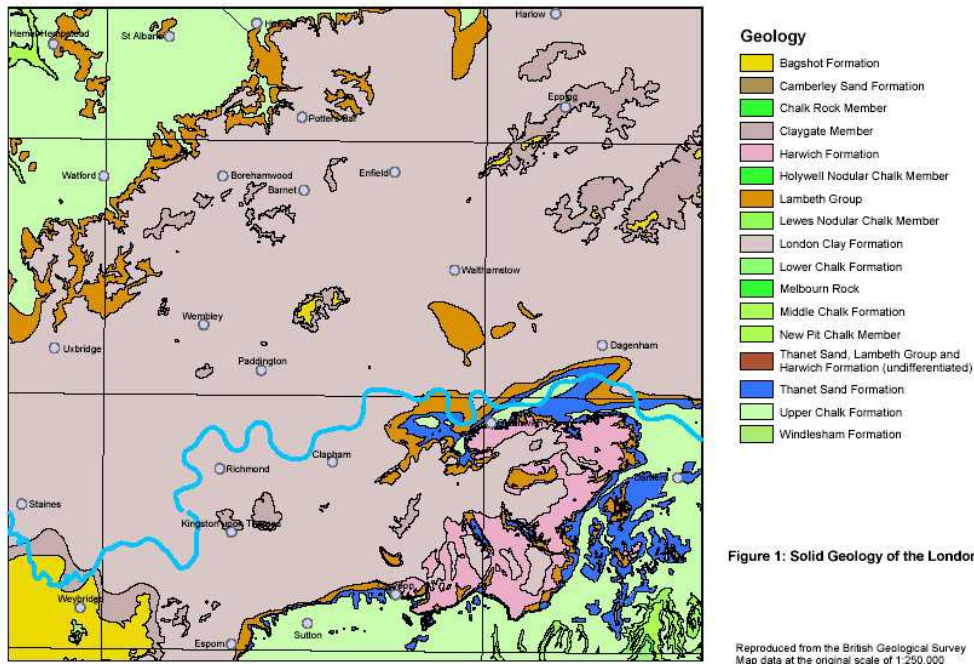
Figure 6.1 Solid Geology of the London Basin (From *Environment Agency Report 2006*)

6.3 Global Positioning System

The following section gives an introduction of the *Global Positioning System* (GPS) for land deformation monitoring. A comprehensive discussion on GPS is out of scope of this thesis. For a more informative and in-depth description of GPS see one of the many books on the subject, for example (*Hofmann-Wellenhof et al, 2001*). It should also be noted that much of this section has appeared previously in *Warren 2003*.

6.3.1 GPS Overview

GPS is a continuous all weather satellite-based positioning system originally designed by the US Department of Defense (DoD) in the 1970s for military purposes, but civilians also have access to it. It consists of a constellation of 24 satellites in 6 orbital planes, which each emit a coded signal on the L1 and L2 frequencies (L1=1575.42 MHz, L2=1227.60 MHz). This constellation was chosen so as to have at least 4 satellites visible anywhere in the world at any time, which is the minimum required number of satellites to get a good position

estimate. There is also a ground control segment that monitors and maintains the satellites and uplinks new improved data to the satellites.

A receiver on the ground can then use the coded signals to calculate the pseudorange from the satellite to the receiver, and then position itself relative to a global geodetic reference frame. To get a good 3-dimensional position estimate at least four satellites must be in view due to uncertainties in the receiver clocks. If there are two receivers available then the carrier phase can be used to enable a more precise and accurate relative position, via a post-processing technique. The L1 and L2 carrier signals have wavelengths of 19cm and 24cm respectively, which give this method a resolution of a few mm. The carrier phase is more difficult to process and measure than the code pseudoranges, and has the added difficulty of introducing an integer ambiguity. This arises due to the receiver only being able to measure the phase of the signal and not the number of wavelengths between satellite and receiver.

6.3.2 GPS for Land Deformation

GPS is a useful tool for measuring land deformations. Much work has been completed in the past on using GPS for detecting small movements. This includes work on structural deformation (see for example *Ashkenazi and Roberts 1997, Wieser and Brunner 2002*) and more general land deformation/subsidence (e.g. *Ashkenazi et al 1993, Maciaszek and Szewczyk 2001*).

Networks have been set up around the world to try to model and understand the Earth's deformations. The Southern Californian Integrated GPS Network (SCIGN) is a GPS network situated in Southern California, with emphasis around the city of Los Angeles. By July 2001 the network had a total of 250 operating GPS stations (*Hudnut et al* 2001). The SCIGN work hopes to further understanding of earthquake faults, provide the potential for estimating earthquakes, and to measure permanent crustal deformation.

Japan also has implemented a large GPS monitoring network due to seismic and volcanic activity on the islands (*Imakiire and Nakahori 2001*). The GPS Earth Observation Network (GEONET) consists of approximately 1000 continuous GPS stations, with an average spacing of 25-30km, to give nationwide coverage of Japan. It is capable of measuring crustal deformation and detecting co-seismic movement, which are helpful towards the study of geodynamics and earthquake monitoring. The accuracy when using dual frequency data is reported as being better than 2mm horizontally and 6mm in height (*Rizos et al 2000*).

6.3.3 GPS Limitations

Potentially there are many limitations to the accuracy of relative carrier phase GPS, the main ones being due to systematic biases in the observation equation. These can be classified into three general groups: satellite based, atmospheric and station based.

6.3.3.1 Satellite Based

These are problems due to errors in the satellite coordinates. They can be effectively mitigated through the post processing technique due to the observable used (the double differenced observable) and the use of the final precise ephemeris available from the International GNSS Service (IGS).

6.3.3.2 Atmospheric

The atmosphere interacts with the signal and affects its propagation path. The atmosphere can be considered made up of two parts, the ionosphere and the troposphere. The ionosphere has the effect of advancing the carrier phase by an amount dependant on the signal frequency. The effect of the ionosphere can be mitigated by using dual frequency receivers and forming the ionospherically free observable.

The lower part of the atmosphere is known as the troposphere and it has the effect of delaying and refracting the signal. It can be considered to be made up of a 'wet' part and hydrostatic part, with the 'wet' part being the hardest to model due to difficulties modelling the water vapour. The effect of the troposphere cannot be mitigated by using a dual frequency observable as was the case with the ionosphere. There exist models of the troposphere, such as the Saastamoinen model (*Saastamoinen 1973*), which can be used with effective post processing techniques to get an estimate of the total tropospheric delay; however the tropospheric delay is one of the major limiting factors to GPS and is an area of ongoing research.

6.3.3.3 Station Related

These errors and biases are due to the receiver and the surrounding region. Antenna phase centre variations arise due to the fact that the physical, geometric centre of the antenna is not usually identical as the electronic centre. This offset can change depending on the signal strength and frequency, elevation and the azimuth of the satellite. The IGS supply models of the phase centre variations, which can be used during the processing of the data to model the effect.

Tidal forces such as Earth Body tides, which is a 'stretching' of the Earth resulting from the gravitational pull of the Sun and Moon, and Ocean Tide Loading also have an effect on GPS positioning, since they result in a displacement of the Earth's surface. These effects can be modelled using the coefficients supplied by the IERS, and corrections can be applied to the receiver coordinates.

Multipath is another of the major limiting factors. It is a station specific problem, but also gives different effects depending on the GPS satellite positions. This means there is no particular model to mitigate it, but there are techniques that can aid in its removal. Multipath is caused by signals being reflected before they reach the antenna (Figure 6.2). Therefore the path length of the multipath signal is greater than the direct path from satellite to receiver. The consequence being that the receiver gives a noisier position estimate. These

effects can be minimised by selecting a suitable place to set up the station, (avoiding trees and structures that may reflect the signals), using choke ring antennas and observing for long periods of time.
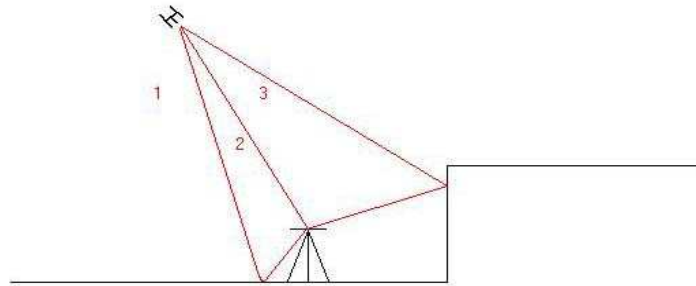
Figure 6.2 Multipath effects on GPS. Paths 1 and 3 are indirect from satellite to receiver, bouncing off structures before being received and giving false distances. Path 2 is direct from satellite to receiver, giving correct distance.

Cycle slips are also a major limiting factor to the accuracy of GPS. These occur when the receiver loses lock on a satellite, for example because of an obstruction (e.g. a tree). So when the receiver locks on to the satellite again a new integer ambiguity is created. This causes problems in the processing stage because the least squares processing method assumes there is only one integer ambiguity for each satellite. Cycle slips can be detected in a pre-processing step of the data by examining the double-difference phase residuals over time, and they can then be corrected.

Another major limitation of GPS is a problem arising from the geometry of the satellites, known as Dilution of Precision (DOP). To get high quality observations good satellite geometry is required. This means, ideally, that the satellites should be spread evenly around the receiver. For example if the satellites are all to the south of the receiver then this will give a high (bad) DOP value, whereas if there are some to the north, some to the south and one directly above the receiver, this will give a much better (lower) DOP value.

A further limitation of GPS is that it is only feasible on sparse networks. Due to the high cost of dual frequency CGPS stations it would not be a viable option to

cover vast areas with thousands of these. This means subsidence with small spatial scales may not get detected by the GPS network.

6.3.4 Summary of GPS for Deformation Detection

An overview of GPS has been given, concentrating on its application to land deformation monitoring. It is a satellite technique that can position points on Earth to high accuracy using the carrier phase information of the satellite signal. For long term monitoring of land movements accuracies of less than 1mm are feasible. It is a method that is available 24 hours every day and is used world wide to high precision. The GPS observations result in 3-dimensional position/movement vectors for the point where the GPS station is located.

Various limitations exist that need to be overcome at the processing stage. These range from atmospheric biases, motions due to tidal forces, errors in the satellite coordinates, detection and mitigation of cycle slips, and errors due to the receiver and its location. For most of these limitations there exist models that can be applied to effectively eliminate any biases, or techniques that can be used to reduce the effect of any biases. But other limitations such as multipath or interference effects are hard to eliminate and separate from detected small movements and can only be minimised by careful selection of GPS station location.

6.4 Thames Regional GPS Network

A GPS network in the Thames Region was set up in 1997 for an Environment Agency project to monitor changes in ground level and tie the results into tidal sea levels (*Bingley et al 1999*). The initial network consisted of three continuous GPS (CGPS) stations and 22 stations that were monitored episodically. A map of the station locations was given as Figure 4.6. The CGPS record data 24hrs a day at 30 second intervals, while the episodic GPS stations were surveyed every 3 months for a 9hr period between 9am and 6pm. A processing strategy was designed where the three CGPS stations were processed together with continuous data from the International GNSS Service

(IGS) global GPS network. This was followed by the episodic GPS being processed together with the corresponding 24hr data from the three CGPS stations, and finally the results of these two stages were combined. In other words, the episodic data are monitored relative to the CGPS stations, which in turn are monitored relative to the IGS stations used in the project. No GPS station is presumed stable, but rather the IGS stations have a known velocity which is assumed to be correct. More details on the processing and design of the GPS network can be found in *Bingley et al 1999.*

6.5 SAR Data

After deciding on the test site, the SAR data was ordered. It was decided that the satellite to be used should either be the European Space Agency's Envisat or ERS satellites. This is because these satellites have better orbital data and are the best to use for interferometric purposes. To get a stack of at least 30 SAR images meant that Envisat could not be used, since it was only launched in 2002 and a data stack large enough did not exist. This left the ERS 1/2 satellites. Because the SAR instruments on board the two satellites are virtually identical to each other, it is possible to combine radar images from the two of them without problems. The latter part of the ERS 2 mission has been frustrated with problems with the onboard gyroscopes, with failures occurring in early 2000 and the gyros being completely switched off by the start of 2001. This affected the Doppler values of the radar image and made interferometry with these SAR images more difficult. Therefore it was decided to use data acquired prior to 2000 to avoid these issues. The GPS network mentioned above was set up at the start of 1997, and so to be consistent with this it was decided to use SAR data from the start of 1997 to the end of 1999, which equated to 31 SAR images. Table 6.1 shows the dates of the SAR data used together with their orbit, frame number and satellite.

Satellite	Orbit	Frame	Date
ERS-2	8923	2565	03-Jan-97
ERS-2	9424	2565	07-Feb-97
ERS-1	29598	2565	13-Mar-97
ERS-2	9925	2565	14-Mar-97
ERS-2	10426	2565	18-Apr-97
ERS-2	10927	2565	23-May-97
ERS-2	11428	2565	27-Jun-97
ERS-2	11929	2565	01-Aug-97
ERS-2	12430	2565	05-Sep-97
ERS-1	32604	2565	09-Oct-97
ERS-2	12931	2565	10-Oct-97
ERS-2	13432	2565	14-Nov-97
ERS-2	13933	2565	19-Dec-97
ERS-2	14434	2565	23-Jan-98
ERS-2	14935	2565	27-Feb-98
ERS-2	15436	2565	03-Apr-98
ERS-2	15937	2565	08-May-98
ERS-2	16438	2565	12-Jun-98
ERS-2	16939	2565	17-Jul-98
ERS-2	17440	2565	21-Aug-98
ERS-2	17941	2565	25-Sep-98
ERS-2	18943	2565	04-Dec-98
ERS-2	19444	2565	08-Jan-99
ERS-2	20446	2565	19-Mar-99
ERS-2	20947	2565	23-Apr-99
ERS-2	21448	2565	28-May-99
ERS-2	21949	2565	02-Jul-99
ERS-2	22450	2565	06-Aug-99
ERS-2	22951	2565	10-Sep-99
ERS-2	23452	2565	15-Oct-99
ERS-2	24454	2565	24-Dec-99

Table 6.1 SAR data used in the project.

6.6 Test sites

A SAR image covers an area of approximately 100km x 100km, which is too large an area to test the algorithms with. Within the SAR images, two small separate test sites were identified: the Greenwich area and the Westminster area.

6.6.1 Greenwich

The Greenwich test site is an area of approximately 5km by 5km, and encompasses two of the episodic GPS stations in the aforementioned network: GRPK and SILV. The GRPK station is located in Greenwich Park and SILV is located in Silvertown, north of the Thames Barrier. These are shown on Figure

6.3 below. The area is bisected by the River Thames and also contains an airstrip and a large park. Large parts of the region are residential, commercial and industrial.

Figure 6.3 Google Earth image of the Greenwich test site: with the 2 GPS points shown.

6.6.2 Westminster

The Westminster test site corresponds to an area approximately 5km by 5km in size. The test site comprises of regions of residential, commercial and park land, and is bisected by the River Thames. Although there were no GPS stations in this region, it was selected as a test site because of the engineering works of the Jubilee line extension on the Underground Rail Network. Through a PS analysis of this region it is expected that the subsidence due to these works can be identified. An aerial image of the test site is shown below in Figure 6.4.

Figure 6.4 Google Earth image of the Westminster test site.

6.7 Summary

The reasons for selecting test data have been explained and why the City of London was selected as the test area. Within the city, two separate test sites have been selected, Greenwich and Westminster, and the sites described. A brief outline of using GPS for land deformation has been given and a regional GPS network has been introduced. The SAR data used in the project has been displayed in the form of a table showing the ERS satellite orbit and frame numbers together with the dates of acquisition.

7. Persistent Scatterer Software Developments

7.1 Introduction

At the start of this project there was very little persistent scatterer software available. The different software that was available were very much "black box" systems in that the software code was usually not made accessible nor changeable. This makes it difficult to adapt the software to your specific needs. It was clear that a set of tools for persistent scatterer interferometry would need to be developed. The advantages of developing our own software are clear: we have complete control of what it does and how it represents the results. It is also easy to add future functionality to the software such as new improved algorithms or further elements of research. The collection of tools that have been developed is imaginatively titled "*3-Pass Persistent Scatterer Processor*" or *3PaPS*. It is split into two parts; the first being written in C++ and the second being a collection of MATLAB scripts. There is also a set of HTML help files that describe the software which can be easily amended or added to by users of the software. A description of the software developed and its usage follow.

7.2 3PaPS

The 3PaPS collection of tools allows a 3-pass persistent scatterer process to be applied to a stack of Synthetic Aperture Radar images. As it stands, the use of 3PaPS is very much a linear process without much choice in the algorithms used. It is hoped that future research projects will add to the functionality of the tools giving greater depth in the choice of algorithms implemented.   The software is divided into two main stages:

- Identification of candidate PS points and the generation of differential phase (C++)
- Analysis of the differential phase data (MATLAB)

The front end of the 3PaPS software is shown below in Figure 7.1. It uses a Windows GUI (Graphical User Interface) instead of DOS prompts for ease of

usability for the novice user. The buttons on the main window are split into three sections:

- Pre-processing
- Processing
- MATLAB Scripts.
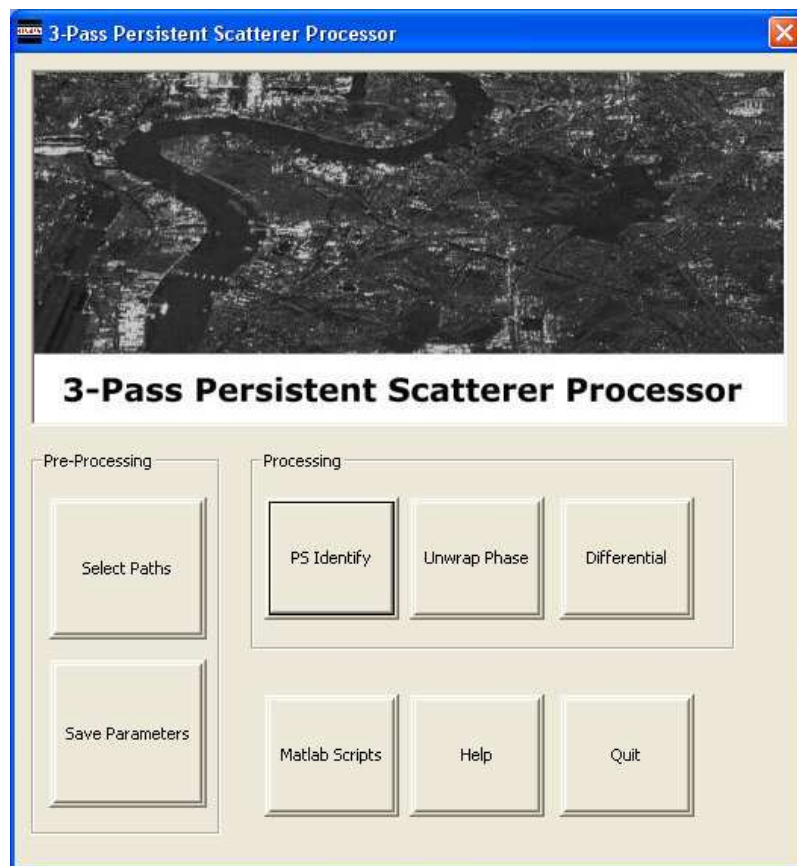
Figure 7.1 Front end of the 3PaPS processor software.

Each section has its own role to play in the processing of the data and shall be discussed below. Another important piece of software that is used in the processing chain is for the Kriging of the atmospheric phase screens. This is achieved in MATLAB using scripts from the GLOBEC Kriging Software Package, EasyKrig v3.0, from the Woods Hole Oceanographic Institute (*Chu 2004*). This is freely available for non-commercial purposes.

7.2.1 Pre-Processing Stage

The pre-processing stage is used to get the input data for the 3PaPS processing into a suitable format. Examples of the input data would be: orbit data, radar parameters and intererogram parameters. The method implemented in the 3PaPS software is designed to take input from the Doris (*Kampes and Usai 1999*) software, since this was the interferometric processing software available to the author. To use inputs from another interferometric processor, a new function should be added to the 3PaPS software to read the data from the new format.

There are two stages to the pre-processing which should be run in sequence.

- Select Paths – Use this to identify where the Doris output files are located on the computer Hard Drive, and also to select a location for the outputs of 3PaPS.
- Save Parameters – After the Doris output files have been identified, this step in the processing will extract the relevant data from the files and save it in the 3PaPS format.

After the pre-processing stage, a series of files will be output from 3PaPS which contain certain information on each interferogram such as: orbital data, interferogram size, radar wavelength, pulse repetition frequency and range sampling rate.

7.2.2 Processing Stage

With the input data in the format required for the 3PaPS software, the processing stage can proceed. This stage can be broadly divided into three steps, which again, should be run in sequence.

- PS Identify – This step is dedicated to identifying candidate PS points from the amplitudes of the SAR images. The GUI for this step is shown below in Figure 7.2. As input it takes the number of SAR images in the stack, which have been cropped and resampled to the master SAR image

grid. The size of the images, as number of rows and columns is also needed. The location of the folder which contains the resampled SAR images is needed, together with a file that contains details about the calibration constants for each SAR image. This is required so as to make the amplitude values of the SAR images comparable. The outputs of this step are binary raster files that contain the amplitude for each interferogram, a file of the mean amplitude of the stack and a file that lists the identified candidate PS point's row and column location.
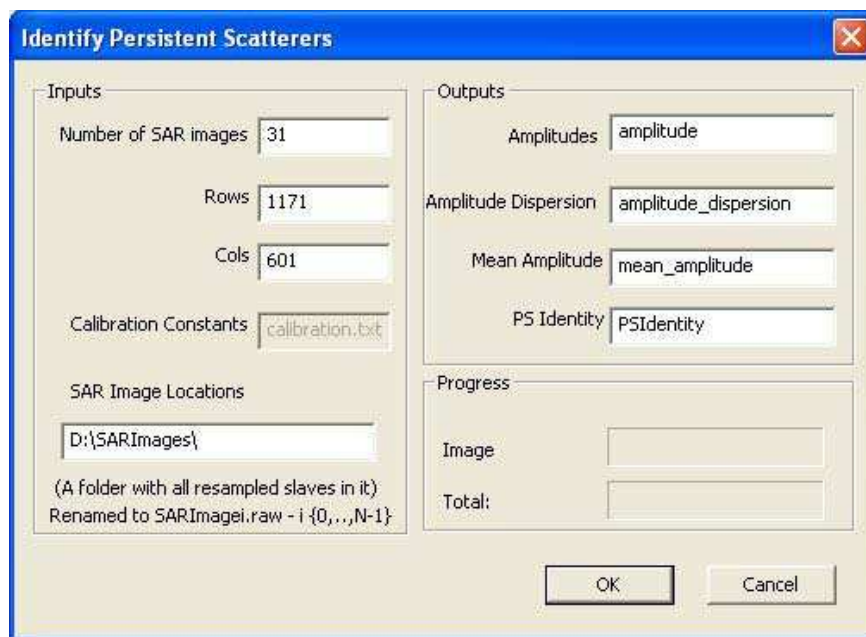
Figure 7.2 GUI for the 3PaPS PS Identify stage of processing

- Unwrap Phase – This step is concerned with unwrapping the phase interferograms. The process requires a DEM as input to aid in the unwrapping of the noisy interferograms. The DEM height values are converted to phase, and registered to the interferogram grid, to generate simulated interferograms. Using the simulated interferograms, the real interferograms are unwrapped using the process described in chapter 5. The user interface for this step is shown in Figure 7.3. The outputs for this stage include the simulated interferograms, the unwrapped interferograms and the SAR coregistered DEM.
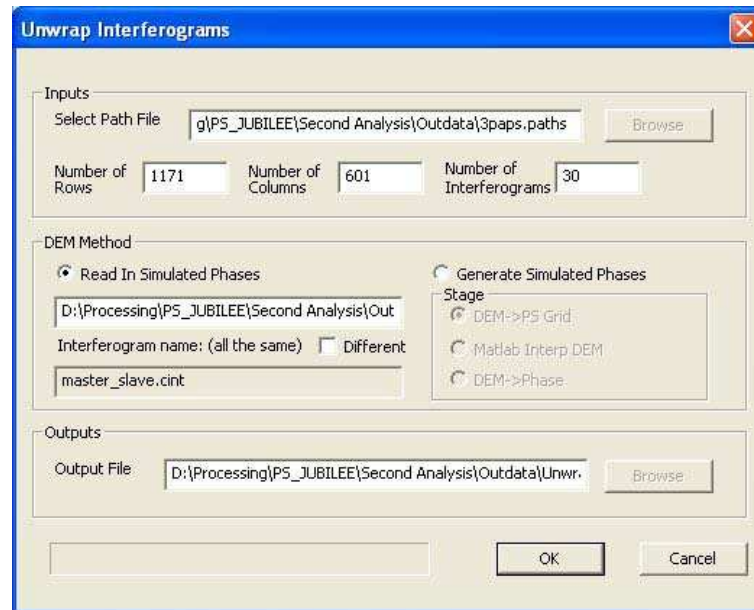
Figure 7.3 GUI for the 3PaPS Unwrap Phase stage of processing

- Differential – The final step in the Processing stage of the 3PaPS software is concerned with calculating the 3-pass differential phase interferograms. The user interface is shown in Figure 7.4. This step takes the number of PS candidates, the coregistered DEM and the unwrapped phase interferograms as input. One of the input interferograms is selected (by the user) as the reference interferogram, which is used as the topographic pair for each 3-pass differential result. This step can be carried out at the candidate PS points only or the full interferogram. This should only be carried out at the candidate PS points for the first run, and then when the atmospheric phase screen has been removed from the interferograms, it should be re-run for the full interferogram. If "RemoveDPhi" is checked then an estimate of the topographic error is calculated and removed from the differential phase. The outputs of this stage are the differential phase files and, if selected, the topographic error estimate and correlation fit.
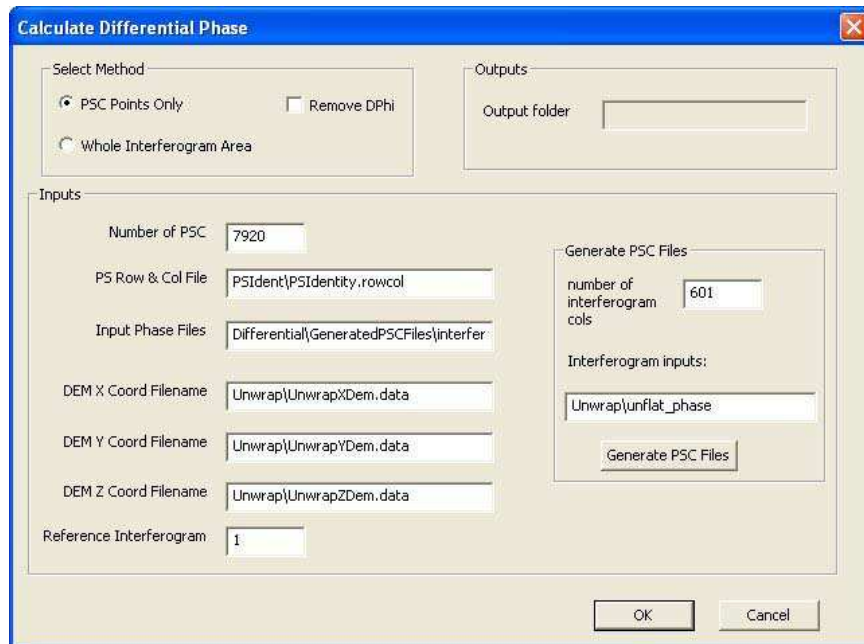
Figure 7.4 GUI for the 3PaPS differential phase stage of processing.

7.2.3 MATLAB Scripts

The final part of the processing is undertaken using scripts written for use in MATLAB. They have been tested with and are compatible with MATLAB version 6.5. The scripts are generated by selecting the "MATLAB Script" button on the main window of the 3PaPS application. The scripts are primarily for the temporal analysis of the data that was described in the previous chapter. When the "MATLAB Script" button is selected, the graphical user interface shown in Figure 7.5 is displayed. The scripts that are checked will be generated and output to the computer Hard Drive.

A brief description of the function of each script follows.

- Atmospheric Periodogram – Script which takes in the differential phase stack at the candidate PS points and tries to fit a planar model to each interferogram layer to represent the atmospheric phase screen (see equation 5.13). This is run iteratively in conjunction with Velocity Periodogram.

- Velocity Periodogram – Script which tries to model a constant linear velocity to the stack of differential phase data at each candidate PS point (see equation 5.15).

118
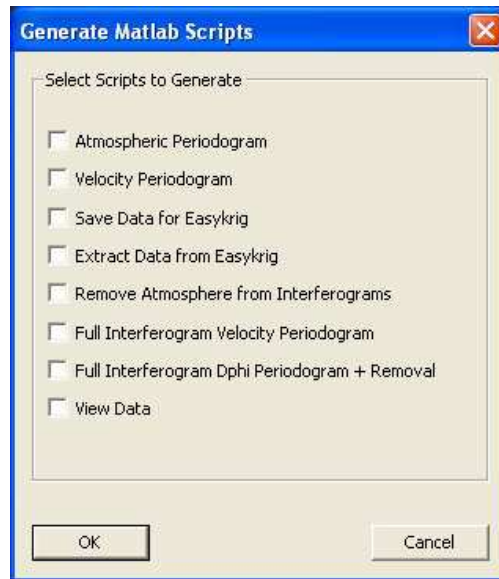
Figure 7.5 GUI for the 3PaPS MATLAB script generation.

- Save Data for Easykrig – Script which saves the phase residuals from the iterative algorithm into a format suitable for Easykrig.

- Extract Data from Easykrig – Script that takes the Kriged atmospheric phase screen from the Easykrig software format and saves it as binary data.

- Remove Atmosphere from Interferograms – Script that subtracts the atmospheric phase screen from the original phase interferograms.

- Full Interferogram Velocity Periodogram – Script that uses a periodogram on the stacked, full differential interferogram data to estimate a constant linear velocity for each pixel of the interferogram. As well as the velocity estimate, a goodness-of-fit parameter is given and also the standard deviation of the data to the linear velocity fit.

- Full Interferogram DPhi Periodogram – Optional script that will implement a periodogram to estimate if there is a residual topographic phase error in the differential phase stack. An estimate is given for each pixel of the interferogram.

- View Data – A script that will plot the time series for the given point of interest, together with a straight line velocity fit to the data.

7.3 Software Testing with Simulated Data

The 3-pass IAS PSInSAR algorithms developed were first tested using simulated data. This simulated data has been created from four components: topography, deformation, atmosphere and random noise. The sum of these components has been wrapped and called the simulated interferogram. These have then been used with the 3-pass IAS PSInSAR method to test the algorithms. The approximate size of the simulated data is 5km x 5km.

7.3.1 Topography

The simulated topographic phase data has been generated from a SRTM 90m Digital Elevation Model (*Jordan et al 1996*) and ESA ERS-1,-2 precise orbit data (*Scharroo et al 1998*). The DEM has been oversampled and interpolated to the same pixel size as the range oversampled ESA SLC data (i.e. 10m x 4m pixel size). An example of the simulated topographic phase is shown in Figure 7.6.
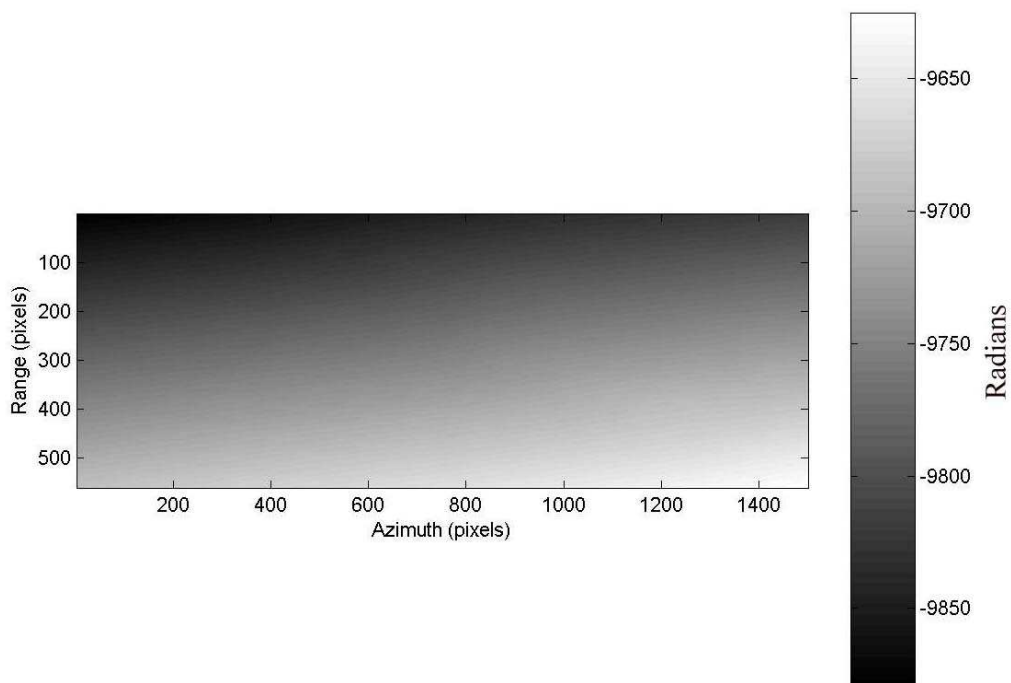
Figure 7.6: Simulated topographic absolute phase interferogram: in radar coordinates, where X-axis is azimuth direction, Y-axis range direction and units are interferogram column and row number.

The simple equation

$$\phi_{topo} = \frac{4\pi}{\lambda}\left(\rho_i - \rho_j\right) \qquad\qquad 7.1$$

was then used to convert the DEM heights to topographic phase, where ρ_i and ρ_j are the ranges from the radar position in orbits i and j to the DEM pixel.

Thirty simulated topographic phase interferograms were made in this way. Table 7.1 below shows the temporal and spatial baselines used; these are dictated by the actual ERS orbits used to simulate the phase.

Number	Baseline (m)	Time (days)
1	157.4	-455
2	594.8	-420
3	464.1	-386
4	336.4	-385
5	827.0	-350
6	123.1	-315
7	83.9	-280
8	194.7	-245
9	720.6	-210
10	342.3	-176
11	559.3	-175
12	219.7	-140
13	114.1	-105
14	-47.5	-70
15	-745.8	-35
16	804.0	35
17	1127.6	70
18	-551.8	105
19	-357.7	140
20	663.2	175
21	-250.1	245
22	-867.4	280
23	228.6	350
24	264.3	385
25	753.9	420
26	408.9	455
27	696.8	490
28	-484.7	525
29	48.2	560
30	202.0	630

Table 7.1: Baseline distribution of simulated SAR data. The distribution of the spatial and temporal baselines of the simulated interferograms used in the analysis.

7.3.2 Deformation

The second component of the interferometric phase is the phase due to a deformation. For simplicity, here this is considered to behave as a linear motion with a constant velocity throughout the time period covered by the interferograms. The equation used to calculate the deformation phase was:

$$\phi_{defo} = \frac{4\pi}{\lambda} T_i v_{(r,c)} \qquad\qquad 7.2$$

where T_i is the temporal baseline (in years) of interferogram i and $v_{(r,c)}$ is the constant linear velocity (in metres per year) at interferogram pixel (r,c). The velocities used to generate the deformation field range from 0 to 20mm/yr in the form of a subsidence bowl. This is similar to known subsidence patterns that occur, for example with mining subsidence (*Raucoules et al 2003*). The deformation phase for simulated interferogram 1 is shown below in Figure 7.7, together with a cross-section of the velocities along range line 300.
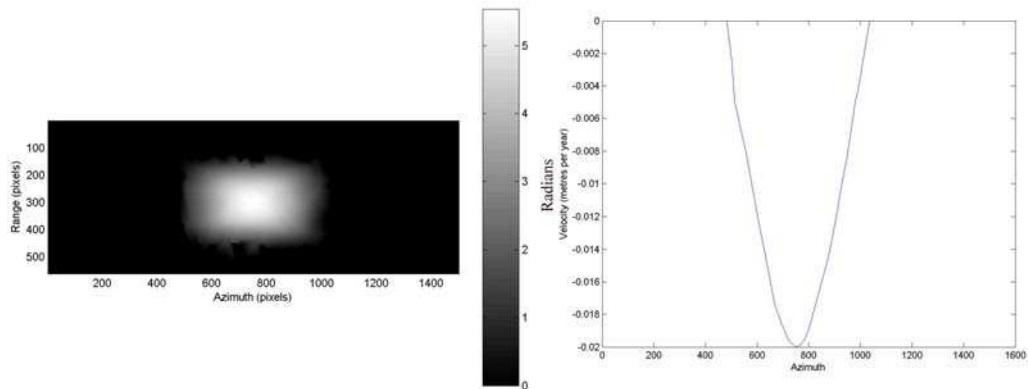
Figure 7.7: Simulated deformation phase. The image on the left shows the deformation phase component (in radians) for simulated interferogram 1 created using equation 7.2 with velocities ranging from -20 – 0mm/yr. The image on the right shows a cross section of the velocities used along range line 300.

7.3.3 Atmosphere

The third component of the interferometric phase is due to the differences between the atmospheric delay in the two SAR images. The atmospheric phase anomalies are spatially correlated but temporally random. Each simulated interferogram atmosphere was generated by using a very simple model, where a sparse grid of values are created from a Normal distribution with mean 0 and

variance 4.8mm. The sparse grid is then interpolated on to the regular interferogram grid resulting in a smooth phase image. The value used for the variance has been reported in (*Goldstein 1995*) for atmospheres over an area of approximately 20km x 20km in the Mojave Desert. Although the values are from a desert they are suitable for the purpose of the simulation. One of the generated atmospheric phase screens is shown below in Figure 7.8.
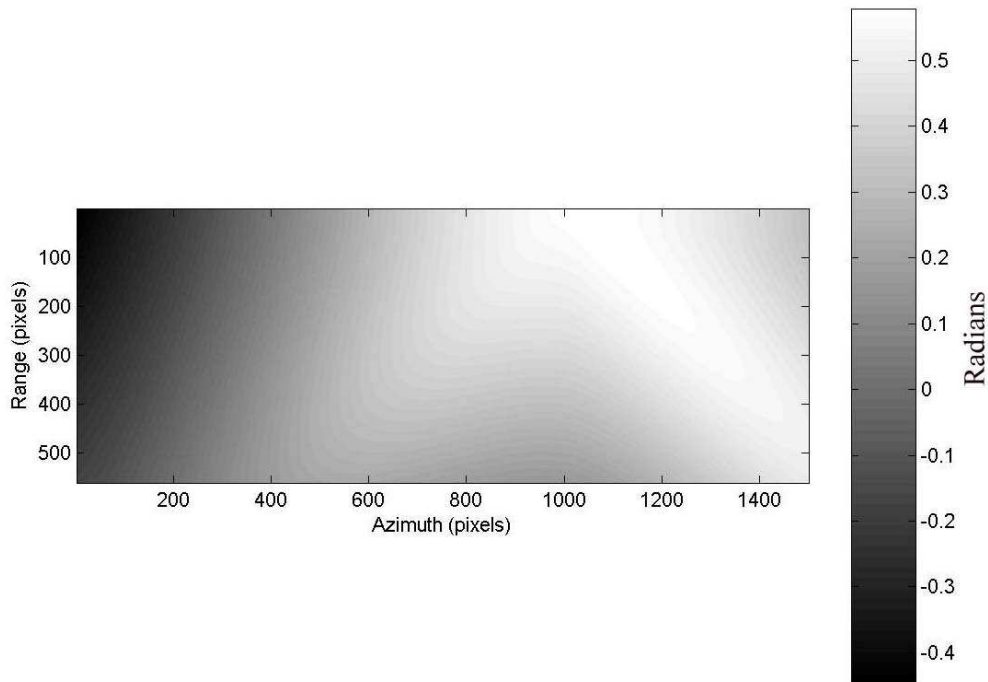
Figure 7.8: Simulated atmospheric phase: for one of the interferograms, scale in radians.

7.3.4 Decorrelation Noise

The fourth component that makes up the simulated interferogram phase is the decorrelation noise. This has been created by using a Normal distribution with mean 0 and variance $\pi/6$ radians. This variance is approximately equal to 40° which is in agreement with models used in similar studies (*Worawattanamateekul at al 2004*). The same distribution has been used to create a spatially random noise component for each interferogram. An example is shown in Figure 7.9.
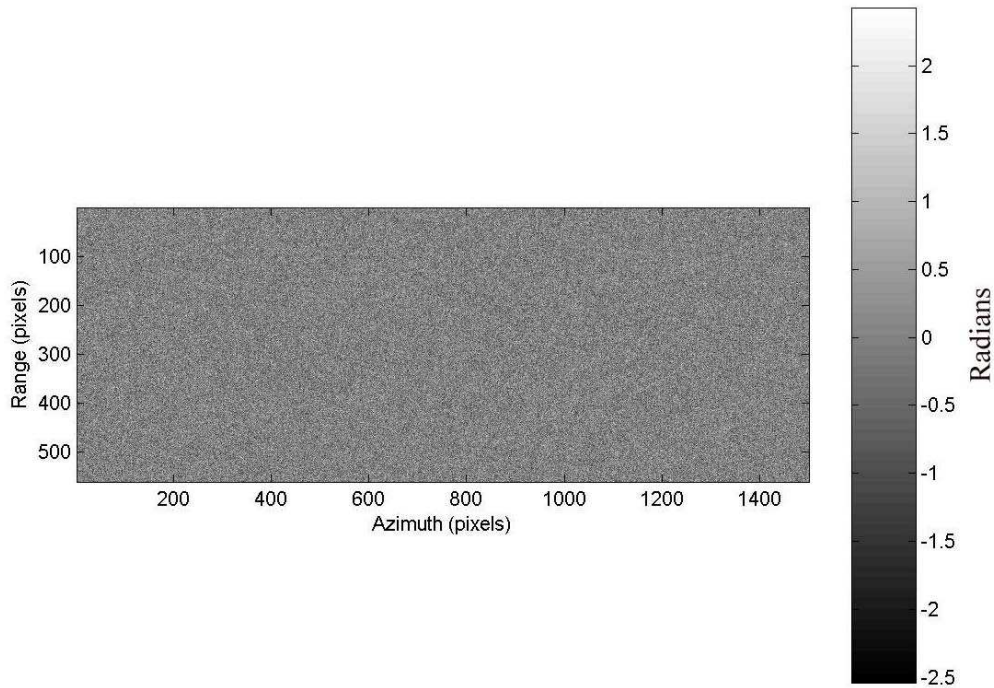
Figure 7.9: Simulated phase noise. Spatially random noise component added on to the synthetic interferogram to represent decorrelation noise, scale in radians.

7.3.5 Total Simulated Interferogram

Each of the four components above were generated and summed together, before being wrapped to create a synthetic interferogram. Figure 7.10 below shows the wrapped sum of the four components in the figures above which correspond to simulated interferogram 1 from Table 7.1. The geometric baseline is 157 metres and the temporal baseline is 455 days.

7.4 Processing

The simulated data has been processed using the 3PaPS software based on the IAS 3-pass PSInSAR algorithm described in section 5.5 and 7.2. Real SAR data (see chapter 6) corresponding to tables 6.1 and 7.1 was used to identify candidate PS points for the simulated trial. The simulated interferograms have then been unwrapped and the differential phase at each candidate PS point has been generated and an estimate of the topographic interferogram phase error removed. The processing was undertaken three separate times using a different
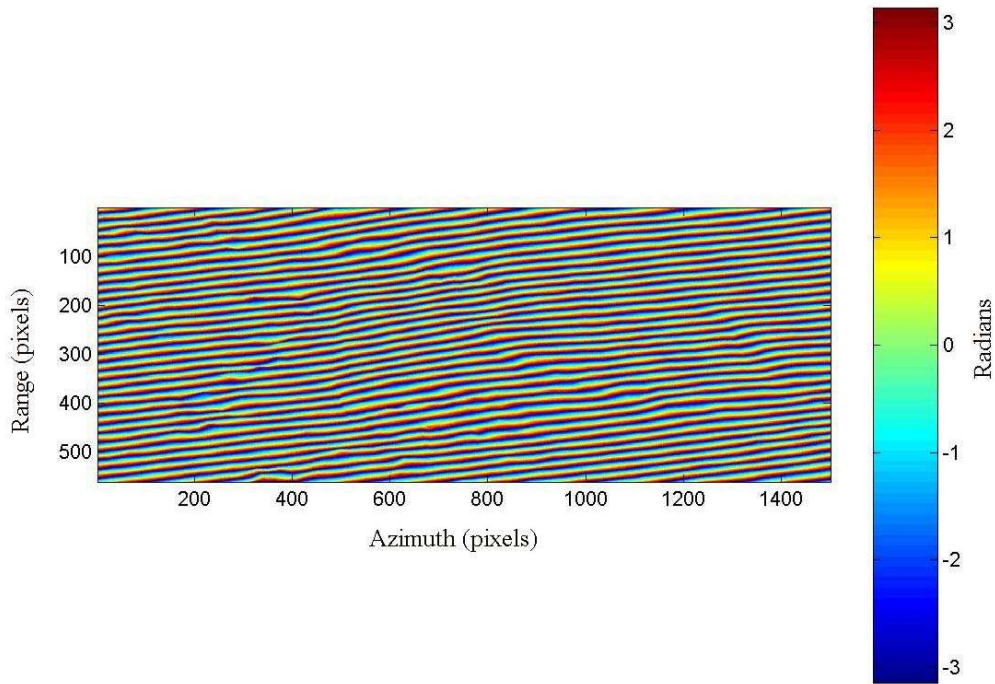
Figure 7.10: Wrapped simulated interferogram. Consists of four components: topography, deformation, atmosphere and random noise. Scale in radians.

topographic interferogram to observe the effects this has in the processing. The interferograms selected as the topographic interferograms for the test were numbers 1, 7 and 17 from Table 7.1. This selection gives a good combination of geometric and temporal baselines. Interferogram 1 has a relatively short geometric baseline of 157m which should allow for any topographic error to be estimated easier, but a large temporal baseline of 455 days (hence a large deformation phase component). Interferogram 7 also has a relatively short geometric baseline of 84m and a shorter temporal baseline of 280 days. Interferogram 17 has a large geometric baseline of 1.1km and a short temporal baseline of 70 days. The processing of the data with each topographic interferogram is identical and is as follows. The differential phases are generated and an estimate for the topographic phase error is removed. Estimates of the planar APS and linear velocity have then been calculated using the iterative approach, and removed, to result in phase residuals that relate to atmospheric perturbations and random decorrelation noise. The residuals have been interpolated and smoothed using the Easykrig software and the atmospheric phase screens produced were removed from the simulated

interferograms. Finally, the differential phase was generated for each pixel of each interferogram and an estimate of the linear velocity produced.

7.5 Results

Some results of the above processing will now be shown. The distribution of the initial candidate PS points is shown below, in Figure 7.11, overlaid upon the mean amplitude image of the real SAR data. It can be seen that there is a wide distribution of points across the image, with only the areas of Greenwich Park and the Thames River showing a lack of candidate points. This is to be expected due to the reflective properties of water and vegetation and their respective coherence over time (see chapter 2).
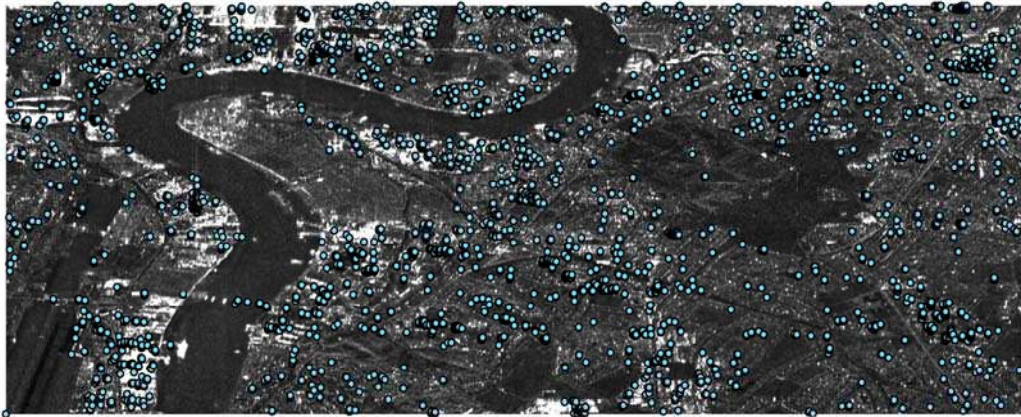
Figure 7.11 Distribution of candidate PS points. Distribution is shown against the mean amplitude image created from the amplitudes of the stack of real SAR data.

7.5.1 Topographic Interferogram 1

The first processing was undertaken using interferogram 1 as the topographic interferogram. The first stage of the verification of the processing was to examine the atmospheric phase screen estimates achieved from the Kriging step to see if they matched up with the simulated atmospheres. Figure 7.12 shows thumbnails of the 29 atmospheric phase screens, estimated from the Kriging step. Figure 7.13 shows the true atmospheric phase screens of the simulated data. Both sets of images are shown using the same colour scale and so can be qualitatively compared with each other. It can be seen that the Kriged APS and the true APS are broadly similar in shape and structure. That is, where there is

126

red or blue in the true APS there is red or blue in the estimated APS. The shades of colour are darker in the Kriged atmospheres which suggest there could be an overestimation in some areas, causing a larger magnitude in the APS.
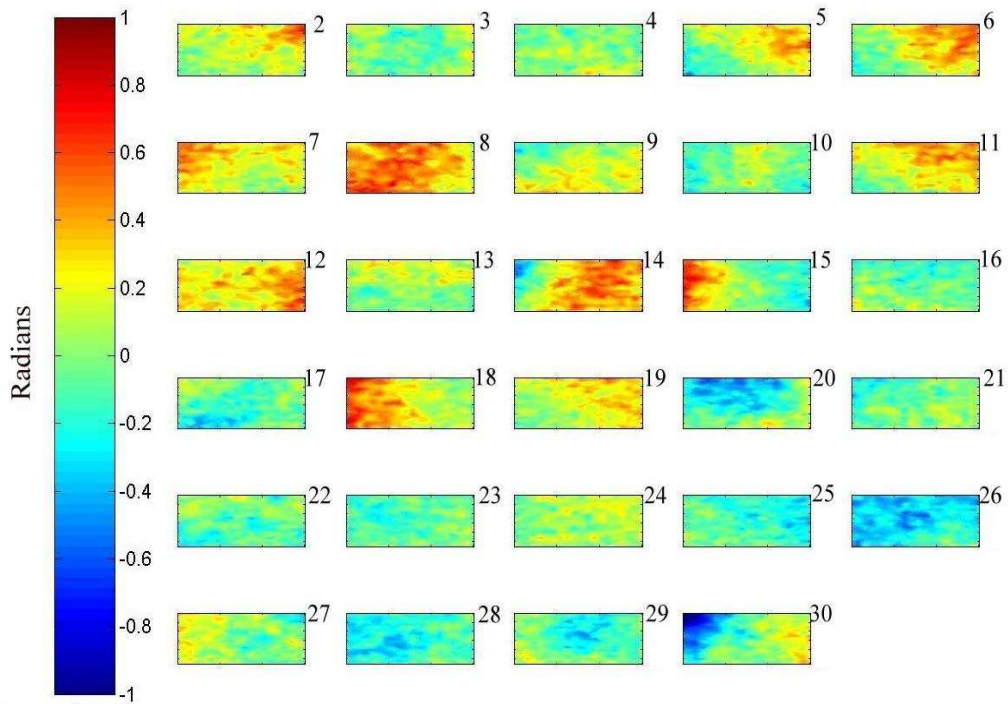
Figure 7.12 Thumbnail images of the Kriged estimated atmospheric phase screens: for the simulated interferograms.
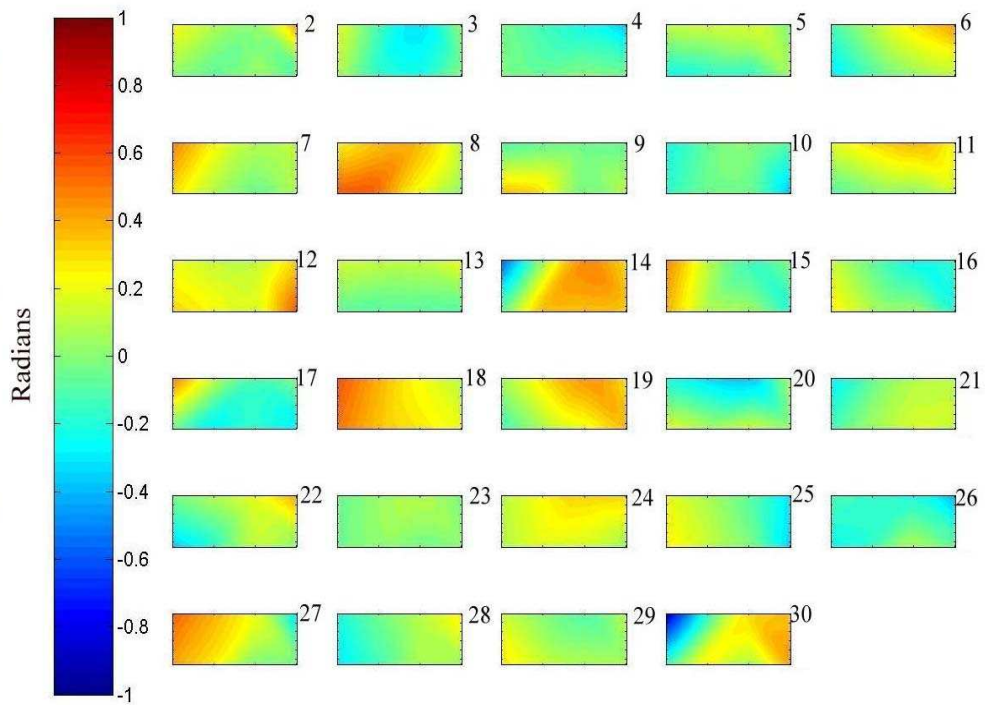
Figure 7.13 Thumbnail images of the true atmospheric phase screens: for the simulated interferograms.

The Kriged atmosphere is not expected to be identical to the simulated atmosphere due to the sampling effect and the interpolation errors that are introduced from the Kriging. This can be seen as the 'roughness' in the estimated APS.

The topographic interferogram error, at this stage, consists of all the phase components other than topography. The comparison of the actual values and the estimated values can be seen in Figure 7.14. For each candidate PS the difference of the true and estimated values is plotted. The errors between the two have mean 0.0015 radians and standard deviation 0.0675 radians.
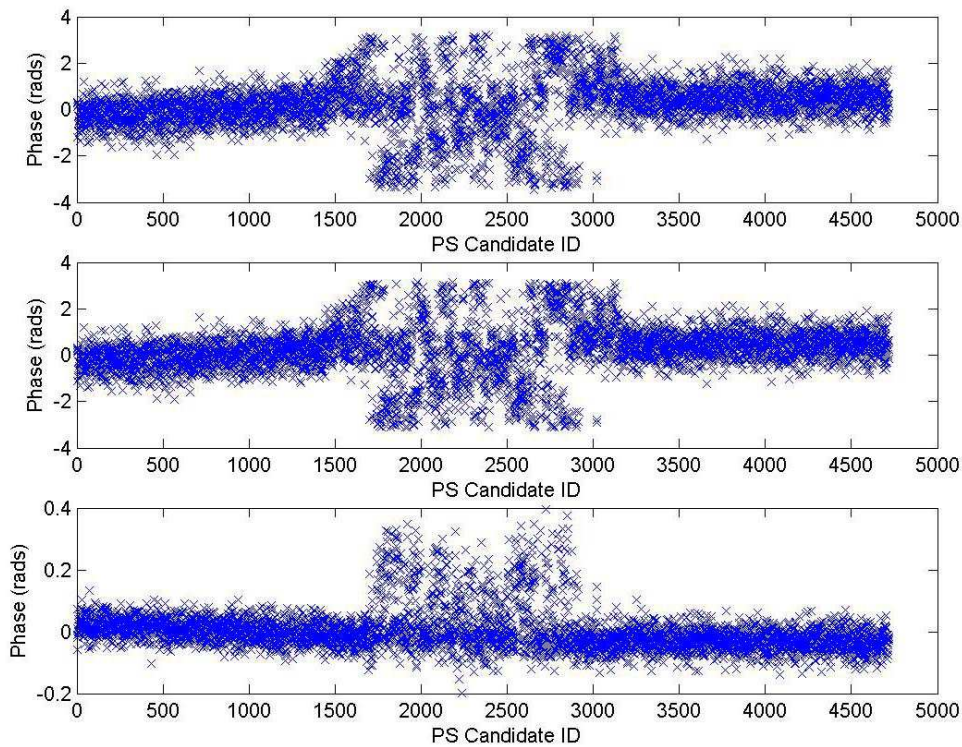
Figure 7.14 Simulation 1: Estimated topographic phase error. The top image shows the actual topographic error term, the middle image the estimated error and the bottom image shows the difference between them. The error distribution has mean 0.0015 rads and standard deviation 0.0675 rads.

Using the estimate of the linear velocity up the stack, it is possible to remove the component due to deformation from the topographic error term. This leaves the phase components due to atmosphere and random decorrelation noise. These then can be Kriged to give an estimate for the atmospheric phase screen of the

topographic interferogram. This estimate together with the actual simulated atmosphere of the topographic interferogram is shown below in Figure 7.15.
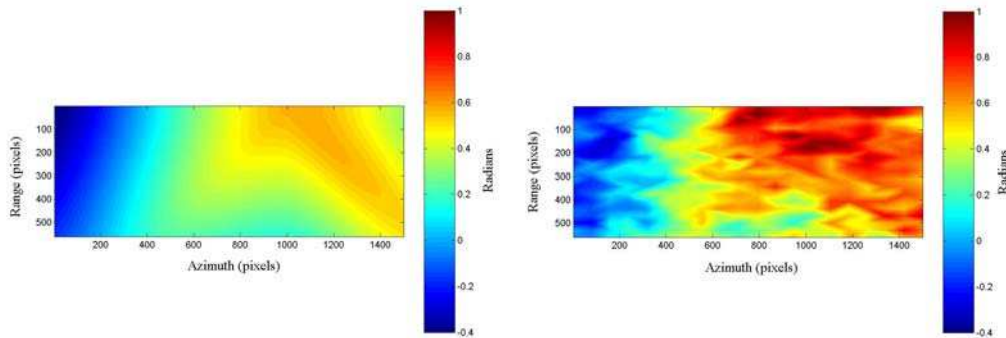
Figure 7.15 Simulation 1: Topographic APS. The image on the left is the actual (simulated) atmosphere of the topographic interferogram, the image on the right is the Kriged estimate of the atmospheric phase screen for the same interferogram.

Again the two images show qualitatively similar results albeit that the values of the estimated atmospheric phase error are larger than the simulated values.

After the removal of the atmospheric phase screens from the interferograms, the differential phase is recalculated and a velocity estimate is derived for each image pixel. The decision whether the point is a PS or not is based on the value of the goodness of fit of the velocity estimate, i.e. the ensemble phase coherence γ. Figure 7.16 below shows the derived estimated velocity for each pixel, together with a cross-section plot of range line 300. This can be compared with the previous Figure 7.7 that shows the true simulated velocity of range line 300.
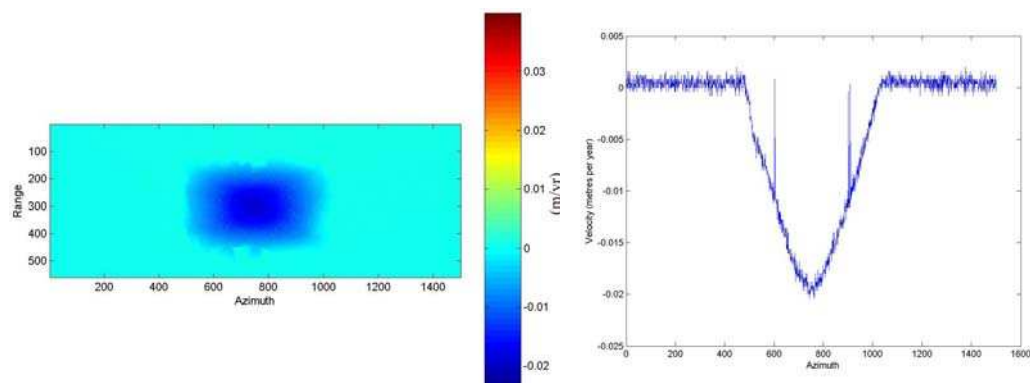
Figure 7.16 Simulation 1: Estimated velocities. The image on the left shows the estimated velocity (m/yr) derived from the PS analysis. The image on the right shows a cross section of velocities along the range line 300.

It can be seen that the shape of the deformation field broadly matches that of the simulated velocities that were used to create the interferogram data. From the cross-section plots of the velocities it can also be seen that the estimated values follow closely the true velocity values. The difference between the derived velocity field and the true velocity field is shown below in Figure 7.17. The mean of the differences is -0.59mm/yr with a standard deviation of 0.63mm/yr.
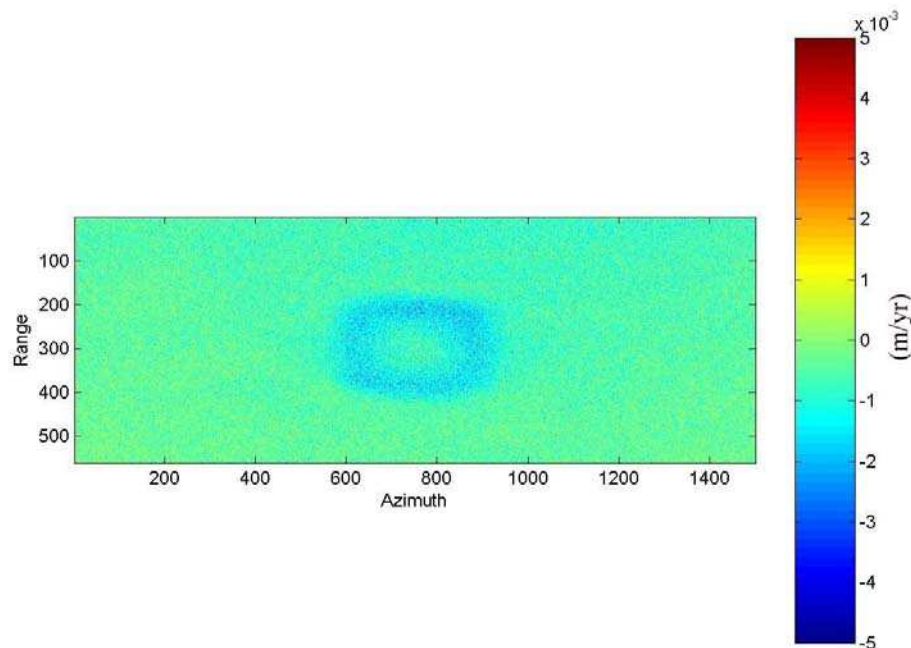
Figure 7.17 Simulation 1: Error in the estimated velocities. Difference between the true velocity field and the estimated velocity field. The standard deviation of the error is 0.63mm/yr.

The larger errors appear to be located in a ring corresponding to the deformation area where velocities are approximately 9-15mm/yr. This also corresponds to regions where discontinuities due to phase wrapping occur. Figure 7.18 below shows the cross sections of the wrapped deformation phase component of the differential phase along range line 300 for certain interferograms. It can be seen that the discontinuities occur in the region of higher noise present in Figure 7.17.

Due to the relatively simple construction of the simulated interferograms, a lot of persistent scatterers are identified. This is most likely because of the simple treatment of decorrelation noise as a spatially and temporally random noise with relatively low standard deviation. For example, in areas of vegetation (or other low coherent areas) the decorrelation noise would be much larger than this.
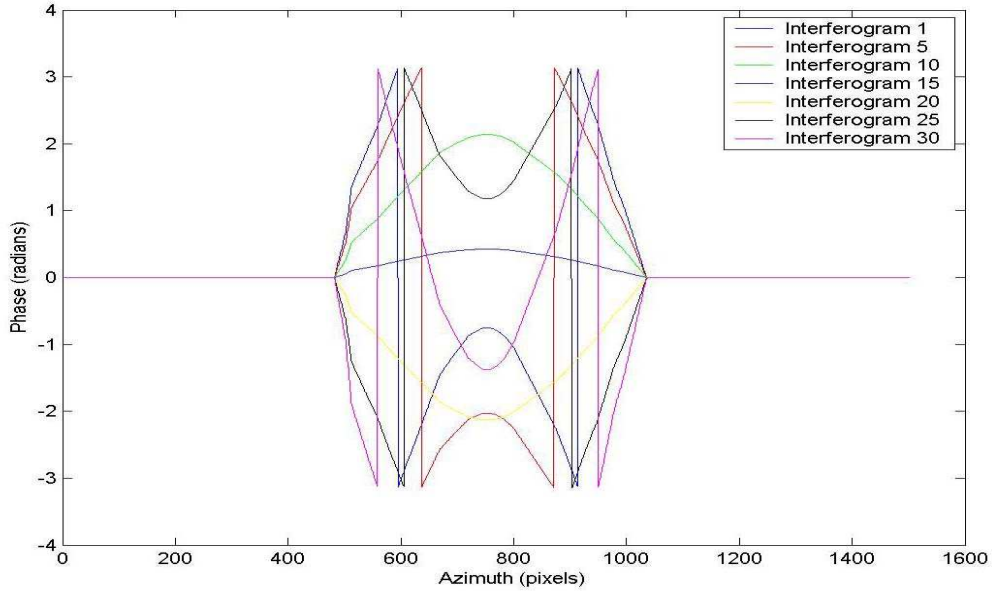
Figure 7.18 Simulation 1: Discontinuities in wrapped interferograms. Cross-sections of the wrapped deformation phase component of the simulated interferograms. Cross-sections are taken along range line 300 for interferograms 1, 5, 10, 15, 20, 25 and 30.

This reduces the confidence in the underlying interferometric phase value. The persistent scatterer points have been selected by thresholding the ensemble phase coherence, γ, at 0.8. Here, this results in 94% of the points being selected as PS points.

A time series of a point outside the deformation zone and a point inside the deformation zone is shown in Figure 7.19. The straight line is a fit of the linear velocity to the data.
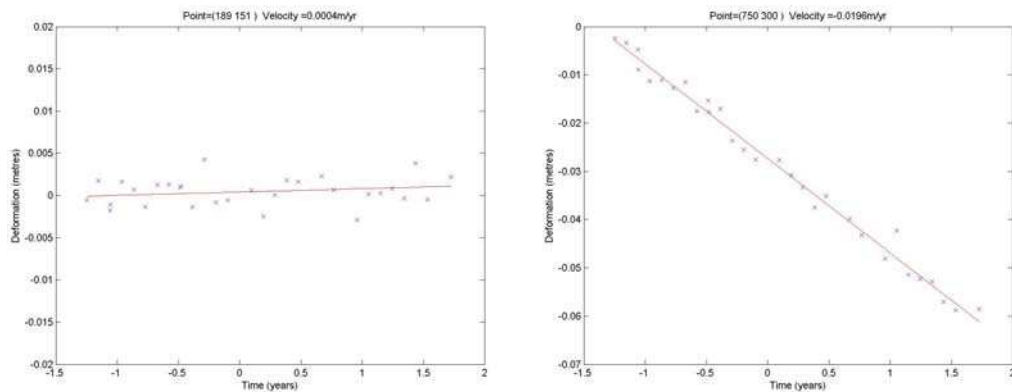
Figure 7.19 Simulation 1: time series plots. The plot on the left shows a PS point outside the deformation zone, with estimated velocity 0.4mm/yr and γ =0.937. The plot on the right shows a PS point in the deformation zone with estimated velocity -19.6mm/yr and γ =0.907.

131

7.5.2 Topographic Interferogram 7

Similarly the above procedure has been applied to the data using interferogram 7
as the topographic interferogram. Figure 7.20 shows the error between the
estimated topographic phase error and the actual topographic phase error for the
candidate PS points. The error is between ± 0.15 radians for every point, with a
mean of 0.002 radians and a standard deviation of 0.0252 radians. It is
noticeable that the spread of errors is larger in the deformation zone which could
imply that where the topographic error is larger there is more uncertainty in
estimating it. But a plot of the estimated topographic phase error against its
correlation coefficient, shown in Figure 7.21, does not support this assertion. It
shows that smaller phase estimates have a smaller correlation and hence more
uncertainty. So instead of this it could mean that because there is a larger
velocity component here, it is more difficult to estimate the topographic error as
accurate as when there is no velocity component in the phase.
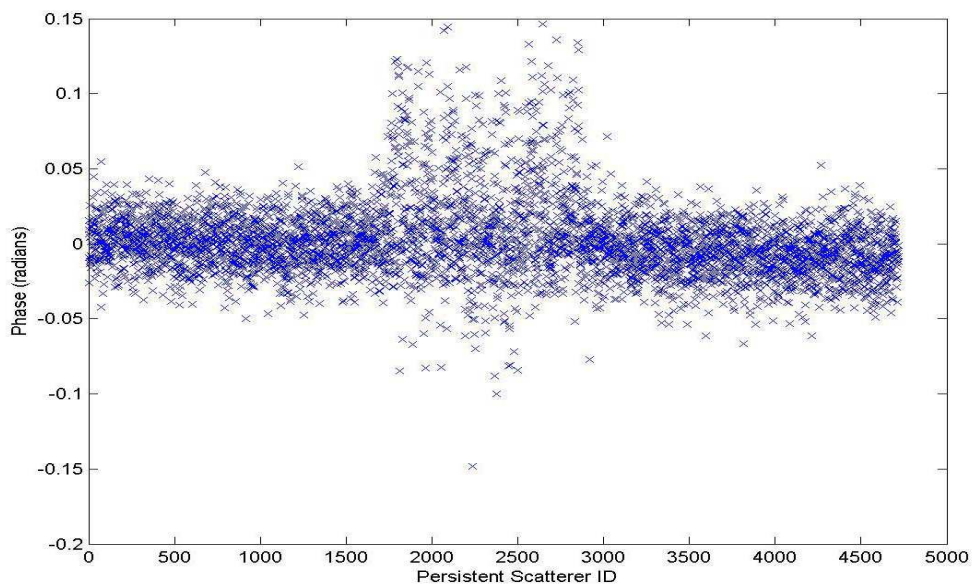
Figure 7.20 Simulation 2: Estimated topographic phase error. The mean is 0.002 radians with a
standard deviation of 0.0252 radians.
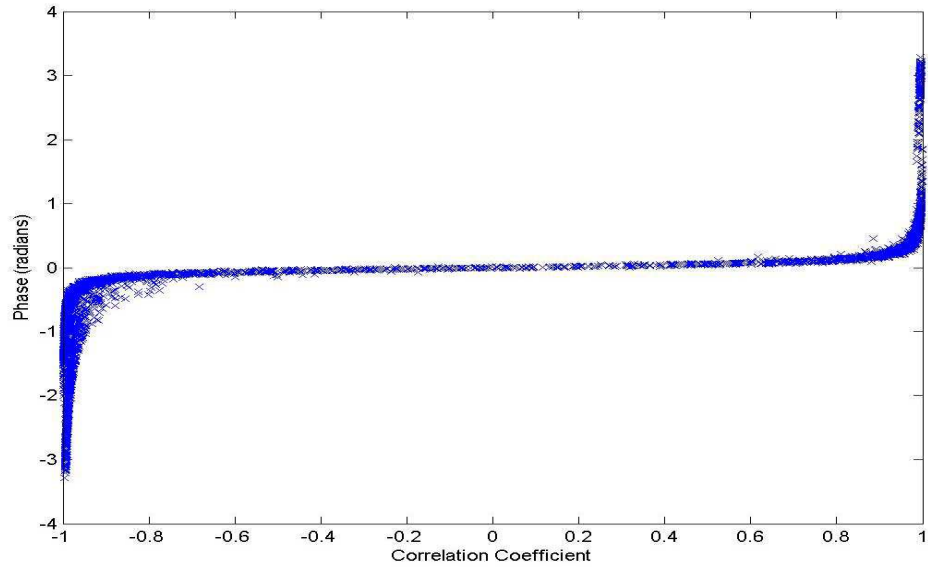
Figure 7.21 Simulation 2: Topographic phase error vs. correlation (coefficient of the data fit).

The final velocity map is shown below in Figure 7.22 together with the error between this and the actual velocities. The mean of the errors is 0.4mm and they have a standard deviation of 0.55mm. The range of the errors spread from a minimum of -2mm to 14mm. This includes *every* pixel not just the persistent scatterers. When only the persistent scatterers are used, the mean is 0.39mm with a standard deviation of 0.54mm and a range spreading from -2mm to 3.2mm, based on the 91.8% persistent scatterer coverage.
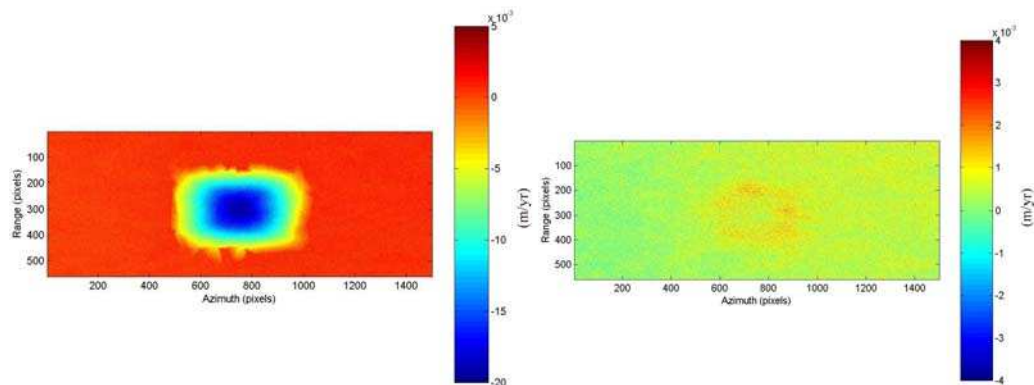
Figure 7.22 Simulation 2: Estimated velocities and velocity error. The image on the left is the final velocity map of every pixel (not just PS points), whilst the image on the right is the error between these velocities and the true velocities.

Plots of the two persistent scatterers corresponding to the ones in Figure 7.19 are shown in Figure 7.23. Qualitatively they both appear similar to, and both give

the same velocity estimates, as the corresponding graphs of Figure 7.19. The values of γ are close enough to be effectively the same too. So at these two PS points, changing the topographic interferogram has had no significant effect.
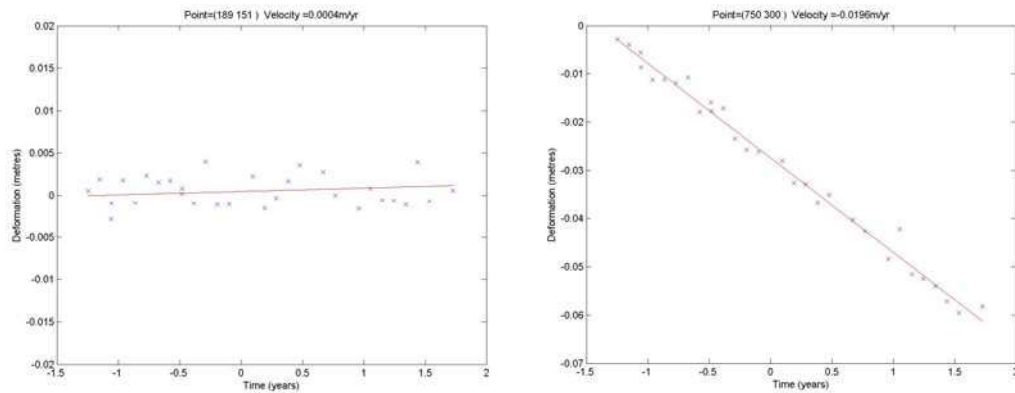
Figure 7.23 Simulation 2: time series plots: of same 2 persistent scatterers from Figure 7.18. The plot on the left shows the point outside the deformation zone, with estimated velocity 0.4mm/yr and γ=0.926. The plot on the right shows the point in the deformation zone with estimated velocity -19.6mm/yr and γ=0.909.

7.5.3 Topographic Interferogram 17

The procedure has been repeated using interferogram 17 as the topographic interferogram. The error between the estimated topographic phase error and the actual topographic phase error is shown in Figure 7.24, and the correlation of the estimates is shown in Figure 7.25. It can be seen that the error is approximately between -1.5 and +2.4 radians, with a mean of 0.117 radians and a standard deviation of 0.4347 radians. For the points corresponding to the deformation zone, i.e. points approximately between 1700 and 2700, the spread of this error term is larger as can be seen from Figure 7.24.

From Figure 7.25 it can be seen that the correlation of the fit of the topographic phase error is weak, with the vast majority of points having a correlation magnitude of less than 0.6. This suggests there is lower confidence in the knowledge of the estimated values.

134
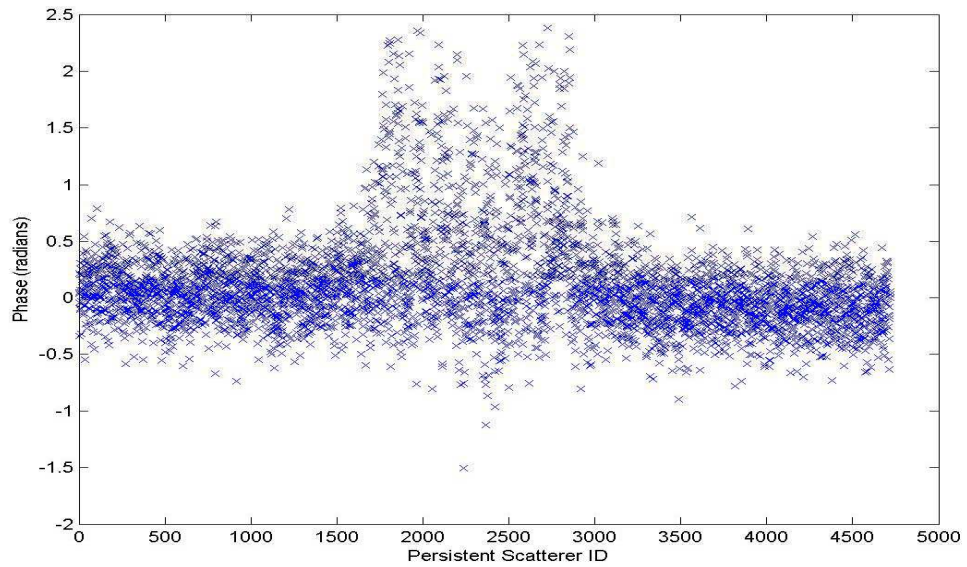
Figure 7.24 Simulation 3: Estimated topographic phase error. The mean is 0.117 radians with a standard deviation of 0.4347 radians.
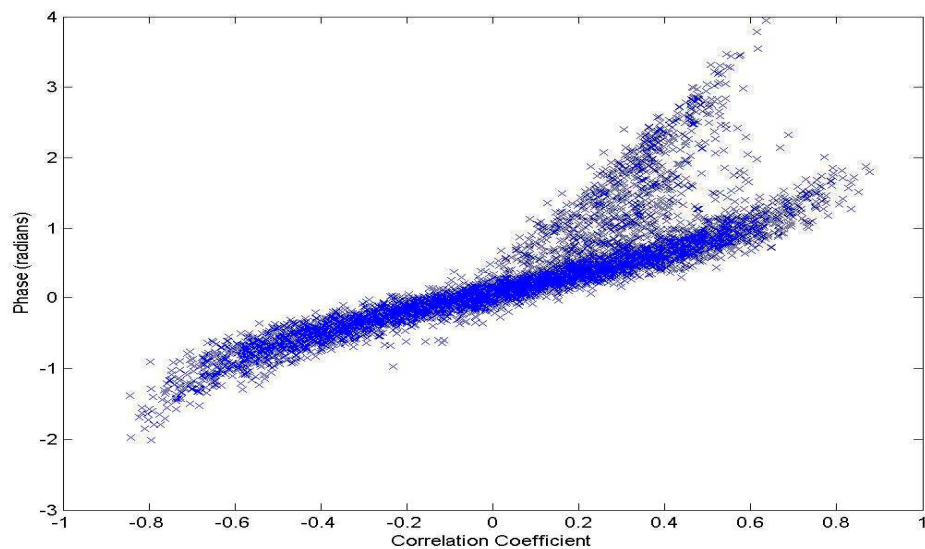
Figure 7.25 Simulation 3: Topographic phase error vs. correlation (coefficient of the data fit).

The final velocity map and the error of the velocities are shown below in Figure 7.26. As with the previous examples, the shape and magnitude of the final velocity map appears good. When examining the velocity errors it can be seen that some large errors occur. The mean of the errors is 0.51mm with a standard deviation of 0.59mm and a spread ranging from -2mm to +53mm. Again it is stressed that this includes every pixel and not just PS points. When only PS points are examined the mean becomes 0.48mm with a standard deviation of

0.56mm and the range of errors from -2mm to 15.2mm. Here PS points are identified with 92% coverage.
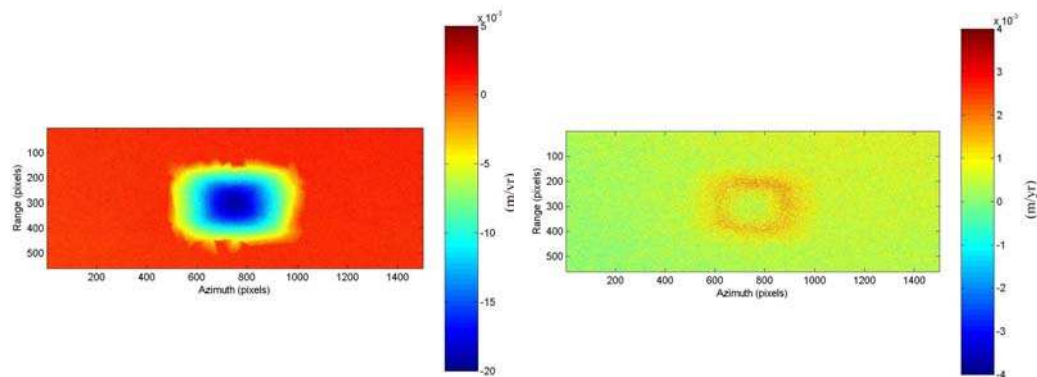
Figure 7.26 Simulation 3: Estimated velocities and velocity error. The image on the left shows the final velocity map from the analysis, whilst the image on the right shows the error between these estimated velocities and the true ones.

As before, the two PS points' time series are plotted and shown below in Figure 7.27. They give the same velocity estimates as the previous cases, albeit with slightly lower γ values. Recall that the PS points are selected based on having a γ value greater than 0.8. Therefore PS point 2, with a γ value of 0.800, was only just included as a persistent scatterer here.
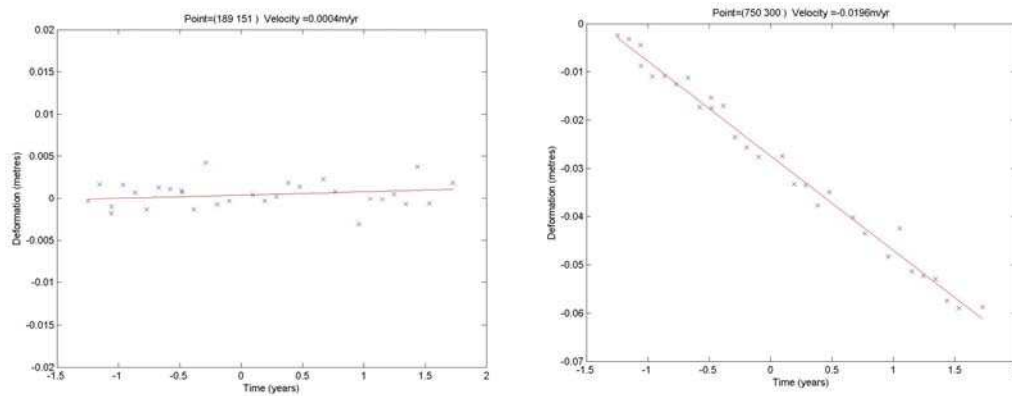
Figure 7.27 Simulation 3: time series plots: of same two persistent scatterers as previously. The plot on the left shows the point outside the deformation zone, with estimated velocity 0.4mm/yr and γ =0.860. The plot on the right shows the point in the deformation zone with estimated velocity -19.6mm/yr and γ =0.800.

136

7.5.4 Comparisons

The results of the three processing tests above will now be compared with each other to see if earlier ideas on the selection of the topographic interferogram were correct, or if there should be a more definitive selection criteria. The results are summarised in Table 7.2 below.

		Topographic Interferogram		
		1	7	17
Baseline	Geometric (m)	157	84	1130
	Temporal (days)	455	280	70
Topographic Phase Error (radians)	Min	-0.1986	-0.1484	-1.5087
	Max	0.3945	0.1465	2.3774
	Mean	0.0015	0.0021	0.117
	Standard Deviation	0.0675	0.0252	0.4347
Velocity Field Error - every point (mm/yr)	Min	-11.7	-2	-2
	Max	53.7	14	53
	Mean	0.59	0.4	0.51
	Standard Deviation	0.63	0.55	0.59
Velocity Field Error - PS points only (mm/yr)	Min	-1.7	-2	-2
	Max	3.4	3.2	15.2
	Mean	0.54	0.39	0.48
	Standard Deviation	0.53	0.54	0.56
PS Point Properties	PS Points Coverage	94%	91.78%	92.08%
	Mean of γ	0.88	0.86	0.87
	Standard Deviation γ	0.03	0.03	0.03

Table 7.2 Summary of the results from sections 7.5.1 - 7.5.3.

Firstly, examining the topographic phase error shows what was predicted in chapter 5. Namely, that with larger baseline topographic interferograms it is harder to initially estimate the topographic phase error accurately. It can be seen that using interferograms 1 and 7 as the topographic pairs, which both have short geometric baselines, that the estimate of the topographic phase error is good. The errors in the estimates lie within a narrow range of 0.3 radians for case 7 and 0.5 radians for case 1 with both cases having mean value approximately 0 and low standard deviations. However, case 17 with the large

geometric baseline shows much worse errors in the estimates, with errors in a range of almost 4 radians and a standard deviation greater than 0.4 radians.

Examining the errors in the derived velocity estimates at the PS points also suggests that using a smaller baseline interferogram is better. The errors in cases 1 and 7 lie within a range of approximately -2mm/yr to 3.5mm/yr, whereas with case 17 the maximum error in the velocity reaches 15.2mm/yr. The percentage of PS points identified is relatively similar for all pairs, as are the mean and standard deviations of the ensemble phase coherence values γ. The results do however show that there is a slight bias present, with the mean of the velocity errors being approximately 0.5mm/yr for each case.

In conclusion, the overall number of PS points identified and their "goodness" is similar for the three cases shown. But to get a good initial estimate of the topographic phase error it is important to use a small baseline topographic interferogram. Since this estimate is fed back into the algorithm it is important to get a good estimate and so it is suggested that a topographic interferogram with a small baseline is used.

7.6 Summary

This chapter has introduced the 3PaPS software package and described its use for generating IAS 3-pass PSInSAR results. By following a modular approach to the software design and using well known languages (C++ and MATLAB) it should make the software easier to update or improve in future developments. A simple simulated set of data has been constructed and used to test the algorithms in the 3PaPS software. The data has been used within three scenarios, where each case uses a different topographic interferogram. The atmospheric phase screen estimated by the 3PaPS software agrees well with the actual atmospheric phase in the simulated case shown. It was shown that to get a good initial estimate of the topographic phase error a small baseline pair is needed as the topographic interferogram. But all three test cases produced a similar amount of PS points with similar ensemble coherence values, so there is

no conclusive evidence that larger baselines are any worse overall. Still, to get a good estimate of the topographic phase error it is important to use a small baseline interferogram.

8. Linear IAS 3-Pass PSInSAR Results

8.1 Introduction

The linear IAS 3-pass PSInSAR algorithms have been tested with simulated data; in this chapter they are tested on some real data. The data set and test sites used for the analysis have been described previously in chapter 6. The following sections give an overview of the processing of the data and the results from the two test sites used. The results are discussed and possible improvements to the algorithm and the linear IAS 3-pass PSInSAR technique are considered. For further details on the processing algorithms refer to chapter 5.

8.2 Formation of Interferograms

The processing of the data has been performed on a desktop PC with 1GB of internal RAM and a Pentium 4 2.4GHz processor. The interferograms were generated using the Doris InSAR software operated in the Cygwin environment, which is a UNIX-type environment. All other processing is done under the Microsoft Windows XP environment.

The first stage of the processing is to select a SAR image as the master image for each interferogram. Based on its temporal and geometrical position being relatively central in the stack of images, the SAR image acquired on 3rd April 1998 was selected for use as the master image.

Using Doris, together with precise orbits where available, the stacks of interferograms for the two test sites were generated. Two of the SAR images did not have precise orbits available, namely the two images acquired by the ERS-1 satellite. This is because during these acquisition dates (between July 1996 and July 1998) the satellite was not tracked by any laser systems and so it is impossible to generate precise orbits for these dates.

The interferograms were generated without any filtering procedures or mutlilooking of the interferogram pixels, so as not to 'contaminate' the phase values of any persistent scatterers. The original SAR data has been oversampled in range by a factor of two to reduce anti-aliasing in the interferogram creation stage. The data was not oversampled in the azimuth direction because Doris does not include an option for this; the pixel resolution is already much finer in azimuth than in range and, in general, the phase gradient in the range direction is much greater than in the azimuth direction, so it is more critical to oversample in the range direction than azimuth. After interferogram formation the data is compressed back to the original size by discarding the extra columns created from the oversampling procedure.

8.3 Greenwich

The first test site used is the Greenwich area. The pre-processing step of the 3PaPS software was run to extract the required information from the Doris generated outputs and saved to a collection of files. A stack is created from the master SAR image and the resampled slave SAR images (i.e. the slave images that have been sampled onto the same image grid as the master SAR image). From this stack the candidate PS points are selected and the temporal average of the amplitudes created. Figure 8.1 below shows the image created from the mean amplitude values with the candidate PS points overlaid. The 2411 candidate PS points are spread over the image and located in the regions where
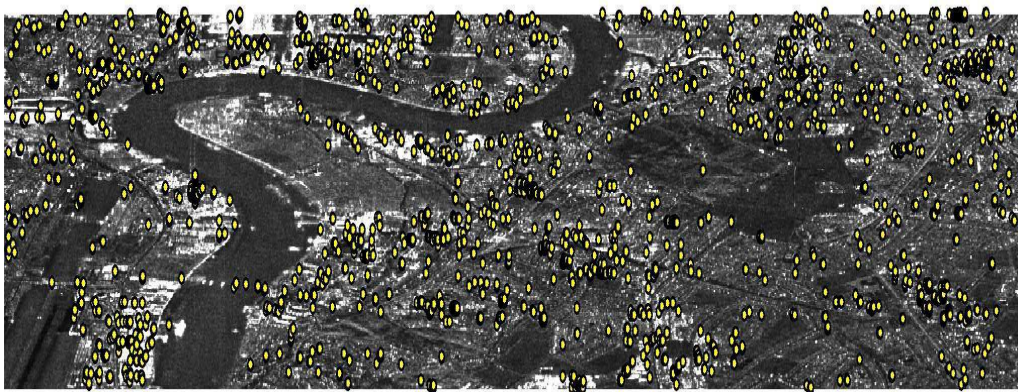
Figure 8.1 Greenwich: candidate PS points. Mean amplitude image of the Greenwich test site with candidate PS points overlaid.

they are expected, i.e. bright amplitude urban areas, and absent from the river and vegetated areas.

Using the 3PaPS software, together with MATLAB, a SRTM Digital Elevation Model was cropped and transformed into a simulated phase interferogram in radar coordinates for each interferogram in the stack. This was then used as described in chapter 5 to aid the unwrapping of the topographic phase component of each interferogram, resulting in an estimate for the absolute phase of the interferograms.

An interferogram must be selected as the topographic interferogram before the differential phase can be calculated. Based on the results of chapter 7 it was decided that the interferogram should have a short geometric baseline. Interferogram 14 was initially chosen as the topographic interferogram because of its short geometric and temporal baselines, but it would not generate stable differential results with all of the interferograms[1]. Interferogram 7 was selected as a second choice because it too has a short geometric baseline and relatively short temporal baseline. The differential phase was then generated at the candidate PS points for each interferogram, and an initial estimate for the topographic phase error ϕ_E was made. Figure 8.2 below shows the estimates of ϕ_E for each candidate PS point against the correlation coefficient of the data fit. From this we can conclude that the estimates of ϕ_E are likely to be good due to 82% of them having a correlation greater than 0.8.

After removal of the initial topographic phase error term the iterative procedure described in chapter 5 was undertaken. The outputs of this step (atmospheric and decorrelation phase noise) were imported into the Easykrig software package for interpolation. In the Easykrig package a semi-variogram was created from the actual data and a model was fit to this using least squares techniques. The basic model used was a spherical equation since this matched

---

[1] This has since been identified as a software bug and solved.
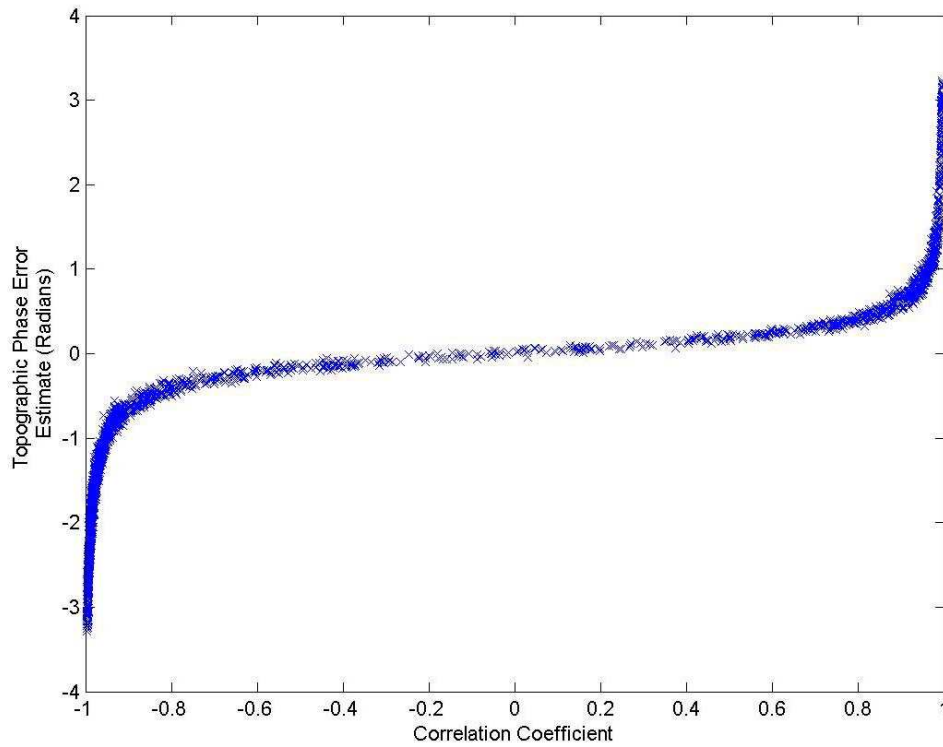
Figure 8.2 Greenwich: Topographic phase error vs. correlation. Graph of ϕ_E estimates against

correlation coefficient of the least squares fit of ϕ_E to the data.

the shape of the data semi-variogram well. Equation 8.1 below describes the spherical model

$$sv = \begin{cases} c_0 + c_S \left\{ (3/2)(\|h\|/a_S) - (1/2)(\|h\|/a_S)^3 \right\} & 0 < \|h\| \le a_S \\ c_0 + c_S & \|h\| \ge a_S \end{cases}, \qquad 8.1$$

where h is the *lag*, c_0 is the *nugget*, c_S is the *sill* and a_S is the *range* and $\| \|$ denotes magnitude. The lag is the distance between the two points in question, the sill is the maximum value of the semi-variogram (i.e. the semi-variogram value as h tends to infinity), the nugget represents sub-scale variation or measurement error and is the semi-variogram value at h=0 and the range is a scalar that controls the correlation between points. (*Cressie 1993*) gives a detailed overview of semi-variogram estimation and fitting as well as a thorough description of the kriging technique. Figure 8.3 below shows a graph of the

143

semi-variogram model (line) together with the data semi-variogram (circles) given by the Easykrig package. The model has a nugget = 0.28, sill = 0.99 and range = 0.33.
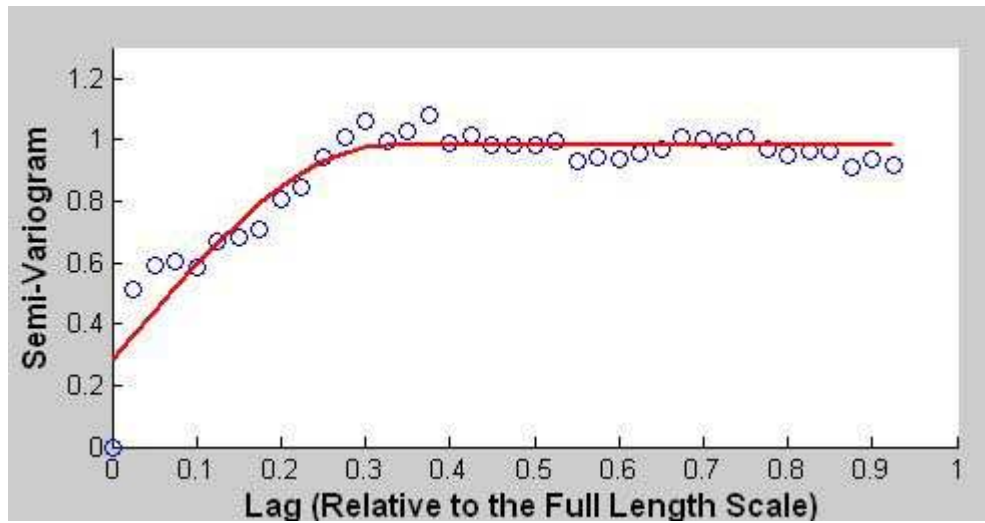
Figure 8.3 Greenwich: Kriging semi-variogram. Graph of the actual data semi-variogram (circles) together with the model semi-variogram (solid line) given by the Easykrig package.

The Kriging output is given on a grid with pixel size approximately 300m x 300m which is then interpolated back to the original size. This has the effect of spatially smoothing the phase data such that the decorrelation noise is reduced whilst the atmospheric phase noise is left unchanged, due to spatial scales of approx. 0.5 - 1km (*Hanssen 2001*). The smoothed and interpolated atmospheric phase screens (see Figure 8.4a) are then removed from each respective interferogram. The same procedure was applied to the topographic phase error minus the velocity estimates, to give an atmospheric phase screen for the topographic interferogram (see Figure 8.4b). The differential phase was then created for every image pixel.

An estimate of ϕ_E for each point is derived from a linear least squares fit, and since the atmospheric phase has been removed from the topographic interferogram, ϕ_E is assumed to be mainly due to deformation. This is then fed back into the stack of the differential phase as a deformation observation. A second estimate of ϕ_E is then made using a periodogram method, in case a residual, possibly wrapped, effect remains. From the stack of data and by using
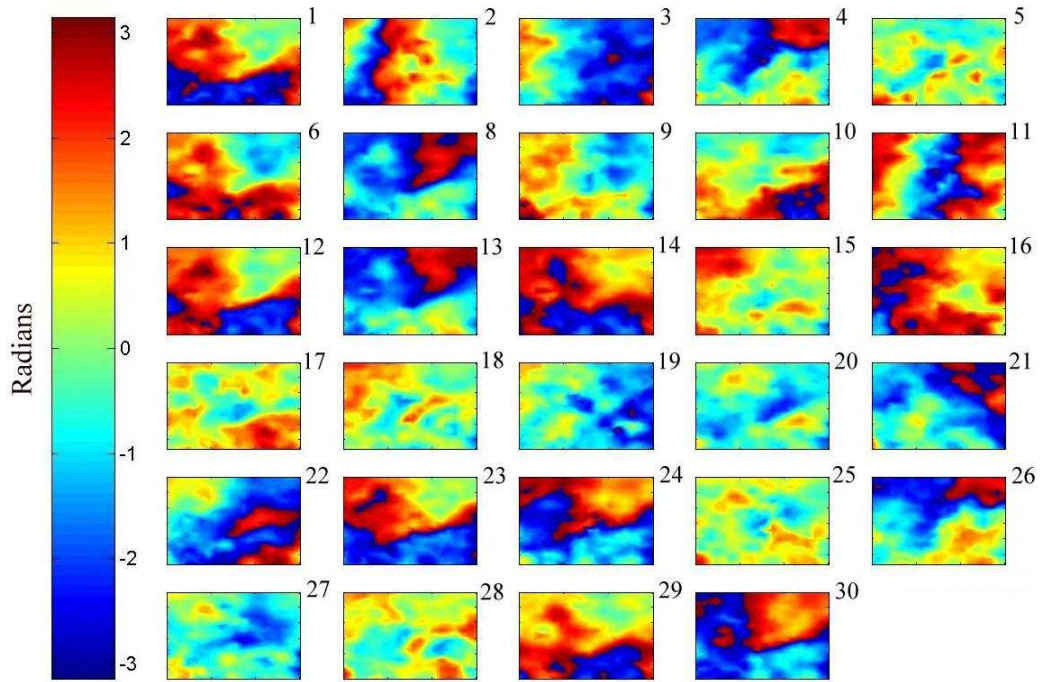
Figure 8.4a Greenwich: Wrapped Atmospheric Phase Screens of the 29 deformation interferograms. Scale in radians.
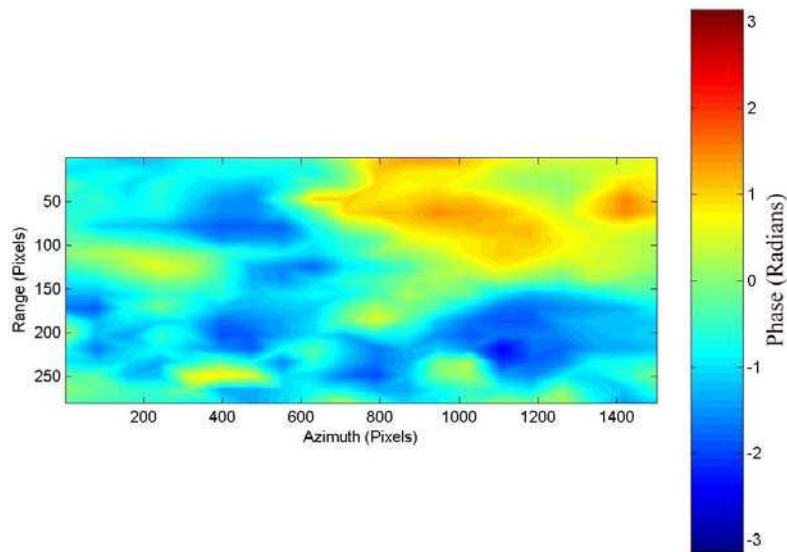
Figure 8.4b Greenwich: Wrapped Atmospheric Phase Screen for the topographic interferogram (interferogram 7).

a periodogram, velocities together with a corresponding γ value are calculated. The data has then been geocoded into a WGS84 UTM Zone 31 coordinate system using the IAS technique together with the topographic interferogram after removal of atmospheric and deformation phase terms.

The final PS points have been selected using a γ threshold of 0.8. These are shown in Figure 8.5 and overlaid onto the geocoded mean amplitude image where the colour of the PS points is related to their respective velocities. The two purple triangles correspond to the two GPS points in the region. Table 8.1 also shows the number of PS points within each of the velocity bounds.
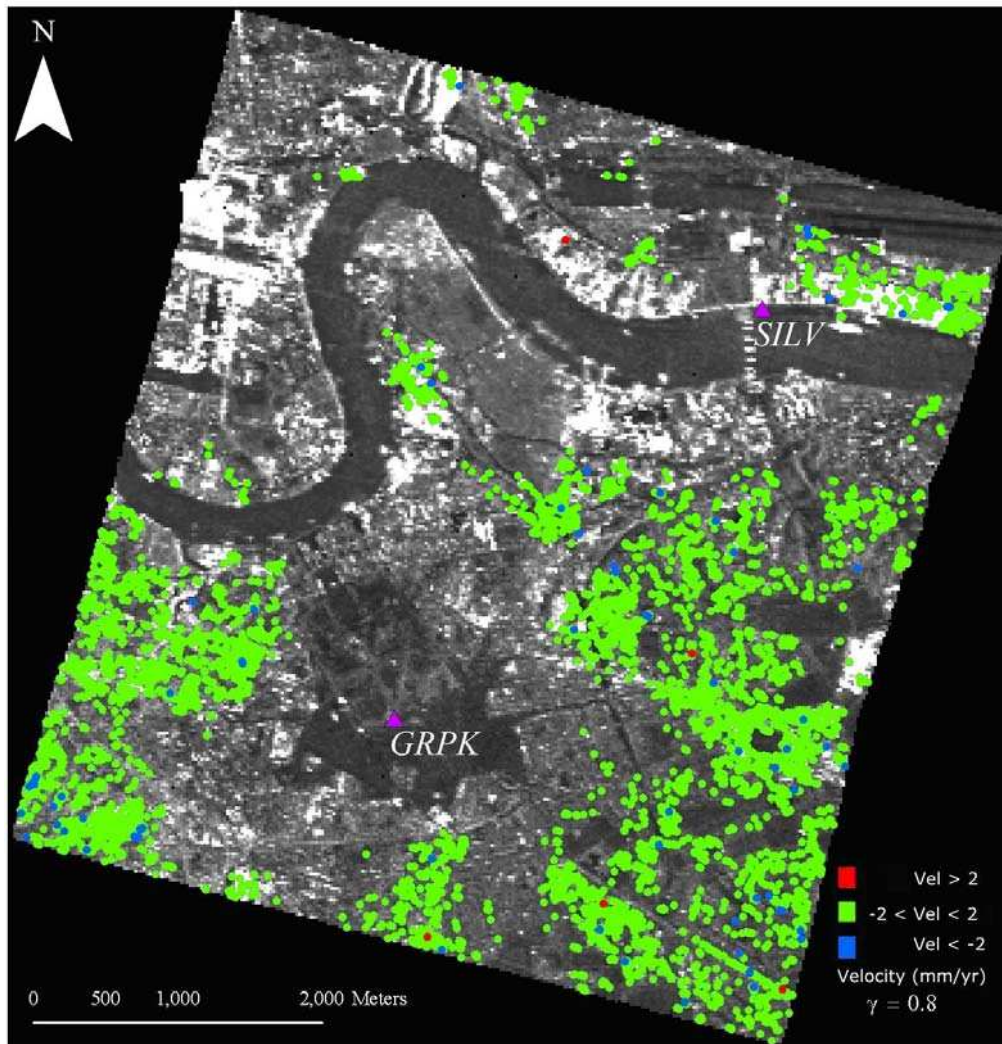
Figure 8.5 Greenwich: PS point velocity map. Background image is the mean amplitude of the SAR data, geocoded to a WGS84 UTM Zone 31 coordinate system. PS points are shown as coloured dots, with the colour related to their velocity.

	V>2	30
	1<V≤2	284
Number of PS Points with	0<V≤1	1687
	-1<V≤0	3058
	-2<V≤-1	519
	V≤-2	138
	Total	5716

Table 8.1 Greenwich: Classification of PS points in relation to their velocity V in mm/yr.

The PS point coverage appears to be mainly south of the river. There are few regions north of the river with a high density of PS points. The region around Greenwich Park is also absent of PS points. This could be due to a lower number of candidate PS points being available in these areas, and so accurate atmospheric phase estimation is more difficult. Hence the incorrect atmospheric phase is removed, the differential phase is less stable (temporally) and points with high γ are fewer. Or it could purely be due to the area being vegetation and there being no PS points there because of the scattering properties of vegetation.

It can be seen that the majority of the 5,716 PS points of Figure 8.5 have a velocity of between ± 2mm/yr, with only a few points of a higher magnitude. These few points appear to be scattered about the image 'randomly' and not confined to local areas. This suggests that if they are showing accurate deformation information it is likely to be localised to that scatterer and not a wide reaching subsidence problem. The majority of the points however show that there is no significant motion occurring. The limits of the velocity subsets in Figure 8.5 (e.g. ± 2mm/yr) have been chosen to reflect the confidence of the final results. Because only a small set of 31 SAR images have been used in the study, the accuracy and precision of the velocity estimates are lower than what could be achieved if the full set of available SAR images is used. Studies by other people using a similar amount of SAR images have attained precisions of ± 2mm/yr (*Worawattanamateekul et al 2004*), and so these bounds have been used here. The values within the table are shown in millimetre intervals to give a more detailed view of the data set.

A feature of points can be seen in the bottom right corner of the image that lie on a straight line. This area corresponds to that shown below in Figure 8.6, an image from the Google Earth package. The PS points have been added onto this image to try and find what physical features they agree with. It can be seen that there is a dual carriageway, railway track and houses that are in the area and run parallel to the PS points.

Also, a PS point in the docklands near the London City Airport is shown in Figure 8.7. The point is located out in the water, which suggests that a

Figure 8.6 Greenwich: Aerial image of straight-line feature of PS points (in the bottom right corner of Figure 8.5). PS points colour does not represent velocity here.

geocoding error has occurred. To try and account for this error the geocoded mean amplitude image (Figure 8.5), which is geocoded using the same equations as the PS points, has been overlaid onto the aerial image, using visual tie points such as the river bank and barrier to place it correctly. Figures 8.8, 8.9 and 8.10 show 3 areas where the radar image is overlain on the aerial image, with the PS points located on the radar image shown as green/blue filled circles as in Figure 8.5. Using these images we can see where the PS points should be located on the aerial image.

It can be seen from Figure 8.8 that the geocoded PS points on the aerial image are offset by a vector mainly in the West direction with a slight North bias, with a magnitude of approximately 100m. The PS point from Figure 8.7 appears that it should be located on the south side of the Connaught Swing Bridge, and could be related to the large operator's tower structure.

Figure 8.7 Greenwich: Aerial image of Docklands PS point (just west of the London City Airport).

Figure 8.8 Greenwich: Aerial image with PS points overlain (of the London Docklands region). Red squares denote PS points as geocoded onto the aerial image, green and blue circles denote corrected PS location using the radar image.

It can also be seen that the two points in the river at the south of Figure 8.8 should be located on the pier. The offset between the two sets of data appears to be approximately 100m for each point, with the error vector being in a West and North direction.

From Figure 8.9 the PS point locations appear that they should be in the road. In the centre of the dual carriageway there are streetlamps at regular intervals, which could be what the PS points are related to. This is further supported by the fact that the buildings either side of the road do not continue as far as the line of PS points.
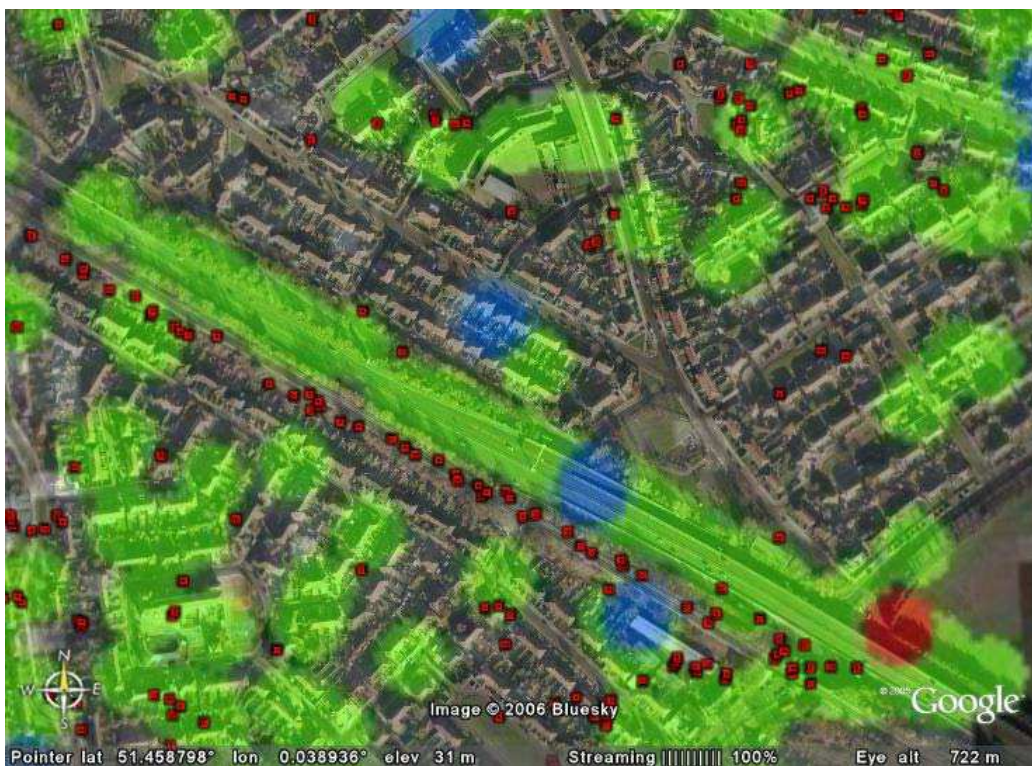
Figure 8.9 Greenwich: Aerial image with PS points overlain. Geolocated PS points are shown as red squares, the coloured circles represent the PS locations on the mean amplitude radar image.

Figure 8.10 shows an aerial image of Charlton Athletic Football Club's stadium. It can be seen that the PS point locations derived from the mean amplitude radar image appear to relate to the stadium structure. Again, the offset between the two sets of PS points is in the region of 100m.

Figure 8.10 Greenwich : Aerial image with PS points overlain.

Unfortunately there are no PS points close to the GPS points to do a meaningful comparison with. The GPS data, shown below in Figure 8.11, does however independently agree with the overall trend of the PS data, that there is no significant motion occurring over the time period. The error bars on the GPS relate to the standard deviation of the observations and are typically a few cm in magnitude.
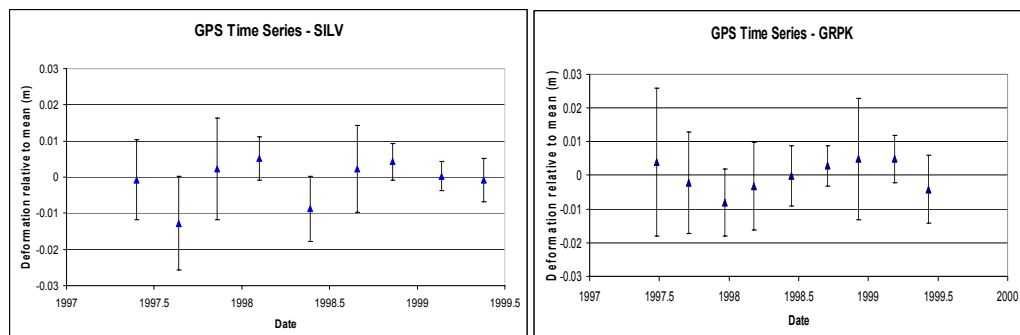
Figure 8.11 Greenwich: GPS time series (for the two GPS stations, SILV and GRPK). Both show that there is no significant motion occurring over the 3 year time period (*Bingley et al 1999*).

A time series for the docklands PS point (the point from Figure 8.7) is shown below in Figure 8.12. The scale on the y-axis shows deformation in metres (relative to the master SAR image) plotted against time (relative to the master SAR image) in years.
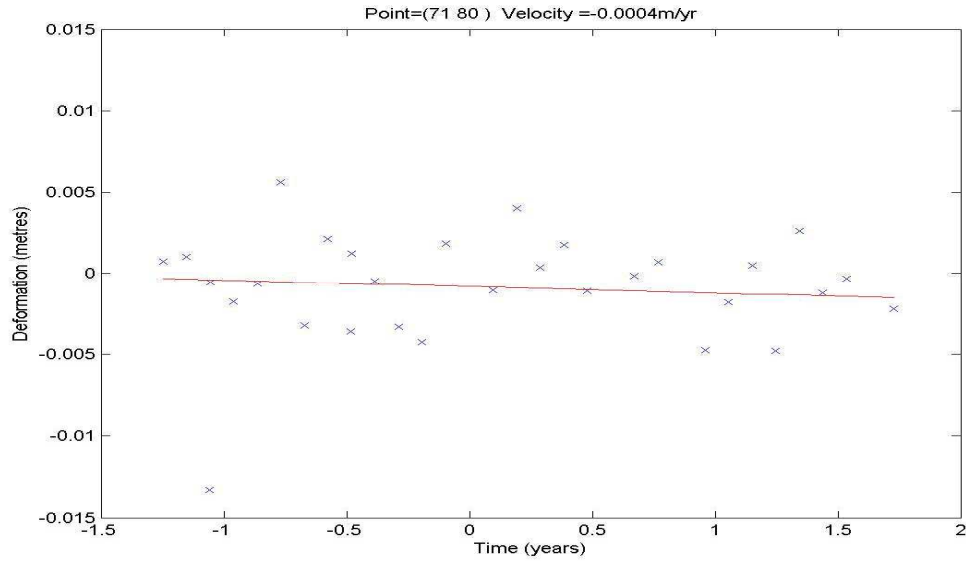
Figure 8.12 Greenwich: PS point time series (of the "Docklands PS point"). It shows no significant motion over the time period. The red line shows the linear velocity fit to the data and observation 3 appears as an outlier in the data.

8.4 Westminster

The second test site was of the Westminster area. Similarly for the first test site the pre-processing step of the 3PaPS software was run to extract the required information from the Doris generated outputs. The candidate PS points were selected from a stack of the SAR amplitude data, and the mean amplitude image created. Figure 8.13 below shows the image created from the mean amplitude values with the candidate PS points overlaid. The 2389 candidate points are spread across the image giving a good coverage.
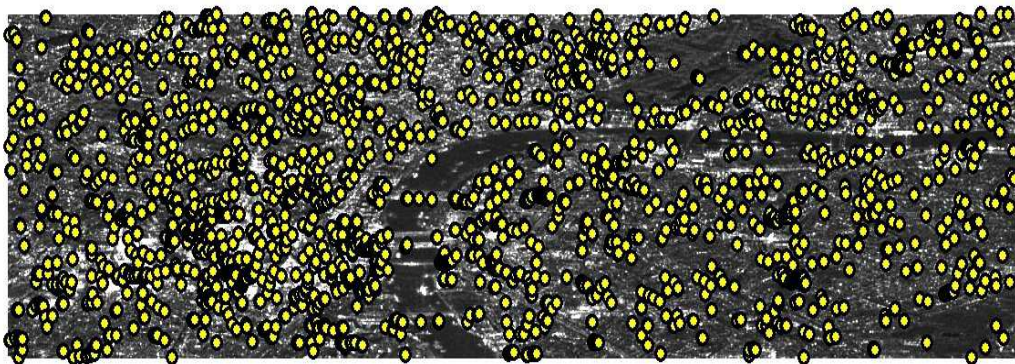
Figure 8.13 Westminster: Candidate PS points. Mean amplitude image of the Westminster test site with candidate PS points overlaid.

As before, the interferograms were unwrapped and an estimate for the absolute phase generated. The same interferogram has been chosen as the topographic interferogram here, since the same data is used except that it is of a different area. The differential phase was then generated at the candidate PS points for each interferogram, and an initial estimate for the topographic phase error ϕ_E was made. Figure 8.14 below shows the estimates of ϕ_E for each candidate PS point against the correlation coefficient of the data fit. From this we can conclude that the estimates of ϕ_E are likely to be good due to 95% of them having a correlation greater than 0.8.
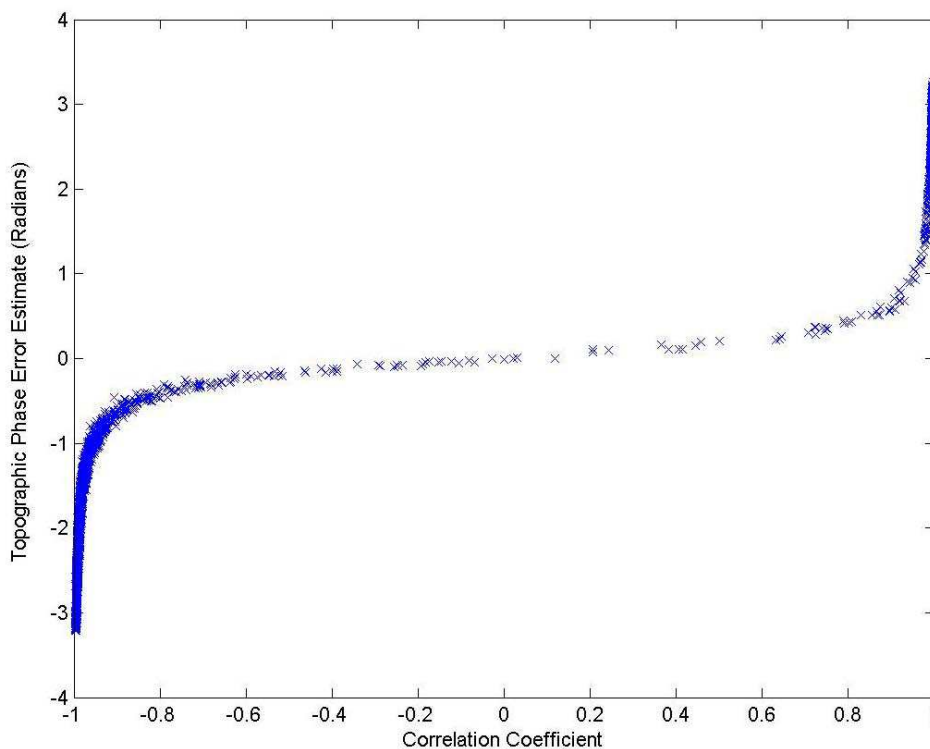
Figure 8.14 Westminster: Topographic phase error vs. correlation. Graph of ϕ_E estimates against correlation coefficient of the least squares fit of ϕ_E to the data.

After removal of the initial topographic phase error term the iterative procedure was undertaken. The outputs of this step (atmospheric and decorrelation phase noise) were imported into the Easykrig software package for interpolation. As before, a spherical semi-variogram model was used, except with different values for the parameters. Figure 8.15 below shows a graph of the semi-variogram model (line) together with the data semi-variogram (circles) given by the

Easykrig package. The model has a nugget = 0.29, sill = 1.03 and range = 0.108.
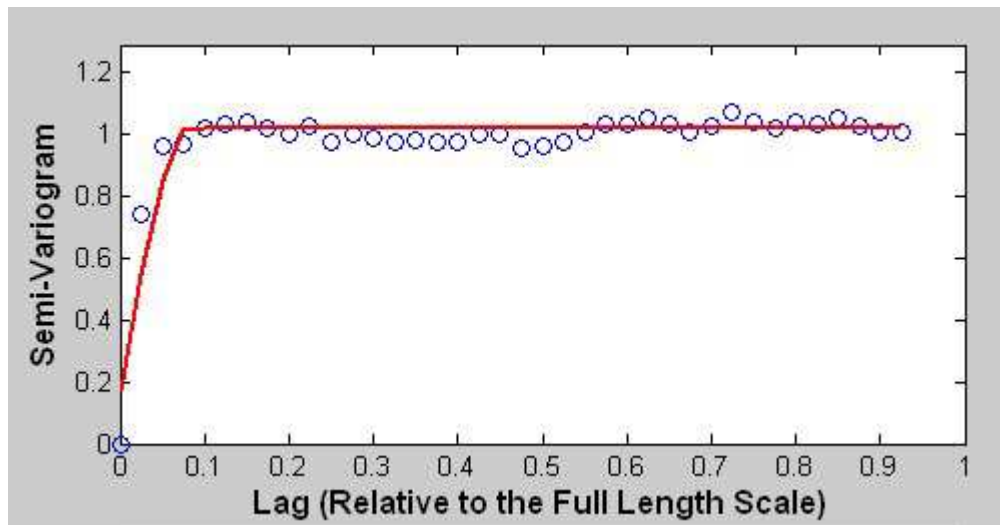
Figure 8.15 Westminster: Kriging semi-variogram. Graph of the actual data semi-variogram (circles) together with the model semi-variogram (solid line) given by the Easykrig package.

The Kriging output is given on a grid with pixel size approximately 300m x 300m which is then interpolated back to the original size. The smoothed and interpolated atmospheric phase screens (Figure 8.16a) have been removed from each respective interferogram. The same procedure was applied to the topographic phase error minus the velocity estimates, to give an atmospheric phase screen for the topographic interferogram (Figure 8.16b). The differential phase is then created for every image pixel.

An estimate of ϕ_E for each point is derived from a linear least squares fit, and since the atmospheric phase has been removed from the topographic interferogram ϕ_E is assumed to be mainly due to deformation. This is then fed back into the stack of the differential phase as a deformation observation. An estimate of any residual topographic phase error, using a periodogram technique, is then performed. From the stack of data and by using a periodogram, velocities together with a corresponding γ value are calculated. The data has then been geocoded into a WGS84 UTM Zone 31 coordinate system using the IAS technique together with the topographic interferogram after removal of atmospheric and deformation phase terms.
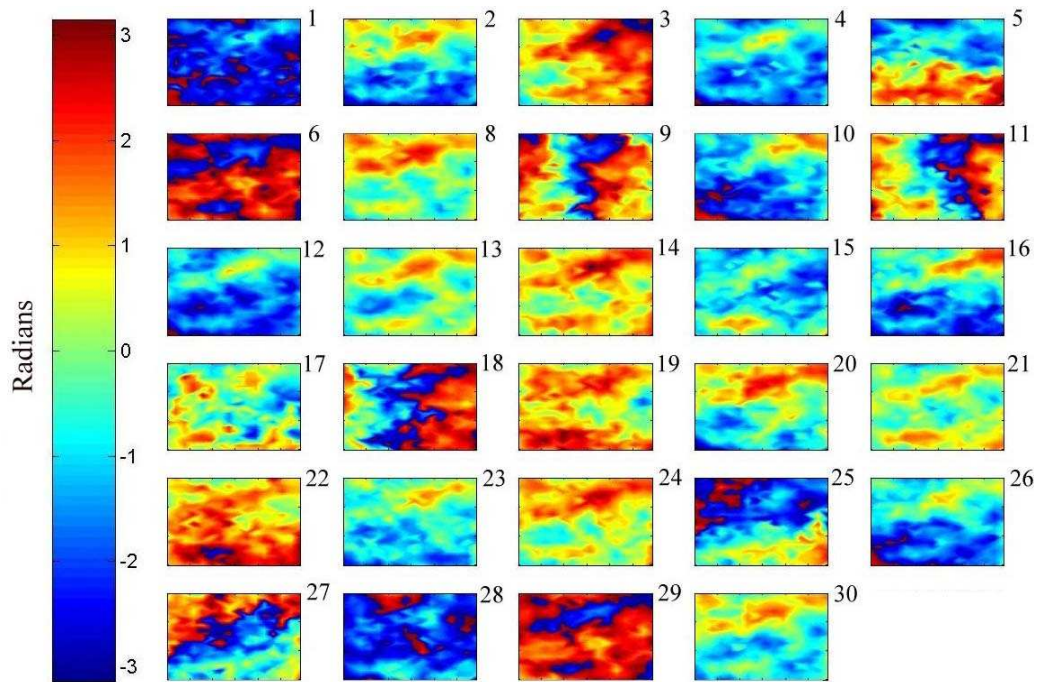
Figure 8.16a Westminster: Wrapped Atmospheric Phase Screens for the 29 deformation interferograms. Scale in radians.
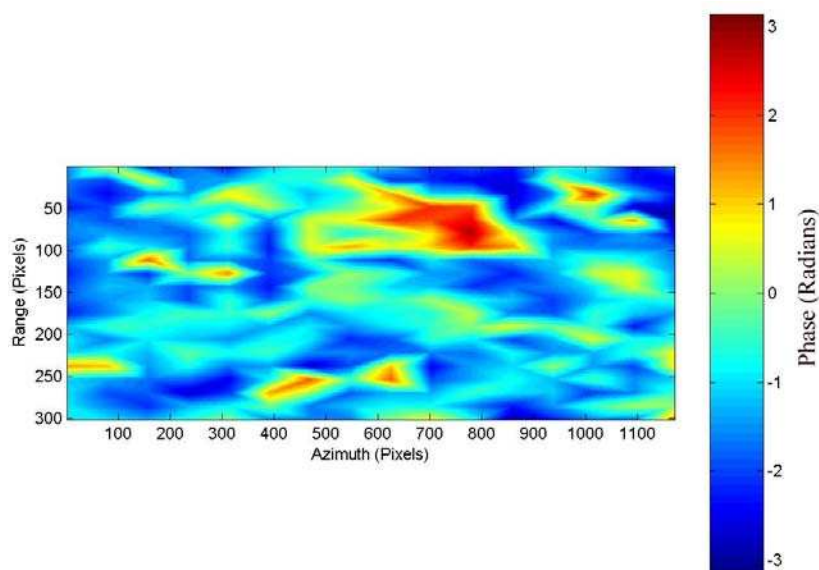
Figure 8.16b Westminster: Wrapped Atmospheric Phase Screen for the topographic interferogram (interferogram 7).

The final PS points have been selected using a γ threshold of 0.8. These are shown in Figure 8.17 and overlaid onto the geocoded mean amplitude image where the colour of the persistent scatterers is related to their respective velocities. Table 8.2 shows the number of persistent scatterers within each of the velocity bounds.
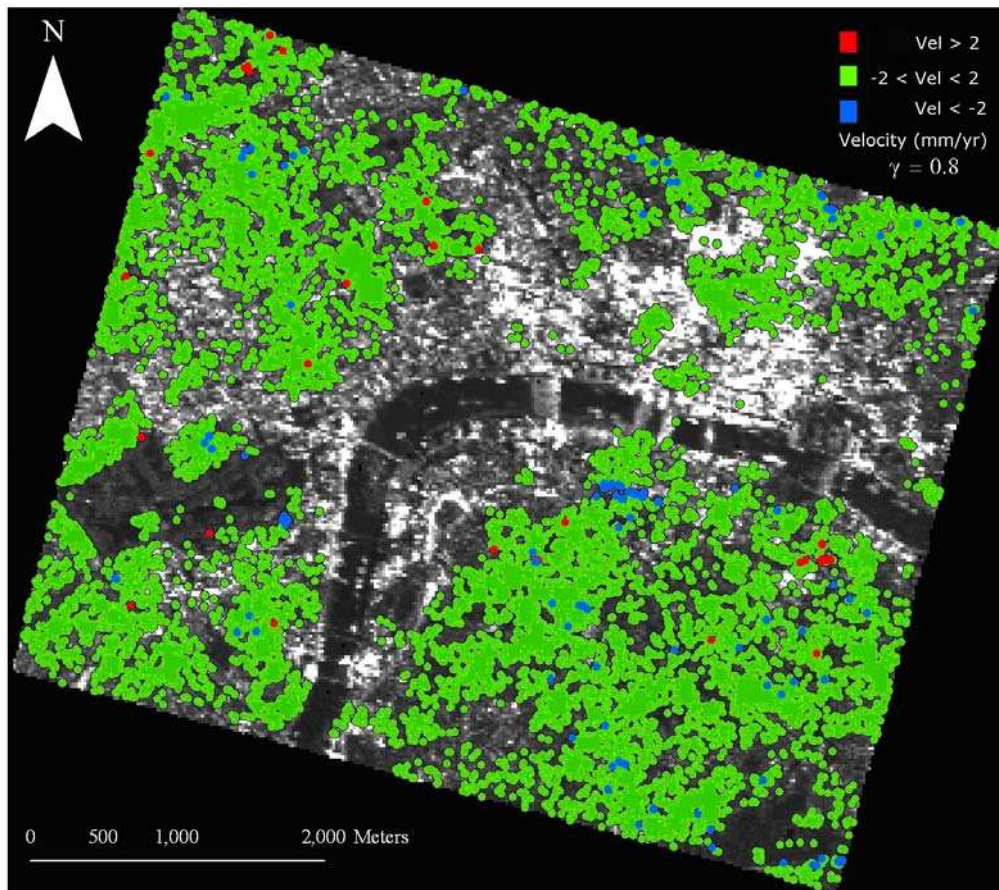
Figure 8.17 Westminster: PS point velocity map. Background image is the mean amplitude of the SAR data, geocoded to a WGS84 UTM Zone 31 coordinate system. PS points are shown as coloured dots, with the colour related to their velocity.

	V>2	232
	1<V≤2	1546
Number of PS Points with	0<V≤1	5207
	-1<V≤0	6793
	-2<V≤-1	1109
	V≤-2	355
	Total	15242

Table 8.2 Westminster: Classification of PS points (in relation to their velocity V in mm/yr).

The majority of PS points are green, showing a velocity of ± 2mm/yr, which suggests there is no significant motion at these points. There is also a scattering of points with velocities greater than this. However, unlike test site 1, some of these points show patterns. For example, south of the river there is a large cluster of blue pixels and west of the river next to the park there is a smaller cluster of blue pixels, each showing velocities of less than -2mm/yr. There is also a small cluster of red points south of the river near the east of the image.

156

The clusters of blue points are located on parts of the Jubilee Rail extension. Unfortunately there were no PS points found on most of the rail extension except for these two clusters. Figure 8.18 shows the velocity map for every pixel (not just PS points) overlaid upon the mean amplitude image. It is possible to see from this image that there is a blue line where there is a deformation velocity of less than -2mm/yr, which travels across the image East to West. This is where the Jubilee line extension runs.
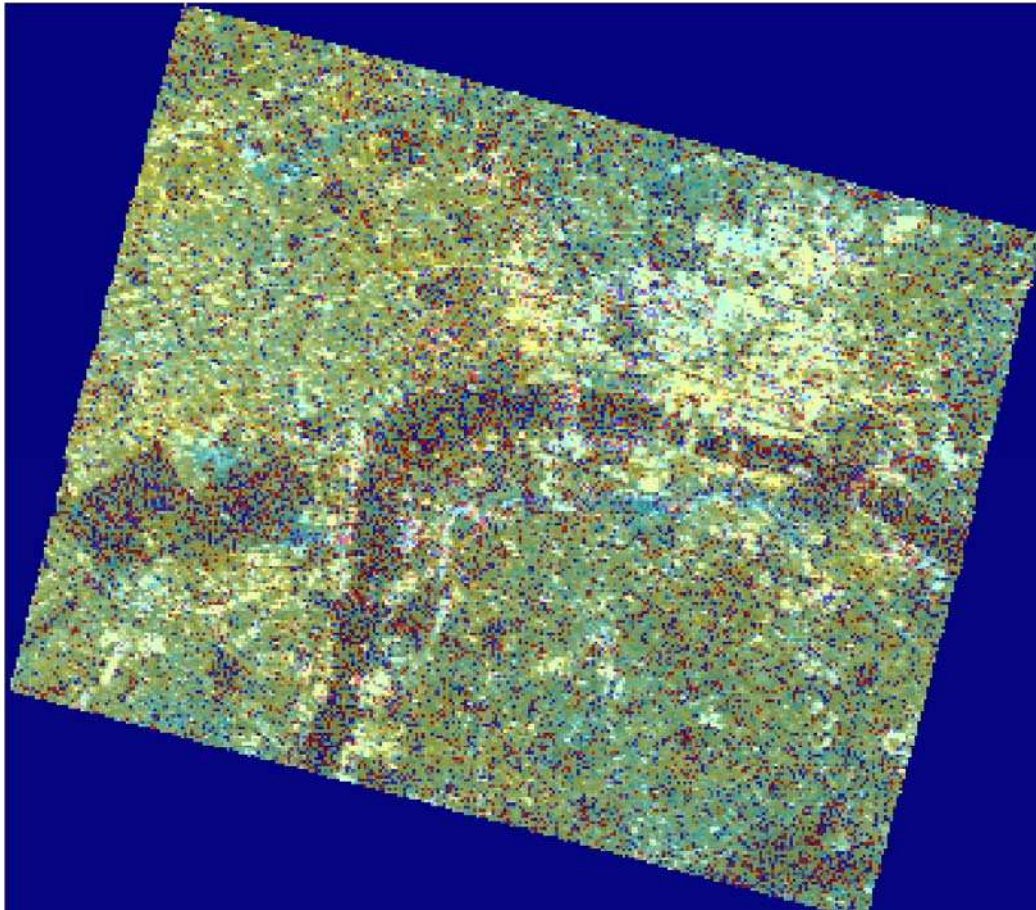
Figure 8.18 Westminster: Velocity map for every pixel (overlaid upon the mean amplitude image). The blue line that runs East to West south of the Thames shows deformation that has occurred on the Jubilee Rail Line extension.

The two clusters of PS points lie on this blue line. A time series plot for one of these points is shown below in Figure 8.19. It shows a deformation velocity of approximately -5mm/yr.
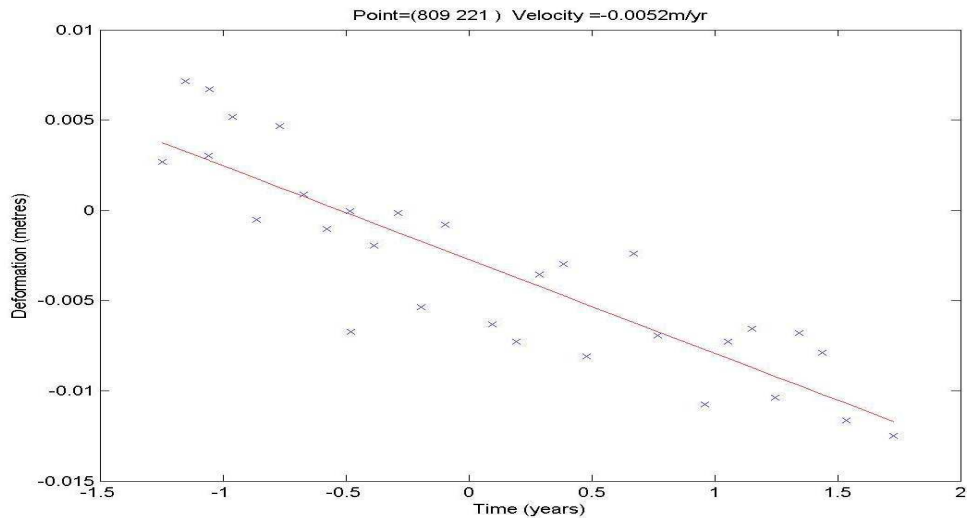
Figure 8.19 Westminster: PS point time series (for a point on the Jubilee Line Extension).
Estimated deformation velocity is approximately -5mm/yr.

The PS points have been imported into the Google Earth package and do not
show any definite geolocation errors. Unlike the Greenwich park area there are
no linear features of PS points in Westminster to investigate. It is out the scope
of this thesis to do an in-depth positioning test of the PS point locations, but it
may be useful to use a tool such as Google Earth to get an overview of the PS
point locations. There are no points geolocated in regions which are
unexpected, i.e. there are no points geolocating to the river or grassy areas. An
image of Buckingham Palace is shown in Figure 8.20 with PS points overlaid.
There are no PS points located on the open grassy areas but are on the buildings
or trees around the outskirts of the park.

Figure 8.20 Westminster: Aerial image with PS points overlain.

158

8.5 Conclusions

8.5.1 Test Site 1: Greenwich

The results of the Greenwich test area show that there is very little deformation occurring at any of the PS points, with 98.6% of the PS points showing a velocity of between ± 2mm/yr. This is within the bounds expected for the noise of the PS analysis and so no significant deformation can be derived. The two GPS sites located in the region also show that there is no significant motion occurring in the area.

A geolocation error is present in the data and appears to be a constant bias of approximately 100m, with the majority of the error in the West direction and a smaller error in the North direction.

8.5.2 Test Site 2: Westminster

The results of the Westminster test area show that, for the majority of PS points, there is no deformation occurring: 98.9% of the PS points showing a velocity between ± 2mm/yr. Some of the PS points in the region of the Jubilee Line Extension do show a deformation that is similar to previous studies. Unfortunately the majority of the area of the Jubilee Line Extension is free from PS points. A geolocation of the points does not show a large error as occurred with the Greenwich test area.

8.5.3 Algorithm Performance

The IAS 3-Pass PSInSAR algorithm has performed reasonably well in these two test areas. It has identified approximately 1.5% of the pixels as PS points for Greenwich and 4% for Westminster. This agrees well with other algorithms that typically find 100 PS points (or more) per square km (*Bovenga et al 2004*, *Zirnig et al 2004*). In Figure 8.5 of Greenwich there are large regions that exist without any PS points identified. It is unclear as to whether this is because the atmosphere has not been estimated so well here, due to a smaller number of

candidate PS points, or whether there is some other reason for it such as urban regeneration. Obviously the park will have very few PS points located there due to the scattering properties of the park land. If a lot of building work is occurring during the period of the analysis then PS points may not exist there because the scattering characteristics of the area will constantly be changing. This will certainly be true for the Greenwich peninsular region since the Millennium Dome was being constructed during the time frame of the SAR acquisitions.

For the Westminster region, there is a fairly consistent spatial coverage of PS points identified. But very few points on the Jubilee Line Extension have been identified. This could mean that: the implemented algorithms have trouble identifying PS points with a large deformation velocity; that there are simply no PS points in that region; or that some error has occurred in the processing of the phase data introducing some noise.

Of the PS points that have been identified, the vast majority of them suggest that there is no motion occurring in the region, within a tolerance of 2mm/yr, which is what was expected prior to the study. The GPS stations that have been used in the study also suggest that there is no significant motion occurring at the Greenwich test site over the same period.

It has been shown that a 3-Pass PSInSAR approach using the Integer Ambiguity Search (IAS) is possible. By using this method, the use of a DEM as a topographic model has been avoided and therefore the error associated with the inaccuracies of the DEM has been removed from the analysis. It has, however, been 'replaced' with an atmospheric phase error term which must be removed in a similar fashion to the DEM error term of the 2-Pass PSInSAR technique. By estimating this term and using the estimated deformation velocity from the stack of N-1 differential phases from the initial candidate PS point analysis, it is possible to have N observations (1 from each of the N interferograms) in the final search for PS points. Therefore, the IAS 3-Pass PSInSAR method solves for N atmospheric phase screens and uses N observations in the final PS

analysis, whereas the 2-Pass method solves N atmospheric phase screens and a topographic height correction term and uses N observations in the final analysis.

As stated in chapter 5, there are problems associated with the implemented algorithm. The main problem being that it can only be used on small regions of approximately 5km by 5km in size. This is due to the assumption that the atmospheric phase error can be effectively modelled as a linear phase plane, leaving only small perturbations. For larger regions this assumption fails because of the spatial scales of the atmospheric phase, and further parameters would have to be introduced to the atmospheric model. Another problem with the method arises with the treatment of the phase residuals from the iterative routine. By interpolating and smoothing the residuals to give the atmospheric phase screens, any deformation that does not fit the linear model used will be mistakenly included in the atmospheric phase screen. These problems were raised in *Ferretti et al (2000a)*, where a new algorithm was introduced to overcome these limitations. This "Non-Linear" method is described in the next chapter together with an IAS 3-Pass version of the algorithm.

8.5.4 Algorithmic Improvements

Before discussing the "Non-Linear" method, some other improvements to the linear method can already be proposed. As it stands the algorithm follows the 2-Pass PSInSAR method fairly closely. By making a few changes to the algorithm procedure it could improve the results, as follows.

8.5.4.1 Changing Topographic Interferogram

One possible improvement could come from changing the topographic interferogram at the midpoint of the processing, i.e. after the candidate PS point analysis. It has been shown that using a small baseline topographic interferogram allows for easier identification of the topographic phase errors. This is because the baseline ratio used in the 3-Pass method will usually be greater than 1, and therefore increase the magnitude of the topographic error term in the differential phase. Recall the differential phase equation 4.19:

$$\partial\phi = (\phi_{13} + 2\pi\Delta n_{13} + \frac{4\pi}{\lambda}\delta e_{13}) - \frac{B_{13}}{B_{12}}(\phi_{12} + 2\pi\Delta n_{12} + \frac{4\pi}{\lambda}\delta e_{12})$$
$$- B_{13}(\frac{4\pi}{\lambda}\cos(\beta_{12} + \gamma) - \frac{4\pi}{\lambda}\cos\beta_{12})$$

8.2

In the same way, if the topographic interferogram has a large baseline then the topographic phase error term will be multiplied by a scalar that has magnitude less than 1, i.e. the topographic phase error term will have less of an effect in the differential phase. So it might be an improvement to use a small baseline interferogram to identify the topographic phase error and the atmospheric phase screens for the interferograms, and then swap to a large baseline interferogram to calculate the differential phase for the full test site and do the final analysis.

8.5.4.2 A 4-Pass Method

Using a 3-Pass framework means that the interferograms are restricted to having the same master image, and therefore limits the way in which the interferograms can be formed. By implementing a 4-Pass technique, this restriction would be removed and would allow greater freedom in generating interferograms, e.g. only using small baseline interferograms. This would obviously mean the algorithms would need complete reworking, but it would allow a DEM-free PSInSAR method that could follow in similar veins to the Small Baseline Subset approach or the Coherent Scatterer approach. A 4-Pass version of the Integer Ambiguity Search DInSAR technique is shown in Appendix A.

8.6 Summary

The Linear IAS 3-Pass PSInSAR process has been tested using real SAR data of two test sites in the City of London. The results have been shown and discussed, and in general show that there is little significant deformation occurring, which has also been shown by the GPS in the region. The Jubilee Line Extension deformation has been identified at some points, but the majority of the line is absent of PS points and so the deformation cannot be fully identified reliably here. The full deformation map of every interferogram pixel has been shown and the Jubilee Line deformation can be identified on this map.

There is no reliability measure on these deformations and it is used purely to check if the Jubilee Line deformation is noticeable above the surrounding deformation estimates. The performance of the algorithm has been acceptable, giving a similar percentage of coverage of persistent scatterers to other techniques, and showing believable velocity estimates. Some possible algorithmic improvements have been described that could be implemented at a later date.

9. Nonlinear Deformation Detection

9.1 Introduction

A Persistent Scatterer technique has been described which works well for linearly deforming scatterers in small confined areas. This is good for certain studies, but many users of subsidence maps need larger areas to be examined and also want to know about subsidence that does not fit a constant velocity model. In 2000, *Ferretti et al (2000a)* published a paper that addressed these two problems and demonstrated a second persistent scatterer approach. This will be called Ferretti's Non-Linear PSInSAR technique in this thesis. This PSInSAR approach will be described in the forthcoming section, followed by a section dedicated to the Non-Linear IAS 3-Pass method. The Non-Linear 3-Pass PSInSAR method will then be demonstrated using both simulated data and real SAR data over the previously described test sites of chapter 6. These results will be discussed and conclusions about the method drawn.

9.2 Ferretti's Non-Linear PSInSAR Technique

This section aims to describe the important differences between Ferretti's Non-Linear method and the method described earlier in chapter 5. This algorithm is described in full in *Ferretti et al 2000a*, and is summarised in the flow diagram of Figure 9.1. The basic steps involve forming the stack of SAR images, generating differential phase interferograms and selecting the candidate PS points as before. Then phase increments between nearby candidate PS points are estimated by examining the difference in the PS differential phase, and removing estimates of the linear deformation and DEM error, which can be derived as before by examining the stack of data. This results in the unwrapped phase residuals at each PS point (i.e. the unwrapped differential phase minus the effects of a linear velocity and DEM error). Using these unwrapped values a filtering process is carried out which aims to separate and remove any non-linear deformation from the phase residuals. The resulting phase residuals are then spatially smoothed and interpolated to generate atmospheric phase screens for

each interferogram. The algorithm then continues as per the linear method; that is the APSs are removed from the interferograms, the differential interferograms are regenerated and a final examination of the phase data up the stack identifies persistent scatterers and their respective deformation velocity.

```
┌──────────────┐   ┌──────────────┐
│ Stack of     │   │ Digital      │
│ N SAR        │   │ Elevation    │
│ Images       │   │ Model        │
└──────┬───────┘   └──────────────┘
       │
       ▼
┌────────────────────────┐
│ Identify candidate PS  │
│ points and generate    │
│ differential phase.    │
└───────────┬────────────┘
            │
            ▼
┌────────────────────────┐        ┌────────────────────────┐
│ Unwrap phase spatially │        │ Unwrap DEM error to    │
│ and temporally by      │───────▶│ refine DEM at candidate│
│ exploiting estimates   │        │ points.                │
│ for relative DEM error │        └────────────────────────┘
│ and velocity terms.    │
└───────────┬────────────┘
            │
            ▼
┌────────────────────────┐
│ Apply temporal and     │
│ spatial filtering to   │
│ isolate the atmospheric│
│ phase.                 │
└───────────┬────────────┘
            │
            ▼
┌────────────────────────┐
│ Interpolate atmospheric│
│ phase to get APS for   │
│ each interferogram.    │
└───────────┬────────────┘
            │
            ▼
┌────────────────────────┐
│ Remove APS,            │
│ recalculate differential│
│ phase and look for PS  │
│ points.                │
└───────────┬────────────┘
            │
            ▼
    ┌───────────────┐
    │ PS  Velocities│
    └───────────────┘
```

Figure 9.1 Flow diagram of the Ferretti Non-Linear algorithm described in (*Ferretti et al (2000a))*

The main differences between this algorithm and the linear one are:

- *Unwrap the Phase Data* – A filtering regime is applied to the differential phase data to try and separate the atmospheric phase noise from any possible nonlinear target motion. To this end the phase data must be unwrapped both spatially and temporally. Because of the noise present in the interferogram phase this can only be performed using the candidate PS points, because of their low noise properties. The differential phase of nearby pixels is differenced so that the spatially correlated atmospheric and orbital baseline effects are minimised. This gives equation 9.1.

$$\Delta \partial \phi = \partial \phi_{P1} - \partial \phi_{P2} = \Delta K_\varepsilon b_i + \Delta K_v t_i + \Delta w_i \qquad 9.1$$

  where $\partial \phi_{P1}$ and $\partial \phi_{P2}$ are the differential phases at nearby PS candidate points P1 and P2, ΔK_ε and ΔK_v are constants proportional to the difference of DEM error and mean velocity of the targets respectively, b_i and t_i are the geometric and temporal baselines of interferogram i and Δw_i is the sum of the phase terms due to difference in APS, nonlinear motion and noise.

  Using a periodogram technique, *relative* velocity and DEM error terms can be estimated from the temporal stack of differential phase differences $\Delta \partial \phi$. That is, by using the stack of $\Delta \partial \phi$, best estimates for ΔK_ε and ΔK_v are found. Using these estimates together with the assumption that $|\Delta w_i| < \pi$ the phase data can be unwrapped.

- *Filtering Regime* – A filtering regime is applied to the unwrapped phase data (after removing the trends due to DEM error and mean velocity) to attempt to separate nonlinear deformation from atmospheric phase. The mean (up the stack) of the de-trended phase data, w_i gives an estimate of the atmospheric phase error of the master SAR image. By removing the mean the temporal data is 'whitened' i.e. assumed to be random with mean 0. Nonlinear motion is assumed to be slow and temporally

correlated, so low-pass filtering the whitened phase residuals gives an estimate of the non-linear phase residue. Removing this estimate and adding the temporal mean back on gives the estimate for the atmospheric phase noise. This is summarised in Equation 9.2,

$$\alpha(x)_i = \left(\left[w(x)_i - \overline{w}(x) \right]_{HPTIME} + \left[\overline{w}(x) \right] \right)_{LPSPACE} \qquad 9.2$$

where $\alpha(x)_i$ is the atmospheric phase error at point x for interferogram i, $\overline{w}(x)$ is the temporal mean of the unwrapped, de-trended phase residuals for point x, and the subscripts $_{HPTIME}$ and $_{LPSPACE}$ mean temporal high-pass and spatial low-pass filtering respectively. As with the linear case, the residuals $\alpha(x)_i$ are interpolated and smoothed using the kriging interpolator.

In this way, the iterative procedure of the linear method has been replaced with a network approach. Unfortunately phase residuals need to be unwrapped here, but this is made possible due to the temporal framework and the candidate PS points (i.e. points with low decorrelation noise). However this does require a stable reference point and all velocity estimates will be relative to this.

9.3 Non-Linear IAS 3-Pass Method

The Non-Linear IAS 3-Pass PSInSAR algorithm is based upon the Ferretti algorithm described above. An in-depth discussion of the algorithm follows. The early stages of the algorithm are as with the linear one. That is, the differential phase and candidate PS points are calculated as before (see chapter 5). Because a higher number of candidate PS points than needed are found, an algorithm to reduce the number of points is run. This step is required to optimise the algorithm so that needless data processing does not take place. The reduction algorithm is based upon an algorithm described in *Kampes and Nico (2003)*. A grid is placed over the interferogram and for each grid cell the 'best' of the PS candidate points from that grid cell is selected. The criterion for selecting the best point is based upon which candidate has the highest ratio of mean to standard deviation of amplitude values. Using an algorithm like this

reduces the number of candidate PS points but retains a uniform spread of points over the image.

The initial stage in the processing requires the construction of a network. This is done using a Delaunay triangulation (*Bern and Eppstein 1992; Delaunay 1934*) of the PS candidate points. The Delaunay triangulation (usually) results in a unique triangular network which maximises the minimum angle of all the angles of the triangles. An example of a Delaunay triangulation of a set of points is shown in Figure 9.2.
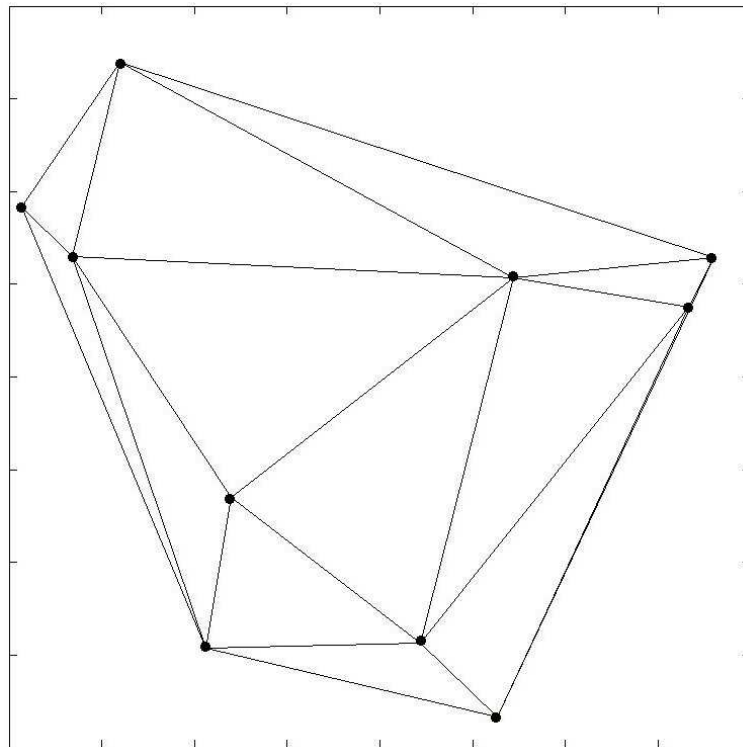
Figure 9.2 Example Delaunay triangulation. 10 points connected using a Delaunay Triangulation.

After creation of the network, an algorithm is run to remove any sides of the triangles which are greater than a certain length. This is because we are only interested in points which are close to each other, so that the difference in the phases reduces the effect of the atmospheric and orbital baseline phase errors.

Using the network the differential phase values of connected PS points are subtracted from each other. This reduces the effect of the spatially correlated phase error terms to leave, for each pair of PS points,

$$\Delta\partial\phi^i = \Delta\phi^i_{defo} + \Delta\phi^i_E + \Delta\phi^i_{atm} + \phi^i_n \qquad\qquad 9.3$$

where the orbital baseline errors have been coupled with the atmospheric phase errors for easier representation. Using the temporal stack of these values, an estimate for the $\Delta\phi^i_E$ term is made by using a periodogram technique. This is repeated for every connected pair of candidate PS points in the network and results in an estimate for the relative topographic phase error term for each pair. These are then unwrapped from a reference point using a least squares network adjustment model (see Appendix B) to get an estimate for ϕ^i_E, the topographic phase error term at the candidate PS points for each interferogram i. This is then removed from the candidate PS point's differential phase and the differences on the network are created again. This gives

$$\Delta\partial\phi^i_{adj} = \Delta\phi^i_{defo} + \Delta\phi^i_{atm} + \phi^i_n \qquad\qquad 9.4$$

where $\partial\phi^i_{adj}$ is the adjusted differential phase where $\Delta\phi^i_E$ is assumed to be 0. An equivalent procedure is now applied to the $\Delta\phi^i_{defo}$ term to get a mean linear velocity estimate at each of the candidate PS points. Removing this mean velocity estimate from the candidate PS points and recreating the differential phase differences on the network results in

$$\Delta\partial\phi^i_{adj} = \Delta\phi^i_{NL\_defo} + \Delta\phi^i_{atm} + \phi^i_n \qquad\qquad 9.5$$

where $\Delta\phi^i_{NL\_defo}$ is due to deformation that does not fit the linear model.

The values of $\Delta\partial\phi^i_{adj}$ should now be small and so the assumption that $\Delta\partial\phi^i_{adj} < \pi$ is likely to hold. The values of $\Delta\partial\phi^i_{adj}$ are integrated (unwrapped) on the network, from a stable reference point, using a least squares network adjustment technique, where the goodness-of-fit parameter for the linear velocity fit is used to weight the observations. This results in an estimate for the unwrapped atmospheric phase screen plus nonlinear deformation and noise for each of the candidate points.

Before the estimates are smoothed and interpolated to create an atmospheric phase screen for each interferogram, a filtering regime is applied to try and separate the nonlinear deformation term from the atmosphere term. As with the

Ferretti technique this consists of removing the temporal mean of each point and applying a low-pass filter up the stack to identify any nonlinear motion. Temporally, the nonlinear motion is assumed to be a low frequency, slowly varying term, whilst the atmosphere is assumed to be random with mean zero. Removing the estimated nonlinear term and adding the temporal mean back onto the stack results in the estimate for the atmospheric phase screen at the candidate points. This is then interpolated and smoothed using the kriging technique to get the APS for each of the full interferograms. The technique now follows as per the linear technique, by removing the APS from the interferograms and examining each pixel to identify PS points. This algorithm is summarised below in the flow diagram of Figure 9.3.

9.4 Simulated data

As with the Linear IAS 3-pass PSInSAR method this algorithm has been first tested using simulated data. The data used is the same as that described in chapter 7. There has been no non-linear deformation added to the data, as this test was to examine if the results were similar to those attained using the Linear method. The algorithms were implemented using a mixture of C++ programs and MATLAB scripts. Interferogram 7 has been used in this analysis as the topographic interferogram.

9.4.1 Network Creation

The first stage of the processing is to generate the network of candidate PS points. Starting from the original collection of candidate PS points (see Figure 7.11), this is reduced to a much smaller number of candidate PS points, but which is still of sufficient size to estimate the atmospheric phase screens. This modified candidate PS point network is shown below in Figure 9.4, where a grid size of approximately 100m by 100m has been used to reduce the network size. The candidate PS points are then 'connected' to neighbouring points via a Delaunay triangulation. The MATLAB Delaunay triangulation routine has been
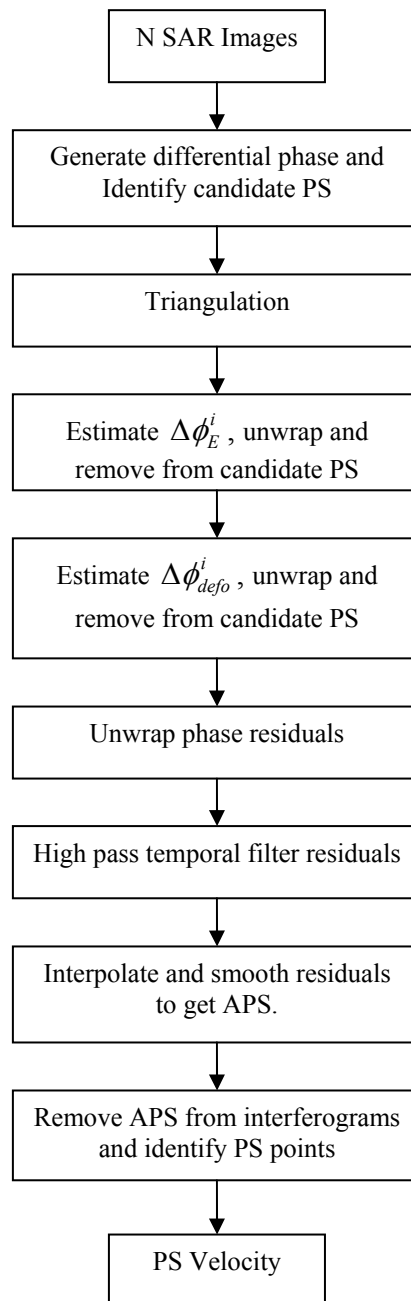
Figure 9.3 Flow diagram of the Non-Linear IAS 3-pass PSInSAR algorithm.

The flow diagram contains the following sequence of boxes connected by downward arrows:

1. N SAR Images
2. Generate differential phase and Identify candidate PS
3. Triangulation
4. Estimate $\Delta\phi_E^i$, unwrap and remove from candidate PS
5. Estimate $\Delta\phi_{defo}^i$, unwrap and remove from candidate PS
6. Unwrap phase residuals
7. High pass temporal filter residuals
8. Interpolate and smooth residuals to get APS.
9. Remove APS from interferograms and identify PS points
10. PS Velocity

Figure 9.4 Reduced network of candidate PS points. Compare to original one shown in Figure 7.11.

used to do this. A 2-dimensional array is created in MATLAB to store the indices of the candidate points for each respective pair that makes up the edges of the triangles. Then, any edges that are greater than a certain length are removed from the analysis. The length used as a cut off point was 900m, since it resulted in a good network with all points still connected in some way and is within the spatial distances of the atmosphere. This 'new' network is shown in Figure 9.5 along with the original network. The differential phase at connecting candidate points is differenced from each other to create the differential phase differences.
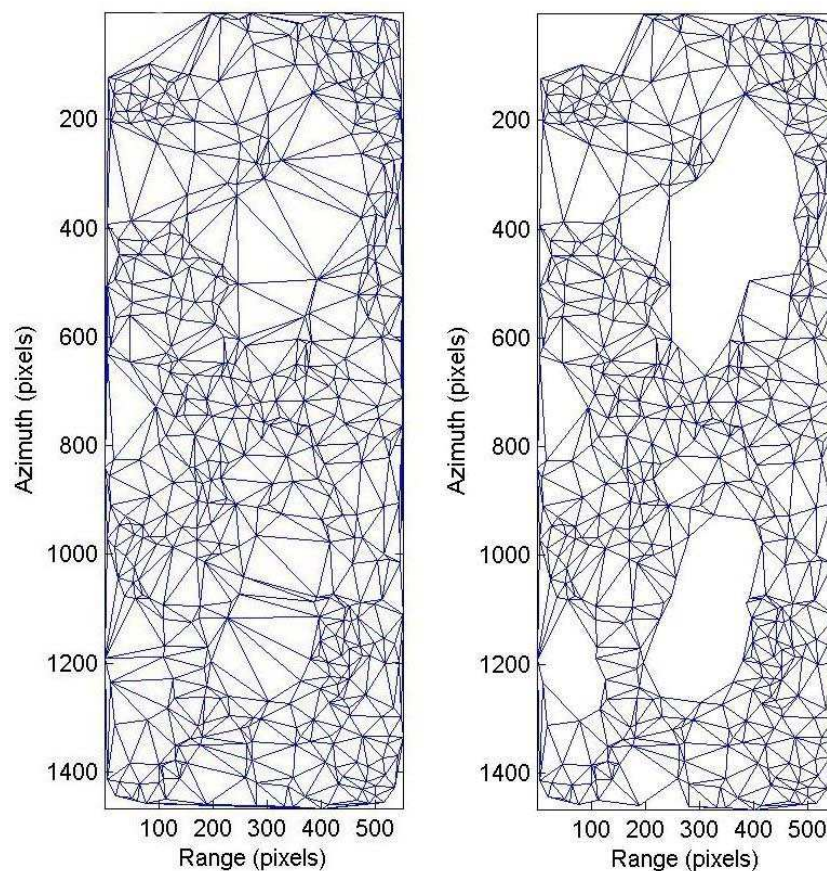
Figure 9.5 Simulation: Delaunay triangulation. Image on the left shows the original Delaunay triangulation of the reduced network. The image on the right shows the triangulation after the removal of lengths greater than 900m

9.4.2 Trend Modelling

Temporal trends due to the topographic phase error term and the linear (mean) velocity terms need to be removed from the differences. The magnitude of the

172

topographic phase error term dominates the velocity term and so is removed first. This is performed as with the Linear algorithm, by fitting a best estimate to the phase data. Figure 9.6 shows the differential phase differences of two candidate PS points plotted against the baseline ratio. The best fit to this data is shown as the straight line, the gradient of which gives the estimate for the relative topographic phase error.
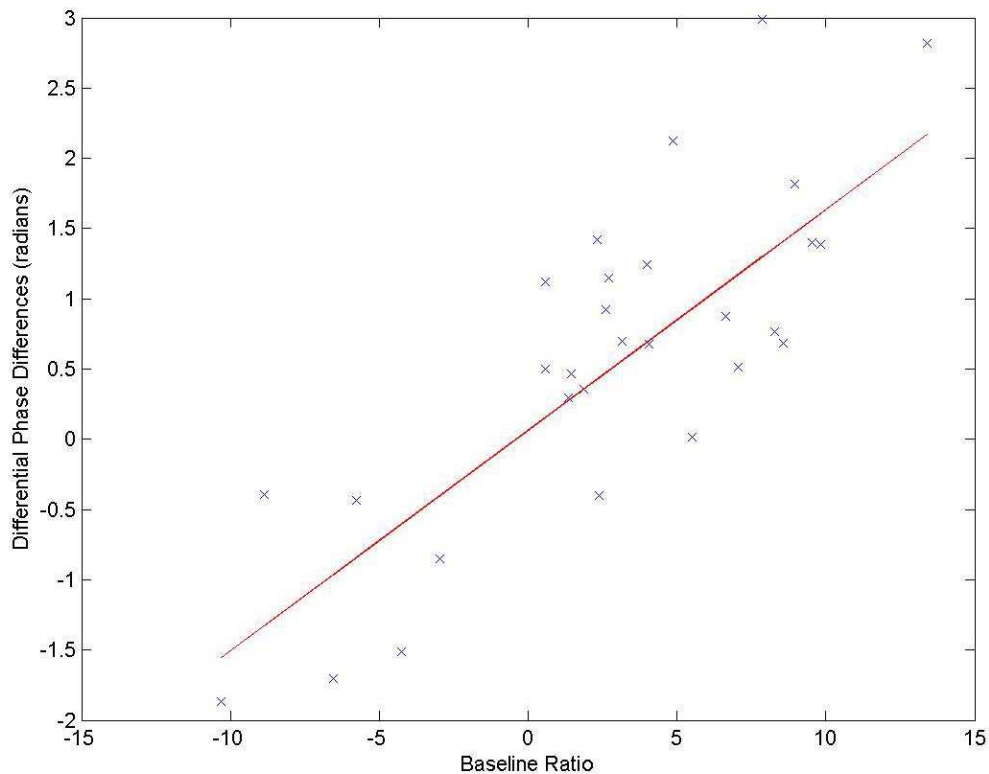
Figure 9.6 Simulation: Difference in differential phase (between two candidate PS points) vs. baseline ratio. The best (linear) fit is shown as the straight line, the gradient of which gives the estimate of the relative topographic phase error for these candidate points.

An estimate is derived for each 'edge' of the network and is then unwrapped from one of the candidate PS points, which is assumed to have a topographic phase error of 0. A simple least squares network adjustment model is used to achieve this, with the goodness-of-fit parameter of the estimates used as weights for the observations. This gives a value of the error at each candidate point rather than the relative value between points. If the true value at the reference candidate point is not 0 then an offset will be present which applies to each candidate point, but this is not important here since these values are not directly being used to correct the topographic interferogram. The estimated error of each

candidate point is removed from the original differential phase at these points and the differential phase differences on the network are recreated. With the dominating topographic phase error now removed, a similar approach is followed to remove any relative linear deformation terms. Figure 9.7 shows the temporal plot of the differential phase differences between two candidate PS points. The estimated linear velocity fit is shown as the straight line.
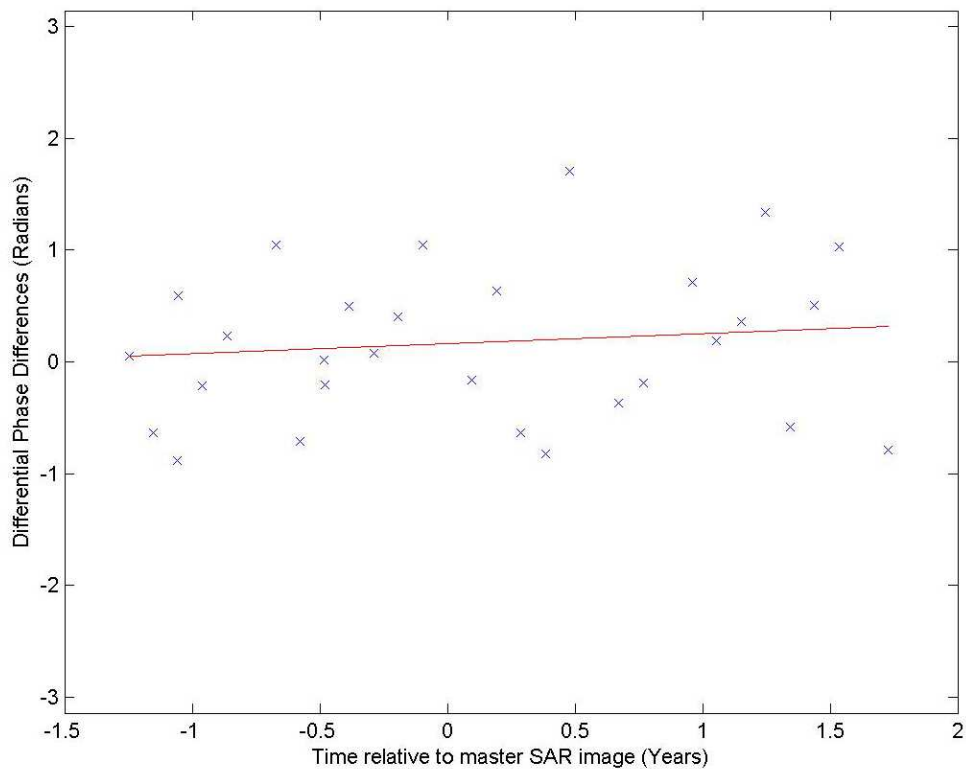
Figure 9.7 Simulation: Difference in differential phase (between two candidate PS points) vs. time. The straight line shows the estimated velocity fit to the data.

The relative velocities are unwrapped using the same technique as for the topographic phase error, resulting in an estimate for the velocity at each candidate point. The velocities are unwrapped from a point which is assumed to be stable. Here, a point outside the deformation zone was used. The phase due to these velocities is removed from the differential phases at the candidate points and the differential phase differences are recalculated again. The estimated velocity at each candidate PS point is shown below in Figure 9.8 as crosses together with the true velocity at the points, shown as circles. The error in the estimation is shown in Figure 9.9.

It can be seen that the errors in the velocity estimation are small, with all errors lying between ± 2mm/yr, having a mean of 0.1mm/yr and a standard deviation of 0.6mm/yr.
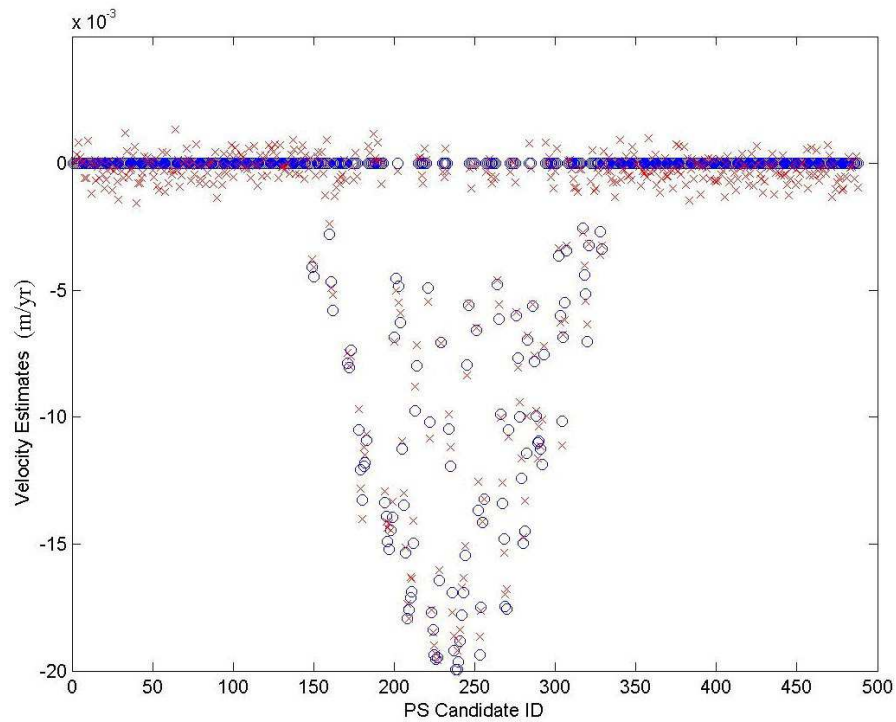
Figure 9.8 Simulation: Estimated velocities at candidate PS points. The estimated velocity (crosses) and true velocity (circles) at each candidate PS point in m/yr.
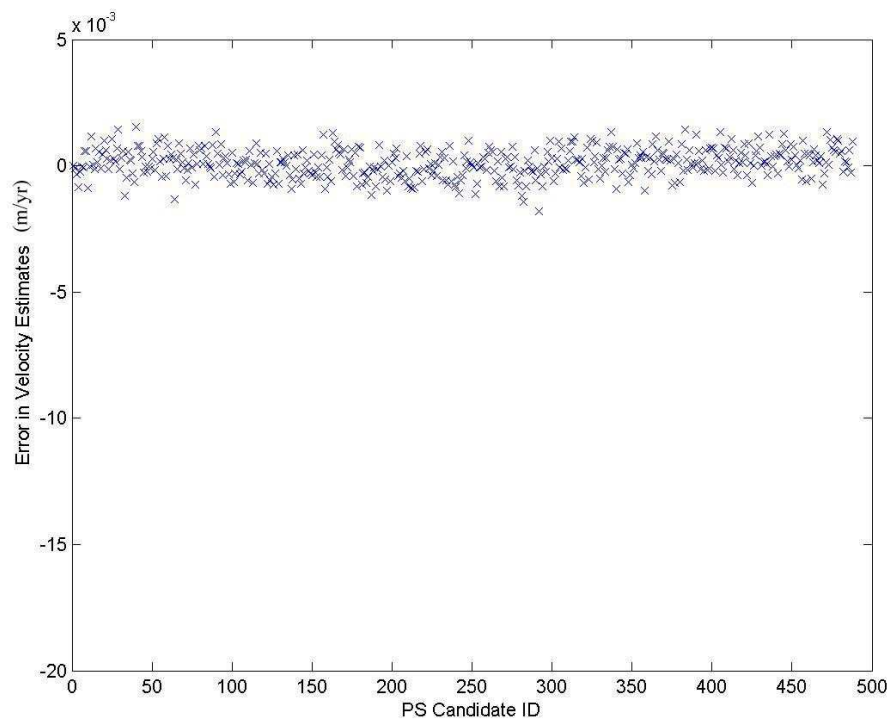
Figure 9.9 Simulation: Velocity error. Error between the estimated velocity and the true velocity at the candidate PS points.

9.4.3 Atmosphere and Nonlinear Deformation Separation

The differential phase differences are integrated (unwrapped) around the network to create the unwrapped atmospheric and nonlinear deformation phase. A least squares approach has been used with the velocity goodness-of-fit parameter used as weights for the differential phase differences. A low-pass temporal filter has then been used on the unwrapped phase values to identify any possible nonlinear motion. The filter used has been a simple triangular filter of length 350 days (which corresponds to approximately 10 samples). Tests with this filter and a rectangular filter of length 350 days on noisy data showed that the triangular filter was the better choice (see Appendix C). Three sets of data were used: a sinusoid with period 1 year, a parabola and a shear, all with a Gaussian random noise with standard deviation 1 radians added on. The triangular filter succeeded in attaining a good estimate of the sinusoid and parabola but failed on the shear, whilst the rectangular filter failed on both the sinusoid and shear. *Ferretti et al 2000a* use a triangular filter in their algorithm. Figure 9.10 shows the mean-zero unfiltered and filtered result for one of the candidate PS points. The filtered phase does show variations from the desired 0 radians that reflects the problem of using filters with short kernels; trends can be identified that do not exist in the data.
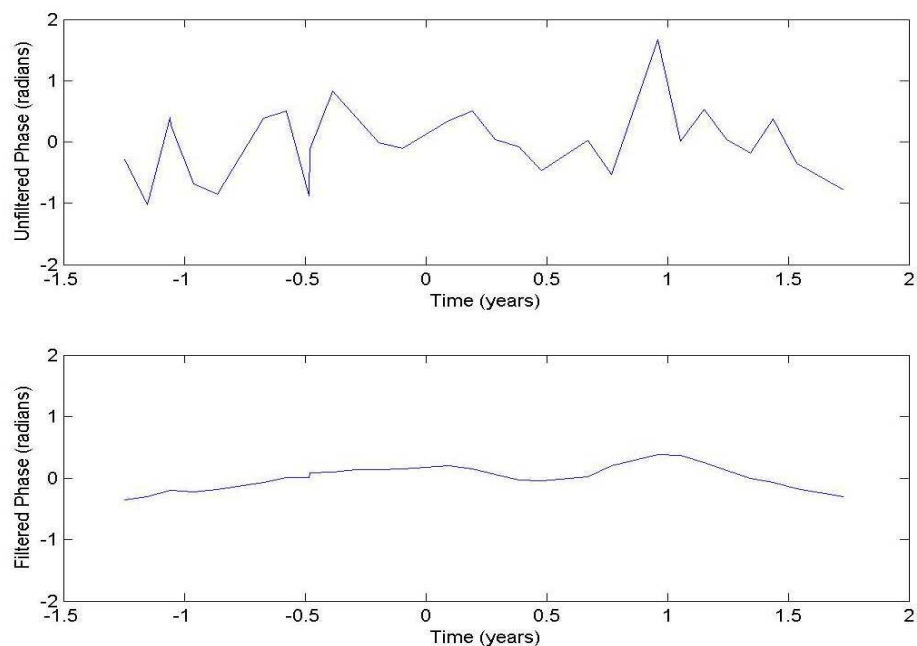
Figure 9.10 Simulation: Phase time series. Image on top shows the unfiltered time series of the unwrapped phase residues, whilst the image on the bottom shows the triangular filtered result.

The low-pass filtered result is removed from the time series to give the estimate for the atmospheric phase, which is then imported into the EasyKrig software for kriging and generation of the atmospheric phase screens. The kriged estimated APS are shown below in Figure 9.11 with the true APS of the simulated data shown in Figure 9.12, with both sets of figures using the same colour scale for comparison.
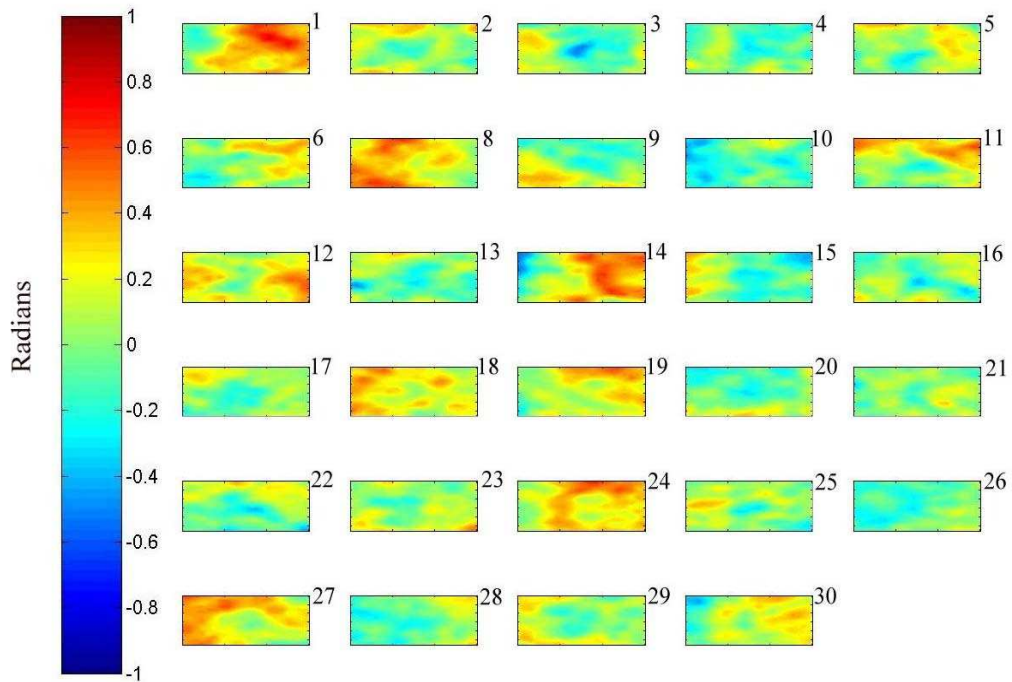
Figure 9.11 Simulation: Kriged APS for the 29 deformation interferograms.
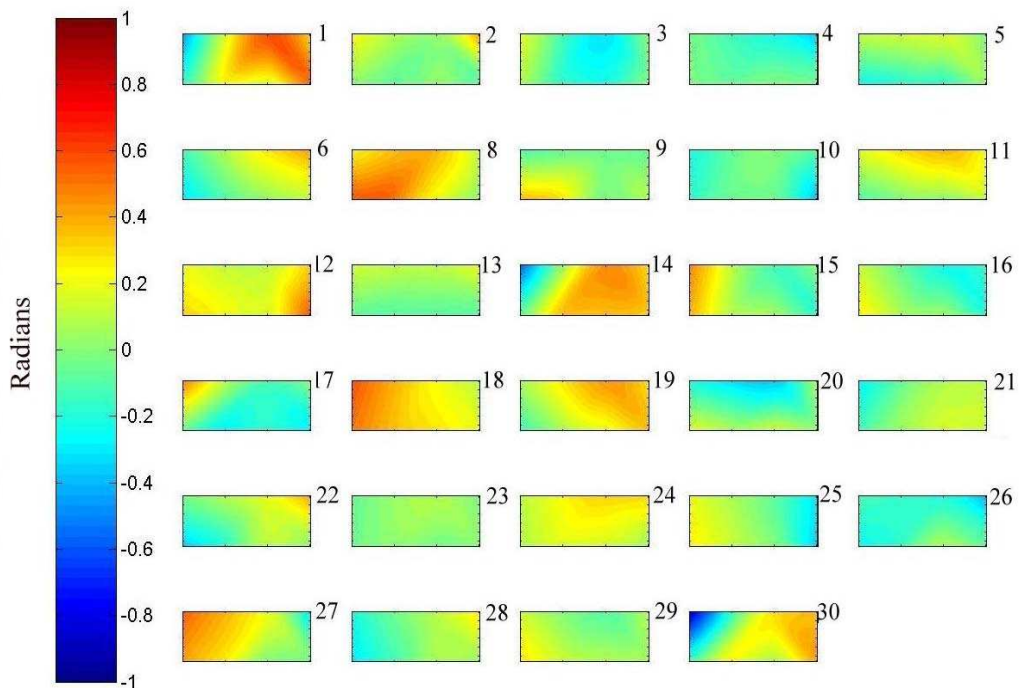
Figure 9.12 Simulation: True APS for the 29 deformation interferograms.

It can be seen that, qualitatively, the majority of the estimated APS show agreement with the true ones. Since the APS have been estimated from only 486 candidate PS points, it is expected that some deviations between true and estimated APS will occur. The true and estimated APS for interferogram 7 (the topographic interferogram) are shown below in Figure 9.13. It can be seen that this has not been estimated very well. This is likely due to the magnitude of the phase values been quite small (approximately 0 - 0.4 radians), and the topographic phase error estimation is more difficult with small magnitudes. Because a large deformation phase was present on the topographic interferogram, the magnitude of the topographic phase error at these points was larger and has been estimated well. Hence there is no deformation signal present on the estimated APS.
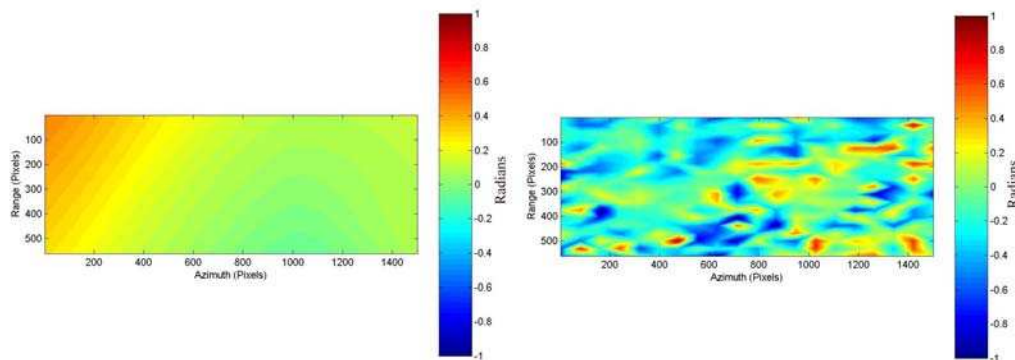
Figure 9.13 Simulation: APS for the topographic interferogram. Image on the left is the actual APS of interferogram 7, the image on the right is the estimated Kriged APS.

The atmospheric phase screens are removed from the interferograms and the differential phase is then recalculated before each pixel is examined to identify the persistent scatterers.

9.4.4 Results

As with the previous Linear Algorithm the ensemble phase coherence, γ, has been used as an indicator for selecting PS points. The value of 0.8 has been used here, with points with a value greater than this being selected as PS points. Again because of the rather simplified simulated data we get a large number of PS points selected; 95.8% of the interferogram pixels have $\gamma > 0.8$. Figure 9.14

shows the error between the estimated velocity and the true velocity for each interferogram pixel. The mean of the error at the PS points is 0mm/yr with a standard deviation of 0.5mm/yr.
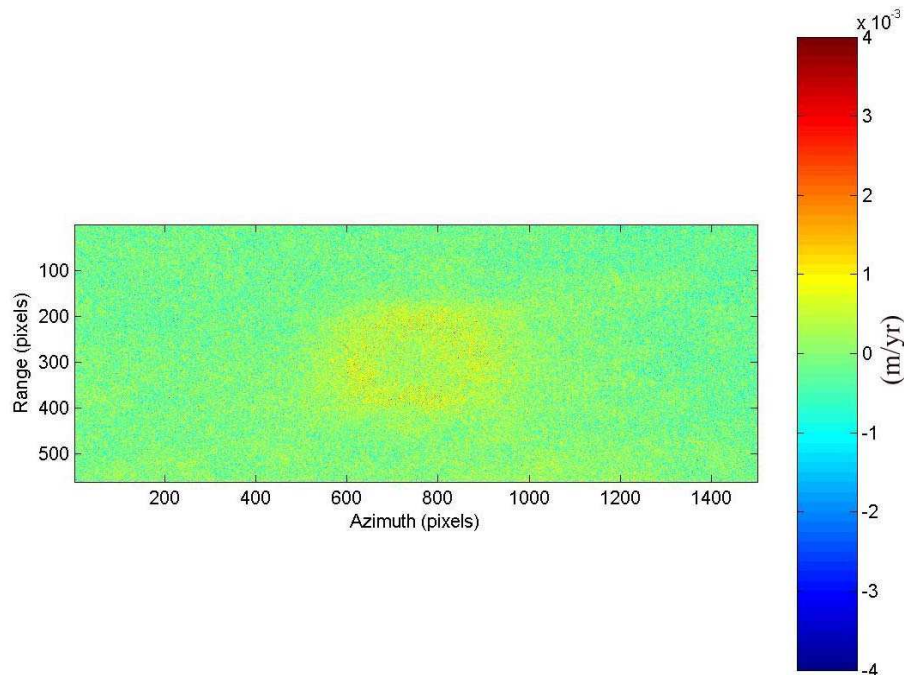
Figure 9.14 Simulation: Error in velocities. Error between the estimated and true velocities for every image pixel (including points which are not PS points). Errors have mean=0mm/yr and standard deviation=0.5mm/yr.

As before, it can be seen that the errors appear larger in the deformation zone where the discontinuities in the phase wrapping occur. Figure 9.15 shows the time series for the same two PS points used in the Linear Algorithm analysis. The point in the deformation zone gives a velocity of -20mm/yr and the point outside the deformation zone gives a velocity of -0.4mm/yr.

The results appear good; PS points have been identified and the error in the velocities is small. The estimated atmospheric phase screens, on the whole, look similar to their true phase screens. The final results are similar to those attained using the linear method albeit that here the Non-Linear Algorithm has identified an extra 4% of the interferogram pixels as PS points.

179
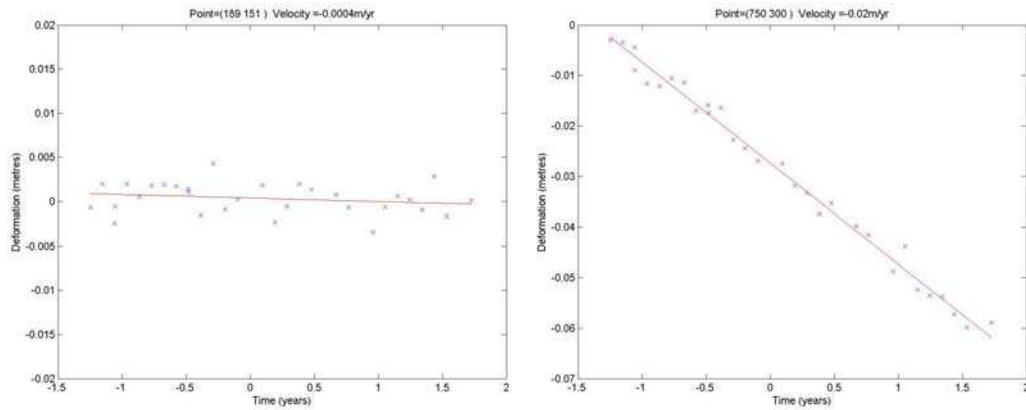
Figure 9.15 Simulation: PS point time series. The image on the left shows the time series for a PS point outside the deformation zone and the image on the right shows the time series for a PS point in the deformation zone. The points are the same as the ones used in the linear analysis.

9.5 Real Data

The same two test sites as for the previous Linear Algorithm have been used to test this algorithm's performance with real data. The same set of SAR data and interferograms have also been used.

9.5.1 Greenwich

The first stage of the processing was to generate the network of candidate PS points. This is shown below in Figure 9.16, where the value of 900m was used as a cut-off point for the lengths of the network edges. This value of 900m was used because it is short enough for the two end points' atmospheric phase component to be spatially correlated, and long enough for all the points of the network to be connected to another.

The differential phase on the network was then differenced along each edge and, using the temporal stack of differences, any relative topographic phase error is estimated, unwrapped and removed from the points. Since all points are equally likely to have no topographic phase error term, a point near the top left corner of the image was used as a reference for the unwrapping. Recall an initial topographic phase error is removed from all points when the differential phase is

first generated, and so the residual topographic phase should be small at the points.
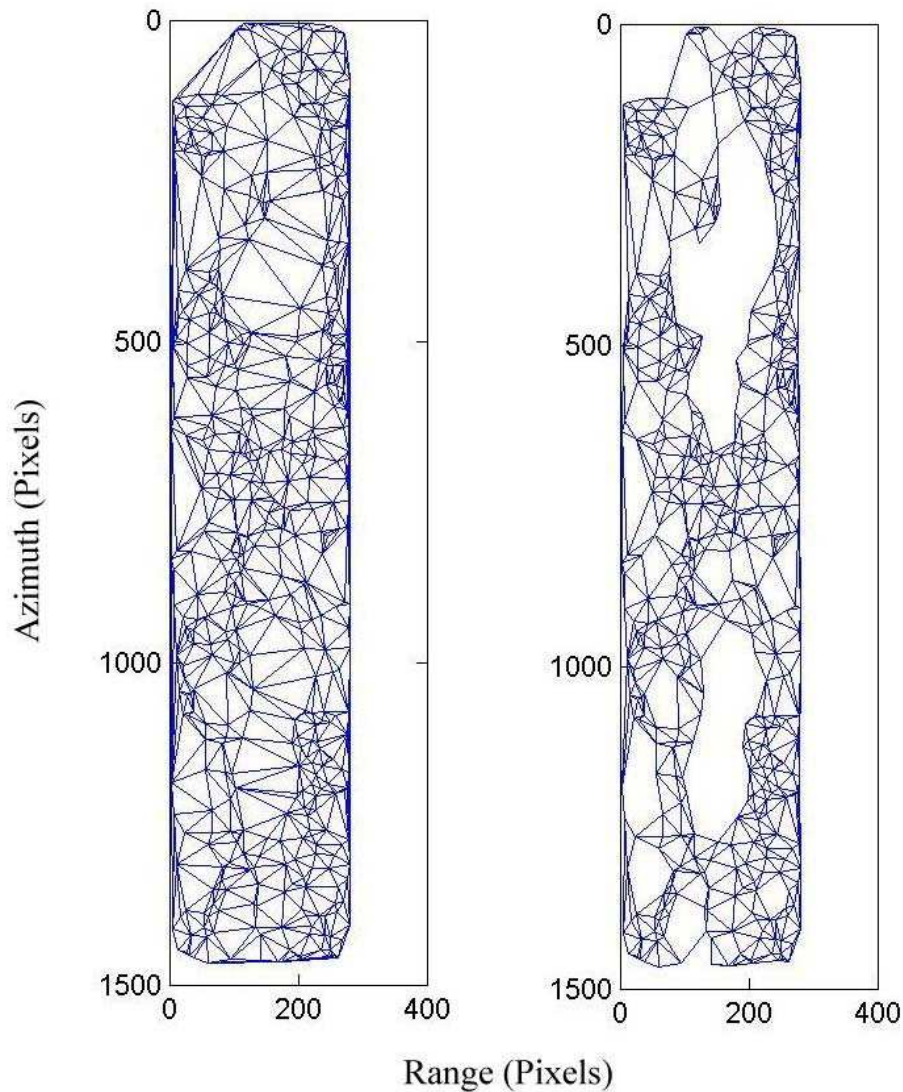
Figure 9.16 Greenwich: Delaunay triangulation (of the network of candidate PS points). Image on the left shows the original Delaunay triangulation whilst the image on the right shows the triangulation after removing lengths of greater than 900m.

9.5.1.1 Data Set 1 – Reference Point (14,101)

After the removal of the topographic phase error, the stack of differential phase differences was examined for any relative velocity components. These were then unwrapped from a reference point. The reference point should be known to be stable. Ideally it would have known ground truth available at that point, such that is available from GPS collocated with a corner reflector (to give a bright radar return). Since this is not available in this test site, the reference point

181

selected here is at the top centre of the image in Figure 9.16 at coordinates (14, 101). This has been selected because it is the first point algorithmically (closest to 0, 0), which simplifies the implemented unwrapping algorithm. Section 9.5.1.2 shows results when a point has been selected based upon the linear results of chapter 8. If the reference point is not stable then any deformation errors will be propagated through onto every point. For example, if the stable point is in fact subsiding at 5mm/yr, then this velocity will be added onto all the others as an offset, giving the impression that the whole region is moving. The unwrapped velocities are shown below in Figure 9.17. The unwrapped velocities appear to show a slight negative bias, which suggests that maybe the point used as the reference point is not stable. But this could also be errors that have propagated along the network whilst unwrapping. The least squares unwrapping technique employed here is very simple and prone to unwrapping errors, which will increase further from the reference point.

The phase due to the velocity at each candidate PS point is removed and the stack of differential phase differences is regenerated. These are then unwrapped (from the same reference point as the velocities) to give an estimate for the atmospheric phase noise and deformation that does not match the linear model. The temporal mean value at each point has been calculated and removed from the stack of data so that it has mean zero at each point. The stack of data has been filtered using a Triangular filter with kernel length 350 days to get the low frequency component of the phase residuals, and then the filtered data has been removed from the stack of data (equivalent to a high pass filter).

The temporal means have then been added back onto the stack of data to result in the estimates for the atmospheric phase screen (plus decorrelation noise) at each PS candidate point. As before, these have been interpolated using the EasyKrig software to result in an APS for each of the deformation interferograms. These APSs are shown below in Figure 9.18. It can be seen that all the APS contain similar shapes/structures, which could mean that the image selected as the master SAR image has a strong dominant atmospheric effect. But this could also be due to some uncompensated error source that has
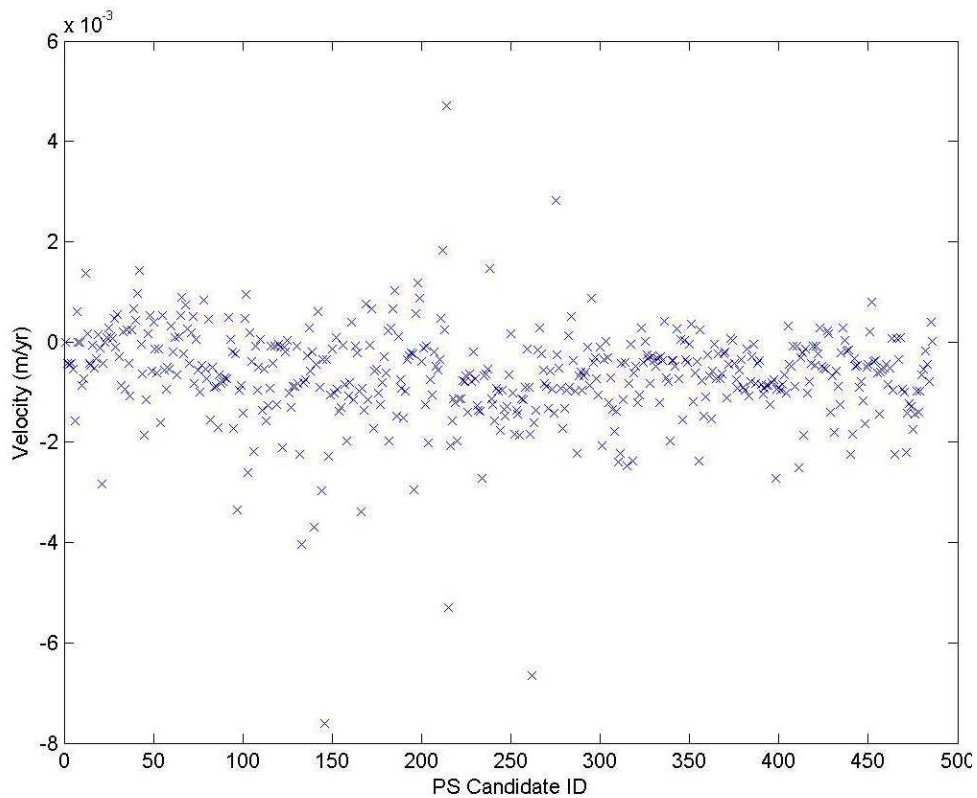
Figure 9.17 Greenwich: Unwrapped velocities (at the candidate PS points). The velocities have been unwrapped from a point which has been assumed stable.

propagated through into the atmospheric phase screens. It is interesting to note that the APSs below do not all agree with those from the Linear analysis of chapter 8. Comparing Figures 8.4 and 9.18 it can be seen that, qualitatively, the APS agree well for interferograms 13, 14, 27, 29 and 30 only. Others such as 4, 12 and 28 appear to show some resemblance in their structures though not in their phase values.

As before, the topographic interferogram atmospheric phase error estimates have also been smoothed and interpolated to create an APS. This is shown below in Figure 9.19. It too shows the same shape/structure that appears in the APSs in Figure 9.18. It also appears similar to the topographic APS derived from the Linear algorithm (Figure 8.4b).
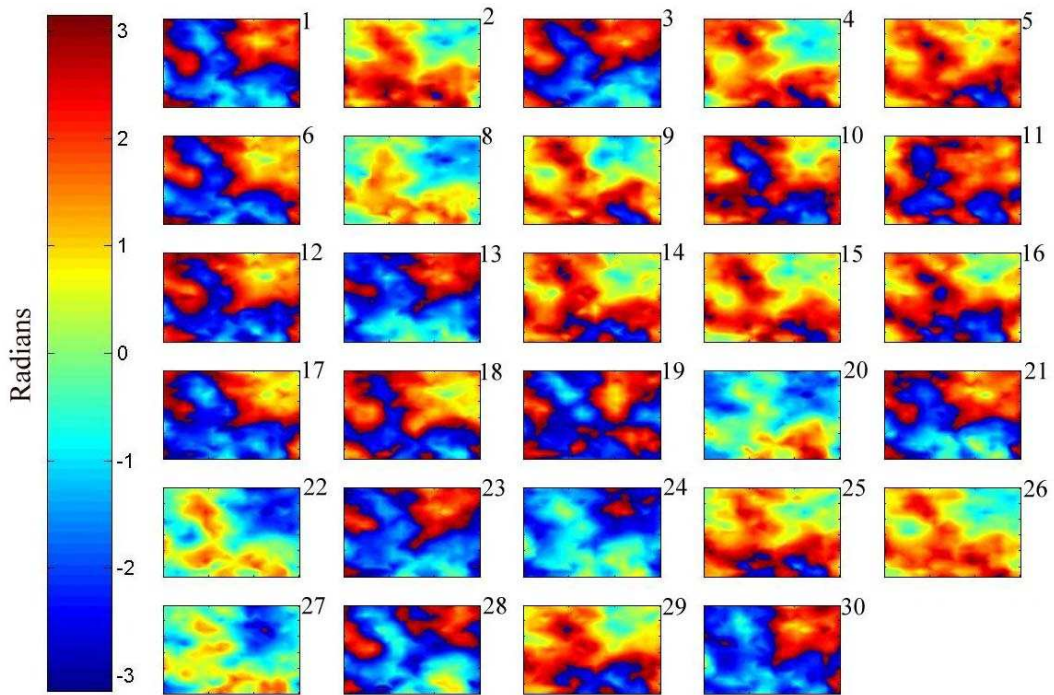
Figure 9.18 Greenwich: Wrapped Atmospheric Phase Screens for the 29 deformation interferograms. Interferogram 7 is the topographic interferogram and not shown here.
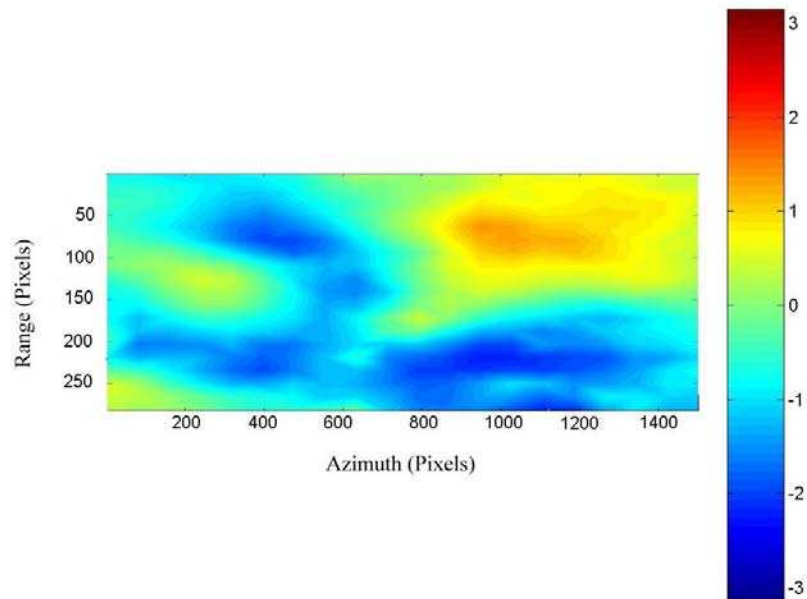
Figure 9.19 Greenwich: Wrapped Atmospheric Phase Screen for the topographic interferogram (interferogram 7).

The APSs have been removed from the interferograms and the differential phase has been recreated. The same analysis as for the Linear Algorithm takes place for each pixel to determine whether it is a PS point or not, i.e. the temporal data is fit to a linear model. The value of the ensemble coherence used for the

identification process was 0.7. A value of 0.8 was initially used but only a few PS points were identified, so the threshold value was lowered. This could suggest that the constant mean linear velocity model that has been used to identify the points is not suitable here. For example, if seasonal deformation is expected it might be more appropriate to use a sinusoidal velocity model to identify the PS points (*Colesanti et al 2003b*). But the higher noise level (i.e. lower ensemble coherence values) could also be attributed to errors that could have occurred in the processing, such as in the atmospheric phase estimation or unwrapping stages.

Figure 9.20 below shows the results of this analysis, with the PS points overlaid upon the mean amplitude image. It can be seen that, as before, there are a large number of green PS points but this time there are also many red points; these have a velocity greater than 2mm/yr. There are also a few blue PS points, with velocities of less than -2mm/yr, whose coverage appears to be random except for a cluster in the central northern part of the image. Table 9.1 shows the persistent scatterer classification information. 7,053 PS points have been identified, which corresponds to 1.7% of the number of image pixels. Of these points, over 75% of them show no significant motion (green PS points). Out of the 1,506 red PS points, only 140 show a velocity greater than 3mm/yr; from the 140 blue PS points, 42 show velocities less than -3mm/yr. Because the ensemble coherence threshold has been lowered to 0.7 we have less confidence in the results than we would have if the threshold was higher. Therefore it might be suitable to change the bounds of the PS classification and use a value closer to $\pm$ 3mm/yr to represent points with no significant motion. The image of Figure 9.21 shows the results when using classification 2 from Table 9.1.

| Classification 1			Classification 2		
				V>3	140
Number of PS Points with	V>2	1506	Number of PS Points with	2<V≤3	1366
	1<V≤2	2434		1<V≤2	2434
	0<V≤1	1925		0<V≤1	1925
	-1<V≤0	867		-1<V≤0	867
	-2<V≤-1	181		-2<V≤-1	181
	V≤-2	140		-3<V≤-2	98
				V≤-3	42
	Total	7053		Total	7053

Table 9.1 Greenwich: Classification of PS points for velocity maps 1 and 2.
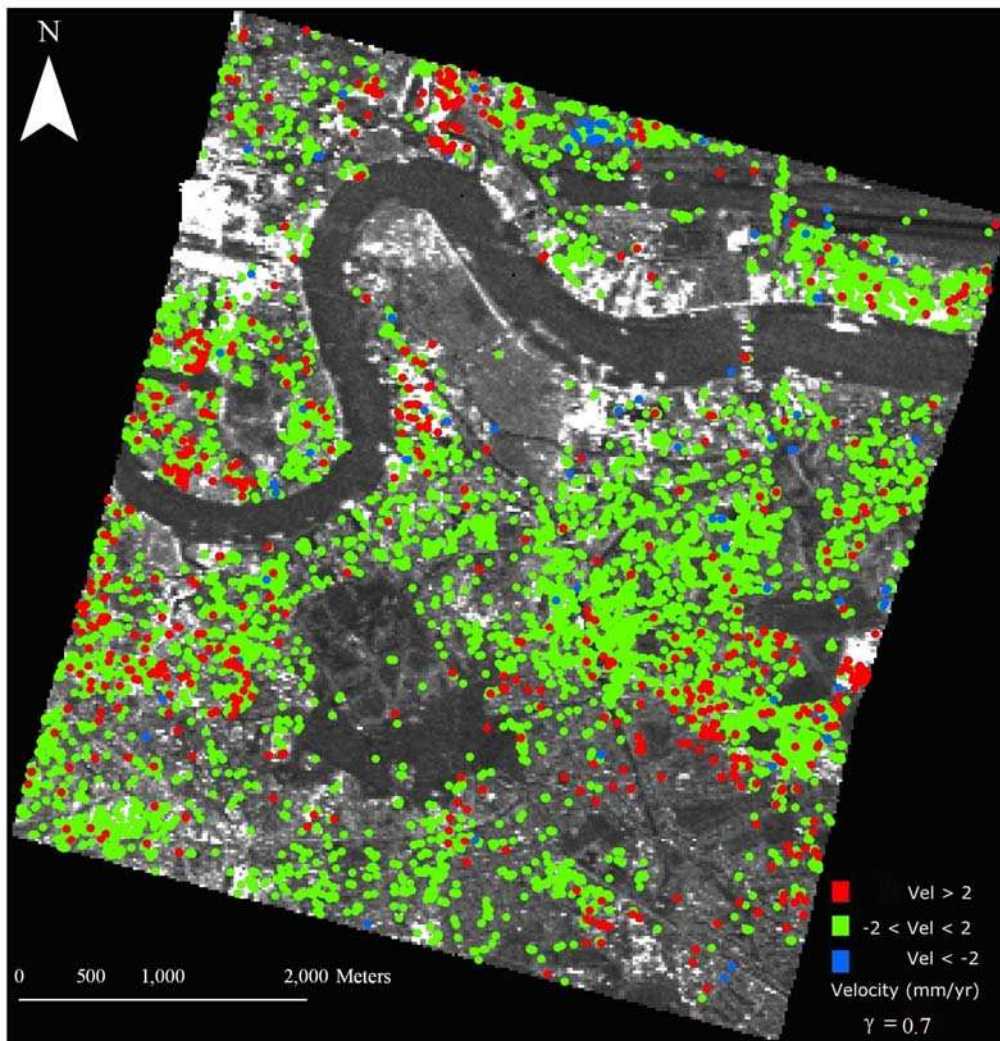
Figure 9.20 Greenwich: Velocity map 1. PS points overlaid upon the mean amplitude image, geocoded to a UTM zone 31 grid. The colour of the PS points represents the proposed linear mean velocity using classification 1 from Table 9.1.

It can be seen that this gives an image which is more in agreement with the results of the Linear analysis, i.e. the majority of the points showing no significant motion. It is interesting to note that the two methods identify different points as persistent scatterers. The Non-Linear method is identifying more points (almost an extra 25%) but at a lower ensemble phase coherence value, and appears to give an approximate uniform coverage (excluding the river and park land), whilst the Linear method appears to give points in concentrated areas, and very few north of the river. The 'straight line' feature of points from Figure 8.9 is not identified in the Non-Linear method, but the Non-Linear method does pick-up points in Greenwich Park and on the Thames Barrier. But

186
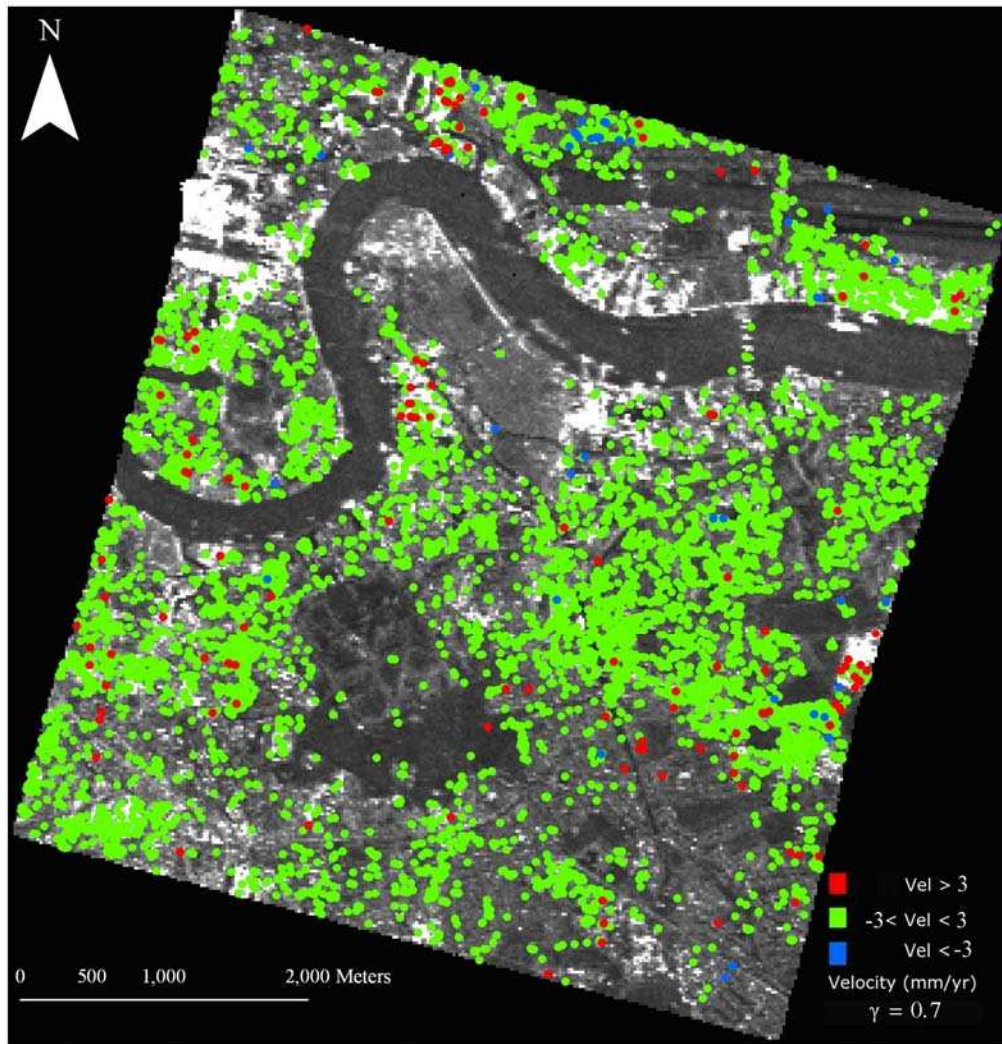
Figure 9.21 Greenwich: Velocity map 2. PS results of Figure 9.20 shown using the new
classification boundaries, classification 2 from Table 9.1.

it should be emphasised that although the results show more points have been
selected covering more areas with the Non-Linear method, the value of the
ensemble coherence is lower and hence there is less confidence in the results.

9.5.1.2 Data Set 2 – Reference Point (154, 8)

The above analysis has been repeated but with selecting a different PS point as
the reference for phase unwrapping. In this analysis a point was selected from
the results of section 8.3 which showed a mean velocity of 0mm per year, and
which also appeared as a candidate PS point in the nonlinear analysis. This
point was then considered stable and used as the reference point. The PS point

used has row and column location (154, 8). All of the above processing was identical apart from this one change. The final results from this analysis are shown below in Figure 9.22 and Table 9.2. It can be seen that these results differ greatly from those attained in the above analysis of section 9.5.1.1. The most striking difference is that far more PS points have been identified; 21,260 compared to the 7,053 for the previous analysis, with PS points occurring in most regions of the image. The majority of the PS points are showing no significant motion, with approximately 2.5% of the points showing a velocity less than 3mm/yr. The reason for why there is such an increase in PS points between the two is unclear. An examination of the time series for some points may help. Four plots are shown in Figure 9.23 below; each plot represents a time series of a PS point from data set 1. The points have been selected at random but such that they are not located near each other. The first thing to note about these graphs is that the points all appear to have a similar overall shape or signature. This appears to be due to the temporal filtering stage which occurs just after the unwrapping stage. All the PS points appear to have a similar shape after the filtering. This could be due to effects that are occurring at the reference point, i.e. deformation, or more likely, it could be edge effects of the filtering due to a small number of observations; 30 observations using a filter with window length 350 days (approx. 10 data points). But this could be the reason as to why using the 2nd data set reference point we identify many more PS points. Since we use a straight line fit to identify PS points, if the time series deviates largely from a linear straight line then the PS identification will fail.

Number of PS Points with	V>3	18
	2<V≤3	114
	1<V≤2	359
	0<V≤1	1938
	-1<V≤0	10639
	-2<V≤-1	5383
	-3<V≤-2	2282
	V≤-3	527
	Total	21260

Table 9.2 Greenwich: Classification of PS points for velocity map 3.
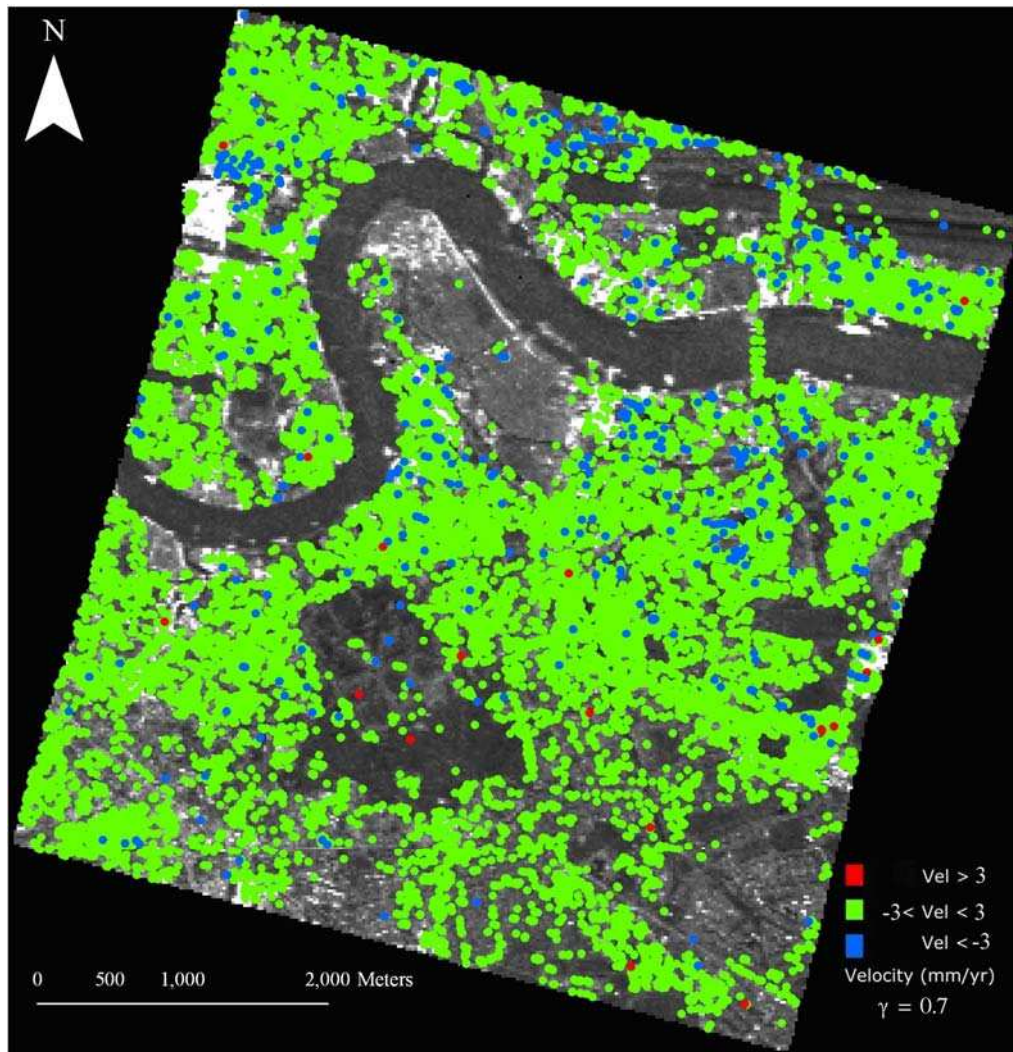
Figure 9.22 Greenwich: Velocity map 3. Results of the analysis using candidate PS (154, 8) as the reference point for the phase unwrapping.

The triangular filter that has been used to low-pass filter the phase has been tested on 2 sets of randomly generated data with mean 0 and standard deviation 1. The unfiltered and filtered results are shown in Figure 9.24. It can be seen that these random time series generate a nonlinear signature in the filtered result. It is proposed that the filter is creating these effects due to the number of observations and the size and shape of the kernel used. The Slutsky Effect (*Slutsky 1927; Kedem 1984*) also suggests that filtering and differencing on time series can give rise to sinusoidal-like effects due to the expected number of crossings on the axis.
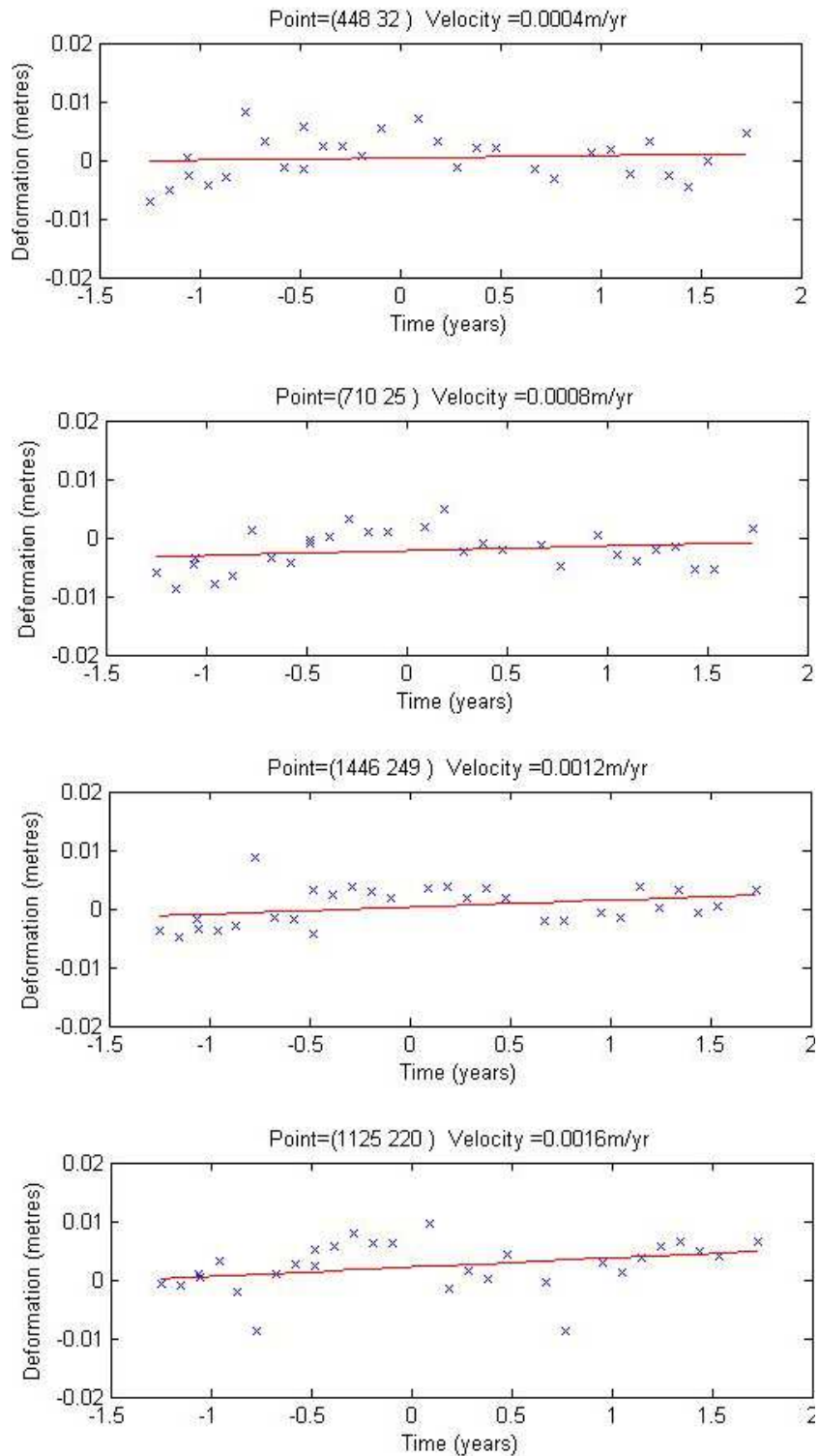
Figure 9.23 Greenwich: Time series plots for four PS points (in data set 1). The points have been randomly selected but such that they are not nearby each other. Each plot shows a similar shape as the others suggesting that there might be a bias in the data. The ensemble phase coherence values of the points are 0.707, 0.776, 0.803 and 0.713 respectively.
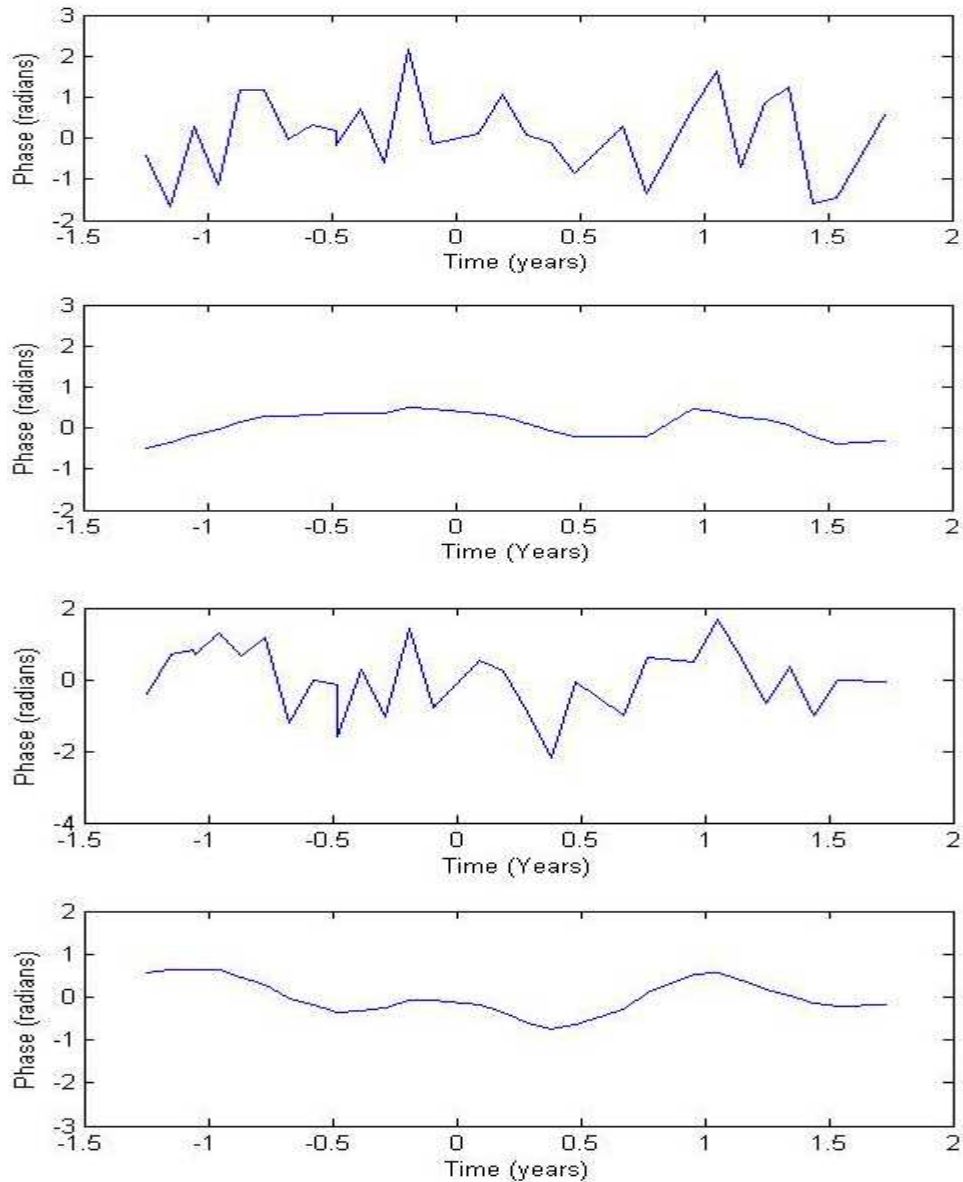
Figure 9.24 Greenwich: Filtered results. Random noise time series' and their triangular low-pass filtered results.

The reference points used for unwrapping are assumed stable. Therefore any signature at these points from the temporal filtering is considered to be due to the effects described above, and should be removed so that the assumption of stability holds. The filtered time series of the reference point of data set 1, as shown in Figure 9.25, has been removed from every point prior to PS identification. Note how the shape of this filtered signature follows a similar shape to the time series of Figure 9.23. After removing this, the PS points identified are shown in Figure 9.26 together with Table 9.3. This clearly shows that more PS points have been identified.
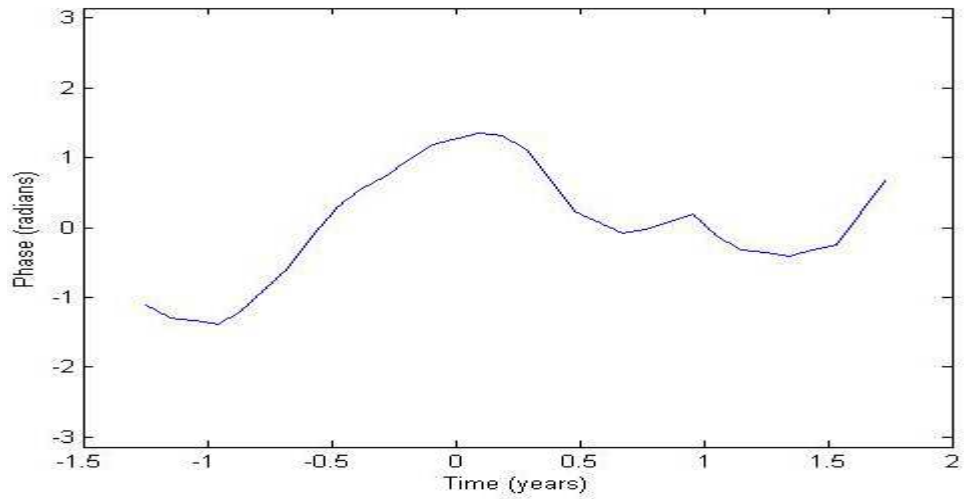
Figure 9.25 Greenwich: Low-pass filtered phase time series of the reference point. This has been removed from every interferogram pixel before identification of PS points.
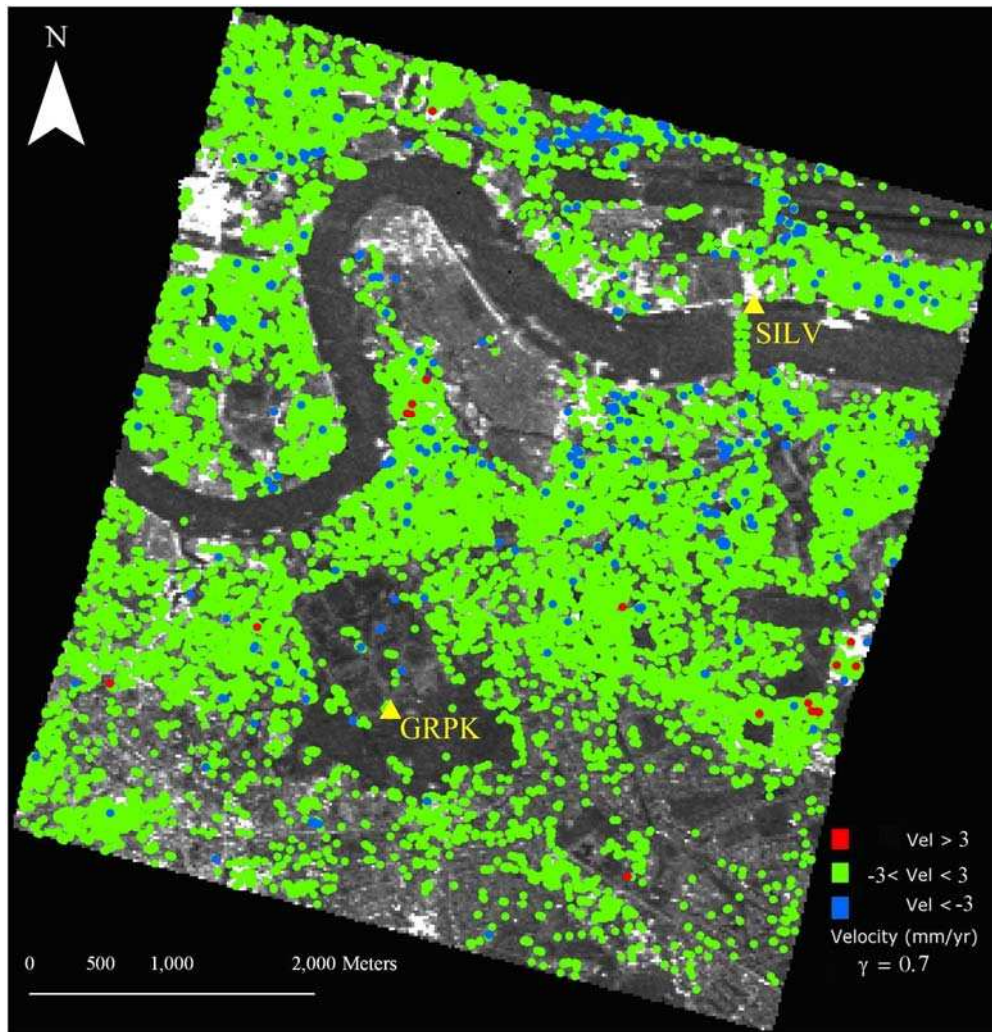
Figure 9.26 Greenwich: Velocity map 4. PS points of data set 1 identified after removal of the reference point post-filtering signature.

Number of PS Points with	V>3	18
	2<V≤3	127
	1<V≤2	792
	0<V≤1	3233
	-1<V≤0	10024
	-2<V≤-1	3513
	-3<V≤-2	1457
	V≤-3	390
	Total	19554

Table 9.3 Greenwich: Classification of PS points for velocity map 4.

Recall the 2 GPS stations GRPK and SILV that were shown in chapter 8. They exhibited no significant motion over the time period of the study. Their locations are shown in Figure 9.26 as the two labelled triangles. Examining their time series together with those of nearby persistent scatterers, as in Figure 9.27 below, shows that the PS results agree with what the GPS suggests, i.e. that no significant motion is occurring. The deformation of the PS points in the study is relative to the stable reference PS point as was discussed above, whilst the GPS results have been plotted relative to their mean deformation.
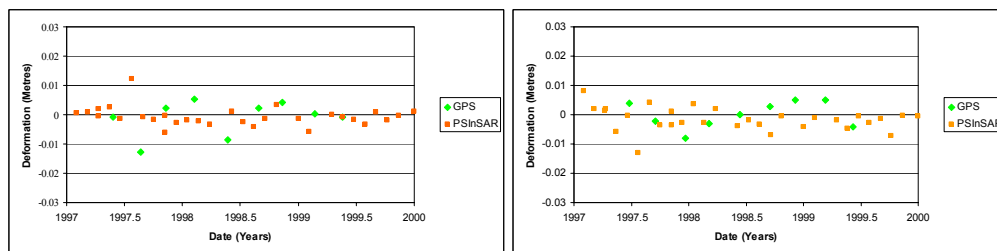
Figure 9.27 Greenwich: Comparison of GPS and PS point time series. The time series of the GPS stations plotted together with the time series of a nearby PS point. The image on the left relates to the SILV GPS station whilst the image on the right relates to the GRPK GPS station. The data suggests that there is no significant motion occurring at the sites.

9.5.2 Westminster

The same analysis as in section 9.5.1 has been applied to test site 2, the Westminster area. The network of candidate PS points used in the analysis is shown below in Figure 9.28. The image on the left is the original network whilst the image on the right shows the network with edges greater than 900m removed.
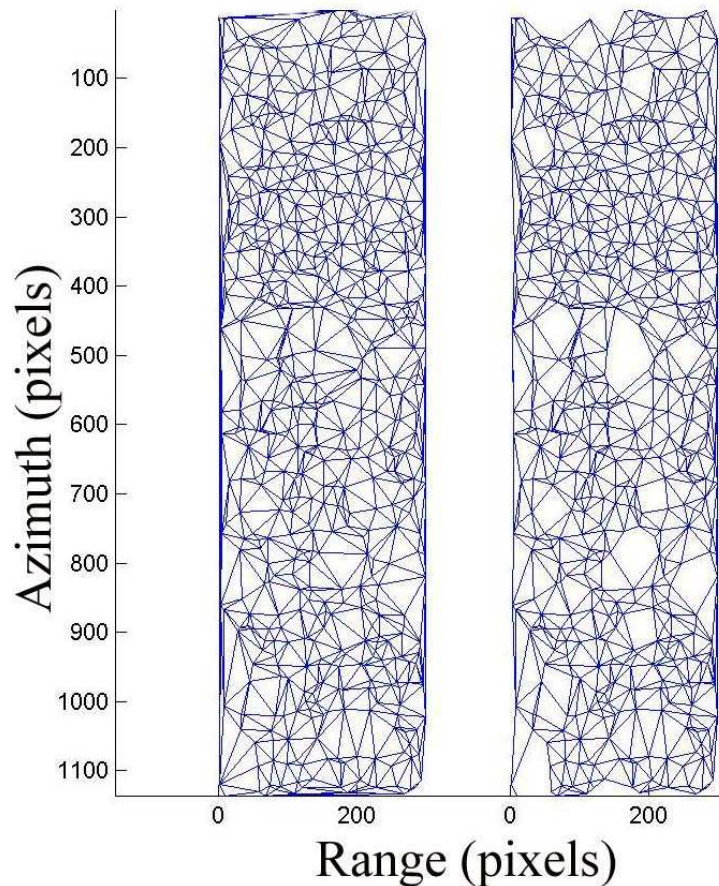
Figure 9.28 Westminster: Delaunay triangulation. The network of candidate PS points used in the analysis. The image on the left shows the original network. The image on the right shows the same network with edges greater than 900m removed.

The phase unwrapping has been done using reference point (11, 1) which is the first point algorithmically. The unwrapped velocities are shown in Figure 9.29 below. The majority of the points show velocities of between ± 2mm/year, but there are also a few points showing velocities of around -4 and -6 mm/year.

As with the Greenwich test site, the APS have been generated next and are shown in Figure 9.30a. Again it can be seen that some of the APSs agree with those of the Linear Algorithm shown in Figure 8.16, but some of them differ significantly. The APS of interferograms 3, 4, 6, 8, 10, 12, 13, 14, 19, 21, 23, 28, 29 and 30 all agree well with the Linear Algorithm's APSs, with some of the

194
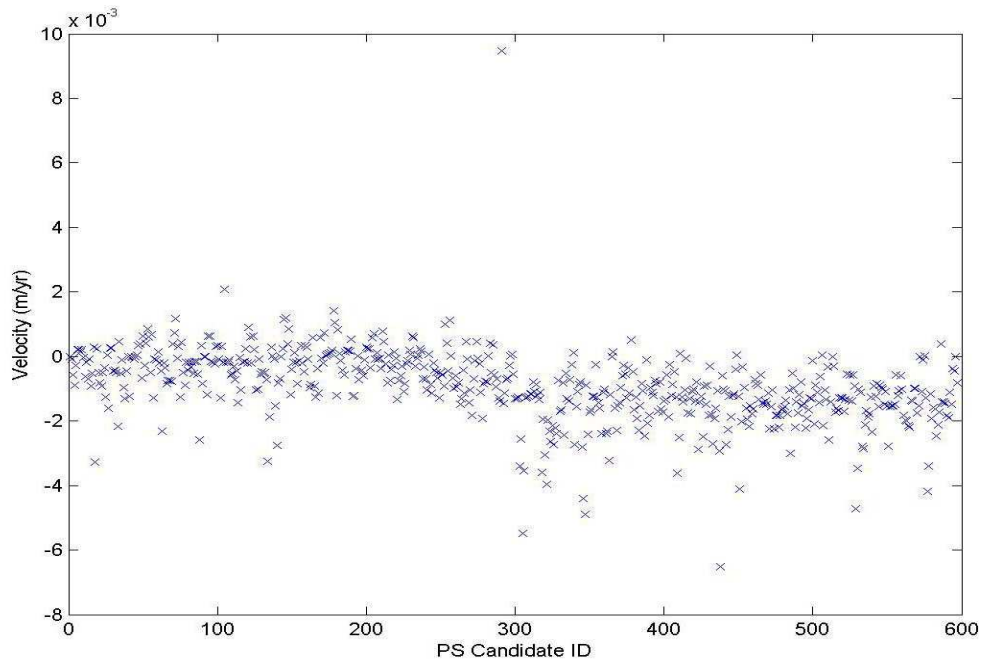
Figure 9.29 Westminster: Unwrapped velocities (of the candidate PS points, unwrapped from point (11, 1))

other APSs agreeing to some extent. This is noticeably more than agreed between the Linear and Non-linear Greenwich park test sites. Without additional data of the atmosphere it is impossible to say which atmospheres between the Linear and Non-Linear algorithms are most accurate. The topographic interferogram APS is shown in Figure 9.30b. It appears similar to the APS from the Linear algorithm (Figure 8.16b).

The APSs have been removed from the interferogram data and PS points have been identified as before; using a linear mean velocity fit and this time an ensemble phase coherence of 0.8. The results are shown in Figure 9.31 overlaid upon the mean amplitude image of the test site. The PS classification information is shown in Table 9.4.
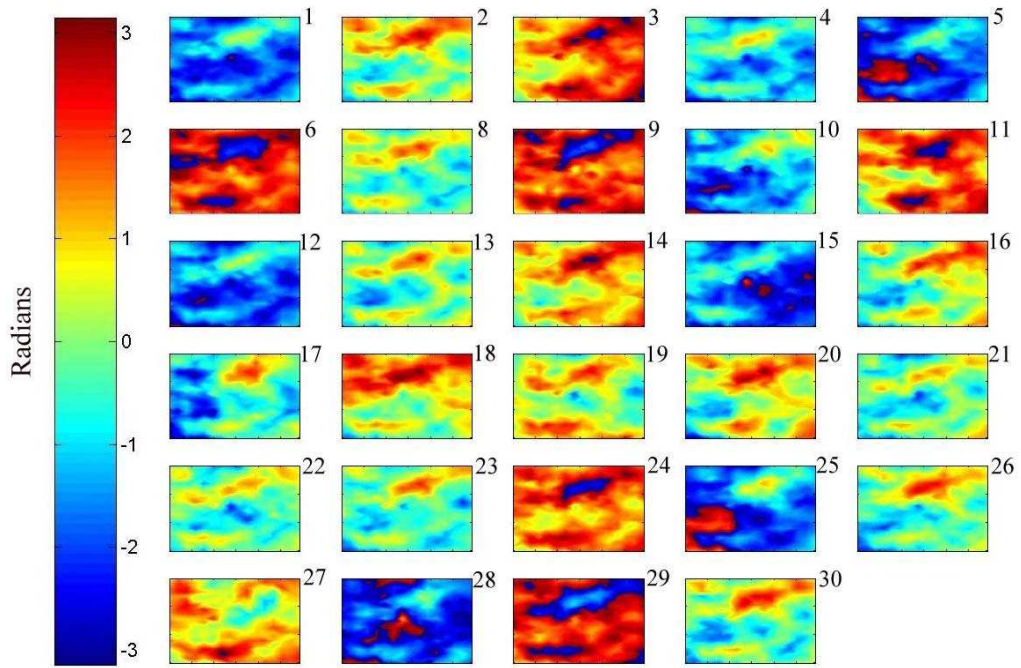
Figure 9.30a Westminster: Wrapped Atmospheric Phase Screens for the 29 deformation interferograms.
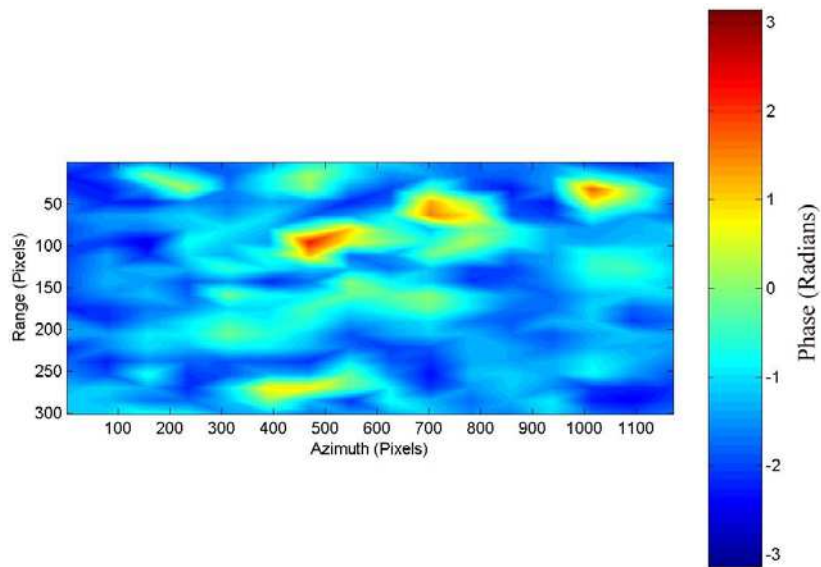
Figure 9.30b Westminster: Wrapped Atmospheric Phase Screen for the topographic interferogram (interferogram 7).
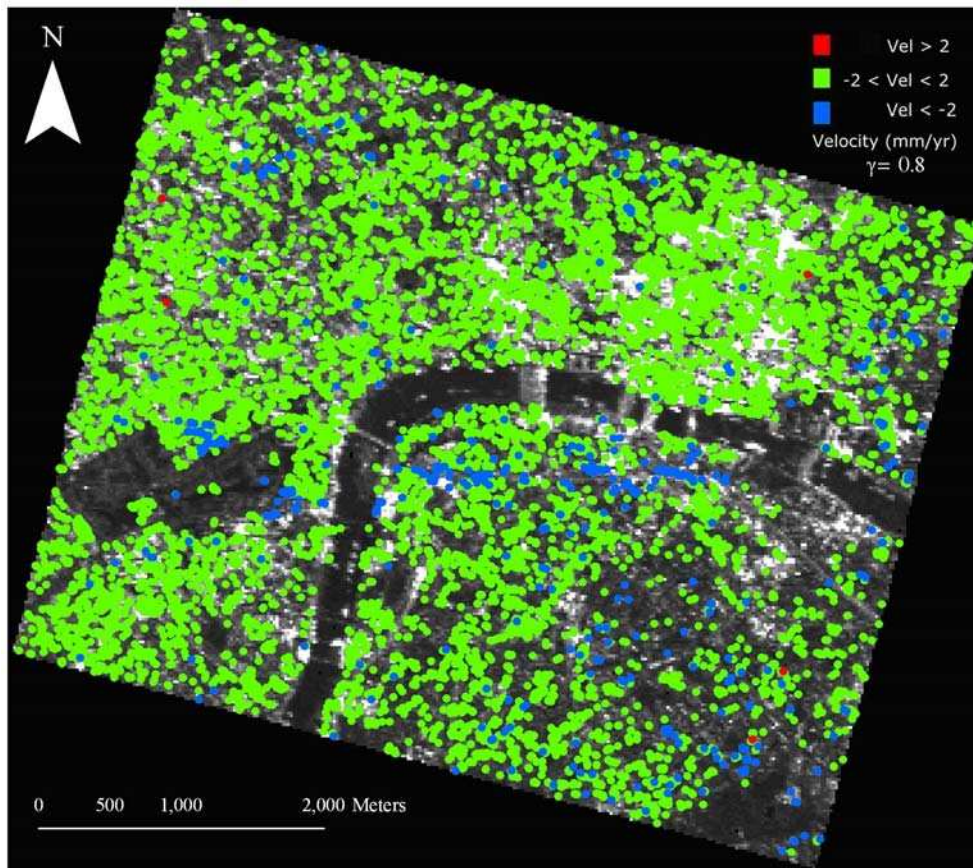
Figure 9.31 Westminster: Velocity map 1. Mean amplitude image of the Westminster test site with PS points overlaid.

	V>2	15
	1<V≤2	148
Number of PS Points with	0<V≤1	1149
	-1<V≤0	5751
	-2<V≤-1	2452
	V≤-2	937
	Total	10452

Table 9.4 Westminster: Classification of PS points for velocity map 1.

The PS coverage is good, with points occurring in many regions of the test site. The majority of the PS points are green showing no significant motion, but there are also quite a few blue PS points, with velocities less than -2mm/yr. Deformation due to the Jubilee Line extension can clearly be seen south of the Thames as the line of blue PS points going in a westerly direction and crossing the river. A time series of one of the PS points on the Jubilee Line is shown below in Figure 9.32. There are also other points suggesting deformation around the image; there is a line of PS points in the top left corner of the image,

197

a group on the right hand side of the image and south of the Thames there appears to be a random coverage.
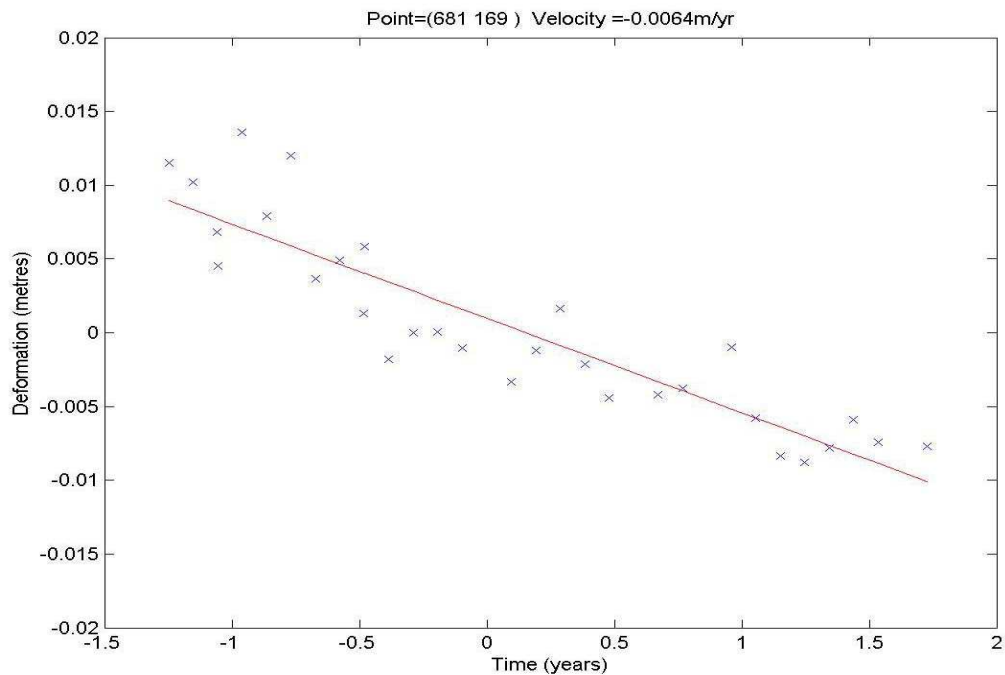
Figure 9.32 Westminster: PS point time series (for a point located on the Jubilee Line Extension). The linear fit shows a mean velocity of -6.4 mm/yr.

9.5.2.1 Using Methods of 9.5.1

Using the same procedure as in section 9.5.1, the results have been re-processed at a PS candidate point which appeared as a stable point in the Linear Algorithm analysis. The signature of the reference point from the filtering step has been removed from every pixel before identification of PS points takes place. The reference point selected has row and column location (336,219). The result is shown in Figure 9.33 and Table 9.5. Again the area of deformation due to the Jubilee Line extension can clearly be seen, though with fewer PS points, and also the deformation at the top left corner of the image is identified. But there also appears to be some large areas that suggest uplift is occurring, represented by the red dots. Because these were absent from the previous analysis (Figure 9.31) it is suggested that these are caused by errors in the phase unwrapping, which in turn passes through into the APSs.
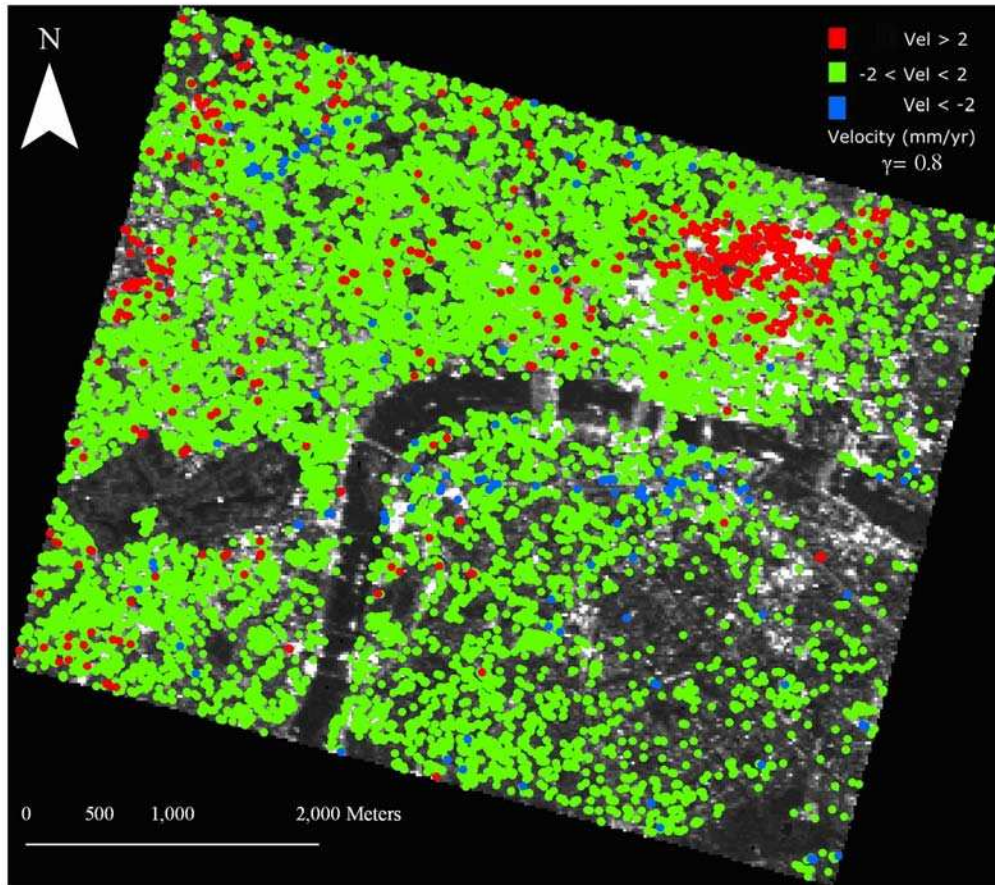
Figure 9.33 Westminster: Velocity map 2. PS points identified after removal of reference point filter signature phase. Reference point used to unwrap is (336,219).

		V>2	1395
Number of PS Points with		1<V≤2	4087
		0<V≤1	5929
		-1<V≤0	3221
		-2<V≤-1	331
		V≤-2	149
		Total	15112

Table 9.5 Westminster: Classification of PS points for velocity map 2.

The APSs for this set of data are shown in Figure 9.34. The only difference in the generation of these APSs and the ones shown previously in Figure 9.30 is the reference point used in the phase unwrapping stage. Comparing the two sets of images it can be seen that, although the structure of the APSs is largely the same the average value of them has changed. For example, APS 1 in Figure 9.30 has values largely less than 0 radians, whilst in Figure 9.34 APS 1 has many areas greater than 2 radians. On many of the APSs there is a circular area in the bottom right of the images that appears as tightly wrapped fringes; this

corresponds to the Buckingham Palace/Green Park/St James's Park area of the test site. Because there are only two candidate PS points in this region (both relating to Buckingham Palace) the APS estimation here is limited and could cause this anomaly. To see what could be causing the areas of uplift it is easier to view the differences between the APSs.
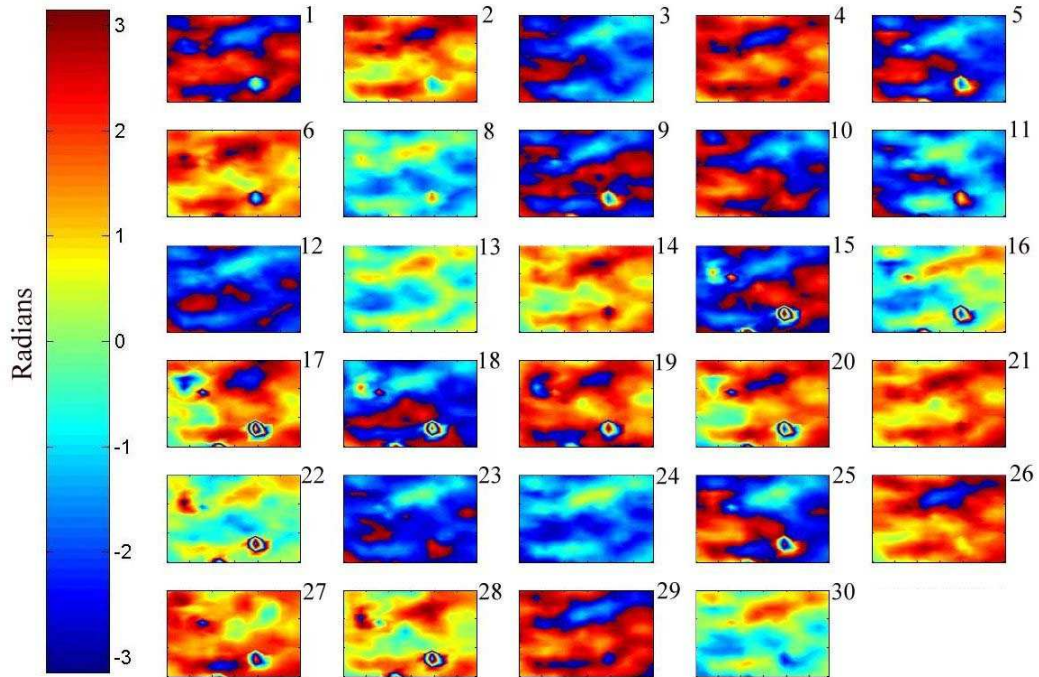
Figure 9.34 Westminster: Wrapped Atmospheric Phase Screens for the 29 deformation interferograms (where the reference point for the phase unwrapping is (336,219)).

These are shown in Figure 9.35 below. From these it is much easier to see that the mean value of each APS has changed but that the structure remained virtually the same. The main differences occur at the aforementioned Green Park region and at regions in the top left and bottom centre of the images. The top left region corresponds with the large area of red PS points north of the Jubilee Line, whilst the bottom centre region corresponds with the cluster of red points on the east of Figure 9.33. It is proposed that it is these differences in the estimated APS that has caused the large regions of red PS points in Figure 9.33. The APS anomalies are likely to have been caused by phase unwrapping errors.
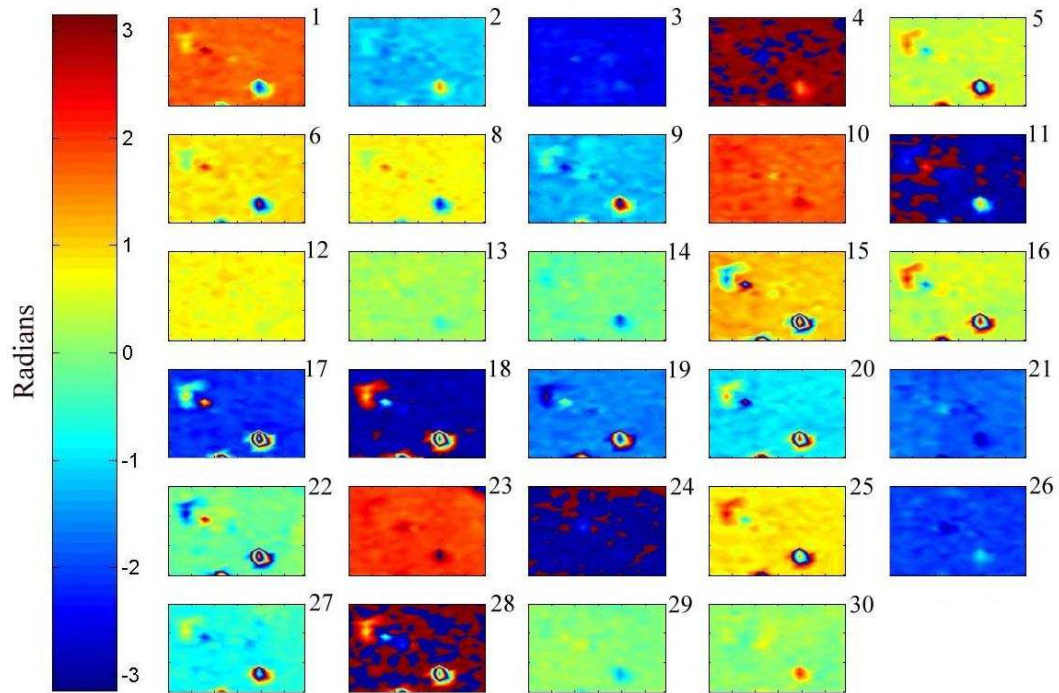
Figure 9.35 Westminster: Differences in the Atmospheric Phase Screens for the 29 deformation interferograms (Figures 9.30 & 9.34).

9.6 Summary

A method of PSInSAR, demonstrated by Ferretti, has been discussed and the differences between this and the previous Linear Algorithm have been highlighted. The method has been used as a basis for the development of the Non-Linear IAS 3-pass PSInSAR Algorithm, which uses a 3-Pass framework rather than the 2-Pass framework of Ferretti. The 3-Pass algorithms have been tested using the same simulated data as in chapter 7. The results look promising and similar to those attained in chapter 7 using the Linear Algorithm. The algorithm has then been tested using real data, using the same configurations as in chapter 8 for the Linear Algorithm and over the same test sites. The results from this have highlighted the importance of the various stages in the processing chain.

- Choice of Reference Point – Different results have been attained when using different reference points. It is important that the point selected is stable, i.e. suffering from no deformation. Ideally a candidate PS point

201

with known deformation history should be used, e.g. a corner reflector with GPS observations.

- Phase Unwrapping – Due to the noisy interferograms phase unwrapping is difficult, and can only be achieved over the sparse network of candidate points using many interferograms (*Ferretti et al 2000a*). Even so, errors still occur and can easily pass through into the APS estimates and cause erroneous measurements to be made. Errors from phase unwrapping will often increase in magnitude as points get further away from the reference point.

- Choice of Filter – When filtering the data to retrieve the low-pass temporal phase component, different results will be got from different filters. The triangular filter was seen to give a non-linear signature on purely random data, and therefore is likely to give erroneous results on the real data. A rectangular convolution was found to be inappropriate for identifying the non-linear motion. The filter signature of the reference point should be removed, since this is assumed stable and therefore deviations from 'stability' are considered errors due to the filter.

The results attained from the Non-Linear Algorithm, in general, agree well with those from the Linear Algorithm; the majority of PS points are showing that there is no significant deformation occurring, yet in the area of known subsidence some deformation is being detected. The quantitative values of the measured deformation cannot be validated properly without further ground measurements being available for comparisons. The two GPS stations used in the Greenwich test area suggest that no significant motion is occurring, which support the PS point results in the area.

10. Conclusions and Recommendations for Future Work

10.1 Introduction

The thesis has introduced a novel Persistent Scatterer method, with the developed algorithms implemented into a software framework. Using the software, the IAS PSInSAR method has been demonstrated over two test sites in the City of London, UK. The purpose of this chapter is to highlight the conclusions and give recommendations for future work in this area of research.

10.2 Integer Ambiguity Search

In chapter 4 the Integer Ambiguity Search (IAS) was introduced and the results of using it in three applications were shown:

1. Target Positioning

It has been shown that it is possible, using a ground control point (GCP), to reconstruct the absolute phase of the radar signal. Using this we can position the InSAR data into a geodetic data frame and get a 3-dimensional target position. If the interferogram has been phase unwrapped then it is possible to use this technique to generate a DEM from only one GCP.

2. Differential Interferometry

The method also has implications for differential interferometry. A re-working of Zebker's 3-pass DInSAR equations has been shown, taking advantage of the absolute phase rather than the flattened phase. By using the so called IAS 3-Pass method, the floating point offset due to elevation differences that was present in the traditional 3-Pass equations is no longer present. The IAS 3-Pass method was shown to give a result closer to a 2-Pass result than a traditional 3-Pass did with no post-processing applied.

3. Improved Differential Interferometry using a DEM

It was also shown in chapter 4 how, by using a coarse DEM to remove atmospheric anomalies from the topographic phase interferogram, it was possible under certain configurations to get better differential results using 3-

Pass than 2-Pass using the same coarse DEM. This is similar to methods employed in DEM generation routines.

10.3 Linear PSInSAR Algorithm

Using the Ferretti algorithm as a guide, a Persistent Scatterer Interferometry algorithm has been designed using an IAS 3-Pass method. This replaces the need for a DEM in constructing the differential interferograms and therefore DEM errors are not present in the differential phase, which in turn means that topographic height corrections do not need to be derived. In the atmospheric phase estimation stage of the algorithm, there is one less observation than there would be in a 2-Pass algorithm, but in the final velocity estimation there is the same and hence no loss of degrees of freedom. The IAS 3-Pass method has a clear benefit in that no topographic height error is present or needs to be modelled out.

Software has been created that implements the 3-Pass PSInSAR algorithms which allows for easier adaptation for future improvements and error budgeting. The software has been tested using simulated interferometric phase data before running it over the real SAR data.

The results of the real SAR data test were presented in chapter 8. The results of the Greenwich test site suggest that there is no significant motion occurring. The two GPS stations that are in the Greenwich area independently suggest that there is no significant motion also. A few points suggest that there is deformation occurring with velocities greater than 2mm/yr. These appear to be randomly distributed around the image and could be due to noise. The Westminster test site identified many more PS points, most of which suggested there was no significant motion occurring in the region. There are a few clusters of PS points suggesting deformation with velocities greater than 2mm/yr which correspond to areas of known subsidence, i.e. the Jubilee Line extension, but also a few PS points in areas outside of the extent of the Jubilee Line. There also appears to be a cluster of points showing uplift south of the Thames.

In general, the results show what was expected in these regions – that no overall relative motion is occurring. In the area of known deformation, some PS points have been identified which do show a deformation. These results show that a 3-Pass PSInSAR methodology is possible and gives promising results. Without further ground truth data a proper validation of the results is impossible. The restrictions on the size of the processing area mean this algorithm is not suitable for mapping large areas.

10.4 Non-Linear PSInSAR Algorithm

To avoid the restrictions on the size of the area to be processed, a non-linear algorithm based upon Ferretti's non-linear algorithm has been implemented. Again, it is based upon the IAS 3-pass algorithm and therefore does not require the use of a DEM to remove the topography nor does it introduce a topographic height error. The results of chapter 9 raise some interesting points. The first to note is that there are differences between the linear and non-linear results. Examining the Greenwich test site first shows the overall deformation given by the two methods agrees; there is no significant motion detected. But the number of PS points identified and their locations differs. In the non-linear case, the threshold for identifying PS points was lowered from 0.8 to 0.7 due to the low number of PS points identified at 0.8; the PS velocity classification boundaries were correspondingly increased. This could be a side-effect of the APSs being different for both methods; for some of the interferograms the APS agree between the two methods but for some they do not. Without additional information about the atmospheric delay it is impossible to say which APS result is closest to the correct result. Further work is needed to discover why this is, but it may be to do with the phase unwrapping in the non-linear method. With the use of extra data sources it could be possible to examine which of the APS results are good or even use the data to aid the atmospheric estimation. Data sources that could be useful for this are Met Office GPS ZTD/IWV data and Advanced Very High Resolution Radiometer (AVHRR) imagery data (*Leighton et al 2005*) or Medium Resolution Imaging Spectrometer (MERIS) or Moderate Resolution Imaging Spectroradiometer (MODIS) data (Moisseev *et al*

2003; Li 2005). GPS IWV or ZTD data is unlikely to be dense enough to use alone.

By phase unwrapping from different reference points, different results are attained. This could be due to both the behaviour of the reference scatterer over time and also phase errors that occur in the unwrapping process. An important assumption in the process is that the reference point is stable, i.e. no deformation is occurring there. If this does not hold then the deformation propagates through into the other PS points as the deformation at these points is measured relative to the reference point. The differences between Figures 9.21 and 9.22 are clear to see; although both show in general that no significant motion is occurring, Figure 9.21 has clusters of points with a velocity greater than +3mm/yr whilst Figure 9.22 has clusters of points with a velocity less than -3mm/yr. Without extensive ground truth and surveys of the region it is impossible to say which of the results are better.

Another interesting outcome of the results is shown in Figure 9.23; that points from the same data processing set exhibit similar time series trends. This appears to be due to the temporal filtering stage giving erroneous results. The reference point, which must be assumed stable, is showing artefacts after the filtering stage suggesting some kind of sinusoidal motion. Tests have shown this type of signature is produced even from random data (Figure 9.24), and so it is assumed to be errors from the filter and must be removed. The signature from the reference point is removed from every other point (and itself) prior to PS identification. This resulted in almost tripling the number of PS points that was identified.

For the Westminster test site the PS analysis has highlighted the area of known deformation. It also helped to highlight that errors in the APS estimation can cause errors in the velocity estimations, causing apparently deforming zones. The PS measured deformation rates of the Jubilee Line Extension vary between approximately -2mm/yr and -7mm/yr.   To do a quantitative analysis on the measurements of the deformation more ground truth is required.

These results highlight the importance of both needing a stable reference scatterer and applying a suitable filter to remove any non-linear motion.

10.5 Overall Conclusions

A recap of the original project aims and objectives follows together with a discussion on whether each one has been met or not.

- *Validate that the Integer Ambiguity Search (IAS) method works with real satellite SAR data* – In chapter 4 the IAS has been tested with real data of the London region, UK, and the results have been reported. The resulting DEM from the process has accuracies similar to those reported elsewhere. A precise measurement validation could be achieved if the InSAR and GPS/levelling data can be tied together, e.g. using corner reflectors with known phase centres.

- *Test the theory that the Integer Ambiguity Search method can improve upon current 3-pass Differential Interferometry by using experimental results* – In chapter 4 the results of an IAS differential analysis have been reported. The results show that the IAS method eliminates the need to post-process 3-Pass data to remove the floating point offset which is caused by height discrepancies between the modelled and true surfaces. The IAS 3-Pass and 2-Pass results are equivalent except for errors in 2-Pass being DEM related, errors in 3-Pass being related to topographic interferogram. In general, DEM errors will be smaller in magnitude.

- *Develop a Persistent Scatterer algorithm and processing chain that does not output a topographic height model, i.e. it does not need to calculate reference surface corrections* – A novel 3-Pass PSInSAR method has been proposed in chapter 5 and in chapter 9, in which a reference surface error correction term is absent. A DEM has been used to aid in phase unwrapping the interferograms. This is done in a way such that the floating point DEM error does not propagate through into the phase values, although it is possible to get errors of integer multiples of 2π. This will be more problematic for large baseline interferograms or if a coarse DEM is used.

- *Test and validate the Persistent Scatterer Algorithm using a suitable test site* – The developed algorithms have been tested first using simulated data so as to check how accurate the derived results were. The results attained, shown in chapter 7, demonstrate that the algorithms appeared to work well on the simulated test data, and the derived APSs largely agreed with the input atmospheres. Two test sites encompassing areas of London have been selected to test the two 3-Pass PSInSAR algorithms using real SAR data, the results for which have been presented and discussed in chapters 8 and 9. Results have successfully been achieved from a 3-Pass PSInSAR method, showing that it is possible to get results without introducing a topographic height error. In chapter 8 GPS data from two stations have been shown for one of the test sites. From the GPS no significant motion can be detected, which agreed with the PS results in that area. In chapter 9 there are PS points located nearby to the two GPS stations. A time series plot of each GPS station's data together with the data from a nearby PS point have been shown and both plots suggest that no significant motion is occurring.

It is also prudent here to mention the accuracy and precision of PS InSAR. At the moment there is no one parameter that can give a definite measurement of the accuracy and precision of the individual PS points, due to the complex nature of the various processes involved in deriving the PS results. Factors that could affect the precision and/or accuracy of the results range from the initial processing of the raw SAR data to SLC format to the interferometric processing and the choice of filters, unwrapping techniques and interpolation methods used in the processing of the data. Also the amount of data used in the study, the area under study, the radar, the weather and the quality of any reference points used can affect the quality of the results. A full error budgeting of the PS techniques is a key process to try and identify a sufficient parameter to describe the quality of the results. The quality of results is one question that arose from the PSIC4 validation study *(Crosetto and Engdahl 2006)*.

10.6 Future directions

There is much future research that is needed in the field of PSInSAR. As far as the IAS 3-Pass PSInSAR algorithms go, future research should be focussed in two directions:

- Improving the algorithms
  - Adding 4-Pass capability – With a 4-Pass PSInSAR framework differential interferograms can be formed without the constraint of a single master image. This gives greater freedom to choose how to construct the interferogram pairs, e.g. only select baselines (temporal or geometric) under a certain size. This may allow specific algorithms to be used for different regions, which could give better results.
  - Less phase unwrapping – At present the algorithm needs to unwrap all the interferograms before generating the 3-Pass results. With a small change to the software it would be possible to generate results with only unwrapping the topographic interferogram. This would reduce the possibility of 2π phase errors being introduced but would mean that a linear method of finding the topographic phase error is no longer suitable; a periodogram method would be needed.
  - Further research on atmospheric estimation – The atmospheric estimation is key to getting good results. The simplistic filtering regime employed should be reworked to better estimate the temporal non-linear motion.   The network adjustment phase unwrapping routine could also be updated to a more robust phase unwrapping algorithm.
  - Extend the software – The software has been written to test the algorithm over small areas. It should be reworked so that larger areas can be examined. Also, further functionality could be introduced into the software including a choice of different algorithms for sections of the processing.

- Better PS position information
  - The IAS allows 3-D positions of InSAR data to be attained in a geodetic reference frame. With an estimate from each interferogram, this allows N separate estimates of the PS position to be derived. By averaging these estimates we could get an improved estimate by reducing the random errors.
  - Integration of PSInSAR data with GPS is much desired. To do a full integration it is required that precise observations are available for both the GPS and InSAR data. The IAS uses the phase of the scatterer to derive its full 3-D position, whereas 2-Pass methods use a PS height-corrected DEM. The IAS method should be more appropriate for integration since it derives the full 3-D position and not just the height position.

Appendix A – 4-Pass IAS Geometry

The main difference between 3-Pass and 4-Pass DInSAR is that there is no common SAR image in the 4-Pass technique. However, the interferograms will have to be generated onto a common grid so that the phase can be differenced. The difficulty with 4-Pass in the IAS framework is in constructing the deformation pair baseline declination angle. Recall, from chapter 4, that the interferometric phase can be calculated by the equation:

$$\frac{4\pi}{\lambda} B \cos \beta = \phi + \frac{4\pi}{\lambda} \delta e \qquad\qquad \text{A1}$$

and the differential phase by solving:

$$\phi_{diff} = \left(\phi_D + \frac{4\pi}{\lambda} \delta e_D \right) - \frac{B_D}{B_T} \left(\phi_T + \frac{4\pi}{\lambda} \delta e_T \right) + \frac{4\pi B_D}{\lambda} \left(\cos \beta_T - \cos \beta_D \right) \qquad \text{A2}$$

where β_D is constructed via β_T and the angle between the two baselines, as shown in Figure 4.6 repeated here as Figure A1, with subscripts D and T replaced with 13 and 12 respectively.
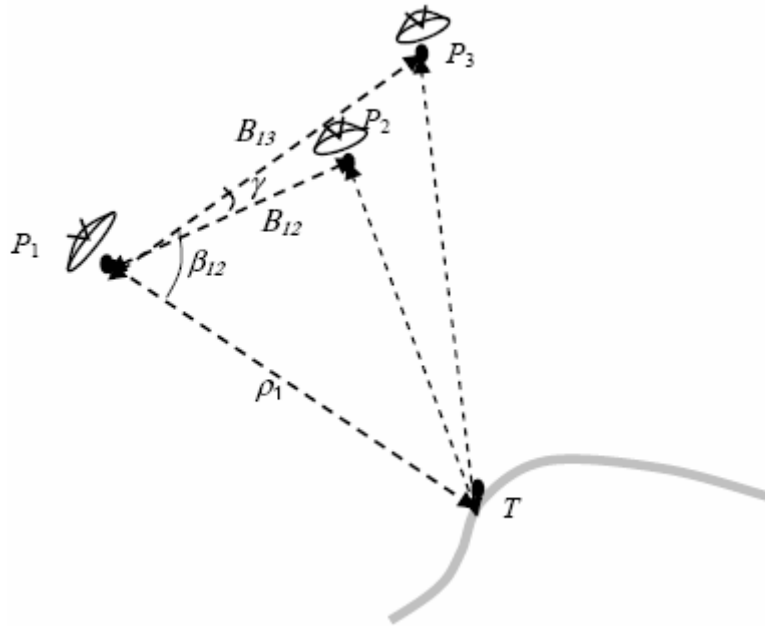

Figure A1 Geometry of the IAS 3-Pass technique

To calculate the 4-Pass differential phase the same equation A2 can be used with β_D again calculated using β_T and the angle between the two baselines. This can be accomplished by a series of rotations and translations such that the

4-Pass geometry resembles that of the 3-Pass, i.e. all satellites are in the plane with the two masters coincident. Suppose, without loss of generality, that the geometry of Figure A2 is appropriate, where MT, ST and MD, SD are the satellites of the topographic and deformation pairs respectively. β_T and β_D are the respective baseline declination angles and P is the target. Essentially there are 2 planes, PMTST and PMDSD, which bisect at point P. One such way to proceed would be to apply a rotation to PMDSD about P such that the result is that all MD, MT, P and ST lie in a plane. Then a second rotation, applied this time to SD about MD such that all satellites are in the same plane along with P.

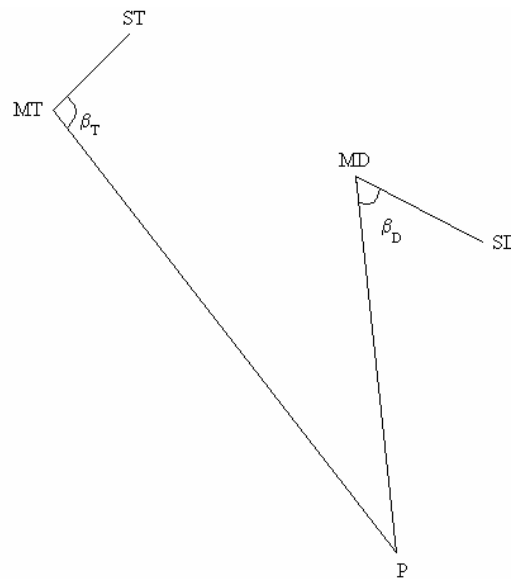Figure A2 4-Pass Satellite Geometry

Then translate the vector MDSD such that MD and MT are coincident and apply a rotation such that vectors MTP and MDP are coincident also, as shown in Figure A3. Now we have geometry similar to that of 3-Pass and can proceed with the calculation of β_D and the differential phase.
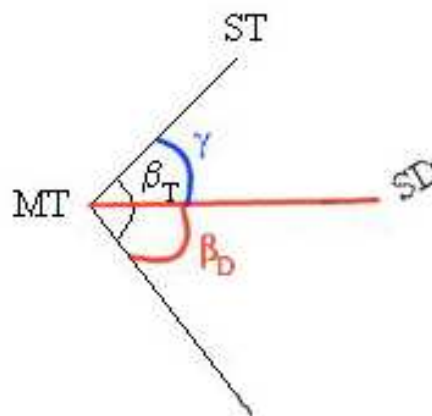
Figure A3 Final 4-Pass geometry (now equivalent to the 3-Pass geometry).

Appendix B – Phase Unwrapping

The unwrapping of the phase residuals in the Non-Linear IAS 3-pass PSInSAR technique is performed using a least squares technique. It is similar to a simple network adjustment. The problem and model are described below.

Problem:

Consider a collection of n points in a triangular network with unknown phase values. If there are m observations of the gradients (phase differences) between the n points, estimate the phase values of the n points.

Solution:

The problem can be described by Figure B1. Here we have 5 points connected in a triangular network with unknown phase values x_0, x_1, x_2, x_3, x_4. There are 7 observations of the phase differences, l_i, where $l_i = x_j - x_k$ with $i = 1, 2, \ldots, m$ and $j, k \in \{0, 1, \ldots, n\}$ where $j \neq k$. We need to estimate the 5 values of x_i using the 7 observations l_i.
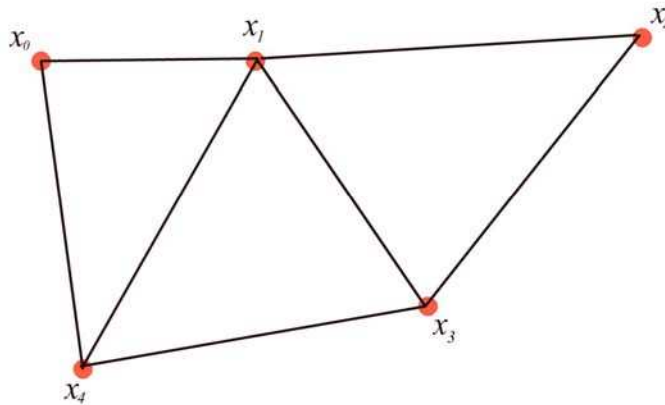
Figure B1 Description of the phase unwrapping problem.

To start the unwrapping we need a stable reference point. Consider, without loss of generality, that x_0 is stable and has been observed with value l_0. Then a system of equations can be formed such that:

$$
\begin{aligned}
v_0 &= \hat{x}_0 - l_0 & & i = 1, 2, \ldots, m \\
v_i &= \hat{x}_j - \hat{x}_k - l_i & & j, k \in \{0, 1, \ldots, n\}
\end{aligned}
$$

where $\hat{x}_i$ are estimates of x_i and v_i are residuals to be minimised. This system of equations can be easily described in matrix notation as:

$$v = A\hat{x} - l$$

where v, $\hat{x}$ and l are vectors of the residuals, estimates and observations respectively. A is the design matrix made up of 1's and 0's.

To minimise v in this equation we use the simple least squares solution which can be solved easily. The solution to the problem, when introducing weights to the observations, is given by:

$$\hat{x} = (A^T W A)^{-1} A^T W l$$

where superscript T denotes matrix transpose and W is the matrix of weights.

Appendix C – Filter Tests

As mentioned in chapter 9, the filtering of the data is an important step. Some tests have been completed using different filters to examine which perform best. The first set of tests was mentioned in chapter 9; a rectangular and a triangular filter have been used on different data sets to try and identify the original signal buried in noise. The variance of the noise used here was 1 radian. The second set of tests were to proceed through the processing chain using a triangular filter, rectangular filter and no filter to see what the PS coverage was like. The results of the tests follow.

The first test was to see how well a triangular filter and rectangular filter could work on retrieving the signal from 3 different data sets; a sinusoidal signal with period 1 year, a sinusoidal signal with period 6 years and a signal with a sudden shift. The results for these tests are shown below.

Figure C1 Filtering a noisy sinusoidal signal of period 1 year. The top graph shows the original signal, the second graph shows the original signal + noise, the third graph shows the filtered signal using a triangular filter and the bottom graph shows the filtered signal using a rectangular filter.

It can be seen from Figure C1 that out of the 2 filtered results the triangular filter gives the better result, at least showing a sinusoidal result, whereas the rectangular filtered result is unrecognisable.
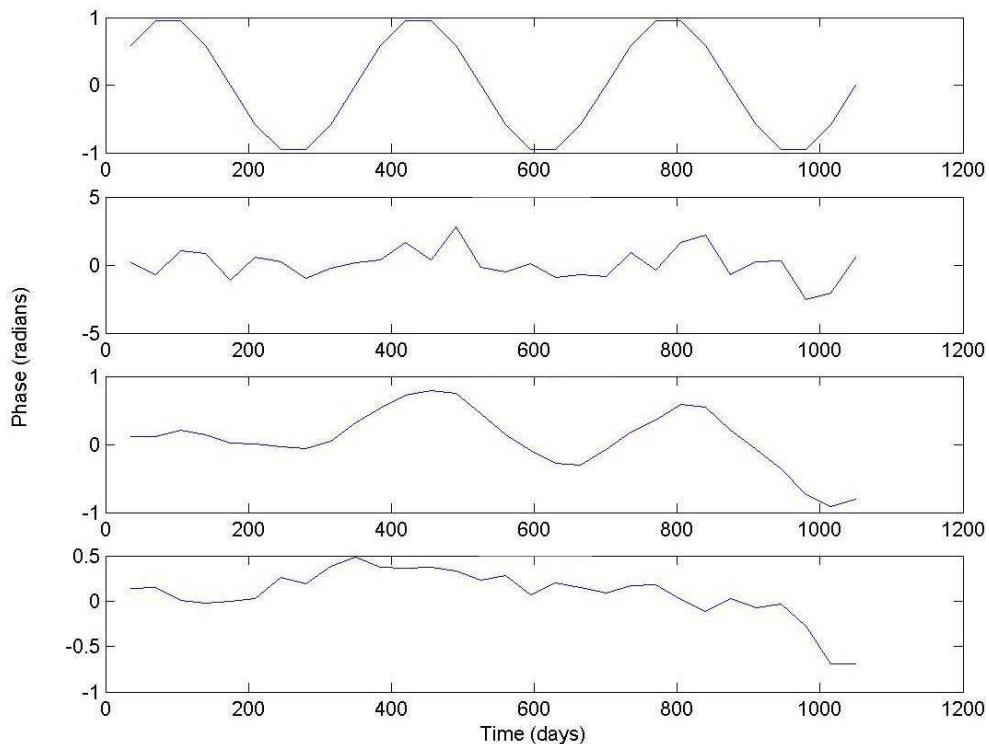

Figure C2 Filtering a noisy sinusoidal signal of period 6 years. The top graph shows the original signal, the second graph shows the original signal + noise, the third graph shows the filtered signal using a triangular filter and the bottom graph shows the filtered signal using a rectangular filter.

Figure C2 shows the results of filtering a noisy sinusoid on period 6 years. Both filters have identified a similar shape as to the true signal, but the triangular filter has produced a smoother result than the rectangular one.

Figure C3 shows that neither of the filters identify the shift present in the original phase signal, but both smooth the noise significantly. From the 3 sets of results we can conclude that the triangular filter has been a better performer overall, since it identified the two sinusoidal signals reasonably well but failed on identifying the phase shift. The rectangular filter only identified the larger period sinusoid signal. Since the PS points may show seasonal deformation, it is important to be able to identify sinusoids of period 1 year, so it is recommended that the triangular filter is used and not a rectangular filter.
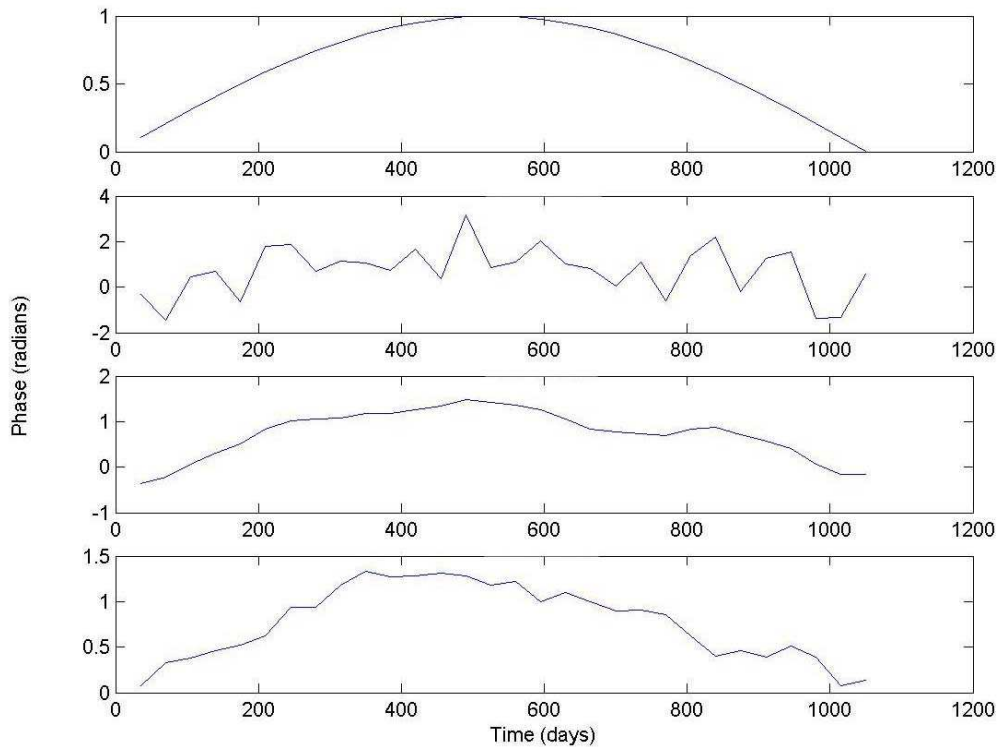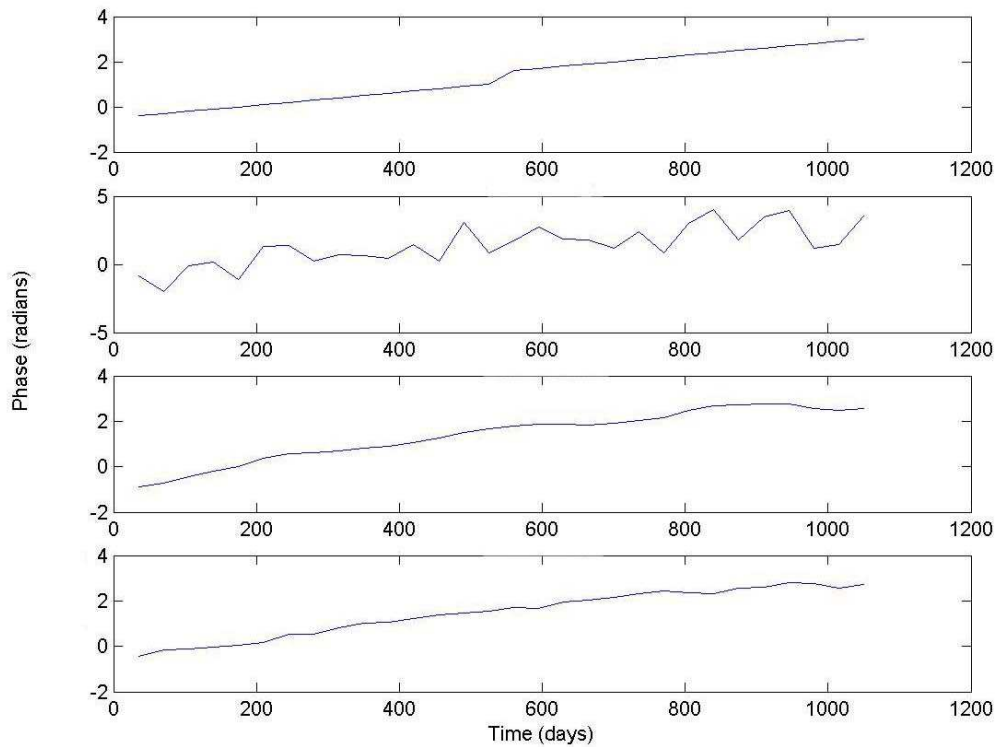
Figure C3 Filtering a noisy signal with a sudden shift. The top graph shows the original signal, the second graph shows the original signal + noise, the third graph shows the filtered signal using a triangular filter and the bottom graph shows the filtered signal using a rectangular filter

Three further tests have been completed; the full processing chain has been performed using a different filter: a triangular filter of length 350 days, a rectangular filter of length 350 days and no filter. The final PS location map of each test is shown below in Figure C4. The filtered signature at the reference point has not been removed from the results here, which may explain why doing no filtering appears to identify more PS points. The rectangular filter identifies more PS points than the triangular filter, which is likely due to the signature of the reference point. A rectangular filter, because of its equal weights, will produce a 'flatter', more linear signature than the triangular filter. Using no filter will mean that any non-linear motions are passed through into the atmospheric phase screens which will then be smoothed and lost.

217

(i)

(ii)

(iii)
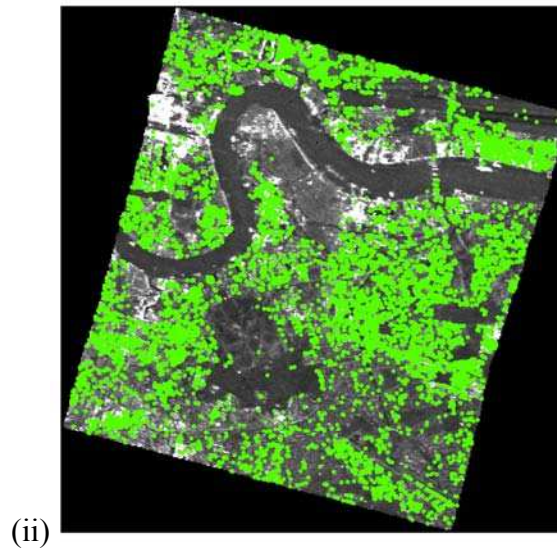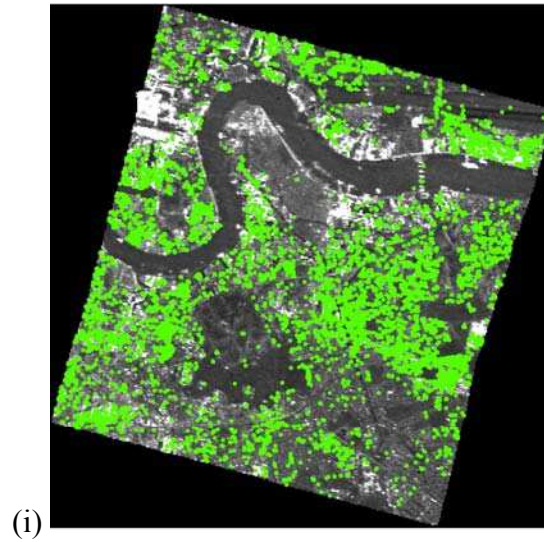
Figure C4 Final PS point location maps for the 3 filtering tests. (i) shows the PS point locations
when a triangular filter has been used to identify the non-linear motion. (ii) shows the PS point
locations when a rectangular filter has been used to identify the non-linear motion. (iii) shows
the PS point locations when no temporal filtering takes place.

References

Ashkenazi, V., Jones, D.E.B., Lowe, D.P., and Woodhams, J.W. (1993), "Reservoir deformation monitoring by GPS satellites", *Surveying World,* September 1993.
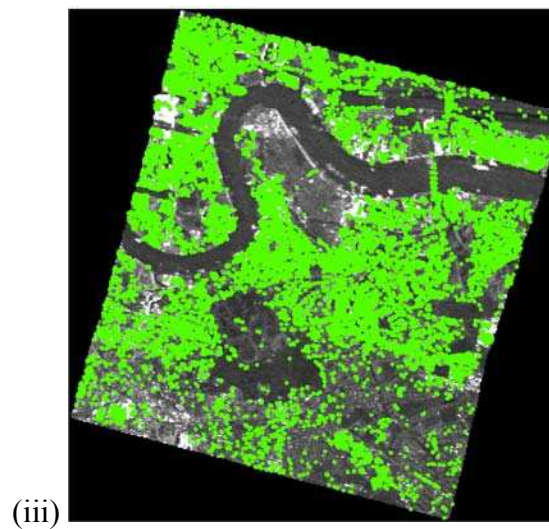
Ashkenazi, V., and Roberts, G.W. (1997), "Experimental monitoring of the Humber bridge using GPS", *Proceedings Institute of Civil Engineering*, November 1997, pp177-182.

Askne, J., and Smith G. (1996), "Forest INSAR decorrelation and classification properties", *Proceedings of the Fringe Workshop 1996, Zurich, Switzerland*, pp 95-103.

Bamler, R, and Hartl, P. (1998), "Synthetic aperture radar interferometry." *Inverse Problems* 14: R1-R54.

Beradino, P., Fornaro, G., Lanari, R., and Sansosti, E., (2002), "A new algorithm for surface deformation monitoring based on small baseline differential SAR interferograms", *IEEE Transactions on Geoscience and Remote Sensing,* Vol. 40, No. 11, pp 2375-2383.

Bern, M., and Eppstein, D. (1992), "Mesh generation and optimal triangulation", *Computing in Euclidean Geometry,* 2nd Edition, D.-Z. Du and F. K. Hwang (editors), World Scientific, pp 47-123.

Bingley, R.M., Ashkenazi, V., Penna, N.T., Booth S.J., Ellison, R.A., and Morigi, A.N. (1999), "Monitoring changes in regional ground level using high precision GPS", *Environment Agency R&D Technical Report W210.*

Bovenga, F., Nutricato, R., Refice, A., Guerriero, L., and Chiaradia, M.T. (2004), "SPINUA: A flexible processing chain for ERS/Envisat long term

interferometry", *Proceedings of the 2004 Envisat & ERS Symposium (ESA SP-572). 6-10 September 2004, Salzburg, Austria.*

Campbell, J.B. (1996), "Introduction to remote sensing, 2nd Edition", *Taylor and Francis Ltd.,* London, ISBN: 0748406638.

Chen, C. W., and Zebker, H.A. (2000), "Network approaches to two-dimensional phase unwrapping: intractability and two new algorithms." *Journal of the Optical Society of America,* Vol. 17, No. 3, pp 401-414.

Chen, C. W., and Zebker, H.A. (2001), "Two-dimensional phase unwrapping with use of statistical models for cost functions in non-linear optimization." *Journal of the Optical Society of America A,* Vol. 18, pp 338-351.

Chu, D. (2004), "The GLOBEC Kriging software package – EasyKrig3.0", [online], *http://globec.whoi.edu/software/kriging/easy_krig/easy_krig.html*

Closa, J. (1998), "The influence of orbit precision in the quality of ERS SAR interferometric data." *ESA Document No: ES-TN-APP-APM-JC01.*

Colesanti, C., Ferretti, A., Novali, F., Prati, C., and Rocca, F. (2003a), "SAR monitoring of progressive and seasonal ground deformation using the Permanent Scatterers technique", *IEEE Transactions on Geoscience and Remote Sensing*, Vol. 41, No. 7, pp. 1685-1701.

Colesanti, C., Ferretti, A., Prati, C., and Rocca, F. (2003b), "Monitoring landslides and tectonic motions with the Permanent Scatterers technique", *Engineering Geology,* Vol. 68, pp3-14.

Constantini, M. (1998), "A novel phase unwrapping method based on network programming." *IEEE Transactions on Geoscience and Remote Sensing,* Vol. 36, No. 3, pp 813-821.

Cressie, N.A.C. (1993), "Statistics for spatial data, revised edition", *John Wiley and Sons,* ISBN: 0471002550.

Crosetto, M. (2002), "Calibration and validation of SAR interferometry for DEM generation." *ISPRS Journal of Photogrammetry & Remote Sensing,* Vol. 57, pp 213-227.

Crosetto, M., and Engdahl, M., (2006), "PSI validation workshop, ESRIN 18-19 September 2006: Open questions & appendix", [online] http://earth.esa.int/psic4/PSI_Validation_workshop_report.pdf

Curlander, J., and McDonough, R. (1991), "Synthetic aperture radar: systems and signal processing", *John Wiley and Sons*, ISBN: 047185770X.

Dixon, T. H. (1991), "An introduction to the Global Positioning System and some geological applications." *Review of Geophysics* , Vol. 29, No. 2, pp 249-276.

Delaunay, B. (1934), "Sur la sphere vide", *Bulletin of the Academy of Science USSR 7: Classe des Science Mathematiques et Naturelles,* pp 793-800.

Dominguez, J., Romero, R., Carrasco, D., Martinez, A., Mallorqui, J.J., Blanco, P., Navarrete, D. (2005), "Advanced DInSAR based on coherent pixels: development and results using CPT technique", *Proceedings of the FRINGE 2005 Workshop,* Frascatti, Italy, 28th November – 2nd December 2005.

Driscoll, R. (1983), "The influence of vegetation on the swelling and shrinking of clay soils in Britain", *Geotechnique,* Vol. 33, pp 93-105.

Driscoll, R. (1984), "The effects of clay soil volume changes on low-rise buildings", In *Ground Movements and their Effects on Structures*, Surrey University Press, ISBN: 0412003910.

Duro, J., Inglada, J., Closa, J., Adam, N., and Arnaud, A. (2004), "High-resolution differential interferometry using time series of ERS and Envisat SAR data", *Proceedings of the 2004 Envisat & ERS Symposium (ESA SP-572).* 6-10 September 2004, Salzburg, Austria.

Elachi, C. (1991), "Spaceborne imaging radars", *International Journal of Imaging Systems and Technology,* Vol 3, Issue 2, pp167-185.

Environment Agency Report, (2006), "Groundwater levels in the Chalk-Basal sands aquifer of the London Basin", [online], available: *http://www.environment-agency.gov.uk/commondata/acrobat/2006_reportfinal_1410644.pdf*

Farr, T.G. (1993), "Radar interactions with geologic surfaces", *in Guide to Magellan Image Interpretation, JPL Publication 93-24.*

Fernandez, J., Yu, T., Rodriguez-Velasco, G., Gonzalez-Matesanz, J., Romero, R., Rodriguez, A., Quiros, R., Dalda A., Aparicio, A., and Blanco, M. (2003), "New geodetic monitoring system in the volcanic island of Tenerife, Canaries, Spain; combination of InSAR and GPS techniques", *Journal of Volcanology and Geothermal research,* 124, pp241-253.

Ferretti, A., Prati, C., and Rocca, F. (1999), "Permanent Scatterers in SAR interferometry", *Proceedings IGARSS 99*, Hamburg, Germany, June 28-July 2.

Ferretti, A., Prati, C., and Rocca, F. (2000a), "Nonlinear subsidence rate estimation using Permanent Scatterers in differential SAR interferometry", *IEEE Transactions on Geoscience and Remote Sensing*, 38, pp. 2202-2212.

Ferretti, A., Prati, C., Rocca, F., and Colesanti, C. (2000b), "Validation of the Permanent Scatterers technique in urban areas", *Proceedings of ERS-Envisat symposium 2000,* Gothenburg, Sweden,

Ferretti, A., Prati, C., and Rocca, F. (2001), "Permanent Scatterers in SAR

interferometry", *IEEE Transactions on Geoscience and Remote Sensing*, Vol. 39, No. 1, pp. 8-20.

Fruneau, B., Achache, J., and Delacourt, C. (1996), "Observation and modelling of the Saint-Etienne-de-Tinée landslide using SAR interferometry", *Tectonophysics,* Vol. 265, pp 181-190.

Funning, G. J., Parsons, B., Wright, T. J., Jackson, J. A., and Fielding, E. J. (2005), "Surface displacements and source parameters of the 2003 Bam (Iran) earthquake from Envisat advanced synthetic aperture radar imagery", *Journal of Geophysical Research*, Vol. 110, B09406, doi:10.1029/2004JB003338.

Gabriel, A., and Goldstein R. M. (1988), "Crossed orbit interferometry: theory and experimental results from SIR-B" *International Journal of Remote Sensing,* Vol. 9, No. 5, pp 857-872.

Gabriel, A.K., Goldstein, R.M., and Zebker, H. (1989), "Mapping small elevation changes over large areas: differential radar interferometry" *Journal of Geophysical Research*, Vol. 94, No. B7, pp 9183-9191.

Ge, L., Han, S., and Rizos, C. (2000), "The Double Interpolation Double Prediction (DIDP) approach for InSAR and GPS integration"*, International Archives of Photogrammetry and Remote Sensing (IAPRS)*, Vol. XXXIII, Amsterdam.

Ghiglia, D., and Pritt, M. (1998), "Two-dimensional phase unwrapping: theory, algorithms and software", *John Wiley and Sons*. ISBN: 0471249351.

Goldstein, R.M., Zebker, H., and Werner, C.L. (1988), "Satellite radar interferometry: two-dimensional phase unwrapping" *Radio Science,* Vol. 23, No. 4, pp 713-720.

Goldstein, R. M., Engelhardt, H., Kamb, B., and Frolich, R.M. (1993), "Satellite radar interferometry for monitoring ice sheet motion: application to an Antarctic ice stream", *Science,* Vol. 262, December, pp 1525-1530.

Goldstein, R. M. (1995), "Atmospheric limitations to repeat-track radar interferometry", *Geophysical Research Letters,* Vol. 22, No. 18, pp 2517-2520.

Goldstein, R. M., and Werner, C. L. (1998), "Radar interferogram filtering for geophysical applications", Vol. 25, No. 21, pp 4035-4038.

Goodman, J.W. (1976), "Some fundamental properties of speckle", *Journal of Optical Society America*, Vol. 66, No. 11, pp 1145-1150.

Graham, L. C. (1974), "Synthetic interferometer radar for topographic mapping", *Proceedings of IEEE,* Vol. 62, pp 763-768.

Hanssen, R., and Feijt, A. (1996), "A first quantitative evaluation of atmospheric effects on SAR interferometry", *Proceedings of the Fringe Workshop 1996,* Zurich, Switzerland, September/October.

Hanssen R.F. (1998), "Atmospheric heterogeneities in ERS tandem SAR interferometry", *DEOS Report no 98.1, Delft University Press*, ISBN: 9040717745.

Hanssen, R., and Bamler, R. (1999), "Evaluation of interpolation kernels for SAR interferometry", *IEEE Transactions on Geoscience and Remote Sensing,* Vol. 33, No. 1, pp 318-321.

Hanssen, R. (2001), "Radar interferometry: data interpretation and error analysis", *Kluwer Academic Publishers*. ISBN: 0792369459.

Haynes, M., Culshaw, M., and Marsh, S. (2001), "Remote monitoring of natural survey point networks – for precision surveying of structural and ground movements"*, Engineering Surveying Showcase 2001*, Issue 2*,* October 2001.

Hellwich, O. (1999), "SAR interferometry: principles, processing, and perspectives", *Festschrift für Prof. Dr.-Ing. Heinrich Ebner zum 60. Geburtstag, Technische Universität München*, pp 109-120.

Hofmann-Wellenhof, B., Lichtenegger, H., and Collins, J. (2001), "GPS: theory and practice, fifth edition", *Springer-Verlag Wien*, ISBN: 3211835342.

Hooper, A., Zebker, H., Segall, P., and Kampes, B. (2004), "A new method for measuring deformation on volcanoes and other natural terrains using InSAR persistent scatterers", *Geophysical Reseach Letters,* Vol. 31, No. 23.

Hudnut, K.W., Bock, Y., Galetzka, J.E., Webb, F.H., and Young, W.H. (2001), "The Southern California Integrated GPS Network (SCIGN)", *The 10th FIG International Symposium on Deformation Measurements*, Orange, California, USA.

Imakiire, T., and Nakahori, Y. (2001), "GPS Earth Observation Network (GEONET) Japan", *International Conference - New Technology for a New Century, FIG Working Week 2001* in Seoul, Republic of Korea, 6-11 May 2001.

Jordan, R. L., Caro, E.R., Kim, Y., Kobrick, M., Shen, Y., Stuhr, F., and Werner, M. (1996), "Shuttle Radar Topography Mapper (SRTM)", *in Developments in Satellite Radar Altimetry,* SPIE 2598, pp 412-422.

Just, D., and Bamler, R. (1994), "Phase statistics of interferograms with applications to synthetic aperature radar", *Applied Optics*, Vol. 33, pp 4361-4368.

Kampes, B., and Usai, S. (1999), "The Delft Object-orientated Radar Interferometric Software", *Proceedings of the 2nd International Symposium on Operational Remote Sensing,* ITC, Enschede, The Netherlands, 16th August 1999, 4-pages.

Kampes, B., and Nico, A. (2003), "Velocity field retrieval form long term coherent points in radar interferometric stacks", *Proceedings of the IGARSS'03*, Toulouse, France, 21-25 July.

Kampes, B., and Nico, A. (2005), "The STUN algorithm for persistent scatterer interferometry", *Proceedings of the FRINGE Workshop 2005,* Frascatti, Italy, 28 November – 2 December 2005.

Kedem, B. (1984), "On the sinusoidal limit of stationary time series", *The Annals of Statistics*, Vol. 12, No. 2, pp 665-674.

Kircher, M., Hoffmann, J., Roth, A., Kampes, B., Adam, N., and Neugebauer, H. (2003), "Application of permanent scatterers on mining-induced subsidence", *Proceedings of the FRINGE Workshop 2003,* Frascatti, Italy.

Kocak, G., Buyuksalih, G., and Oruc, M. (2005), "Accuracy assessment of interferometric digital elevation models derived from the Shuttle Radar Topography Mission X- and C-band data in a test area with rolling topography and moderate forest cover" *Optical Engineering*, Vol. 44, No. 3, pp 1-7.

Lawerence Livermore National Laboratory (April 2005), "Monitoring Earth's subsidence from space", *Science and Technology Review* [online], *http://www.llnl.gov/str/April05/vincent.html*

Laur, H., Bally, P., Meadows, P., Sanchez, J., Schaettler, B., Lopinto, E., and Esteban, D. (2002), "Derivation of the backscattering coefficient σ_0 in ESA ERS SAR PRI products", *ESA Document No. ES-TN-RS-PM-HL09*.

Leberl, F.W. (1990), "Radargrammetric image processing", *Artech House*, Norwood, MA. ISBN: 0890062730.

Leighton, J.M., Sowter, A., and Warren M.A. (2005), "Atmospheric effects on 35-day repeat cycle ERS interferograms of London", *Proceedings of the FRINGE 2005 workshop,* Frascatti, Italy, 28 November – 2 December.

Leijen, F.J. van, Ketelaar, V.B.H., Marinkovich P.S., and Hanseen, R.F. (2005), "Persistent scatterer interferometry: precision, reliability and integration*", ISPRS Workshop on High-Resolution Earth Imaging for Geospatial Information,* Hanover, May 17th-20th.

Li, F. K., and Goldstein, R.M. (1990), "Studies of multibaseline spaceborne interferometric synthetic aperture radars" *IEEE Transactions on Geoscience and Remote Sensing,* Vol. 28, No. 1, pp 88-97.

Li, Z. (2005), "Correction of atmospheric water vapour effects on repeat-pass SAR interferometry using GPS, MODIS and MERIS data", *PhD Thesis, University College London,* London.

Lillesand, T., and Kiefer, R. (2004), "Remote sensing and image interpretation; fifth edition", *John Wiley and Sons*, ISBN: 0471152277.

Lopes, A., Nezry, E., Touzi, R., and Laur, H. (1993), "Structure detection and statistical adaptive filtering in SAR images", *International Journal of Remote Sensing,* Vol. 14, No. 9, pp1735-1758.

Maciaszek, J., and Szewczyk, J. (2001), "Use of satellite GPS technique in the measurement of deformations in the areas of mining exploitation", *The 10th FIG International Symposium on Deformation Measurements*, Orange, California, USA.

Mallorqui, J., Mora, O., Blanco, P., and Broquetas, A. (2003), "Linear and non-linear long-term terrain deformation with DInSAR (CPT: coherent pixel technique)", *Proceedings of the FRINGE Workshop 2003,* Frascatti, Italy.

Massonnet, D., Rossi, M., Carmona, C., Adragna, F., Peltzer, G., Feigl, K., and Rabaute, T. (1993), "The displacement field of the Landers earthquake mapped by radar interferometry", *Nature,* Vol. 364, 8th July.

Massonnet, D., and Rabaute, T. (1993), "Radar interferometry: limits and potential", *IEEE Transactions on Geoscience and Remote Sensing,* Vol. 31, No. 2, pp 455-464.

Massonnet, D., Briole, P., and Arnaud, A. (1995), "Deflation of Mount Etna monitored by spaceborne radar interferometry", *Nature,* Vol. 375, 15th June, pp 567-570.

Massonnet, D., Holzer, T., and Vadon, H. (1997), "Land subsidence caused by the East Mesa geothermal field, California, observed using SAR interferometry", *Geophysical Research Letters,* Vol. 24, No. 8, pp 901-904.

Massonnet, D., and Feigl, K.L. (1998), "Radar interferometry and its applications to changes in the Earth's surface", *Review of Geophysics,* Vol. 36, No. 4, pp 441-500.

Meadows, P., and Laur, H. (1998), "Exploitation of ERS SAR imagery for land applications", *Proceedings of the 2nd International Workshop on Retrieval of Bio- and Geo-physical Parameters from SAR Data for Land Applications,* ESTEC, Noordwijk, The Netherlands, 21-23 October.

Meyer, F., Kampes, B., Bamler, R., and Fischer, J. (2005), "Methods for atmospheric correction in InSAR data", *Proceedings of the FRINGE Workshop 2005,* Frascatti, Italy, 28 November – 2 December.

Moisseev, D., Hanssen, R., and Sabater, J. (2003), "Towards an atmosphere free interferogram; first comparison between ENVISAT's ASAR and MERIS water vapour observations", *Proceedings of the International Geoscience and Remote Sensing Symposium 2003 (IGARSS 03)*, Toulouse, France, 21-25 July.

NGA WGS84 geoid calculator, [online],

http://earth-info.nga.mil/GandG/wgs84/gravitymod/wgs84_180/intptW.html

NPA Group Ltd., "Applications and case studies: London, UK", [online], *http://www.npagroup.co.uk/insar/apps/london_psi.htm*

Olmsted, C. (1993), "Scientific SAR users guide", *Alaska SAR Facility*, www.asf.alaska.edu/reference/general/SciSARUserGuide.pdf

Perissin, D., and Rocca, F. (2005), "Urban DEM", *Proceedings of the FRINGE Workshop 2005,* Frascatti, Italy, 28 November – 2 December.

Raucoules, D., Maisons, C., Carnec, C., Le Mouelic, S., King, C., and Hosford, S. (2003), "Monitoring of slow ground deformation by ERS radar interferometry on the Vauvert salt mine (France). Comparison with ground-based measurement", *Remote Sensing of Environment,* Vol. 88, pp. 468-478.

Raucoules, D., Crosetto, M., Engdahl, M., Bourgine, B., Bremmer, C., De Michele, M., Dommanget, J.M., Tragheim, D., Bateson, L., and Veldkamp, H. (2005), "PSIC-4 validation activities", *Proceedings of the Fringe Workshop 2005*, Frascatti, Italy, 28 November – 2 December.

Reigber, C., Xia, Y., Kaufmann, H., Massmann, F., Timmen, L., Bodechtel, J., and Frei, M. (1996), "Impact of precise orbits on SAR interferometry", *Proceedings of the Fringe Workshop 1996,* Zurich, Switzerland, September/October.

Rizos, C., Han, S., Ge, L., Chen, H.Y., Hatanaka, Y., and Abe, K. (2000), "Low-cost densification of permanent GPS networks for natural hazard mitigation: first tests on GSI's GEONET network", *Earth Planets Space,* Vol. 52, pp 867-871.

Rodriguez, E., and Martin, J.M. (1992), "Theory and design of interferometric synthetic aperture radars", *IEE Proceedings- Part F* , Vol. 139, No. 2, pp 147-159.

Sabins, F. F. (1997), "Remote sensing: principles and interpretation", New York, *W. H. Freeman and Company*. ISBN: 0716724421.

Saastamoinen, J. (1973), "Contributions to the theory of atmospheric refraction", *Bulletin Géodésique,* Vol. 105, pp 279-298; Vol. 106, pp 383-397; Vol. 107, pp 13-34.

Scharroo, R., Visser, P.N.A.M., and Mets, G.J. (1998), "Precise orbit determination and gravity field improvement for the ERS satellites", *Journal of Geophysical Research,* Vol. 103, C4, pp 8113-8127.

Schwabisch, M. (1998a). "Large area DEM generation with ERS tandem data", *Proceedings of CEOS SAR Workshop, ESTEC, ESA*, pp 53-57.

Schwabisch, M. (1998b), "A fast and efficient technique for SAR interferogram geocoding", *Proceedings of the International Geoscience and Remote Sensing Symposium (IGARRS) 1998,* 6th-10th July 1998, Seattle, USA.

Skolnik, M. (2001), "Introduction to radar systems, 3rd Edition", *McGraw-Hill*, Singapore, ISBN: 007118189.

Slutsky, E. E. (1927), "The summation of random causes as the source of cyclic processes", English translation in 1937 in *Econometrics,* Vol. 5, pp 105-146.

Small, D. (1998), "Generation of digital elevation models through spaceborne SAR interferometry", PhD Thesis, *Department of Geography*, *University of Zurich*.

Sowter, A., Smith, D.J., Laycock, J.E., and Raggam, H. (1990), "An error-budget for ERS-1 SAR imagery", *GEC-Marconi Research Centre Report under ESA Contract 7689/88/HE-I: 238*.

Sowter, A. (2003a), "Phase ambiguity determination for the positioning of interferometric SAR data" *The Photogrammetric Record,* Vol. 18, No. 104, pp 308-324.

Sowter, A. (2003b), "The derivation of phase integer ambiguity from single InSAR pairs: implications for differential interferometry" *Proceedings of 11th FIG symposium on deformation measurements*, Santorini, Greece 2003.

Sowter, A., Warren M.A., and Bingley, R.M. (2004), "An assessment of the ambiguity search method for three-dimensional target positioning using spaceborne InSAR data", *Proceedings of the 2004 Envisat & ERS Symposium (ESA SP-572),* 6-10 September 2004, Salzburg, Austria.

Sowter, A., and Warren, M.A. (2005), "Reducing the DEM error effect in differential interferometry", *Proceedings of the FRINGE 2005 Meeting,* Frascatti, Italy, ESA.

Sowter, A., Warren, M.A., and Bingley, R.M. (2006), "The absolute positioning of spaceborne InSAR data using the Integer Ambiguity Method", *The Photogrammetric Record,* Vol. 21, No. 113, pp 61-75.

Stow, R. (1996), "Application of SAR interferometry to the imaging and measurement of neotectonic movement applied to mining and other subsidence/downwarp modelling", *Proceedings of the Fringe Workshop 1996,* Zurich, Switzerland, September/October.

Ulaby, F.T., Moore, R.K., and Fung, A.K. (1981), "Microwave remote sensing: active and passive, volume 1", *Artech House Inc.,* ISBN: 0890061904.

Ulaby, F.T., Moore, R.K., and Fung A.K. (1982), "Microwave remote sensing: active and passive, volume 2"*, Addison-Wesley,* London, ISBN: 0201107600.

Ulaby, F.T., Moore, R.K., and Fung A.K. (1986), "Microwave remote sensing: active and passive, volume 3", *Artech House Inc.,* ISBN: 0890061920.

van der Kooij, M. (1999), "Operational production of DEMs from ERS tandem data", *Proceedings of the FRINGE 1999 Workshop*, Liege, Belgium.

Vexcel Corporation, "Coherent target monitoring overview" [online], *http://www.vexcel.com/rd/sar/ctm/index.html*

Waltham, A.C. (1989), "Ground subsidence", *Blackie and Son*, ISBN: 0216925002.

Warren, M.A. (2003), "An assessment of the Thames regional GPS monitoring network for the validation of differential InSAR", *MSc Dissertation*, University of Nottingham.

Warren, M. A., Sowter, A., and Bingley, R.M. (2004), "A re-appraisal of the 1992 Landers earthquake InSAR data using the ambiguity search method", *Proceedings of the 2004 Envisat & ERS Symposium (ESA SP-572),* 6-10 September 2004, Salzburg, Austria.

Werner, C., Wegmuller, U., and Strozzi, T. (2002), "Processing strategies for phase unwrapping for InSAR applications", in *Phase Unwrapping with GAMMA ISP, Technical Report, 13-May-2002,*Gamma Remote Sensing.

Werner, C., Wegmuller, U., Strozzi, T., and Wiesmann, A. (2003), "Interferometric point target analysis for deformation mapping", *Proceedings of the IGARSS'03,* Toulouse, France, 21-25 July.

Whittaker, B., and Reddish, D. (1989), "Subsidence: occurrence, prediction and control", *Elsevier Science Publishers*, ISBN 0444872744.

Wieser, A., and Brunner, F.K. (2002), "Analysis of bridge deformations using continuous GPS measurements", *INGEO2002 2nd Conference of Engineering Surveying,* Bratislava, November 2002, pp45-52.

Williams, S., Bock, Y., and Fang, P. (1998), "Integrated satellite interferometry: tropospheric noise, GPS estimates and implications for interferometric synthetic aperture radar products", *Journal of Geophysical Research,* Vol. 103, No. B11, pp 27051-27067.

Worawattanamateekul, J., Hoffmann, J., Adam, N., Kampes, B., and Altermann, W. (2004), "Radar interferometry technique for urban subsidence monitoring: a case study in Bangkok and its vicinity", *Proceedings of the 2004 Envisat & ERS Symposium (ESA SP-572).* 6-10 September 2004, Salzburg, Austria.

Zebker, H.A., and Villasenor, J. (1992), "Decorrelation in interferometric radar echoes" *IEEE Transactions on Geoscience and Remote Sensing*, Vol. 30, No. 5, pp 950-959.

Zebker, H., Werner, C.L., Rosen, P., and Hensley, S. (1994a), "Accuracy of topographic maps derived from ERS-1 interferometric radar", *IEEE Transactions on Geoscience and Remote Sensing,* Vol. 32, No. 4, pp 823-836.

Zebker, H., Rosen, P.A., Goldstein, R.M., Gabriel, A., and Werner, C. (1994b), "On the derivation of coseismic displacment fields using differential radar interferometry: the Landers earthquake", *Journal of Geophysical Research,* Vol. 99, No B10, 19617–19634.

Zebker, H.A., Rosen, P.A., and Hensley, S. (1997) "Atmospheric artifacts in interferometric SAR surface deformation and topographic maps", *Journal of Geophysical Research,* Vol. 102, No. B4, pp 7547-7563.

Zirnig, W., Pride, R., Lingenfelder, I., Chiles, R., and Hausamann, D. (2004), "The PRESENSE and PIPEMON projects – defining the ways of using space-borne Earth Observation services for pipeline monitoring", *Proceedings of the International Gas Research Conference (IGRC) 2004,* Vancouver, Canada, 1-4 November.